THE UNIVERSITY OF
WARWICK

University of Warwick institutional repository: http://go.warwick.ac.uk/wrap

A Thesis Submitted for the Degree of PhD at the University of Warwick

http://go.warwick.ac.uk/wrap/3681

This thesis is made available online and is protected by original copyright.

Please scroll down to view the document itself.

Please refer to the repository record for this item for information to help you to cite it. Our policy information is available from the repository home page.

High Frequency Acousto-Electric Microsensors for Liquid Analysis

by

Irina Ionela Leonte

School of Engineering

University of Warwick

A thesis submitted to the University of Warwick

for the degree of Doctor of Philosophy

15 April 2008

CONTENTS

LIST OF FIGURES

LIST OF TABLES

ACKNOWLEDGMENTS

I would like to thank my academic supervisors Dr. Marina Cole and Professor Julian W. Gardner for their guidance and support during the course of this project.

My appreciation goes to the University of Warwick and Universities UK, who offered me essential material support during the first three years of my doctoral study.

My research trip to Georgia Tech was a unique professional opportunity which benefited from the constant assistance of Professor Peter Hesketh who welcomed me to his research group and hosted the fabrication process. I would also like to acknowledge Sir Arthur Shercliff Scholarship Fund which covered my travel expenses to the United States.

Many thanks go to my co-workers and co-authors Dr Guri Sehra, Mark Hunt, and Dr. Moses Noh for their help and stimulating exchanges of ideas. The technical support from Frank Courtney and Ian Griffiths has been extremely useful.

I am thankful to the people I have been working with at the Warwick Mathematics Institute, Rosalind Barber, Professor Mark Pollicott and Professor Sebastian van Strien, for their understanding, constant encouragements and, not least, for allowing me more flexible hours when doctoral work was becoming too pressing.

My friends have always been there for me in time of need – Catalina, Nicoleta, Mihai, Pat, Anca and Ovidiu, have shared with me the great and the difficult times alike.

Last but not least, I am most grateful to my parents for their love and unconditional support, for everything they have done for my personal and professional development. I am particularly indebted to my father for his patience and understanding and to my brother for all his support and encouragement.

DECLARATION

The work described in this thesis was conducted by the author, except where stated otherwise, in the School of Engineering, University of Warwick. The thesis has not been submitted for a higher degree at another university.

Parts of this work have been presented at international conferences and published in the scientific literature listed below:

- I. Leonte, M. Hunt, G. Sehra, M. Cole and J.W. Gardner, "SAW Bioliquids Sensor with RF Interrogation", *IEEE High Frequency Postgraduate Student Colloquium*, 6-7 September 2004, Manchester, UK, pp. 47-52.
- I.I. Leonte, M. Hunt, G. Sehra, M. Cole and J.W. Gardner, H.S. Noh and P.J. Hesketh, "Towards a wireless microsystem for liquid analysis", *Proceedings of the 3rd IEEE International Conference on Sensors,* 24-27 October 2004, Vienna, Austria, pp. 919-922.
- I.I. Leonte, G. Sehra, M. Cole, P. Hesketh and J.W. Gardner, "High Frequency SH-SAW Devices for Liquid Sensing", *Proceedings of Eurosensors XIX*, 11-14 September 2005, Barcelona, Spain.
- M. Cole, J.W. Gardner, I.I. Leonte, G. Sehra, H.S. Noh and P.J. Hesketh, "Voltage Modulated SAW Microtrap System: Smart Assaying of Biomaterials", *Proceedings of the 4th IEEE International Conference on Sensors,* 30 Oct.-3 Nov. 2005, Irvine, USA, pp. 1300-1303.
- I.I. Leonte, G. Sehra, M. Cole, P. Hesketh and J.W. Gardner, "Taste sensors utilizing high-frequency SH-SAW devices", *Sensors and Actuators B*, 118 (2006), pp.349-355.

ABSTRACT

Liquid sensors are required for a multitude of applications in the food and beverage sectors, in the pharmaceutical industry or environmental monitoring. The focus of this work is on the development of high frequency shear horizontal surface acoustic wave (SH-SAW) sensors for liquid media identification and characterisation.

Among the various types of surface acoustic wave modes propagating in solids, the SH-SAWs were found to be the most suitable for operation in liquids. Dual delay line and resonator sensor configurations were designed and fabricated on lithium tantalate ($LiTaO_3$) substrates; the design and the subsequent fabrication procedures of the sensors are described in detail. Furthermore, the electrical characterization of the sensors was carried out with a network analyser, and a comparative analysis was performed between sensors with different configurations. The interdigital transducers, used as the interface between the electrical and acoustic domains, presented good reflection coefficients and had near perfect matched impedances and return loss figures up to 45 dB. The insertion loss of the sensors varied with the surface conditions while it was improved by using total or partial metallization of the surface or employing grating structures on the propagation path.

The SH-SAW devices were exposed to basic taste solutions and all the sensor configurations tested were able to discriminate them well. Measurements were done in both standard wired set-ups and a semi-wireless set-up, thus proving the sensor's capability for remote operation. Further investigations regarding the electronic tongue applicability of the SH-SAW sensors were conducted on a two port resonator device. The resonator was tested with six basic taste solutions, with taste solutions with varying concentrations, with binary mixtures of taste solutions and proved successful in identifying all test samples. A multivariate analysis was performed on the resonator data, and confirmed that the sensor's responses are influenced by the physical properties of the tested solutions. The multiple linear models derived are statistically significant and can explain high percentage of the data variability, offering a simplified alternative to the complex analytical models of the SH-SAW sensors.

Also, a voltage modulated sensor system was proposed for smart assaying of biomaterials and its operation principle is described. The preliminary tests carried out showed a significant voltage effect on carbon nanoparticles. The voltage modulated system is proposed as an analytical microsystem for the screening of bacterial cells.

All sensors in this project had no bio-chemical selective layer making them non-specific, yet they create robust, durable and low-cost systems.

CHAPTER 1:

INTRODUCTION

1.1 INTRODUCING THE PROJECT

Human sensory tests are regularly employed in the food and beverages industries, environmental monitoring and other areas but results are based on subjective judgements and variations between panels can be up to 50% in terms of flavour units. Therefore, the development of 'objective' tools to detect taste is very much needed. Previous reports on artificial taste sensors often refer to them as so-called "electronic tongues" [1, 2]. The most common types of sensors used are based on electrochemical techniques, such as potentiometry and voltammetry [3-5]. Potentiometric sensors employ zero-current and utilise either ion selective lipid membranes or ion selective electrodes, and the potential at the working electrode caused by the ion exchange reaction is measured. Voltametric (amperometric) electronic tongues employ a potential

to drive an electrode transfer reaction, and the resulting current, which depends on the concentration of the sample, is measured. Other sensing methods include optical and acoustic techniques. The 'optical electronic tongue' [6] mimics the mammalian tongue and has the ability to assay solution content for Ca^{2+}, Ce^{3+}, H^{+} and fructose using colorimetric indicators. Among the acoustic devices, quartz crystal microbalances (QCM) were the first ones used as sensors and they rely on the frequency changes due to the mass accumulation on the device surface [7, 8]. Using an array of such devices coated with hydrophilic mono- and dicarbon acids, organic and inorganic acids, and amines in drinking water have been detected [9]. There have also been reports on the quartz resonator devices coated with lipid/polymer membranes to measure different taste substances [10].

This project investigates the usability of small surface acoustic wave (SAW) sensors rather than the bulkier coated QCM devices. Operating a SAW device in the liquid phase requires a horizontal-polarized mode of vibration to reduce the acoustic loss in liquids and various devices using different piezoelectric crystals and different wave modes (Love waves, shear horizontal acoustic plate mode, flexural plate waves (FPW) or shear horizontal SAW) have been discussed in literature [7, 11-13]. However, liquid sensing with SAW devices usually employs devices with analytical coating films to enhance the chemical selectivity of the sensors. Also, when using electrochemical techniques ion selective electrodes/membranes are utilised to make them more analyte specific. This project is focused on devices with no bio-chemical layers, thus relying on a purely physical, rather than electrochemical, principle of operation. The adopted principle of operation makes the sensors more robust and durable since they are less susceptible to surface contamination than electrochemical sensors. The reduction in specificity is addressed through the use of dual designs and/or multi-parameter analysis.

This thesis focuses on the design, fabrication and testing of the two types of high-frequency SH-SAW sensors (delay line and resonator configurations). One advantage of high-frequency acoustic devices is that of increased sensitivity – e.g. for quartz crystal microbalances the sensitivity increases with the square power of resonant frequency [8]. The majority of SAW resonators have been used mainly for gaseous phase measurements [14-17] and very few liquid applications with SAW resonators have been reported. Research on a one port resonator [18] showed that the resonance frequency and the Q factor value are influenced by the viscosity of the liquid sample; two port resonators [19] have been reported to respond to both the conductivity and the square root product of the density and viscosity of the liquid. Commercially available STW-resonators on $LiTaO_3$ employing SiO_2 guiding layer have also been investigated for aqueous media [20].

1.2 AIMS AND OBJECTIVES

The main objective of the project is to investigate the suitability of high frequency shear horizontal surface acoustic wave sensors for liquid media applications. Tests are concentrated on two possible applications – one of them is an electronic tongue sensor and the other is a voltage modulated bio-sensor. The aims of the project are summarized below:

- Review and relatively assess the various surface acoustic wave modes suitable for liquid media;
- Identify the theoretical framework and models for surface acoustic waves – liquid interactions;

- Design of several surface acoustic wave sensor configurations for comparative analysis;
- Microfabrication of the surface acoustic wave sensors, of the liquid reservoirs and development of the sensing systems;
- Electrical characterization of SAW sensors and assessment of various designed configurations;
- Experimentation of selected dual sensor configurations with various liquid solutions and verify their ability to discriminate between them;
- Experimentation of SH-SAW sensors in semi-wireless operation;
- While the main focus of the project is on electronic tongue SAW sensors for liquid samples identification, a voltage modulated bio-sensors principle of operation is also proposed and verified experimentally;
- Experimentation of a resonator SH-SAW configuration for E-tongue applications;
- Employment of multivariate data analysis to the model the E-tongue resonator response.

1.3 THESIS OVERVIEW

This first chapter gives a short introduction to the research context by generally describing electronic tongue technologies and instruments and their applications. Also, the introduction states the aims and the objectives of the thesis.

The second chapter is an overview of the generation and propagation of acoustic waves in both non-piezoelectric and piezoelectric solids. The basic theory of waves in

elastic media is outlined, then the mathematical model is adapted to include the contribution of the piezoelectric effect present in discussed acoustic devices. A comparison between the bulk acoustic waves (BAW) and surface acoustic waves (SAW) is given, and various acoustic modes are discussed. This section also introduces the acoustic sensors with emphasis on SAW device principles and applications. Then the focus is shifted towards liquid sensing and the current state of the art of the SAW liquid sensors is presented.

Chapter 3 describes the main theoretical models that define the research framework of surface acoustic waves in liquid media. The focus is on the perturbation mechanisms of the surface acoustic waves, particularly SH-SAW.

The details of the design configurations considered for the SH-SAW liquid sensors are comprised in Chapter 4. The fundamental guidelines for the SAW design are revised and then various layout configurations are presented.

The microfabrication techniques and equipment employed to fabricate the devices are described in Chapter 5. The sensing system comprises two major components, namely the SH-SAW device and the liquid reservoir; fabrication of each sub-system follows a modular approach and details of the fabrication recipes are given.

Chapter 6 reviews in short the surface acoustic wave sensor set-ups and measurement instrumentation, with an emphasis on the network analyser and vector voltmeter equipments that were used for electrical characterization of devices and liquid samples testing. The chapter also presents a wireless SH-SAW measurement set-up and describes its operating principle.

Chapter 7 presents the two port resonator device that was employed for several experiments involving taste solutions and the results are reported.

Finally, Chapter 8 briefly summarizes the conclusions of the thesis and of the experimental results.

1.4 REFERENCES

[1] K. Toko, "A taste sensor", *Meas. Sci. Technol.*, vol. 9, pp. 1919-1936, 1998.

[2] K. Toko, "Electronic tongue", *Biosensors and Bioelectronics*, vol. 13, pp. 701-709, 1998.

[3] A. J. Bard, L. R. Faulkner, *Electrochemical Methods – Fundamentals and Applications*, John Wiley & Sons, Inc., 1980.

[4] A. Legin, A. Rudinitskaya, Y. Vlasov, C. Di Natale, F. Davide, A. D'Amico, "Tasting of beverages using an electronic tongue based on potentiometric sensor array", *Technical digest of Eurosensors X*, Leuven, Belgium 1996, pp. 427-430.

[5] F. Winquist, P. Wide, I. Lundström, "An electronic tongue based on voltammetry", *Anal. Chimica Acta*, vol. 357, pp. 21-31, 1997.

[6] J. J. Lavigne, S. Savoy, M. B. Clevenger, J. E. Ritchie, B. McDoniel, S-J. Yoo, E. V. Anslyn, J. T. McDevitt, J. B. Shear, D. Neikirk, "Solution-based analysis of multiple analytes by a sensor array: toward the development of an 'Electronic tongue'", *Jour. Am. Chem. Soc.*, vol. 120, pp. 6249-6430, 1998.

[7] D.S. Ballantine, R.M. White, S.J. Martin, A.J. Ricco, E.T. Zellers, G.C. Frye, H. Wohltjen, *Acoustic Wave Sensors Theory, Design and Physico-chemical Applications*, Academic Press, 1997.

[8] F. Herrmann, B. Jakoby,, J. Rabe and S. Buttgenbach, "Microacoustic Sensors for Liquid Monitoring", in: H. Baltes, J. Hesse, and J. Korvink, (Eds.), *Sensors Update* 9, Wiley VCH, 2001, pp. 105-160.

[9] R. Borngräber, J. Hartmann, R. Lucklum, S. Rösler, P. Hauptmann, "Detection of ionic compounds in water with a new polycarbon acid coated quartz crystal resonator", *Sens. Actuators* B, vol. 65, pp. 273-276, 2000.

[10] S. Ezaki, S. Iiyama, "Detection of interactions between lipid/polymer membranes and taste substances by quartz resonators", *Sens. Materials, vol.* 13(2), pp. 119-127, 2001.

[11] E. Gizeli, "Design considerations for the acoustic waveguide biosensor", *Smart Mater. Struct.*, vol. 6, pp. 700-706, 1997.

[12] J. Kondoh, K. Saito, S. Shiokawa, H. Suzuki, "Simultaneous measurement of liquid properties using multichannel shear horizontal surface acoustic wave microsensor", *Japn. J. Appl. Phys.*, vol. 35, pp. 3093-3096, 1996.

[13] J. Kondoh, S. Shiokawa, "New application of shear horizontal surface acoustic wave sensors to identifying fruit juices", *Japn. J. Appl. Phys.*, vol. 33, pp. 3095-3099, 1994.

[14] A. Mauder, "SAW gas sensor: comparison between delay line and two port resonator", *Sens. Actuators B*, vol. 26-27, pp. 187-190, 1995.

[15] D. D. Stubbs, Sang-Hun Lee and W. D. Hunt, "Molecular recognition for electronic noses using surface acoustic wave immunoassay sensors", *IEEE Sensors Journal* 2, No. 4, pp.294-300, 2002.

[16] M. Penza, F. Antolini, m. Vittori Antisari, "Carbon nanotubes as SAW chemical sensor materials", *Sens. Actuators B*, vol. 100, pp. 47-59, 2004.

[17] C. Cicala, P Bruno, A. Dragone, A.M. Losacco, C. Sadun, A. Generosi, "PECVD a-C:H films for STW resonator devices", *Thin Solid Films* 482, pp. 264-269, 2005.

[18] T. Nomura and T. Yasuda, "Surface acoustic wave liquid sensor based on one – port resonator", *Jpn. J. Appl. Phys*. 32, pp. 2372-2375, 1993.

[19] T. Nomura, A. Saitoh, Y. Horikoshi, "Measurements of acoustic properties of the liquid using liquid flow SH-SAW sensor system", *Sens. Actuators B*, vol. 76, pp.69-73, 2001.

[20] N. Barie, T. Wessa, M. Bruns and M. Rapp, "Love waves in SiO_2 layers on STW-resonators on $LiTaO_3$", *Talanta,* vol. 62, pp. 71-79, 2004.

CHAPTER 2:

ACOUSTIC WAVES BACKGROUND

2.1 INTRODUCTION

This chapter gives an overview of the generation and propagation of acoustic waves in both non-piezoelectric and piezoelectric solids. The basic theory of waves in elastic media is underlined, and then the mathematical model is adapted to include the contribution of the piezoelectric effect present in discussed acoustic devices.

A brief comparison between bulk acoustic waves (BAW) and surface acoustic waves (SAW) is given, and the various surface acoustic modes are reviewed and discussed.

This chapter also introduces the acoustic sensors with emphasis on SAW devices principles and applications. Then the focus is shifted towards liquid sensing applications and the current state of the art of the SAW liquid sensors is presented.

2.2 PHYSICS OF ACOUSTIC WAVES

2.2.1 Fundamentals of acoustic waves in elastic media

Waves are propagating disturbances within a medium, without giving the medium as a whole any permanent displacement. Acoustics is focused on the study of sound, the time-varying deformations or vibrations within a given medium: gas, liquid or solid [1]. In a solid medium, acoustic waves propagate as the result of a deformation of the elastic material. Waves are described in terms of their amplitude and their spatio-temporal variation.

The two main properties of an ideal elastic medium are inertia (i.e. mass) and elasticity; these allow an elastic medium to be modelled as a distributed mass-spring system. The elasticity of a medium is required in order to provide a force that tends to restore a displaced particle to its original (equilibrium) position while inertia enables the displaced particles to transfer momentum to an adjoining particle. Thus, an elastic wave arises from the interplay of the distributed elastic and inertial forces.

For a small elastic deformation of a non-piezoelectric elastic material, a proportional relation holds between mechanical stress T (force per unit area F/A) and strain S (ratio of the length of the stressed material to its unstressed length). In the one-dimensional case it is Hooke's law (F is proportional to displacement u) and is given by:

$$T = cS \qquad \text{(1-D only)} \tag{2.1}$$

where c is the elastic stiffness coefficient, also known as Young's modulus (N/m^2).

The generalization of (2.1) for a three-dimensional case is

$$T_{ij} = \sum_{k,l=1}^{3} c_{ijkl} S_{kl} \tag{2.2}$$

where T, S and c are the stress, strain and elastic stiffness tensors.

The above relation relates strain to stress and it is called the *elastic constitutive relation.* Its equivalent in reduced (engineering) notation[1] is

$$T_I = \sum_{J=1}^{6} c_{IJ} S_J \tag{2.3}$$

Using Newton's second law of motion, and substituting F with the sum of all the acting forces and mass with $m = \rho \delta x_1 \delta x_2 \delta x_3$, where δx_1, δx_2, δx_3 are the elemental lengths, the equation of motion could be written as:

$$\sum_{j=1}^{3} \frac{\partial T_{ij}}{\partial x_j} = \rho \frac{\partial^2 u_i}{\partial t^2} \tag{2.4}$$

2.2.1.1 Wave equation

The propagation of acoustic waves in non-piezoelectric solids is mathematically described by the wave equation. Assuming that the strain matrix is symmetric (S_{kl} in equation (2.2) is equivalent to $\frac{\partial u_k}{\partial l}$) and differentiating equation (2.2) with respect to x_j the following is obtained:

$$\sum_{j=1}^{3} \frac{\partial T_{ij}}{\partial x_j} = \sum_{j,k,l=1}^{3} c_{ijkl} \frac{\partial^2 u_k}{\partial x_j \partial x_l} \tag{2.5}$$

From (2.4) and (2.5) the expression for the non-piezoelectric wave equation results as:

$$\rho \frac{\partial^2 u_i}{\partial t^2} = \sum_{i,j,k=1}^{3} c_{ijkl} \frac{\partial^2 u_k}{\partial x_j \partial x_l} \tag{2.6}$$

Equation (2.6) represents a set of three wave equations (i=1,2,3) in the particle displacements u_1, u_2, u_3, with summation over the indices j, k, l [2].

---

[1] The symmetry proprieties of the tensors allows the adoption of the engineering notation with a reduced number of indices: a double index (ij) is replaced with a single capital index (I)

2.2.2 Acoustic waves in lossy media

For the derivation of the above wave equation, the medium was considered a lossless one. In the case of a lossy medium, the amplitude of the propagating wave diminishes because of various absorption mechanisms, mode conversion within scattering mechanisms, Raman scattering or thermoelastic attenuation. To take into account the damping mechanism, the elastic constitutive equation needs to change to accommodate a viscous term:

$$T_I = \sum_{J=1}^{6}(c_{IJ}S_J + \eta_{IJ}\dot{S}_J) \tag{2.7}$$

In (2.7) the viscosity tensor η_{IJ} has the same property as the elastic stiffness tensor c_{IJ}.

For harmonic motion $\dot{S}_J = j\omega S_J \Rightarrow T_I = \sum_{J=1}^{6}(c_{IJ} + j\omega\eta_{IJ})S_J$ and thus attenuation may be accounted by representing the elastic constant c_{IJ} by complex elastic constant $c_{IJ} + j\omega\eta_{IJ}$. The wave equation can be then written as

$$\rho\frac{\partial^2 u_i}{\partial t^2} = \sum_{j,k,l=1}^{3}(c_{ijkl} + j\omega\eta_{ij})\frac{\partial^2 u_k}{\partial x_j \partial x_l}. \tag{2.8}$$

For a y-polarized shear wave propagating along the x axis the previous equation becomes

$$\rho\frac{\partial^2 u_2}{\partial t^2} = (c_{44} + j\omega\eta_{44})\frac{\partial^2 u_2}{\partial x^2}. \tag{2.9}$$

The solution for a lossy wave equation can be written like

$$u_2(x,t) = Ae^{j(\omega t - kx)}e^{-\alpha x} \tag{2.10}$$

where α is the attenuation coefficient. From (2.9) and (2.10) the dispersion relation for a shear wave in a lossy medium is obtained:

$$-\rho\omega^2 = (c_{44} + j\omega\eta_{44})(\alpha + jk)^2 \tag{2.11}$$

where real and imaginary parts can be separated as

$$-\rho\omega^2 = c_{44}(\alpha^2 - k^2) - 2\omega\alpha k\eta_{44} \tag{2.12}$$

$$2\alpha k c_{44} + \omega\eta_{44}(\alpha^2 - k^2) = 0 \tag{2.13}$$

The presence of the viscous damping term results in a second-order perturbation of the wave velocity and a first-order contribution to the attenuation. Since for most materials $\alpha << k$, and making use of the two substitutions for the velocity ($v = \frac{\omega}{k}$ and $v = \left(\frac{c_{44}}{\rho}\right)^{1/2}$, c_{44} – shear waves case) the attenuation expression can be easily derived as:

$$\alpha = \frac{\omega^2\eta_{44}}{2\rho v^3} \tag{2.14}$$

where η_{44} characterises the damping of the *y*-polarized shear wave discussed. It is important to note that the attenuation is dependent on the square of the frequency and thus it is essential to use high-quality materials for acoustic sensors operating at high frequency. The frequency dependence has been confirmed experimentally for both bulk and surface waves for a number of materials [2].

2.2.3 Acoustic waves in piezoelectric media

If we consider a simple non-piezoelectric dielectric medium, the surface charge density or displacement field D can be written as $D = \varepsilon_0\varepsilon_r E = \varepsilon E$, where ε_0 is the free space permittivity and ε_r is the relative dielectric permittivity. For a piezoelectric material the above relation no longer holds – to accommodate the contribution of piezoelectricity it needs to be adjusted. In piezoelectric materials, the application of an electric field (E) stimulus results in a mechanical deformation, and vice versa.

Because of both direct and converse piezoelectric effects, an electro-mechanical coupling mechanism has to be considered when deriving the mathematical model for waves propagating in piezoelectric media. This interaction is expressed in terms of a piezoelectric constant matrix, e (C/m^2) such that the electrical displacement density D becomes:

$$D_i = e_{iJ} S_{J+} \varepsilon_{ij}^S E_j \tag{2.15}$$

S = strain matrix - in reduced engineering coordinates it has 6 components,

E_j = electric field components,

ε_{ij} = a 3x3 matrix permittivity constant

e = piezoelectric stress constant, a 3x6 matrix.

The mechanical stress relationship for piezoelectric materials modifies to

$$T_J = c_{IJ}^E S_J - e_{Ij} E_j \tag{2.16}$$

where e_{Ij} is the transposed matrix of piezoelectric constant e_{Ij} from the previous equation.

As equations (2.15) and (2.16) completely describe the interplay of stress, strain and elastic field in a piezoelectric solid, they are named *piezoelectric constitutive equations*. The derivation of the wave equation in piezoelectric media from the constitutive relations follows the same procedure as used for the non-piezoelectric materials.

As $E_k = -\dfrac{\partial \phi}{\partial x_k}$, the equation is typically written in terms of the displacements u_i coupled with the electrical potential ϕ rather than the electric field component. The constitutive relation becomes

$$T_{ij} = \sum_{k,l=1}^{3} c_{ijkl} \frac{\partial u_l}{\partial x_k} + \sum_{k=1}^{3} e_{ijk} \frac{\partial \phi}{\partial x_k} \tag{2.17}$$

and the wave equation can be written as:

$$\sum_{j,k,l=1}^{3} c_{ijkl} \frac{\partial^2 u_l}{\partial x_k \partial x_j} + \sum_{j,k=1}^{3} e_{ijk} \frac{\partial^2 \phi}{\partial x_k \partial x_j} = \rho \frac{\partial^2 u_i}{\partial t^2} \tag{2.18}$$

The term involving an electrical potential ϕ is considered to be a "source" term, responsible for the generation of an acoustic wave by an applied, time-varying electrical potential. Conversely, the wave displacements can be electrically detected.

In a region with no free charges, the electrical displacement is solenoidal $(\nabla \cdot D = 0)$ and the previous equation becomes [2]:

$$\sum_{i,k,l=1}^{3} e_{ikl} \frac{\partial^2 u_l}{\partial x_k \partial x_i} - \sum_{i,k=1}^{3} \varepsilon_{ik} \frac{\partial^2 \phi}{\partial x_k \partial x_i} = 0 \tag{2.19}$$

2.3 SURFACE ACOUSTIC WAVES

2.3.1 SAW versus BAW

The acoustic waves that propagate in an elastic medium depend on the intrinsic proprieties of the medium and its boundary conditions [2].

Considering an infinite homogeneous medium, the most common type of acoustic wave is the bulk or plane elastic wave. Depending on the polarisation and the direction of propagation of the constitutive atoms, the plane waves can be either longitudinal, also known as compressional waves, where the particles vibrate in the propagation direction, or shear waves with particles displacement normal to the propagation direction. Fig 2.1 shows a pictorial representation of the compressional and the shear waves propagating in a given direction.

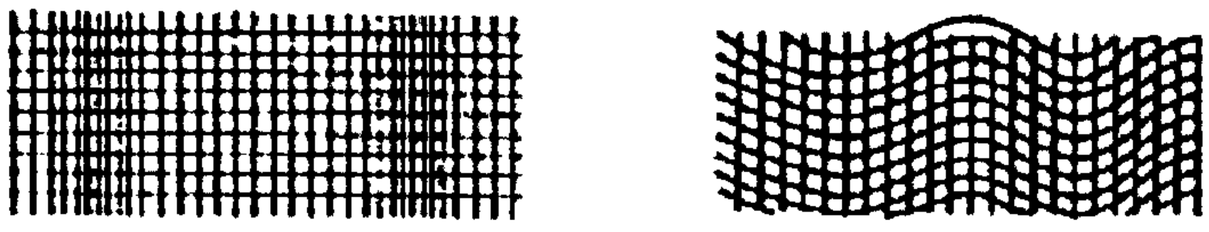

Figure 2.1: Bulk compressional and shear waves

Surface waves are particular solutions of the general class of elastic waves. By comparison with the bulk plane wave case, the propagation medium for a SAW is no longer an infinite one, but has a set of restrictions in the form of material-air interfaces. By definition a SAW is a propagating or standing acoustic wave that is confined to the planar surface of a solid plane and has its energy localised within one wavelength from the surface [2].

While surface wave propagation is restricted to a distance of about one acoustic wavelength from the piezoelectric substrate surface, the bulk waves propagate through the volume of the piezoelectric substrate [3].

2.3.2 SAW generation and detection mechanisms

On piezoelectric substrates surface waves can be electrically generated using special inter-digital transducers (IDTs). Also called inter-digital "fingers", the IDTs are distributed electrodes that rely on both direct and indirect piezoelectric to generate and detect the surface acoustic waves. If high frequency signals are applied to an input side IDT, surface waves are excited by the electric field generated between the electrodes. Vice versa, SAW waves that propagate on the substrate surface are converted by the direct piezoelectric effect into electric charges on the IDT, which finally results in an electric output voltage signal.

Width, spacing and loading of the electrodes determine the functions and electric characteristics of the SAW device. IDTs are usually made of aluminium and sometimes

gold, and the spacing and width of the electrode strips are λ/4 or below (λ-microacoustic wavelength). The associated frequency is known as the synchronous frequency, f_0, and is given by $f_0=v/\lambda$, where v is the propagation velocity of the acoustic waves and a substrate dependent parameter [1].

2.3.3 Surface acoustic waves modes

Surface acoustic waves are characterised primarily by the mode of wave propagation through or on a piezoelectric substrate and also by their velocities and displacement directions. Different types of acoustic waves may be supported by a substrate material and the very nature and characteristics of the acoustic waves depends on the boundary conditions. There are many types of acoustic devices for sensor applications but most of them are based on *Raleigh* waves, *Shear Horizontal Surface Acoustic Waves* (SAW and SH-SAW), *Love waves*, *Acoustic Plate Mode* (APM) and *Flexural Plate Waves* (FPM) [2, 4-5].

2.3.3.1 SAW Rayleigh waves

Named after their discoverer, Rayleigh waves have a longitudinal and a vertical shear component that can couple with a medium in contact with the device surface. Such coupling strongly affects the amplitude and velocity of the wave. This feature enables SAW sensors to directly sense mass and mechanical properties. The energy of a SAW concentrates close to the piezoelectric wafer surface [6] and its surface motion also allows the devices to be used as microactuators. Ralyleigh waves travel along the surface with a retrograde elliptical particle motion [1] and changing to propagate with depth passing through a node where there is no motion at all. Rayleigh wave particle motion is only found in the vertical plane with no tangential motion. The wave has a velocity that is approximately 5 orders of magnitude less than the corresponding

electromagnetic wave, making Rayleigh surface waves among the slowest to propagate in solids. The wave amplitudes are typically ~1 nm and the wavelengths range from few nm to 100 microns.

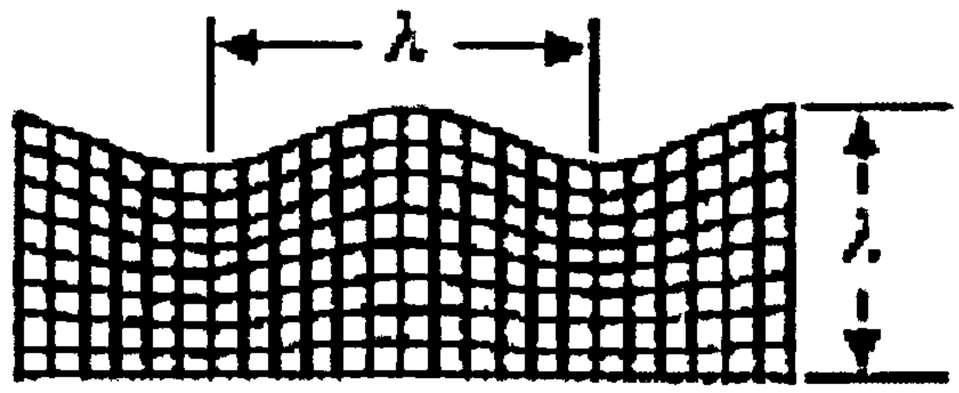

Figure 2.2: Rayleigh surface acoustic wave

The longitudinal u_1 particle displacement in direction x_1 and the shear u_3 vertical displacement in direction x_3 are described by the following formulas:

$$u_1 = [A_1 \exp(-b_1 x_3) + A_2 \exp(-b_2 x_3)] \exp[jk(x_1 - ct] \tag{2.20}$$

$$u_3 = (-b_1 / jk) A_1 \exp(-b_1 x_3) + (jk / b_2) A_2 \exp(-b_2 x_3) \exp[jk(x_1 - ct) \tag{2.21}$$

where $b_1 = k(1 - c^2 / v_l^2)^{1/2}$ and $b_2 = k(1 - c^2 / v_t^2)^{1/2}$, k is the wave number. The longitudinal v_l and transverse v_t velocities are given by

$$v_l = \sqrt{\frac{\lambda + 2G}{\rho}}, \; v_t = \sqrt{\frac{G}{\rho}} \tag{2.22}$$

where G is the Lame constant and is given by $E_m / 2(1+\nu)$, $\lambda = \nu E_m / [(1+\nu)(1-2\nu)$ with ν being Poisson's ratio and E_m being the Young modulus.

Because Rayleigh waves have virtually all their acoustic energy confined within one wavelength of the surface, SAW sensors display a very high sensitivity. One disadvantage of these devices is that Rayleigh waves are surface-normal waves, making them poorly suited for liquid sensing. When a liquid contacts a SAW sensor, the resulting compressional waves cause an excessive attenuation of the surface wave.

2.3.3.2 Flexural plate waves (FPM) and acoustic plate mode (APM)

The flexural plate wave (FPW) device, sometimes referred as "Lamb wave device" [7-8] is made by micromachining a thin membrane on a Si substrate. A piezoelectric film deposited on one side of the supporting membrane is used to excite the SAW by the interdigitated electrodes (IDTs). Because of its location to one side of the neutral plane of the composite membrane, the electrically induced deformation of the piezoelectric excites a propagating wave that involves flexure of the membrane, as shown by the cross section in the FPW view in Fig. 2.3.

Because the phase velocity for the FPW decreases as the ratio of membrane thickness to wavelength decreases, the FPW typically operates in the low MHz range. The FPW phase velocity may be as low as a few hundred ms^{-1}, a value smaller than the speed of sound in water. Even though the FPW membrane moves both perpendicularly and parallel to its surface, as does the surface of a SAW device, the FPW does not radiate a propagating wave into an adjacent fluid, instead an evanescent acoustic disturbance is generated in the fluid [9-11].

Sensitivity of detection is based on the relative magnitude of the perturbation to a parameter of the membrane, in contrast with other acoustic devices that base their detection sensitivity on frequency of operation. For mass, the sensitivity is the ratio of the added mass to the membrane mass. Because the fabrication of very thin membranes is possible, this also allows the achievement of very high detection sensitivities. There are other advantages of the FPW such as low operating frequencies and therefore simpler and cheaper electronic devices to drive and detect the signals. The downsizes of the FPW, on the other side, lay in the underdevelopment of membrane technology which makes it difficult to develop low stress membranes having good acoustic

characteristics. Also, as membranes tend to be very fragile, there is a need to enhance their robustness.

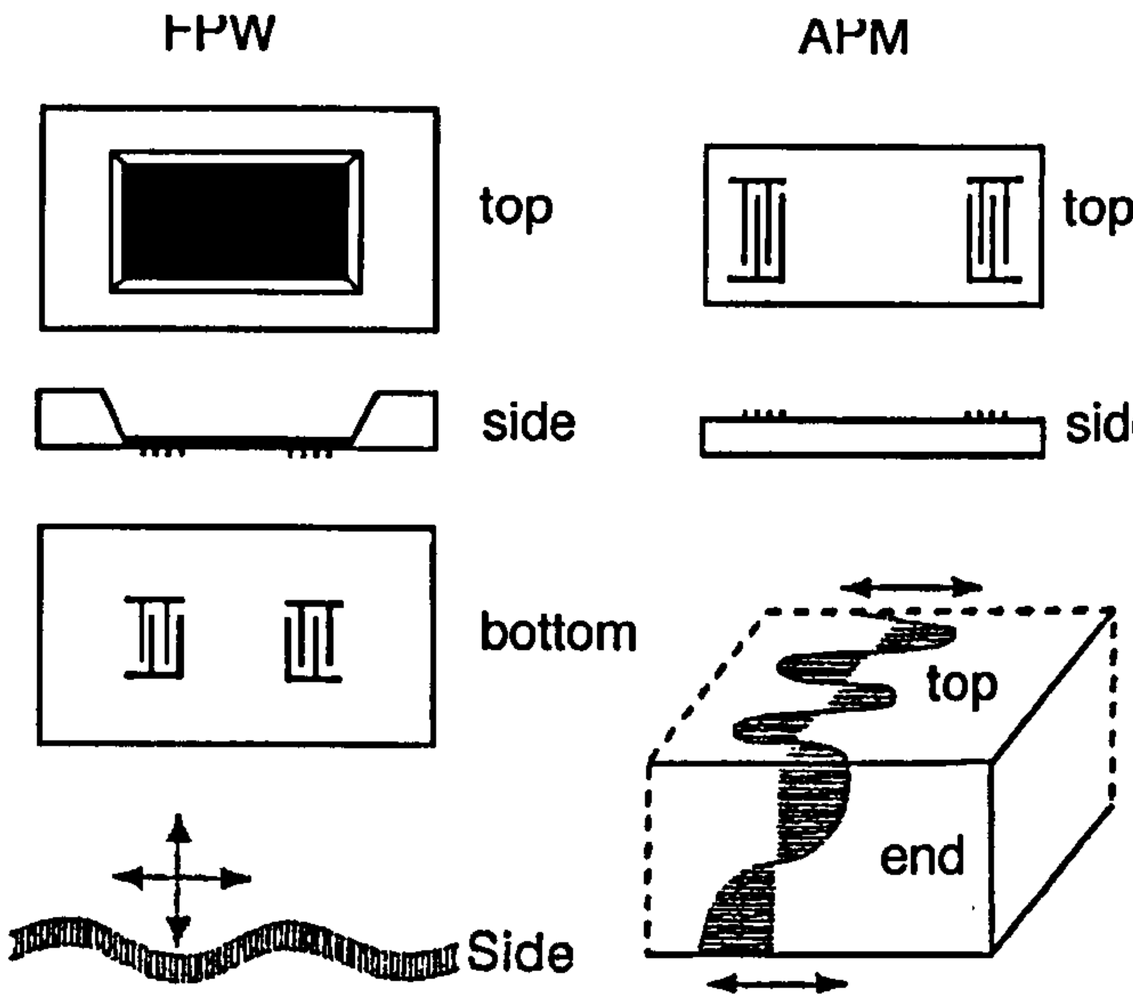

Figure 2.3: Flexural plate wave and acoustic plate mode devices [10]

In the acoustic plate mode (APM) device the particle motions are parallel to the top surface, as a result from the orientation of that surface relative to the crystalline axes of the single-crystal piezoelectric substrate. The configuration of the SH-APM devices is similar to the Rayleigh SAW devices, but the piezoelectric wafer is thinner, typically a few acoustic wavelengths. Just like the SAW device, the APM device is rugged mechanically, but with a lower gravimetric sensitivity due to the acoustic energy which is distributed throughout the relatively thick crystal [12]. The APM devices are less sensitive than the surface wave sensors because the energy of the wave is not maximised at the surface which reduces its sensitivity. Another reason for which APM are less sensitive is due to the fact that perturbations such as sensitivity to mass loading are directly related to the thickness of the substrate and therefore the thinner the device, the more sensitive. Also due to the absence of a surface-normal component of the wave displacement, the main applications of the APM are in liquid sensing. Nevertheless, there are important applications of APM towards biosensor implementation, one of

which being the detection of microgram-per-litre levels of mercury which is of great importance for testing safe drinking water act compliance [13].

2.3.3.3 Shear horizontal surface acoustic waves (SH-SAW)

While the Rayleigh waves are shear vertical surface acoustic waves (SV-SAW) the shear horizontally polarised surface acoustic waves (SH-SAW) have received extensive attention as they have only in-plane components of surface oscillation. Among the SH-SAW modes used in liquid sensing are Love waves, the surface skimming bulk waves (SSBW) and surface transverse waves (STW). If the cut of the piezoelectric crystal material is rotated appropriately, the wave propagation mode changes from a vertical shear SAW sensor to a shear-horizontal SAW sensor. The displacements of these waves' particles are transverse to the wave propagation direction and parallel to the plane of the surface [1]. This dramatically reduces loss when liquids come into contact with the propagating medium, allowing the SH-SAW sensor to operate in liquids e.g. as a biosensor.

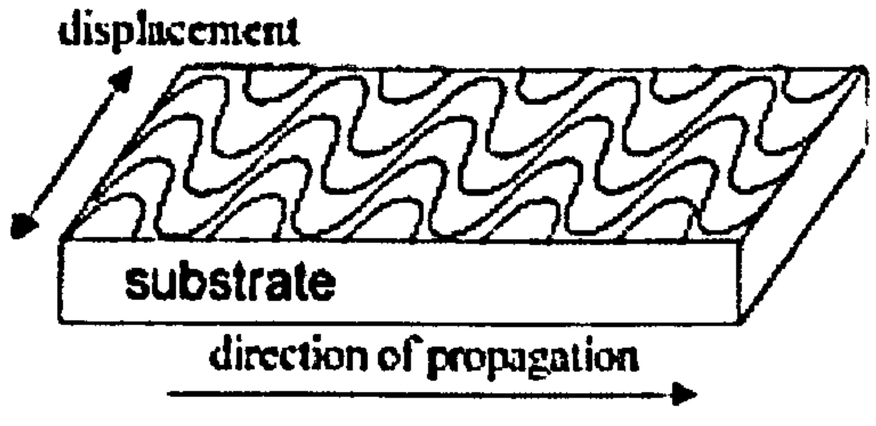

Figure 2.4: SH-SAW propagating on the surface of a substrate

Generally, SH-SAW displays sensitivity to mass-loading, viscosity, conductivity and permittivity of the adjacent liquid [1].

Love waves are guided acoustic modes that propagate in a thin layer of a given material deposited on a substrate made of another material with different acoustic properties and infinite thickness when compared to the original layer. These waves are transverse and they bring only shear stress into action [1]. The acoustic energy is

concentrated in this guiding layer and in the part of the substrate close to the interface. High noise levels, diffraction of acoustic signal into the crystal bulk and background interference from the reflection of the lower surface limit SH waves. The guiding layer has the effect of confining and guiding the wave over the top layer of the device and hence it circumvents the disadvantages (usually, reduced sensitivity at the interface) associated with a similar SH device [1, 2].

To eliminate the influence of the electric properties of the adjacent liquid or gas, a metallisation can be applied to the top of the guiding layer. [14].

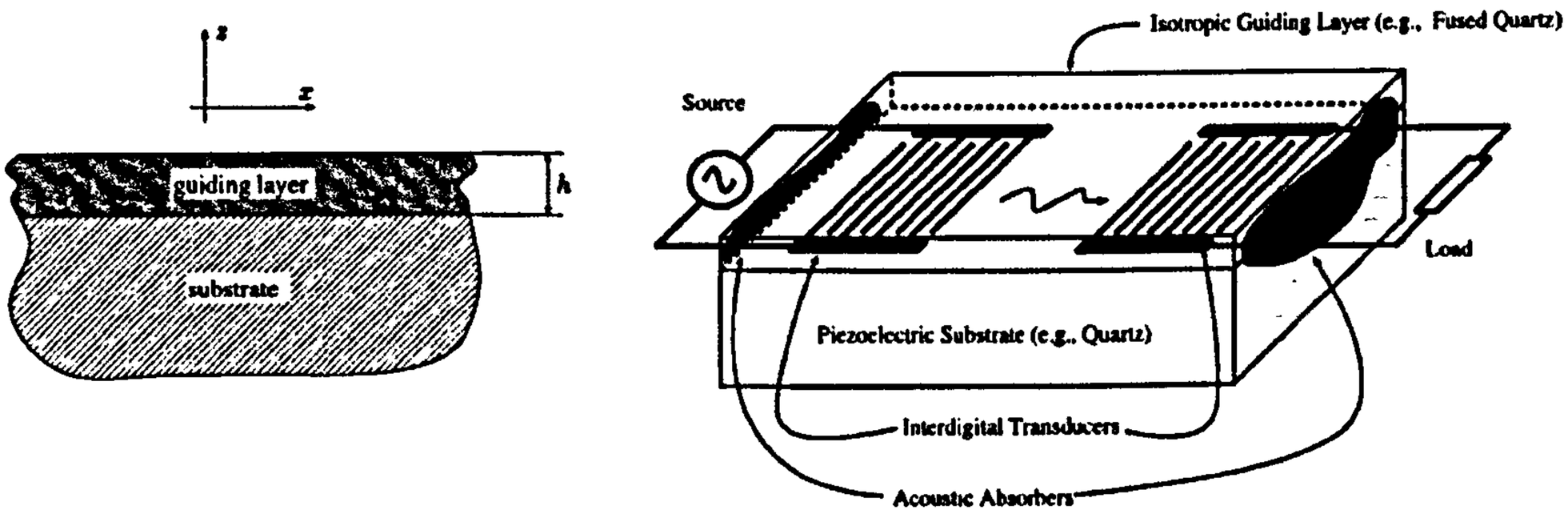

Figure 2.5: Layered structure supporting a Love wave mode - cross-sectional and side view [14]

For the case of a very thin layer, $kh<<1$ (where k is the wave vector, and h is the thickness of the layer), the amplitude of the SH wave in the substrate ($y < 0$) can be written as:

$$u = Ae^{\chi y + j(kx-\omega t)} \tag{2.23}$$

where the penetration depth is

$$\chi = k_{t2}(k_{t2}h)(\rho_1 / \rho_2(1 - v_{t1}^2 / v_{t2}^2)) \tag{2.24}$$

and v_{t1}, k_{t1} and v_{t2}, k_{t2} are SH bulk waves velocities and wave vectors for the layer and the substrate respectively, and ρ_1 and ρ_2 are the corresponding densities of materials. If the SH bulk wave velocity in the layer is smaller than in the substrate, $v_{t1} < v_{t2}$, the layer produces a "slowing-down" of the wave and, the wave acquires a surface character $\chi>0$,

(attracting layer). This is the case with classical Love wave. If, on the other hand, $v_{t1} > v_{t2}$, the layer "accelerates" the wave near the surface and the SH wave in the substrate with respect to the surface becomes "leaky" $\chi<0$, (rejecting layer). In the case of Love waves, a "slowing-down" layer on the surface is an analogue of the dielectric slow-wave waveguide in electrodynamics and optics [15].

These devices, like the SH devices, avoid radiation losses in liquids, still being more sensitive to mass loading by concentrating the energy close to the surface. [8]. The IDTs and the delay line are both coated with a dielectric material (i.e. polymer) that is used as a waveguiding layer to trap the acoustic wave near the surface and which increases sensitivity and at the same time protects the IDTs from the liquid medium [16].

2.3.4 SAW substrate materials and proprieties

SAW devices generate an acoustic wave based on piezoelectric materials. Pierre and Paul Jacques Curie were the first to describe the piezoelectric effect and later on John William Strutt explained the properties of the surface acoustic wave mode of propagation [17]. Piezoelectric materials can generate an electric field on application of a mechanical force and distort on application of an electric field.

The most commonly used platform for acoustic devices is quartz (SiO_2)– also identified as "quartz stable operation" due to its negligible temperature coefficient [2]. Quartz has an interesting property – it allows selection of its temperature dependence coefficient by choosing the right cut angle and the wave propagation direction. The first order temperature effect can be minimized once a proper selection is done. The design of an acoustic wave temperature sensor by maximizing this effect is therefore possible [18].

Other materials with higher coupling coefficient include lithium tantalate ($LiTaO_3$) and lithium niobate ($LiNbO_3$). $LiNbO_3$ possesses a large pyroelectricity and electro-optic properties and it is applicable to SAW devices as well as to optical devices and microwave sensors [19]. The downsize of $LiNbO_3$ use is that it suffers from a very large temperature coefficient and, as consequence, it is thermally fragile and a highly stable temperature is required when using this substrate material to detect anything other than temperature changes. Lithium tantalate possesses the pyroelectricity and electro-optic properties with values lower than those of $LiNbO_3$, but unlike the latter, $LiTaO_3$ has a more stable temperature coefficient and reasonable accuracy of the material constants have been reported [20].

New high temperature materials are berlinite ($AlPO_4$), lithium tetraborate ($Li_2B_4O_7$), langasite ($La_3Ga_5SiO_{14}$) and galiumphosphate ($GaPO_4$), operable up to 1000°C [18-21]. This is because they possess a high Curie temperature. While ($Li_2B_4O_7$) possesses a relatively large piezoelectricity and has been used for resonators, langasite has a temperature stability comparable to the ST-cut quartz and also a large piezoelectricity [21]. In addition to these frequently used substrate materials already mentioned, there are new methods developed for the generation of high acoustic velocity materials such as sapphire, diamond-like carbon, silicon, NbO_3 compounds, AlN, PMN-PT, etc. [22, 23]. Both materials and techniques still need further development and are just finding their way into biosensor technology [17].

2.4 SURFACE ACOUSTIC WAVES SENSORS

2.4.1 Introduction to acoustic sensors and applications

The extreme versatility of the acoustic wave sensors is only one of the qualities that explains their huge commercial potential. The largest consumer is the telecommunications industry which accounts for ~3 billion acoustic wave filters annually, primarily in mobile cell phones and base stations [18]. But there are other emerging applications for acoustic wave devices, including automotive applications like torque and tyre pressure sensors, medical applications such as chemical sensors, and industrial and commercial applications (i.e. vapour, humidity, temperature, and mass sensors). Due to their sensitivity to a wide range of different physical parameters all acoustic wave devices can be exploited as sensors. A valuable feature of acoustic sensors is their direct response to physical and chemical parameters and their variations.

The term acoustic wave sensors comes from their detection mechanism which is a mechanical, or acoustic wave. The acoustic wave propagates through or on the surface of the material, and any changes to the characteristics of the propagation path affect the velocity and/or amplitude of the wave. These changes in velocity can be observed by measuring the sensor's phase properties which can then be correlated to the corresponding physical quantity that is measured [18].

2.4.2 Perturbations of acoustic waves used in sensing

The sensing mechanism of a SAW sensor relies on a change in the acoustic velocity of a surface wave on the surface of the piezoelectric substrate. As the transfer characteristic of the SAW device is changed by the measurand and depends on the propagation of the acoustic wave, many physical parameters like temperature, pressure, strain or stress can

be applied directly on the SAW chip. The coating of the SAW surface with layers sensitive to certain chemical substances makes the device useful as chemical or biological sensors. After transduction from the acoustic to the electrical domain, the frequency and the amplitude of the acoustic wave are measured. This measurement is usually associated with a decrease in acoustic wave amplitude, and this reduction is an indication of viscous-damping effects [24]. Other parameters that can be efficiently measured with acoustic sensors include surface mass, liquid density, viscosity, liquid permittivity and conductivity.

2.4.3 State of the art of the SAW sensors for liquid media

2.4.3.1 APM sensors

APM sensors propagate in a piezoelectric crystal and generate an RF electric field extending into the adjacent liquid and couple to nearby ions or dipoles in solution. This coupling leads to ion and dipole motion which results in the electrical energy storage and dissipation. In a study that reports the electrical interactions between APM devices and solutions contacting the device surface, Niemczyk et al propose a circuit to describe the interaction of the electric field with the ions and dipoles and obtained the velocity shift and attenuation that should occur as a result of this interaction. Their results show that electrical interaction significantly affects acoustic wave propagation properties at a solid/liquid interface [25]. In a later paper, Martin et al. [26] found APM devices to function efficiently in contact with liquids, providing a sensitive means to monitor conditions at solid/liquid interface.

Another study [27] that investigates APM on various quartz substrates in order to determine their usefulness for liquid-sensing applications reports promising characteristics found for rotated Y-cuts of quartz with the direction of acoustic mode

propagation being perpendicular to the X-axis of the quartz crystal. Results show that using thinner crystal plates increases both mass sensitivity and mode separation. Also, it is observed that the use of thin crystal plates significantly improves the detection limit of the devices which can be estimated to be below 0.1μg/mL [27].

2.4.3.2 FPW sensors

Flexural plate wave sensors are also known as Lamb-wave sensors. The propagation of the waves is made through a thin membrane, consisting mainly of SiO_2 which is deposited on the piezoelectric substrate [17]. Unlike Rayleigh waves, the propagation velocity in the membrane is slower than in the fluid that is in contact with the surface. In flexural plate sensors, energy is not dissipated therefore they can be used in both fluid and gaseous and environments. Lamb-wave sensors have a high mass sensitivity, but the membranes need to be very thin in order for such sensitivity to be achieved (a few micrometers) [28]. This makes the sensors very fragile and difficult to fabricate and handle.

2.4.3.3 Love-wave sensors

Of all the acoustic sensors applied to liquid sensing, Love wave sensors are a special class of the shear-horizontal SAW sensors and have the highest sensitivity [29]. To make a Love wave sensor, a waveguide coating is placed on a SH-SAW device such that the energy of the shear horizontal waves is focused in that coating [18]. A biorecognition coating is then placed on the waveguide coating, forming the complete biosensor. A successful detection of anti-goat IgG (a biological antibody) in the concentration range of $3 \cdot 10^{-8}$ to 10^{-6} moles using a 110 MHz YZ-cut SH-SAW with a polymer Love wave guide coating has been achieved by Gizeli et al. [30].

Using a modelling theory derived for polymer-Love plate, Gizeli et al. [31] developed a Love plate device based on an SSBW piezoelectric substrate coated with a PMMA layer in order de detect the deposition of a protein multilayer and found that the device was capable to detect low concentrations of biological materials. In a different study, Stevenson et al. [32] demonstrated that an effective Love device is more dependent on the difference between the shear velocity than the density of the substrate or overlayer and that polymer overlayers offer significant gains in mass sensitivity although they should be accounted for other downsizes such as acoustic loss and instability [32]. A Love acoustic device was used to monitor the formation of supported lipid mono- and bilayers on a thiol-coated surface in the presence of a liquid [33] and results indicated that the device was sensitive enough for detection and that it has potential as a direct immunosensor or biosensor [34]. A theoretical model for the analysis of mass sensitivity of the Love wave device was tested by McMullan et al. [35] and found to be able to predict that the mass sensitivity will increase in the presence of a viscous solution due to the power flow into the liquid. When quantifying the viscoelastic properties and the density of a protein layer deposited on a solid/liquid interface in a waveguide configuration at 108 and 155 MHz [36], the modelling results yield information about the mechanical and chemical interaction between proteins in surface layers and, for the first time using this technique, the authors were able to achieve a simultaneous quantitative, real-time mass and viscoelastic information of protein layers at a solid/liquid interface.

The properties of the Love waves were also studied by Jakoby and Vellekoop [4, 5, 14] who reviewed the basic properties of these waves and their application in sensor devices for biochemical as well as for density and viscosity measurements, concluding

that Love waves sensors are highly sensitive because of the confinement of the acoustic energy to the sensing surface [14].

Novel protocols of coating bacteria on the sensor surface prior to the addition of an antibody were used to simultaneously detect two different microorganisms, *Legionella* and *Escherichia coli* in a study undertaken by Howe and Harding [37]. Quantitative results could be obtained for *Legionella* and *E. coli* down to 10^6 cells per ml within 3 hours and also, *E. coli* was detected down to 10^5 cells per ml in a modified protocol using sheep IgG as a blocking agent. One of the possible applications of these protocols would be for a real time measurement in systems that are relatively clean and where large number of organisms are likely to be present and detected quickly. A second application might be to forgo the rapidity and develop a sensor that can detect a range of organisms of concern from an original lower level of contamination [37].

Josse et al. [38] investigated the design and performance of guided SH-SAW devices for high-sensitivity chemical and biochemical sensors in liquids. Polymers such as PMMA and cyanoethyl cellulose which both have relatively low shear wave velocity, were studied as the guiding layers to trap the acoustic energy near the sensing surface. Thus, in biosensing experiments, using a near-optimal PMMA thickness of approx. 2μm, mass sensitivity greater than 1500 Hz/(ng/mm^2) is demonstrated, and results in a minimum detection limit which is less than 20 pg/mm^2. Another Love-wave bionsensors developed for the detection of bacteria (*Bacillus anthracis* and *Bacillus thuringienisis)* proved to be promising with two waveguide materials which are polyimide and polystyrene [39]. Finally, one of the most recent applications of pulse mode SH-SAW polymer coated biosensors were investigated by sensing a sequence of deposition and removal of a biological layer consisting of vesicles of the phospholipid

POPC [40]. The findings show the ability of the 36*YX* $LiTaO_3$ pulse mode system to provide rapid measurements of both amplitude and phase for biosensing applications.

2.4.3.4 SH-SAW sensors

Because of the high sensitivities that can be obtained, SH-SAW sensors are especially attractive for liquid phase sensing applications [16]. The shear-horizontal surface acoustic wave (SH-SAW) sensor, also known as the surface transverse wave (STW) sensor is one of the most widely used sensors. If the cut of the piezoelectric crystal material is rotated appropriately, the mode of the wave propagation changes from a vertical shear SAW sensor to a shear-horizontal SAW sensor. This significantly reduces loss when liquids come into contact with the propagating medium, thus allowing the SH-SAW sensor to operate as a biosensor [18].

In the late 90's there were several groups of researchers that studied the utilization of SH-SAW in different propagation environments. Welsch et al. (1997) [41] investigated the utilization of horizontally polarized surface acoustic waves for immunosensing in liquids using a dual-delay-line device on a $LiTaO_3$ substrate working at 345 MHz to detect immunoglobulins of type G in phosphate buffer. The experimental results enabled the derivation of a sensitivity of 112.5 kHz and a detection limit of 35 pg for the absolute mass and suggest a quadratic frequency dependence of the sensor signal, indicating a mass-loading effect. Also using $LiTaO_3$ as a substrate material, Campitelli et al. [42] explored the acoustoelectric interaction between a shear horizontally polarised surface acoustic wave sensor and different commercial brands of natural still spring water. The sensing mechanism is based upon perturbation of the electrical properties of the adjacent liquid and SH-SAW devices were fabricated on 36^0 rotated Y-cut $LiTaO_3$. The comparisons between the theoretical and experimental results show a good agreement and support the validity of the SH-SAW sensor model

and pattern recognition using a neural network algorithm is applied for the discrimination between the four types of sample liquids, with an initial recognition probability of 90%.

More recently, a similar device was proposed by Nomura et al. [43] with the SH-SAW sensor excited on a 36^0 YX $LiTaO_3$ and multi-channel delay-lines constructed on the substrate. Both the phase and the amplitude of the SH-SAW reflected from the edge were measured as a sensor response and the properties of the sensor probe show that the reflecting SAW sensor probe is effective for sensing the liquids. Showing a stable response to the mass loading effects of the anti-Hig-G molecule and having the sensitivity up to 10.8 mg/ml/Hz, the SH-SAW sensor developed by Kwon and Roh [44] was aimed to detect protein molecules in liquid solutions applying a particular antibody thin film on the delay line of the transverse SAW devices. The antibody that was investigated was human-immuno-globulin G (Hig-G) to hold the antigens (anti-HigG) in the protein solution to be measured. Also using $LiTaO_3$ as substrate material, the sensor developed by Hur et al. [45] in one of the more recent studies, involved the twin SAW delay line oscillators operating at 100 MHz fabricated on 36^0 rotated Y-cut X-propagation $LiTaO_3$ piezoelectric single crystals for the detection of deoxyribonucleic acid hybridization. The measurements show a good response of the sensor to the mass loading effects of the DNA hybridization with sensitivity levels up to 1.55 ng/ml/Hz.

Using langasite (LGS) for the first time as a substrate material in the SAW-based bionsensor technology, Berkenpass et al. [21, 46] explored the SH-SAW delay line along the novel Euler propagation direction (0^o, 22^o, 90^o). The results support the idea of LGS being an attractive candidate for liquid sensing and demonstrate the capability of these devices to act as biochemical detectors of aqueous solutions. Another application of langasite pure SH-SAW sensors is demonstrated by Berkenpass

et al. [46] is the detection of the toxigenic *Escherichia coli* O157:H7, a bacterium that has been connected with hemorrhagic colitis and haemolytic urenic syndrome which may be characterized by diarrhoea, kidney failure and even death. The findings of the experiment utilizing a small volume fluid injection system, stable temperature control and high frequency phase measurement were able to validate the LGS SH-SAW biosensor for bacterial detection.

An important contribution to the development of the field of SH-SAW sensors is that of Kondoh and colleagues who started in the early nineties [47-52] to look at the different characteristics of SH-SAW devices. Most of the devices used by the authors are fabricated on 36^0 rotated Y-cut X-propagation $LiTaO_3$. The sensors are applied to the study of enzyme-substrate reaction that show the change in pH [47, 50, 52, 53] or in the effective identification and quality control of fruit juices [54, 55], whisky [55], measurements of the acid rain [56] or Japanese tea [57]. Results show that both theoretically and experimentally the SH-SAW devices can detect mechanical effects such as viscosity of the liquid and mass loading, and can also detect the electrical effects such as permittivity and conductivity of the liquid [51, 58, 59]. Also, based on the derivation of a sensor sensitivity equation the research undertaken by Kondoh and Shiokawa [60] demonstrates for the fist time that the permittivity also changes with the conductivity. There are two other approaches that Kondoh et al. take in testing SH-SAW sensors: one refers to gas sensors [61] suggesting that an optimization of the properties and the thickness of the films and the operating frequency is required for designing SAW gas sensors with polymer coatings; a second innovation consists of a new method to estimate components and concentration of ions in aqueous solution using a liquid-flow sensing system with the SH-SAW sensor without any selective organic films [62]. In addition, Kondoh and his team proposed a method to identify and

evaluate the sample solutions called the self-calibrating ratiometric method (SCRM) [63] which is based on the time differences between rise and fall responses and proves to be an effective method based on these transient response used in the identification of electrolytes in aqueous solutions without selective coatings. The most recent research by Kondoh et al. [64] refers to the development of a methanol sensor for direct methanol fuel cell (DMFC). The operating temperature of DMFC is above 50°C and the wave propagation characteristics were calculated while considering temperature coefficient. The results indicate that the sensitivity increases with increasing temperature. Linear relationships between the sensor response and concentration were obtained and the experiments confirmed an increase in the sensitivity. Thus, by using a chemometric method, the authors succeeded in determining the concentrations of both, simultaneously and therefore, proved that the SH-SAW sensor can be used for DMFC [64].

Finally, Kondoh and Shiokawa propose a review [65] of the commonly used acoustic wave sensors and compare their mass sensitivities arguing that because of its high sensitivity of the electrical perturbation, SH-SAW sensors applications based on acousticoelectric interaction are important not only for detection of physical and chemical values, but also for monitoring in the food industry and the environmental science [65].

2.5 CONCLUSIONS

Acoustic wave sensors are highly versatile devices that are just starting to realize their commercial potential. They are competitively priced, inherently rugged, very sensitive, and intrinsically reliable, and can be interrogated passively and wirelessly. Wireless sensors are beneficial when monitoring parameters on moving objects, such as tyre

pressure on cars or torque on shafts [18]. Sensors that do not require operating power are very desirable for remote monitoring of chemical vapours, moisture, and temperature. Other applications include measuring acceleration, shock, angular rate, displacement, viscosity, force, and flow, in addition to film characterization. The acoustoelectric sensitivity of the sensors is also of importance because they allow the detection of pH levels, ionic contaminants, and electric fields. Surface acoustic wave sensors have proved to be the most sensitive in general as a result of their larger energy density on the surface. For liquid sensing, a special class of shear-horizontal surface acoustic wave sensors which are the Love wave sensors proved to be the most sensitive [18]. Nevertheless, much work is continuing in developing these sensors for future applications.

2.6 REFERENCES:

[1] J. W. Gardner, V. K. Varadan and O. O. Awadelkarim, *Microsensors, MEMS and Smart Devices: Technology, Applications and Devices,* Chichester: John Wiley & Sons, 2001, pp. 503.

[2] D. S. Ballantine, J. Martin, A. J. Ricco, E. T. Zellers, G. C. Frye and H. Wohltjen, *Acoustic Wave Sensors: Theory, Design, and Physico-Chemical Applications.* San Diego: Academic Press, 1997, pp. 436.

[3] B. A. Čavić, G. L. Hayward and M. Thompson, "Acoustic waves and the study of biochemical macromolecules and cells at the sensor-liquid interface", *Analyst,* vol. 124, pp. 1405-1420, 1999.

[4] B. Jakoby and M. J. Vellekoop, "Analysis and optimization of love wave liquid sensors", *IEEE Trans Ultrason Ferroelectr Freq Control,* vol. 45, pp. 1293-1302, 1998.

[5] B. Jakoby and M. J. Vellekoop, "Viscosity sensing using a Love-wave device," *Sens Actuators A: Phys,* vol. 68, pp. 275-281, 1998.

[6] D. P. Morgan, *Surface-Wave Devices for Signal Processing*, Studies in Electrical and Electronic Engineering 19, Amsterdam: Elsevier, 1985, pp. 432.

[7] S.G. Joshi and Y. Jin, "Excitation of ultrasonic Lamb waves in composite membranes," *Proceedings of the IEEE Ultrasonics Symposium* 2, pp. 893-896, 1996.

[8] A. F. Collings and F. Caruso, "Biosensors: recent advances," *Reports on Progress in Physics,* vol. 60, pp. 1397-1445, 1997.

[9] R. M. White, "Surface elastic waves," *Proc. IEEE,* vol. 58, no. 8, pp. 1238-1276, 1970.

[10] R. M. White, "Acoustic interactions from Faraday's crispations to MEMS," *Faraday Discuss.*, vol. 107, pp. 1-13, 1997.

[11] R. M. White and F. W. Voltmer, "Direct piezoelectric coupling to surface elastic waves," *Applied Physics Letters,* vol. 7, pp. 314-316, 1965.

[12] R. M. White, "Acoustic sensors for physical, chemical and biochemical applications," *Proceedings of the Annual IEEE International Frequency Control Symposium*, pp. 587-594, 1998.

[13] M. G. Schweyer, J. C. Andle, D. J. McAllister and J. F. Vetelino, "An acoustic plate mode sensor for aqueous mercury," *Sensors and Actuators, B: Chemical,* vol. 35, pp. 170-175, 1996.

[14] B. Jakoby and M. J. Vellekoop, "Properties of love waves: Applications in sensors," *Smart Mater Struct,* vol. 6, pp. 668-679, 1997.

[15] Y. V. Gulyaev, "Review of shear surface acoustic waves in solids," *IEEE Trans Ultrason Ferroelectr Freq Control,* vol. 45, pp. 935-938, 1998.

[16] J. M. Hossenlopp, "Applications of acoustic wave devices for sensing in liquid environments," *Appl Spectrosc Rev,* vol. 41, pp. 151-164, 2006.

[17] T. M. A. Gronewold, "Surface acoustic wave sensors in the bioanalytical field: Recent trends and challenges," *Analytica Chimica Acta,* vol. 603, pp. 119-128, 2007.

[18] B. Drafts, "Acoustic Wave Technology Sensors," *IEEE Transactions on Microwave Theory and Tecniques*, vol. 49, no.4, pp. 795-802, 2001.

[19] K. Hashimoto, *Surface Acoustic Wave Devices in Telecommunications: Modelling and Simulation,* Berlin: Springer, 2000, pp. 330.

[20] G. Kovacs, M. Anhorn, H. E. Engan, G. Visintini and C. C. W. Ruppel, "Improved material constants for LiNbO3 and LiTaO3," in *Proceedings of the IEEE Ultrasonics Symposium,* pp. 435-438, 1990.

[21] E. Berkenpas, S. Bitla, P. Millard and M. P. Da Cunha, "Pure shear horizontal SAW biosensor on langasite," *IEEE Trans Ultrason Ferroelectr Freq Control,* vol. 51, pp. 1404-1411, 2004.

[22] T. B. Pollard, T. D. Kenny, J. F. Vetelino and M. P. D. Cunha, "Pure SH-SAW propagation, transduction and measurements on KNbO3," *IEEE Trans Ultrason Ferroelectr Freq Control,* vol. 53, pp. 199-207, 2006.

[23] T. Pastureaud, M. Solal, B. Biasse, B. Aspar, J. B. Briot, W. Daniau, W. Steichen, R. Lardat, V. Laude, A. Laens, A. Friedt, J. Friedt and S. Ballandras, "High-Frequency Surface Acoustic Waves Excited on Thin-Oriented $LiNbO_3$ Single-Crystal Layers Transferred Onto Silicon," *IEEE Trans Ultrason Ferroelectr Freq Control*, vol. 54 (4), 870-6, 2007.

[24] V. K. Varadan and J. W. Gardner, "Smart tongue and nose," in *Proceedings of the 1999 Smart Structures and Materials - Smart Electronics and MEMS,* pp. 67-76, 1999.

[25] T. M. Niemczyk, S. J. Martin, G. C. Frye and A. J. Ricco, "Acoustoelectric interaction of plate modes with solutions," *Journal of Applied Physics,* vol. 64, pp. 5002-5008, 1988.

[26] S. J. Martin, A. J. Ricco, T. M. Niemczyk and G. C. Frye, "Characterization of SH acoustic plate mode liquid sensors," *Sens Actuators,* vol. 20, pp. 253-268, 1989.

[27] F. Bender, R. Dahint, F. Josse, A. J. Ricco and S. J. Martin, "Characteristics of acoustic plate modes on rotated Y-cuts of quartz utilized for biosensing applications," *Anal. Chem.,* vol. 71, pp. 5064-5068, 1999.

[28] Y. S. Lee, D. S. Yoon and T. S. Kim, "Improvement of the mass sensitivity in flexural plate wave biosensor based on PZT thin film," *Integrated Ferroelectrics* 69, pp. 391-400, 2005.

[29] G. Kovacs and A. Venema, "Theoretical comparison of sensitivities of acoustic shear wave modes for (bio)chemical sensing in liquids," *Applied Physics Letters,* vol. 61, pp. 639-641, 1992.

[30] E. Gizeli, M. Liley, C. R. Lowe and H. Vogel, "Antibody Binding to a Functionalized Supported Lipid Layer: A Direct Acoustic Immunosensor," *Anal. Chem.,* vol. 69, pp. 4808-4813, 1997.

[31] E. Gizeli, N. J. Goddard, C. R. Lowe and A. C. Stevenson, "A Love plate biosensor utilising a polymer layer," *Sens. Actuators B,* 1992.

[32] A. C. Stevenson, E. Gizeli, N. J. Goddard and C. R. Lowe, "Acoustic Love plate sensors: a theoretical model for the optimization of the surface mass sensitivity,"

Sens Actuators, B Chem, vol. B14, pp. 635-637, 13 September 1992 through 17 September 1992. 1993.

[33] E. Gizeli, C. R. Lowe, M. Liley and H. Vogel, "Detection of supported lipid layers with the acoustic Love waveguide device: Application to biosensors," *Sens Actuators, B Chem,* vol. 34, pp. 295-300, 1996.

[34] E. Gizeli and C. R. Lowe, "Immunosensors," *Curr. Opin. Biotechnol.,* vol. 7, pp. 66-71, 1996.

[35] C. McMullan, H. Mehta, E. Gizeli and C. R. Lowe, "Modelling of the mass sensitivity of the Love wave device in the presence of a viscous liquid," *J Phys D,* vol. 33, pp. 3053-3059, 2000.

[36] K. Saha, F. Bender, A. Rasmusson and E. Gizeli, "Probing the viscoelasticity and mass of a surface-bound protein layer with an acoustic waveguide device," *Langmuir,* vol. 19, pp. 1304-1311, 2003.

[37] E. Howe and G. Harding, "A comparison of protocols for the optimisation of detection of bacteria using a surface acoustic wave (SAW) biosensor," *Biosens. Bioelectron.,* vol. 15, pp. 641-649, 2000.

[38] F. Josse, F. Bender and R. W. Cernosek, "Guided shear horizontal surface acoustic wave sensors for chemical and biochemical detection in liquids," *Anal. Chem.,* vol. 73, pp. 5937-5944, 2001.

[39] D. W. Branch and S. M. Brozik, "Low-level detection of a Bacillus anthracis simulant using Love-wave biosensors on 36°YX LiTaO3," *Biosens. Bioelectron.,* vol. 19, pp. 849-859, 2004.

[40] F. Martin, M. I. Newton, G. McHale, K. A. Melzak and E. Gizeli, "Pulse mode shear horizontal-surface acoustic wave (SH-SAW) system for liquid based sensing applications," *Biosens. Bioelectron.,* vol. 19, pp. 627-632, 2004.

[41] W. Welsch, C. Klein, R. M. Öksüzoglu, M. Von Schickfus and S. Hunklinger, "Immunosensing with surface acoustic wave sensors," *Sens Actuators A Phys,* vol. 62, pp. 562-564, 1997.

[42] A. P. Campitelli, W. Wlodarski and M. Hoummady, "Identification of natural spring water using shear horizontal SAW based sensors," *Sens Actuators, B Chem,* vol. B49, pp. 195-201, 1998.

[43] T. Nomura, A. Saitoh and T. Miyazaki, "Liquid sensor probe using reflecting SH-SAW delay line," *Sens Actuators, B Chem,* vol. 91, pp. 298-302, 2003.

[44] Y. Kwon and Y. Roh, "Development of SH-SAW sensors for underwater measurement," *Ultrasonics,* vol. 42, pp. 409-411, 2004.

[45] Y. Hur, J. Han, J. Seon, Y. E. Pak and Y. Roh, "Development of an SH-SAW sensor for the detection of DNA hybridization," *Sens Actuators A Phys,* vol. 120, pp. 462-467, 2005.

[46] E. Berkenpas, P. Millard and M. Pereira da Cunha, "Detection of Escherichia coli O157:H7 with langasite pure shear horizontal surface acoustic wave sensors," *Biosens. Bioelectron.,* vol. 21, pp. 2255-2262, 2006.

[47] J. Kondoh and S. Shiokawa, "Measurements of conductivity and pH of liquid using surface acoustic wave devices," *Jpn. J. Appl. Phys.,* vol. 31, pp. 82-84, 1992.

[48] J. Kondoh, Y. Matsui and S. Shiokawa, "SH-SAW biosensor based on pH change," *Proceedings of the IEEE Ultrasonics Symposium* 1, pp. 337-340, 1993.

[49] J. Kondoh and S. Shiokawa, "SH-SAW taste sensor based acoustoelectric interaction," *Proceedings of the IEEE Ultrasonics Symposium* 1, pp. 421-424, 1993.

[50] J. Kondoh, Y. Matsui and S. Shiokawa, "New biosensor using shear horizontal surface acoustic wave device," *Jpn J Appl Phys Part 1 Regul Pap Short Note Rev Pap,* vol. 32, pp. 2376-2379,.1993.

[51] J. Kondoh and S. Shiokawa, "Liquid sensor based on a shear horizontal SAW device," *Electron. Commun. Jpn. Part II Electron.,* vol. 76, pp. 69-82, 1993.

[52] J. Kondoh, S. Shiokawa and Z. Georgiev, "Shear-horizontal SAW device as a pH monitor," *Sens Actuators, B Chem,* vol. B13, pp. 429-431, 13 September 1992 through 17 September 1992. 1993.

[53] J. Kondoh, T. Imayama, Y. Matsui and S. Shiokawa, "Enzyme biosensor based on surface acoustic wave device," *Electron. Commun. Jpn. Part II Electron.,* vol. 79, pp. 69-75, 1996.

[54] J. Kondoh and S. Shiokawa, "New application of shear horizontal surface acoustic wave sensors to identifying fruit juices," *Jpn J Appl Phys Part 1 Regul Pap Short Note Rev Pap,* vol. 33, pp. 3095-3099, 1994.

[55] J. Kondoh and S. Shiokawa, "Identification of liquid samples using shear-horizontal surface acoustic wave sensors," *Electron. Commun. Jpn. Part II Electron.,* vol. 78, pp. 50-59, 1995.

[56] J. Kondoh and S. Shiokawa, "Liquid-phase microsensor based on surface acoustic wave devices," *Electron. Commun. Jpn. Part II Electron.,* vol. 81, pp. 9-17, 1998.

[57] J. Kondoh, T. Muramatsu, T. Nakanishi, Y. Matsui and S. Shiokawa, "Development of practical surface acoustic wave liquid sensing system and its application for measurement of Japanese tea," *Sens Actuators, B Chem,* vol. 92, pp. 191-198, 2003.

[58] J. Kondoh, K. Saito, S. Shiokawa and H. Suzuki, "Simultaneous measurements of liquid properties using multichannel shear horizontal surface acoustic wave

microsensor," *Jpn J Appl Phys Part 1 Regul Pap Short Note Rev Pap,* vol. 35, pp. 3093-3096, 1996.

[59] J. Kondoh, S. Hayashi and S. Shiokawa, "Simultaneous detection of density and viscosity using surface acoustic wave liquid-phase sensors," *Jpn J Appl Phys Part 1 Regul Pap Short Note Rev Pap,* vol. 40, pp. 3713-3717, 2001.

[60] J. Kondoh and S. Shiokawa, "Shear surface acoustic wave liquid sensor based on acoustoelectric interaction," *Electron. Commun. Jpn. Part II Electron.,* vol. 78, pp. 101-112, 1995.

[61] J. Kondoh, S. Shiokawa, M. Rapp and S. Stier, "Simulation of viscoelastic effects of polymer coatings on surface acoustic wave gas sensor under consideration of film thickness," *Jpn J Appl Phys Part 1 Regul Pap Short Note Rev Pap,* vol. 37, pp. 2842-2848, 1998.

[62] T. Yamazaki, J. Kondoh, Y. Matsui and S. Shiokawa, "Estimation of components and concentration in mixture solutions of electrolytes using a liquid flow system with SH-SAW sensor," *Sens Actuators A Phys,* vol. 83, pp. 34-39, 2000.

[63] J. Kondoh, Y. Matsui and S. Shiokawa, "Identification of electrolyte solutions using a shear horizontal surface acoustic wave sensor with a liquid-flow system," *Sens Actuators, B Chem,* vol. 91, pp. 309-315, 2003.

[64] J. Kondoh, S. Tabushi, Y. Matsui and S. Shiokawa, "Development of methanol sensor using a shear horizontal surface acoustic wave device for a direct methanol fuel cell," *Sens Actuators, B Chem,* vol. 129, pp. 575-580, 2008.

[65] S. Shiokawa and J. Kondoh, "Surface acoustic wave sensors," *Jpn J Appl Phys Part 1 Regul Pap Short Note Rev Pap,* vol. 43, pp. 2799-2802, 2004.

CHAPTER 3:

THEORETICAL MODELS

3.1 INTRODUCTION

While the previous chapter presented an overview of the acoustic waves and modes, along with several sensing applications, this chapter focuses on the perturbation mechanisms of the surface acoustic waves, particularly SH-SAW.

First general perturbations and interaction mechanisms are covered as they are considered a necessary "phenomenological" background for the derivation of specific, tailored models that account for SAW-liquid media interactions. Two theoretical models are given: the first one was developed by Kondoh [1] and is based on Auld's perturbation theory [2]; the second one follows an equivalent circuit approach initially proposed by Niemczyk and Martin [3] to describe the acoustoelectric interaction.

3.2 PERTURBATIONS IN ACOUSTIC WAVES

Perturbation in acoustic wave propagation can be derived from an analysis of wave energy density and its power dissipation. It has been shown that wave velocity changes are related to the changes in wave energy density. Similarly, and perhaps more intuitively, the wave attenuation is linked to the wave dissipated power [4].

Power density P (power/area) carried by the wave can be linked to the wave energy density U (energy/volume) stored in a lossless substrate through the following relation:

$$U = P\tau = P/V \qquad [3.1]$$

where τ is the time a wave (with a phase velocity V) needs to transit a unity volume.

For an ideal lossless medium the power density is considered constant (*P=cst)*, and differentiating [3.1] the following fundamental relation between wave velocity and energy density is derived:

$$\frac{\Delta V}{V_0} = -\frac{\Delta U}{U_0} \qquad [3.2]$$

where V_0 and U_0 refer to unperturbed propagation (phase) velocity and, respectively to energy density. *The fractional change in wave velocity is equal to the negative of fractional change in wave energy density*. A phenomenological explanation is that in a system excited at a certain frequency the wavelength adjusts so that the peak kinetic energy equals the peak potential wave energy [4]. For sensing applications the result is that changes in the medium that impact the wave energy density will also cause changes of the wave velocity.

In lossy media, it is important to consider the effect of power dissipation on wave propagation. Energy conservation considerations require that dissipated power P_d is balanced by a reduction in power transmitted by the wave P, and thus $P_d = -\frac{\partial P}{\partial x}$.

Energy and power flow are proportional to the square of wave amplitude, and for a lossy medium:

$$P(x) = P_0 e^{-2\alpha x} \Rightarrow \frac{\partial P}{\partial x} = -2\alpha P$$

The attenuation formula can be easily obtained by combining the above equations as follows:

$$\alpha = \frac{P_d}{2P} \qquad [3.3]$$

Attenuation α represents half of the ratio of power dissipated to power transmitted by the wave. Both velocity and attenuation changes are independent of wave amplitude because of their dependence on ratios of energy and power, and not on absolute values.

Typically, perturbations tend to change both energy storage and power dissipation and thus result in a mixture of velocity and attenuation changes.

As perturbations generally imply changes in power that is both stored and dissipated, the complex power transfer from the wave can be defined in terms of power dissipation P_d and changes in stored energy ΔU:

$$P_T = P_d + j2\omega\Delta U$$

3.3 PERTURBATION THEORY MODEL FOR SH-SAW

3.3.1 Mechanical perturbations

A wave propagating in the x direction can be described as

$$u(x,y,z,t) = u(y,z)e^{j(\omega t - kx)}e^{-\alpha x} \qquad [3.4]$$

If a shear-horizontal wave (no displacement along the z axis) is considered and the exponential terms rearranged, equation [3.4] can be written as

$$u(x,y,t) = u(y)e^{j(\omega t - \beta x)} \qquad [3.5]$$

where
$$\beta = k - j\alpha = \frac{\omega}{V} - j\alpha \qquad [3.6]$$

is the complex perturbation factor defined as wavenumber (k) and attenuation (α). In its turn, k can be expressed as ω/V, where ω is the angular frequency, and V the phase velocity.

When the frequency is constant, the changes in the wave propagation can be represented as:

$$\Delta\beta = -\omega\frac{\Delta V}{V^2} - j\Delta\alpha \qquad [3.7]$$

or in its normalised form:
$$\frac{\Delta\beta}{k} = -\frac{\Delta V}{V} - j\frac{\Delta\alpha}{k} \qquad [3.8]$$

The perturbation formula for a SH-SAW liquid sensor can be derived from Auld's perturbation theory for gases, extended to the liquid phase. Mathematically, it is given by

$$\frac{\Delta\beta}{k} = -\frac{jV}{4\omega P}(v^* \cdot Z_{Al}{}' v + v \cdot Z_{Al}{}^* \cdot v^*) \qquad [3.9]$$

Where P the flow per unit width, v the particle velocity vector, and Z_{Al} the acoustic surface impedance. Also, ′ indicates a perturbed quantity, * indicates a complex conjugate. $\Delta\beta$ is the perturbation of the complex propagation constant β.

Substituting [3.8] in [3.9] and separating real and imaginary parts, the change in the complex propagation constant can be decomposed into the changes of the velocity and the attenuation as

$$\frac{\Delta V}{V} = -\frac{V}{4\omega P}(v^* \cdot Z_{Ali}{}' \cdot v - v \cdot Z_{Ali} \cdot v^*), \qquad [3.10]$$

$$\frac{\Delta \alpha}{k} = -\frac{V}{4\omega P}(v^* \cdot Z_{Alr}{}' \cdot v + v \cdot Z_{Alr} \cdot v^*). \qquad [3.11]$$

Here the real and imaginary parts of Z_{Al}. are represented by the subscripts r and i.

The SAW liquid interactions that arise from mechanical coupling at the sensor's interface include effects of mass loading and viscoelasticity. Further on the case of a SH-SAW is considered.

3.3.1.1 Mass Loading in Liquid

In the following section the case in which an isotropic thin film of thickness h and density ρ is uniformly loading the metallised surface in a liquid is considered by assuming that the liquid properties do not change before and after perturbation, and the velocity shift and attenuation change can be obtained as [1]:

$$\frac{\Delta V}{V} = -\frac{V h v_2{}^2}{4P}\left(\rho' - \frac{\mu'}{V^2}\right), \qquad [3.12]$$

$$\frac{\Delta \alpha}{k} = 0 \qquad [3.13]$$

where, μ' is the Lamè constant of the film and v_2 is the particle velocity component of the shear horizontal mode.

3.3.1.2 Viscous Coupling

Liquid is assumed to be Newtonian, with a viscosity of η and density ρ_l and being loaded on the metallized surface of the delay line. If the surface acoustic impedance is substituted into equations [3.10] and [3.11] the following expressions are obtained [1]:

$$\frac{\Delta V}{V} = -\frac{V{v_2}^2}{4\omega P}\left(\sqrt{\frac{\omega\eta'\rho_{l'}}{2}} - \sqrt{\frac{\omega\eta\rho_l}{2}}\right) \qquad [3.14]$$

$$\frac{\Delta \alpha}{k} = -\frac{V{v_2}^2}{4\omega P}\left(\sqrt{\frac{\omega\eta'\rho_{l'}}{2}} - \sqrt{\frac{\omega\eta\rho_l}{2}}\right) \qquad [3.15]$$

3.3.2 Acousto-electric interactions

Mechanical strains associated to the SAWs travel in piezoelectric materials and generate a layer of bound charge at the surface that accompanies the mechanical deformations. These induced charges are the sources for the wave potential Φ, and also produce an electric field that extends into the liquid on a distance equal with the electric field decay length ($\lambda/2\pi$). Metallisation of the propagation path allows the charge carriers in the film to redistribute and to compensate for the layer of bound charge generated by the passing surface wave.

The SH-SAW is affected by the electrical properties of the liquid. If the conductivity of an unperturbed (or reference) liquid is equal to zero, its electrical properties are given by

$$\varepsilon_l = \varepsilon_r \varepsilon_0 \qquad [3.16]$$

Here, ε_l and ε_0 are the permittivity of the unperturbed liquid and that of the free space, and ε_r is the relative permittivity of the unperturbed liquid. After perturbation, ε_l changes to the complex permittivity $\varepsilon_{l'}$ expressed by

$$\varepsilon_l' = \varepsilon_r'\varepsilon_0 - j\frac{\sigma'}{\omega} \qquad [3.17]$$

where, σ′ is the liquid conductivity. Taking as a reference point the perturbation theory proposed by Auld, the following relationships for changes in velocity and attenuation of the SH-wave in the presence of a liquid are achieved [5]:

$$\frac{\Delta V}{V} = -\frac{K_s^2}{2}\frac{(\sigma'/\omega)^2 + \varepsilon_0(\varepsilon_r' - \varepsilon_r)(\varepsilon_r'\varepsilon_0 + \varepsilon_P^T)}{(\sigma'/\omega)^2 + (\varepsilon_r'\varepsilon_0 + \varepsilon_P^T)^2} \qquad [3.18]$$

$$\frac{\Delta\alpha}{k} = \frac{K_s^2}{2}\frac{(\sigma'/\omega)(\varepsilon_r\varepsilon_0 + \varepsilon_P^T)}{(\sigma'/\omega)^2 + (\varepsilon_r'\varepsilon_0 + \varepsilon_P^T)^2} \qquad [3.19]$$

where K_s^2 is the electromechanical coupling coefficient when the unperturbed liquid is loaded on the free surface and ε_P^T is the effective permittivity of the SAW crystal, ε_r is the permittivity of the reference liquid, ε_r' and σ' are the permittivity and conductivity (related to loss) of the measurand.

From equations [3.18] and [3.19] by eliminating the conductivity and permittivity of the mesurand, two parametric relations can be determined in the form of circle equations:

$$\left[\frac{\Delta V}{V} + \frac{K_s^2}{4}\frac{\varepsilon_0(2\varepsilon_r' - \varepsilon_r') + \varepsilon_P^T}{\varepsilon_r'\varepsilon_0 + \varepsilon_P^T}\right]^2 + \left[\frac{\Delta\alpha}{k}\right]^2 = \left[\frac{K_s^2}{4}\frac{\varepsilon_r\varepsilon_0 + \varepsilon_P^T}{\varepsilon_r'\varepsilon_0 + \varepsilon_P^T}\right]^2 \qquad [3.20]$$

$$\left[\frac{\Delta V}{V} + \frac{K_s^2}{2}\right]^2 + \left[\frac{\Delta\alpha}{k} - \frac{K_s^2}{4}\frac{\varepsilon_r\varepsilon_0 + \varepsilon_P^T}{\sigma'/\omega}\right]^2 = \left[\frac{K_s^2}{4}\frac{\varepsilon_r\varepsilon_0 + \varepsilon_P^T}{\sigma'/\omega}\right]^2 \qquad [3.21]$$

Giving values for the normalised conductivity σ'/ω in the range $(0.02 \div 2) \times 10^{-8}$ (S/m)Hz and relative permittivity $\varepsilon_r' \in (1 - 100)$, a ε_r' - σ' chart can be obtained [6]:

From the measured values of velocity shift $\Delta V/V$ and attenuation change $\Delta\alpha/k$, electrical properties of the tested liquid can be obtained by solving equations [3.20] and [3.21]; also, the permittivity and conductivity of the liquid can be numerically or graphically evaluated [6].

Alternatively, the derivation of the acoustoelectric interaction parameters can be obtained by the mean of an equivalent circuit model [3].

3.4 EQUIVALENT CIRCUIT MODEL

The induced surface charge density has a sinusoidal variation and has associated an electrical potential Φ, so that a fraction K^2, defined as the electromechanical coupling factor of the wave energy is carried in electrical form. In the absence of ions in solution Φ can be found by solving Poisson's equation, which yields

$$\nabla^2\phi = 0 \quad \Rightarrow \quad \phi(y,x,t) = \phi_0 e^{-ky} e^{j(\omega t - kx)} \qquad [3.21]$$

in which k is the unperturbed wave number, and ϕ_0 is the potential at the solid/liquid interface.

The equivalent circuit model treats the near surface currents induced by the acoustic wave. The elements G, C_l, C_s in Figure 3.1 can be obtained by considering the current flows caused by the varying potential ϕ.

The passing wave induced charges may be represented as an alternative current source. The amplitude i_0 of current density source can be derived from the power flow considerations [1]:

$$i_0^2 = 2K\omega k^2(\varepsilon_0 + \varepsilon_S)P_f \qquad [3.22]$$

The conduction current density arising from drift (migration) is denoted by i_1, the displacement current due to the dipolar nature of the liquid is i_2, and the displacement (capacitive) current density generated in the substrate is i_3 as seen in Figure 3.1a.

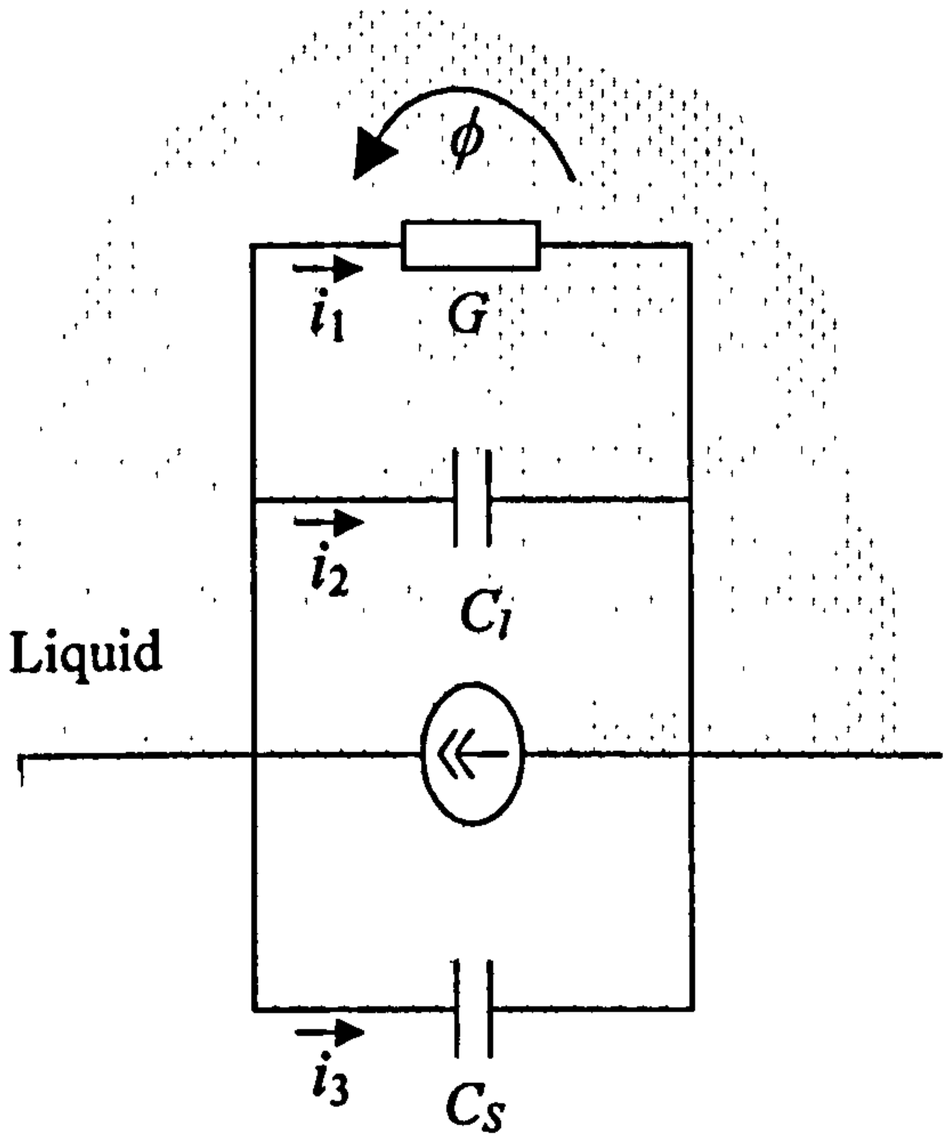

(a). Equivalent circuit of acoustoelectric interaction

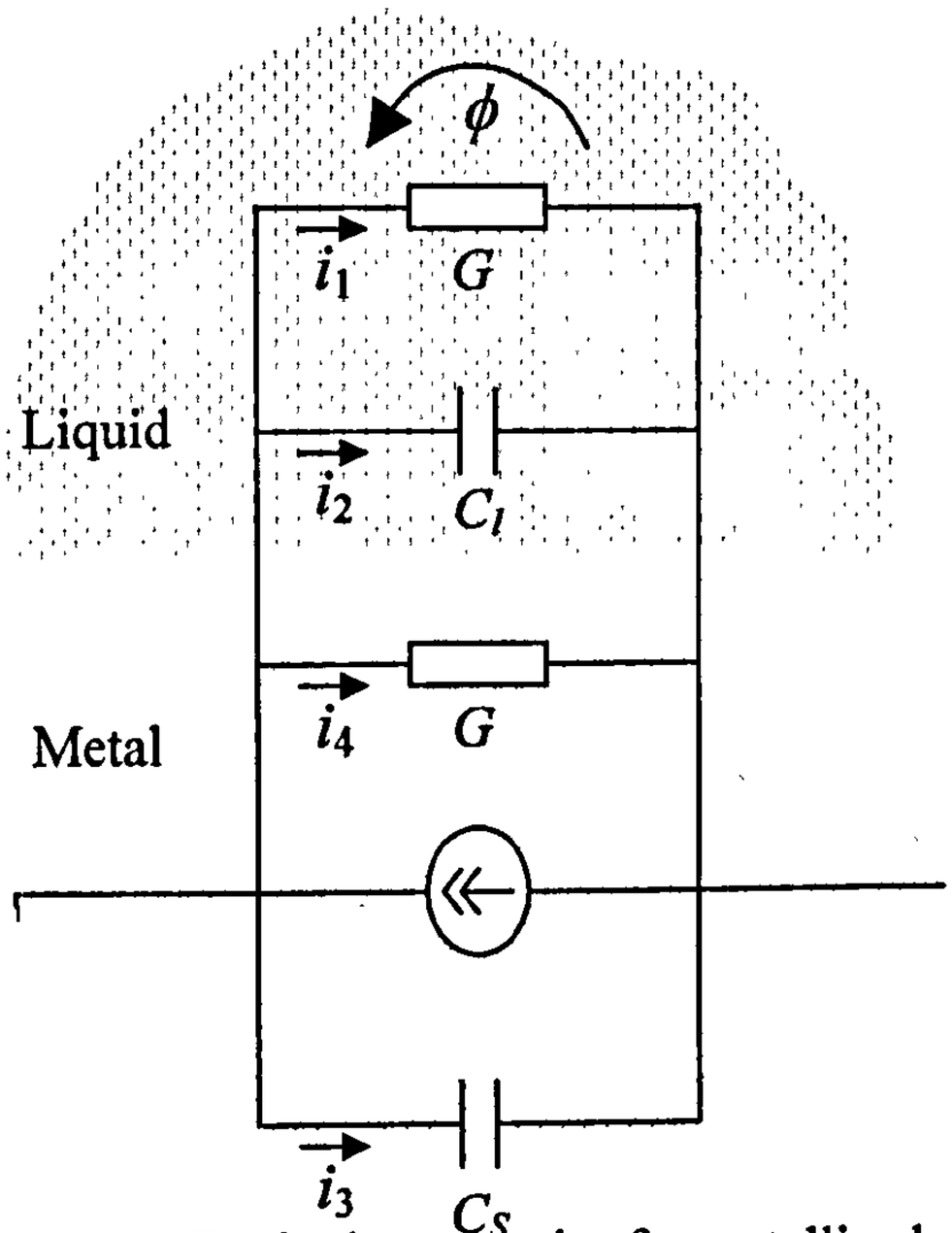

(b) Equivalent circuit of a metallised surface

Figure 3.1: Equivalent Circuits for SAW interaction with liquids

The following formula links the substrate displacement current to the surface potential:

$$i_3 = -j\omega\varepsilon_S E_y = j\omega\varepsilon_S \left.\frac{\partial\phi}{\partial y}\right|_{y=0^-} \qquad [3.23]$$

On the other hand, from the equivalent circuit, i_3 can be written as:

$$i_3 = j\omega C_S \phi_0 \qquad [3.24]$$

so

$$j\omega C_S\phi_0 = j\omega\varepsilon_S k\phi_0 \quad \Rightarrow \quad C_S = k\varepsilon_S \qquad [3.25]$$

Total displacement and drift current following into the liquid is

$$i_1 + i_2 = -(\sigma + j\omega\varepsilon_l)\left.\frac{\partial\phi}{\partial y}\right|_{y=0^+} \qquad [3.26]$$

Also from the circuit given in Figure 3.1a it can be written

$$i_1 + i_2 = (G + j\omega C_l)\phi_0 \qquad [3.27]$$

which implies that:

$$G=k\sigma \qquad [3.28]$$

$$C_l = k\varepsilon_l \qquad [3.29]$$

Using the equivalent circuits in Figures 3.1a and 3.1b the change in electrical power transferred from the wave can be calculated (ΔP_l). P_t is a complex quantity and the principle of this method is based on the identification of the real power component which is the dissipated power associated with attenuation, and the imaginary part which is the reactive power or the stored power in the equivalent capacitance.

Any electrical transfer of power from the acoustic wave must be perfectly well balanced by a change in power carried by the waveguide. The power transferred (per surface area) from the wave P_t may be related to the power flow P_f along the guide by

$$P_t = -\frac{\partial P_f}{\partial z} = 2(\alpha + jk)P_f \qquad [3.30]$$

where α is the attenuation of the wave. The average electrical power is given by $i_0^2/2Y$, where Y stands for the total shunt admittance in parallel with the current source [3].

All the above considerations imply that attenuation and velocity perturbation arising from changes in electrical conditions at the surface can be written as

$$\frac{\Delta\alpha}{k} - j\frac{\Delta v}{v_0} = \frac{\Delta P}{2kP_j} = \frac{i_0^2}{4kP_j}\Delta\left(\frac{1}{Y}\right) \qquad [3.31]$$

which practically relates the changes in propagation characteristics to the changes in total admittance.

For an estimation of these changes, the equivalent admittances are calculated for the cases the liquid is in direct contact with the piezoelectric substrate (Figure 3.1a) and for the case liquid is placed on a metallised region of the substrate (Figure 3.1b).

$$Y_1 = G_l + j\omega(C_S + C_l) = k\sigma_l + j\omega k(\varepsilon_S + \varepsilon_l) \qquad [3.32]$$

$$Y_2 = G_l + G_m + j\omega(C_S + C_l)k\sigma_m + k\sigma_l + j\omega k(\varepsilon_S + \varepsilon_l) \qquad [3.33]$$

After replacing [3.32] [3.33] in [3.31] and separating the real and imaginary part the velocity change and attenuation can be identified as:

$$\frac{\alpha}{k}=\frac{K^2}{2}\omega(\varepsilon_S+\varepsilon_0)\frac{\sigma_m(\sigma_l(\sigma_l+\sigma_m)-\omega^2(\varepsilon_S+\varepsilon_l)^2)}{(\sigma_l(\sigma_l+\sigma_m)-\omega^2(\varepsilon_S+\varepsilon_l)^2)^2+(\omega(\varepsilon_S+\varepsilon_l)(2\sigma_l+\sigma_m))^2} \quad [3.34]$$

$$\frac{\Delta V}{V_0}=-\frac{K^2}{2}\omega^2(\varepsilon_S+\varepsilon_0)\ \frac{\sigma_m(\varepsilon_S+\varepsilon_l)(2\sigma_l+\sigma_m)}{(\sigma_l(\sigma_l+\sigma_m)-\omega^2(\varepsilon_S+\varepsilon_l)^2)^2+(\omega(\varepsilon_S+\varepsilon_l)(2\sigma_l+\sigma_m))^2} \quad [3.35]$$

Using the normalised notation for the conductivity terms ($\sigma_l^{'}=\sigma_l/\omega$ and $\sigma_m^{'}=\sigma_m/\omega$) the above equations become:

$$\frac{\alpha}{k}=\frac{K^2}{2}(\varepsilon_S+\varepsilon_0)\frac{\sigma_m^{'}(\sigma_l^{'}(\sigma^{'}_l+\sigma_m^{'})-(\varepsilon_S+\varepsilon_l)^2)}{(\sigma_l^{'}(\sigma^{'}_l+\sigma_m^{'})-(\varepsilon_S+\varepsilon_l)^2)^2+((\varepsilon_S+\varepsilon_l)(2\sigma_l^{'}+\sigma_m^{'}))^2} \quad [3.36]$$

$$\frac{\Delta V}{V_0}=-\frac{K^2}{2}(\varepsilon_S+\varepsilon_0)\ \frac{\sigma_m^{'}(\varepsilon_S+\varepsilon_l)(2\sigma_l^{'}+\sigma_m^{'})}{(\sigma_l^{'}(\sigma^{'}_l+\sigma_m^{'})-(\varepsilon_S+\varepsilon_l)^2)^2+((\varepsilon_S+\varepsilon_l)(2\sigma_l^{'}+\sigma_m^{'}))^2} \quad [3.37]$$

In the case that $\sigma_m>\sigma_l$ the liquid's conductivity can be ignored, and the equivalent admittance becomes

$$y_2=k\sigma_m+j\omega k(\varepsilon_S+\varepsilon_l) \quad [3.38]$$

and the velocity change and attenuation can now be written:

$$\frac{\alpha}{k}=\frac{K^2}{2}\omega(\varepsilon_S+\varepsilon_0)(\sigma_m-\sigma_l)\frac{\sigma_l\sigma_m-\omega^2(\varepsilon_S+\varepsilon_l)^2}{(\sigma_l\sigma_m-\omega^2(\varepsilon_S+\varepsilon_l)^2)^2+(\omega(\varepsilon_S+\varepsilon_l)(\sigma_l+\sigma_m))^2} \quad [3.39]$$

$$\frac{\Delta V}{V_0}=-\frac{K^2}{2}\omega^2(\varepsilon_S+\varepsilon_0)\ \frac{(\sigma_m^2-\sigma_l^2)(\varepsilon_S+\varepsilon_l)}{(\sigma_l\sigma_m-\omega^2(\varepsilon_S+\varepsilon_l)^2)^2+(\omega(\varepsilon_S+\varepsilon_l)(\sigma_l+\sigma_m))^2} \quad [3.40]$$

For the assumption for which the metal conductivity is extremely large $\sigma_m>>\sigma_l$ – it would mean an infinite y_2 admittance (the metal short-circuits/ annihilates all the liquid electrical parameters), then:

$$\frac{\Delta\alpha}{k} - j\frac{\Delta v}{v_0} = \frac{\Delta P}{2kP_j} = \frac{i_0^2}{4kP_jY_1} \qquad [3.41]$$

where again $Y_1 = k\sigma_l + j\omega k(\varepsilon_S + \varepsilon_l)$

Thus,

$$\frac{\alpha}{k} = \frac{K^2}{2}(\varepsilon_S + \varepsilon_0)\omega\frac{\sigma_l}{(\sigma_l)^2 + \omega^2(\varepsilon_S + \varepsilon_l)^2} \qquad [3.42]$$

$$\frac{\Delta V}{V_0} = -\frac{K^2}{2}(\varepsilon_S + \varepsilon_0)\omega\frac{\omega(\varepsilon_S + \varepsilon_l)}{(\sigma_l)^2 + \omega^2(\varepsilon_S + \varepsilon_l)^2} \qquad [3.43]$$

A particular case of acoustoelectric interaction for the liquids has been modelled by Niemczyk who used a similar circuit approach to investigate how wave/ion coupling affects an APM propagation. He demonstrated that the perturbation in the acoustic wave velocity and attenuation arising from the ion concentration can be explained by the solution conductivity through the following formulas:

$$\frac{\Delta V}{V_0} = -\frac{K^2}{2}\left(\frac{\varepsilon_S + \varepsilon_0}{\varepsilon_S + \varepsilon_l}\right)\frac{\sigma^2}{\sigma^2 + \omega^2(\varepsilon_S + \varepsilon_l)^2} \qquad [3.44]$$

$$\frac{\alpha}{k} = \frac{K^2}{2}\left(\frac{\varepsilon_S + \varepsilon_0}{\varepsilon_S + \varepsilon_l}\right)\cdot\frac{\omega\sigma(\varepsilon_S + \varepsilon_l)}{\sigma^2 + \omega^2(\varepsilon_S + \varepsilon_l)^2} \qquad [3.45]$$

3.5 CONCLUSION

Surface acoustic wave general perturbations were expressed by analytical models. The chapter was then focused on specific liquid wave interactions and two theoretical models that can be used to represent the interactions are reviewed. Kondoh's model is based on Auld's perturbation theory, while Niemczyk et al. are deriving their acoustoelectric interaction based on an equivalent circuit model.

3.6 REFERENCES

[1] J. Kondoh, K. Saito, S. Shiokawa and H. Suzuki, "Simultaneous measurements of liquid properties using multichannel shear horizontal surface acoustic wave microsensor," *Jpn J Appl Phys Part 1 Regul Pap Short Note Rev Pap,* vol. 35, pp. 3093-3096, 1996.

[2] B.A. Auld, *Acoustic fields and waves in solids*, 2nd edn. Krieger Publishing Company, Malabar, Florida, 1990.

[3] T. M. Niemczyk, S. J. Martin, G. C. Frye and A. J. Ricco, "Acoustoelectric interaction of plate modes with solutions," *Journal of Applied Physics,* vol. 64, pp. 5002-5008, 1988.

[4] D. S. Ballantine, J. Martin, A. J. Ricco, E. T. Zellers, G. C. Frye and H. Wohltjen, *Acoustic Wave Sensors: Theory, Design, and Physico-Chemical Applications.* San Diego: Academic Press, c1997., pp. 436.

[5] J. Kondoh, Y. Matsui, S. Shiokawa and W. B. Wlodarski, "Enzyme-immobilized SH-SAW biosensor," *Sens Actuators, B Chem,* vol. B20, pp. 199-203, 7 June 1993 through 10 June 1993. 1994.

[6] G. Sehra, M. Cole and J. W. Gardner, "Miniature taste sensing system based on dual SH-SAW sensor device: An electronic tongue," *Sens Actuators, B Chem,* vol. 103, pp. 233-239, 2004.

CHAPTER 4:

DEVICE DESIGN

4.1 INTRODUCTION

The previous two chapters had set the theoretical framework of acoustic waves, focusing on the physics of surface acoustic waves (Chapter 2) and their interaction with liquid media (Chapter 3). Once the general concepts of surface acoustic waves have been understood one may venture into the design of SAW sensors. High-frequency SAW design is a field on its own and device optimisation constitutes a significant challenge even for RF experts. While a variety of commercial SAW devices (mostly filters) are available on the market, SAW sensors often need tailored configurations for a specific application.

This chapter details the design configurations considered for the fabrication of the SH-SAW liquid sensors. Firstly fundamental guidelines for the SAW design are revised and then various layout configurations are presented. The sensors are grouped

according to their mode of operation into three broad categories - wired, wireless and voltage modulated devices. The wired sensors received a special attention and several subcategories are concentrated around the delay line and resonator configurations. Design parameters are provided and a brief description of each configuration is given.

The liquid cells that will be used to host the test samples on top of the SH-SAW sensors are also described at the end of this chapter. Design details of the MSL micro-reservoirs and SU-8 cages with embedded preconcentrator filters are also presented.

4.2 BASICS OF THE SAW SENSORS DESIGN

This sub-section covers the basic concepts that govern the SAW design, with emphasis on the primary structures used: interdigital transducers (IDTs) and reflectors.

The general electromagnetic wavelength-frequency dependency also holds valid for the acoustic domain, except that the speed of light (c) is replaced by the acoustic velocity (v) of the medium:

$$\lambda = \frac{v}{f}$$

The velocity of an unperturbed acoustic wave is a material constant and the wavelength of the SAW in a particular substrate is determined by the frequency of operation. The higher the frequency the shorter the wavelength. It has been shown that acoustic energy of surface waves is well contained within a depth equal with one wavelength. At higher frequencies the energy is confined closer to the surface and, according to Ballantine et al. the "wave sensitivity to surface perturbations increases" [1].

Surface acoustic waves can propagate in a wide range of elastic substrates and can be generated via many different mechanisms. The focus of this work is on electrical generation and detection of surface acoustic waves and their interaction with liquid

media. To this aim, thin film electrodes deposited on a piezoelectric substrate are employed. The key block elements in surface acoustic wave design are the interdigital transducers (IDTs) and the reflectors, discussed below.

4.2.1 Interdigital transducers (IDTs)

The history of the interdigital transducer goes back to 1965 [2] when lithographically patterned interdigital electrodes were proposed as a new method to launch and detect surface acoustic waves on the surface of a piezoelectric crystal. More specifically, the IDT functionality is based on the iverse piezoelectric effect for generation of the surface waves and on the direct piezoelectric effect for the detection of the waves. The application of an AC voltage to the two comb-like structures of the IDT (Figure 4.1) determines a periodic strain field to be generated in the piezoelectric substrate. A standing wave is thus created (by the periodic time-varying strain) in the IDT area which generates travelling waves propagating away from the IDT, in a direction perpendicular to its electrodes.

A surface acoustic wave propagating on a piezoelectric substrate has an associated electrical potential. A SAW incident on an output/receiving IDT is equivalent with a periodic wave potential that imposed on the IDT electrodes generates a voltage at the output of the IDT [1].

A basic IDT configuration and its principal parameters are illustrated in Figure 4.1.

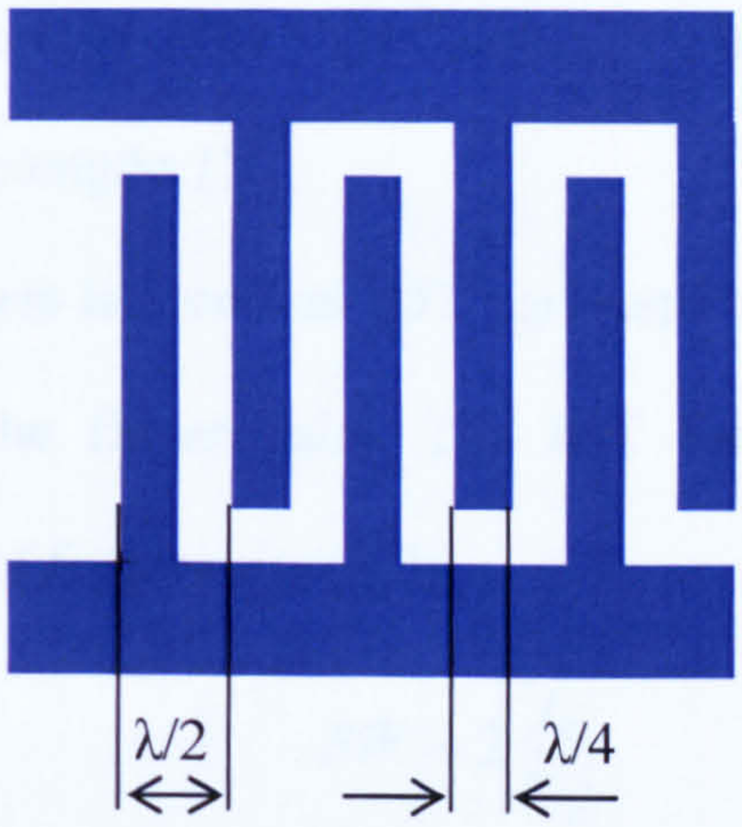

Figure 4.1: Solid finger IDT

The IDT is generally defined by the electrode's geometry (width, length, aperture) by the periodicity of the electrodes and the total number of finger pairs[1]. The IDT characteristics are strongly dependent on the piezoelectric substrate properties (i.e. dielectric constant, coupling coefficient, etc). The IDT design determines the operating frequency of the SAW device, its electrical impedance and bandwidth and delimits the sensing area [1].

The surface acoustic wave is most efficiently excited for the wavelength λ that equals the IDT periodicity p, thus the finger pair spacing is defined in respect to the desired operation frequency (f_0): $p=v/f_0$.

Width w is another design parameter that relates to the acoustic wavelength. The electrodes in Figure 4.1 have a rectangular shape with a $\lambda/4$ width and are known in literature as solid fingers. In this case, consecutive electrodes are uniformly spaced $\lambda/2$ apart with gaps between the electrodes of $\lambda/4$.

The acoustic aperture of the IDT is the length of the overlapping electrodes and has to be chosen carefully in order to avoid diffraction of the acoustic beam. The IDT impedance depends on this parameter and literature reports recommend apertures of at

---

[1] A finger pair is defined as two consecutive/adjacent electrodes connected to the bus-bars with different polarities

least 50 wavelengths. Successful 50Ω impedance IDTs have been designed with an acoustic aperture of 72 wavelengths [1].

The number of fingers is a critical IDT parameter as the SAW generation is a cumulative effect of all the finger pairs. The IDT bandwidth (BW) is inversely proportional to the number of finger pairs (N_p):

$$BW = 2\frac{f_0}{N_p}$$

A large number of finger pairs determine a narrow bandwidth, which can be desired in certain applications to avoid spurious responses and to achieve a higher stability. However, a trade-off needs to be made when choosing the number of fingers in a IDT. If the number is too large, the mass loading effects and scattering from the fingers can degrade considerably the IDT response.

While R. M. White and F.W. Voltmer were the first to employ the solid finger interdigital transducer IDT [3], many other IDTs configurations and electrode geometries have been used since in order to shape the frequency response and/or to optimize the performance of SAW devices.

Here, two types of IDT electrodes were considered in this work: solid finger electrodes discussed above and split finger, also called double electrodes. The split fingers IDTs are employed where the undesirable finger reflections need to be reduced. In the case of solid electrodes IDT, unless compensated for, the reflections occurring at the front and back of a λ/4 electrode usually degrade the amplitude and phase response of the IDT. For mechanical reflection, a solid finger IDT is essentially equivalent to a structure having a grating periodicity p=λ/2, and Bragg reflection occurs at the fundamental resonance frequency.

A split finger IDT has electrode widths and gaps of λ/8, as illustrated in Fig. 4.2.

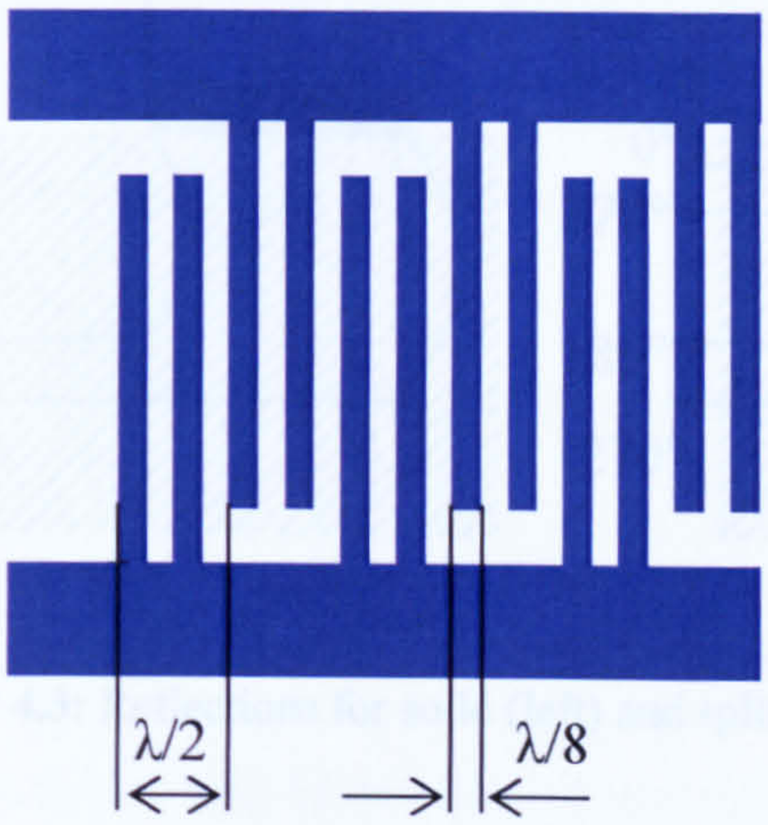

Figure 4.2: Split finger IDT

Due to the narrower strip width, an increased lithographic resolution is required for the definition of this structure. However this pays off considering that the Bragg reflection can be suppressed at the SAW resonance frequency. For mechanical reflection the split finger IDT acts as a structure with grating periodicity of λ/4 [4].

Comparing the solid and split types IDT fingers, Campbell gives a simplified explanation regarding the finger reflections: the differential paths lengths for electrodes with widths and spacing of λ/8 are such that the reflections from each split-electrode pair cancel out at the fundamental frequency rather that add on as it happens for the solid electrode IDTs. Graphical representations of finger reflections show in-phase reflections for the solid electrodes versus the phase cancellation effect for the split electrodes [5].

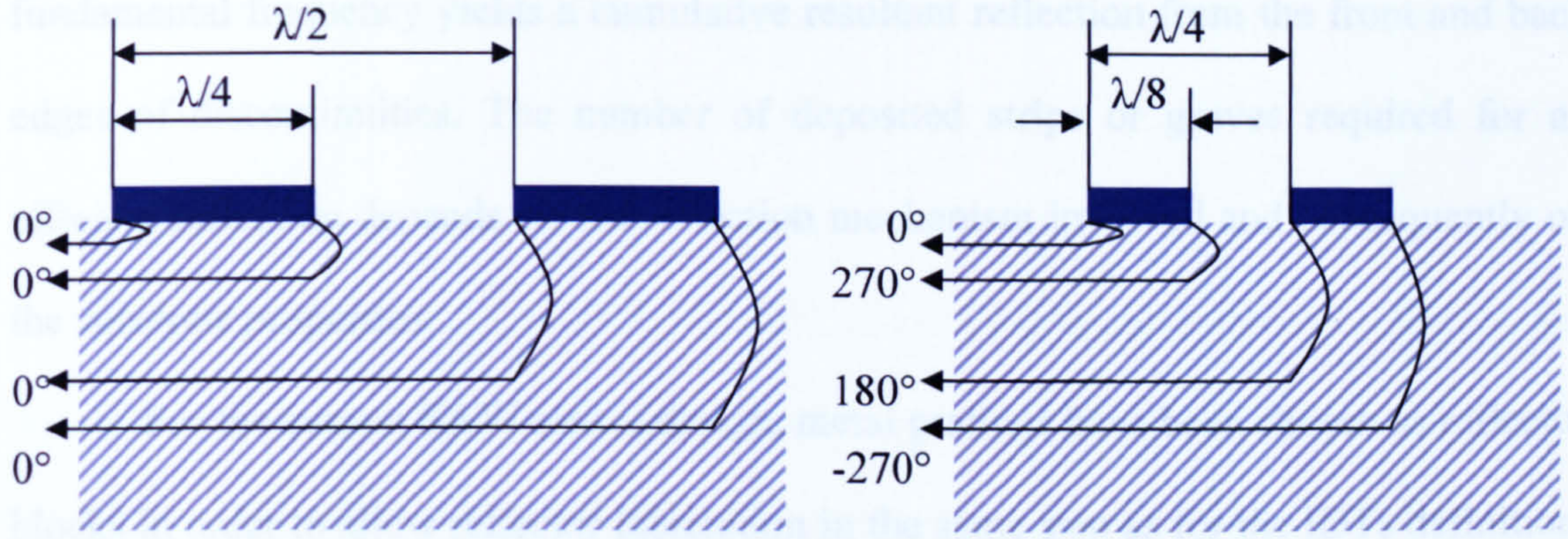

Figure 4.3: Reflections for solid (left) and split (right) fingers IDTs

When split finger IDTs are employed, special attention has to be given to some design parameters. For instance the effective electromechanical coupling coefficient is different than the one for solid electrodes, being affected by a sub-unitary factor. Also, the capacitance for a split electrode IDT is 1.4 times larger than for an equivalent solid finger IDT [5].

The IDTs are the primary structures used for the generation and detection of the surface waves. A simple SAW delay line configuration can operate successfully only with two such structures, one for the signal input and the other for the output. However, SAW resonator or different SAW configurations also employ reflector blocks to achieve the desired performance.

4.2.2 **Reflectors**

Reflection gratings are periodically spaced discontinuities employed to obtain a near-total reflection of the acoustic wave. The easiest gratings to fabricate are the metal film strips deposited on the surface of the substrate. Etched grooves are also employed as reflection gratings and are mostly used when reduction of SAW propagation loss is crucial. Other techniques such as ion implantation and thermal diffusion [4] are applied for definitions of grating structures. For each case, the periodicity of the grating at

fundamental frequency yields a cumulative resultant reflection from the front and back edges of discontinuities. The number of deposited strips or groves required for an efficient reflection depends on the reflection mechanism involved and consequently on the substrate properties.

For the current SAW sensor design, metal gratings have been chosen as reflector blocks in order to allow reflector fabrication in the same step as for the IDTs definition. The configurations considered are made of open strips (Fig 4.4a), short-circuited strips where all the strips are connected in parallel (Fig 4.4b) and a combination of both open and shorted strips (Fig 4.4c).

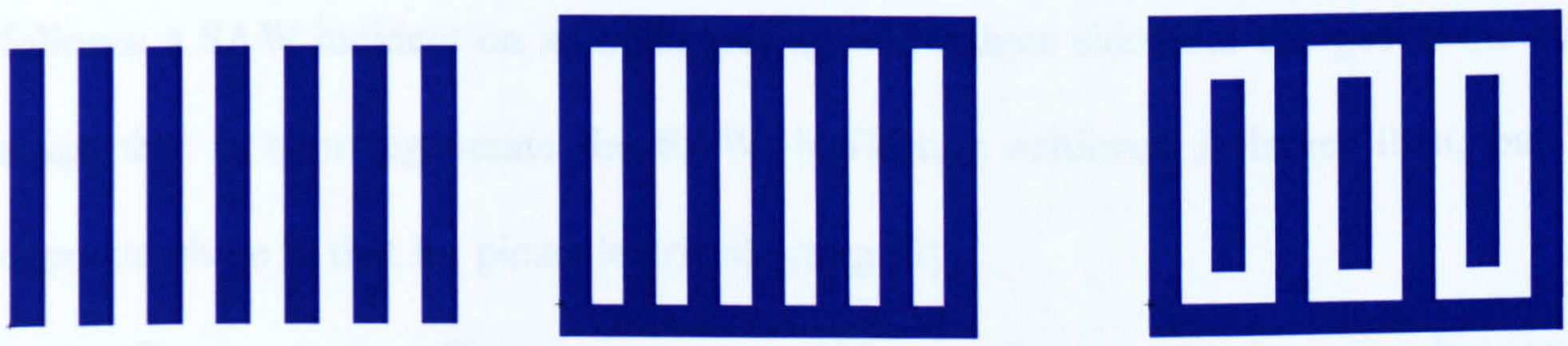

a) Open reflectors b) Short-Circuit reflectors c) Positive and negative reflectors

Figure 4.4: Types of reflector gratings

The reflection mechanisms associated with the reflection grating can be grouped according to the nature of the effects involved into **mechanical discontinuities** and **electrical discontinuities**.

The mechanical SAW reflections occur due to the impedance variation that exists at both edges of each grating element. They can be caused simply by the *geometric discontinuities* that the grooves or metal strips impose to the acoustic wave. The metal film thickness (or the equivalently the grove depth) h is the most important geometric factor for this mechanism. The effect is week for thin films but becomes significant for strips with film-thickness ratios $h/\lambda > \sim 1\%$ and can be the dominant reflection effect for certain weak piezoelectric substrates like quartz. A second mechanism is due to the strips *mass loading effect* that generates "mass-loading"

discontinuities due to the differences in density and elastic properties of the metal film and the substrate. This is associated with the use of groove gratings filled with heavy metal films (like gold) to increase the reflection coefficient.

SAW reflections due to the electrical effects/discontinuities are due to the piezoelectric nature of the substrate. *Piezoelectric shorting* occurs when the electric field associated with the SAW propagation is short-circuited by the strips of the metal film, thus causing a perturbation to the SAW propagation. This effect is stronger for substrates with large coupling coefficient K^2. In addition to this, *electrical regeneration* is another effect that can cause reflections. The electrical regeneration mechanism is as follows: a SAW incident on an open grating will induce electrical charges in the metal strips that in turn regenerate the SAW. Reflection achieved is larger than, but has opposite phase to that for piezoelectric shorting [5].

Two or more effects can occur within a reflective structure simultaneously. When none of them can be considered as having a negligible contribution to reflection, is important to determine each reflection coefficient phase. However, phase determination is not straight forward when different reflection mechanisms can compete in SAW reflection gratings and tend to cancel each other.

4.2.3 **Design parameters**

Despite of the simplicity of the basic SAW design principles, it has to be emphasised that optimization of a SAW device is not a trivial pursuit. On the contrary, SAW design optimisation is a complex endeavour requiring inside knowledge, expertise and specialized packages for design and simulation. Modelling and simulation stages are extremely important for the SAW design, especially at higher RF frequencies, as they can bring to light problems prior the actual fabrication. However, as access to

specialized simulation packages is often prohibitive cost-wise, a common practice in the SAW sensors field is to adopt an 'experimental' trial and error method, and rely on data previously reported in literature, as was the approach for this project.

Four high-frequencies have been considered for the sensors design, and they are grouped around the ISM bands: 433 MHz, 869 MHz, 2.4 GHz and 10 GHz. Designs for 433MHz and 869 MHz devices have been done with a contact lithography process in mind. The higher frequency sensors at 2.4 GHz and 10 GHz have also been designed and expected to be directly written on the wafer, but due to technical problems, the fabrication was not possible. The general design parameters for all these frequencies are summarized in Table 1. The designs were made for a 36° YX $LiTaO_3$ substrate with a surface wave velocity of 4160m/s and a coupling coefficient of k^2=5%.

Table 1: General deign parameters for SAW sensors of 36° YX $LiTaO_3$

Parameters	**Operation frequency (f_0)**			
	433 MHz	**869MHz**	**2.45GHz**	**10GHz**
Acoustic wavelength $\lambda = \frac{v}{f_0}$	9.6 μm	4.78 μm	1.69 μm	0.416 μm
Solid fingers width $a = \frac{\lambda}{4}$	2.4 μm	1.2 μm	0.42 μm	0.100 μm
Split fingers width $a = \frac{\lambda}{8}$	1.2 μm	0.6 μm	0.21 μm	0.050 μm
Acoustic aperture $w \geq 72\lambda$	850 μm	400 μm	200 μm	50 μm
Number of finger pairs Np	N chosen as 25 [Ballantine, 1997]			
Acoustic bandwidth $B = 2\frac{f_0}{N}$	34.64 MHz	69.62 MHz	196 MHz	800 MHz

4.3 LAYOUT OF HIGH FREQUENCY WIRED SENSORS

The layout editor used for the design of the SH-SAW sensors was L-Edit Pro™ 9 (Tanner EDA). The wired high frequency designs are subsequently classified into delay line and resonator configurations as follows:

4.3.1 Delay line configurations

Most of the SAW sensors employ a single delay line, where the space between the input and output IDTs is usually the active sensing area. Devices in this work were designed around dual delay line configurations in which one delay line is metallized and the other one is totally or partially free. Several variations to the delay lines lengths, surface boundary conditions as well as IDTs types are proposed for experimentation. Accordingly to the IDTs electrodes, devices are grouped into solid fingers and split fingers IDTs (Appendix A).

As shown previously in the basics of SAW design section, IDT fingers widths are defined in relation to the device operation frequency. The standard $\lambda/4$ electrodes are known in literature as solid fingers, while IDTs with $\lambda/8$ electrodes are known as split fingers or double electrode IDTs. Solid fingers are the most widely used electrodes for IDT designs and their main advantage relates to the more relaxed fabrication requirements, and implicitly processing costs, when compared to the split electrodes. This advantage becomes more important at borderline high frequencies where for instance patterning of solid fingers can still be achieved with contact lithography while the split fingers necessitate a technique with higher resolution.

Once the electrode has been decided upon, the IDT design can allow for a certain degree of energy/acoustic wave directivity, and further classifications are made accordingly to this criterion. A bidirectional IDT will radiate acoustic energy at both of

its ends, while a unidirectional IDT will focus the acoustic energy predominantly in one direction. Several unidirectional IDT sensors were designed and are included in Appendix A.

4.3.1.1 SRL 207a sensor family

The dual delay line configuration in device SRL 207a (Figure 4.5) has one path metallized while the other one is left entirely free. Both delay lines have the same length and the IDT to IDT distance is 4699.2μm which is equivalent with 489.5λ at a frequency of 433 MHz. The output IDT is 180° degrees rotated with respect to the input IDT. For an IDT aperture of 800μm = 83.3λ the propagation path lays within the Fresnel diffraction region.

Figure 4.5: Layout of SRL 207a

Summarised description:

- operating frequency: 433 MHz
- solid finger, bidirectional IDTs, N_p=25
- one delay line metallised, one totally free
- $d_{IDT\text{-}IDT} = 489.5\lambda$
- possible bulk scattering of the SAW on the free DL

The SAW on an open delay line can be dispersed into the bulk of the crystal much easier then a SAW propagating on a metallized surface [4]. To compensate for the bulk scattering, trapping mechanisms need to be used. The SH mode can be trapped closer to the surface through different methods that includes the deposition on the free surface of metal arrays, without short-circuiting the piezoelectric potential. Such methods have been used for several configurations summarized in appendix A. For illustration purposes layout details for SRL 207ab and SRL 282 are given below in

Figures 4.6 and 4.7, where dots and strips arrays were employed as trapping structures respectively.

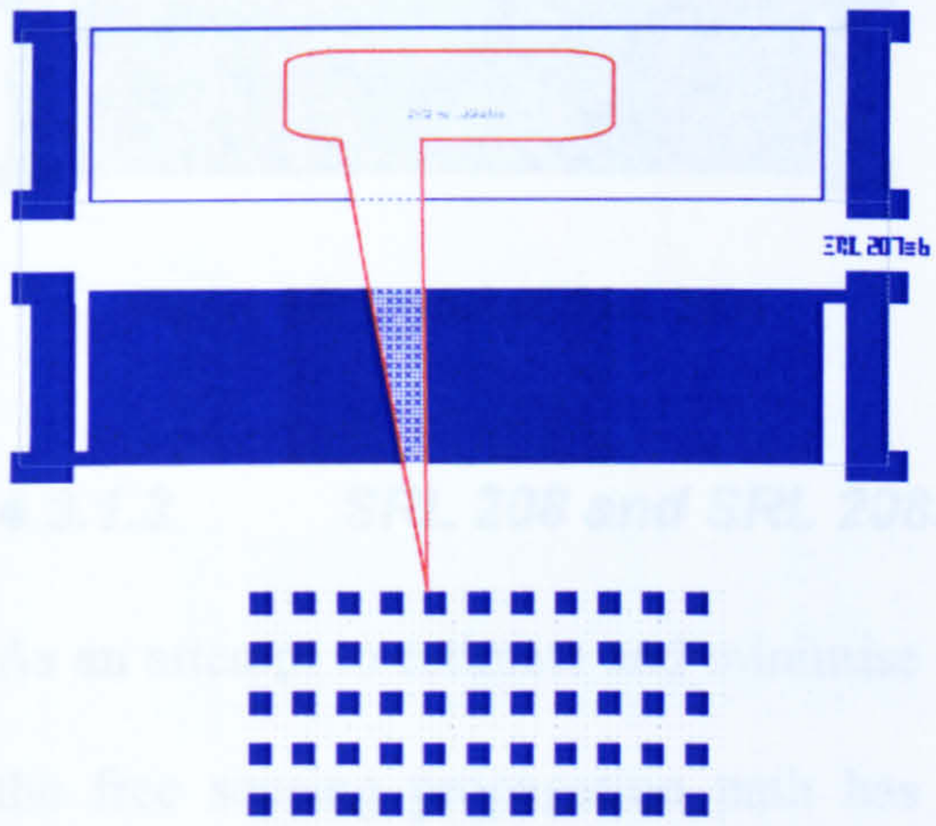

Figure 4.6: Layout of SRL 207ab sensor (top) and its dot structure of the free path (bottom)

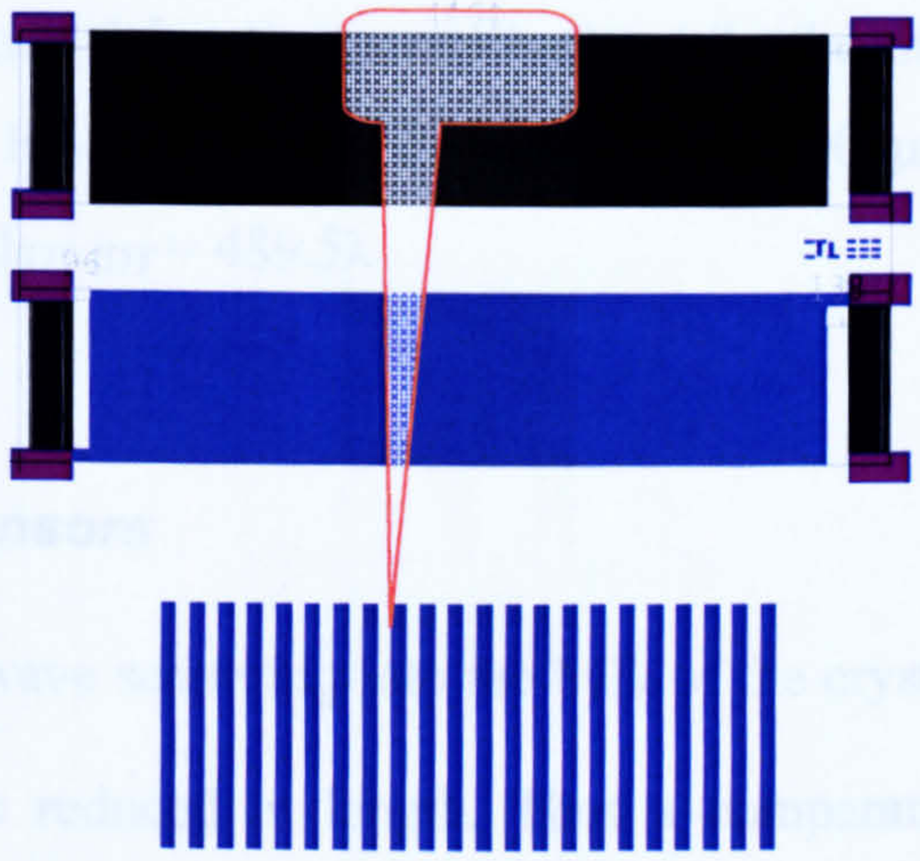

Figure 4.7: Layout of SRL 282c sensor (top) and its grating structure of the free path (bottom)

With the exemption of the free delay line, both configurations have parameters similar to SRL 207a. The SRL 207ab sensor has square dots of 2.1 μm, spaced 4.2 μm apart SRL 282c has strips width of 2.3 μm and a 4.6 μm pitch. The optimal strip and dots dimensions will be determined experimentally. To this aim variations to these devices were designed to accommodate open gratings with different pitch and dot dimensions. The SRL 282, SRL 282a, SRL 282b, SRL 282c, SRL 278b sensors are summarized in Appendix A.

4.3.1.2 SRL 280a sensor

A different approach to combine the advantage of SH-SAW energy trapping with a free surface is to allow for a small opening in a metallized propagation path. An example for such a configuration is SRL 280a, where the window on the so-called 'free' delay line permits both acoustical and electrical interactions with the liquid sample.

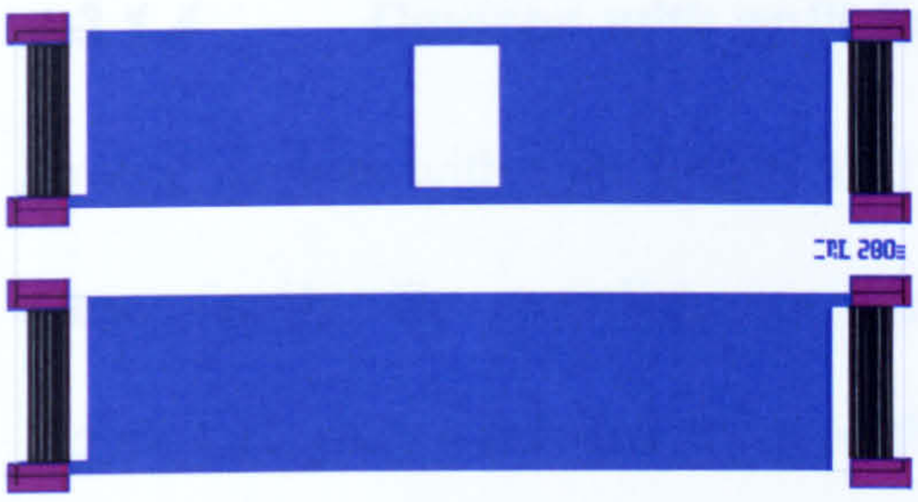

Figure 4.8: Layout of SRL 280a

Summarised description:

- operating frequency: 433 MHz
- solid finger, bidirectional IDTs, N_p=25
- one delay line metallised, while the other has an opening of 480μm=50λ by 800μm
- $d_{IDT-IDT}$ = 489.5λ

4.3.1.3 SRL 208 and SRL 208a sensors

As an attempt to estimate and minimise the wave scattering into the bulk of the crystal, the free sensing propagation path has been reduced in length. Thus a comparative analysis of different path length devices allows establishing the propagation loss (dB/mm) for an open surface. Layout illustrati - - ons of two configurations with reduced length on the free path are given below. SRL 208a and SRL 208 have the free path shorter with 1 mm and 2 mm respectively than the configuration in SRL 207a. The SRL 208 sensor also has its metallised delay line 1 mm shorter than the one in SRL 207a.

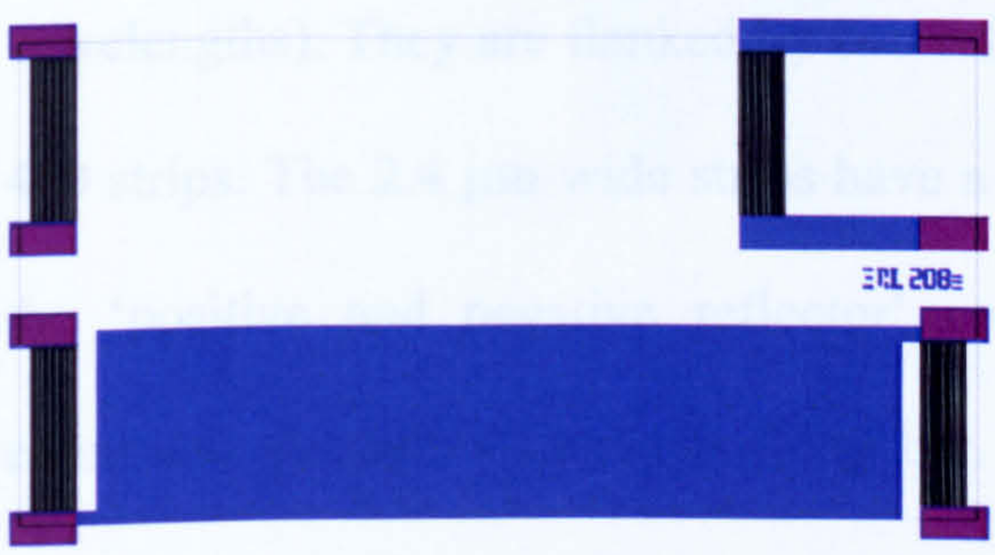

Figure 4.9: Layout of SRL 208a

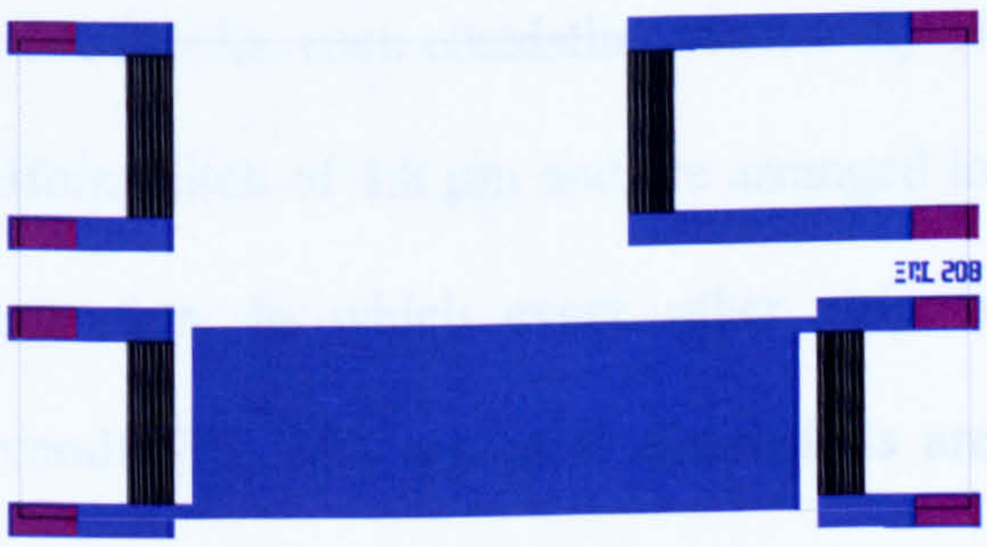

Figure 4.10: Layout of SRL 280a

4.3.1.4 Devices with split fingers IDTs

Several devices with split fingers IDT were designed and they belong to the SRL 278 sensor family. The overall layout design is similar to the one for SRL 207a sensor. Figure 4.11 gives a detailed zoom on the split finger IDT with 1.2 μm electrode width.

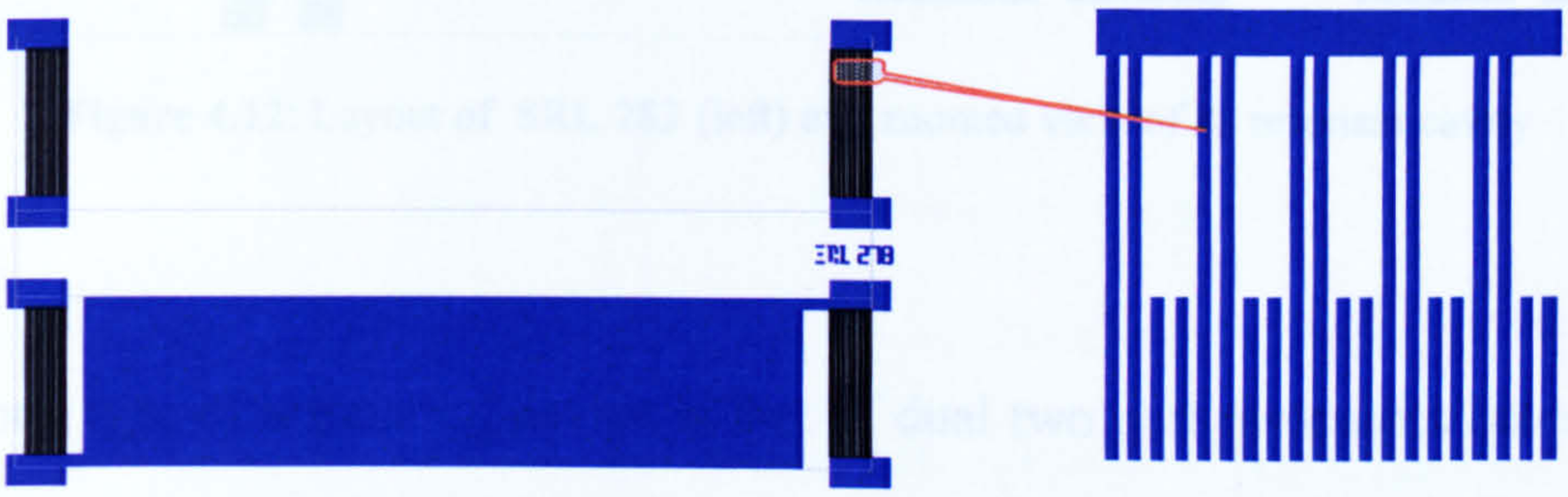

Figure 4.11: Layout of SRL 278 (left) and zoomed view of the split finger IDT

4.3.2 Resonator configurations

In addition to delay line devices, resonator sensors were also designed. The first configuration considered is a simple dual port resonator SRL 283. Two solid fingers IDTs (identical in characteristics with the ones used for the delay line SRL 207a design) were brought closer to form a cavity with an edge to edge distance of 192 μm (20 wavelengths). They are flanked by two reflective blocks, each consisting of an array of 400 strips. The 2.4 μm wide strips have a uniform pitch of 4.8 μm and are arranged in the 'positive and negative reflector' configuration, in which every other strip is connected through a short-circuiting bar. Overall SRL 283 resonator dimensions are 4600 μm × 3000 μm and Figure 4.12 shows the layout details.

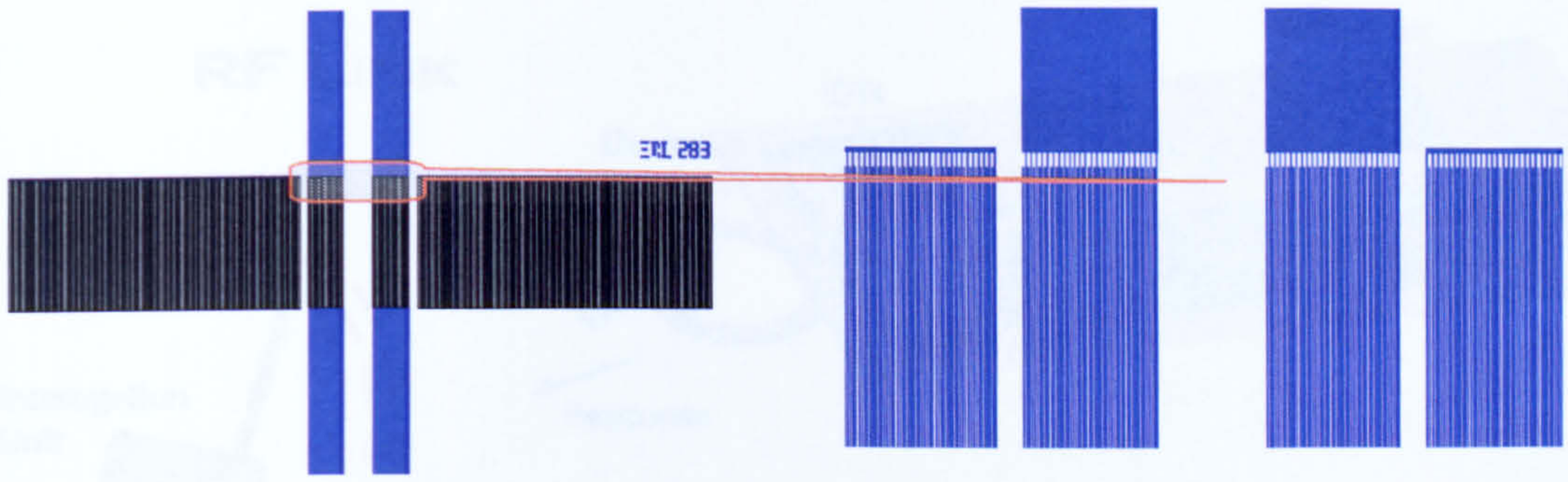

Figure 4.12: Layout of SRL 283 (left) and zoomed view of its resonant cavity

A second type of resonating device is that of dual two port resonators belonging to the SRL 284-286 series. In a sense it could be seen as the equivalent of the dual delay line devices in a resonating configuration. They essentially consist of two resonators, one with an electrically free cavity (the top one in Fig. 4.13) while the other has a metallised cavity. The two resonators share a common ground electrode. Both input and output IDTs of this class of resonators have solid electrodes with 2.5 finger pairs each.

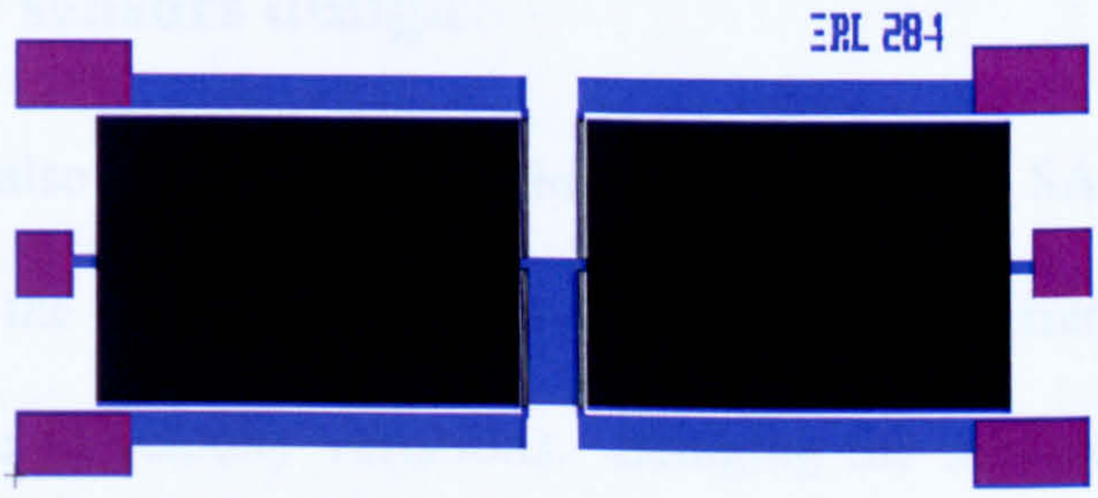

Figure 4.13: Layout of SRL 284

4.4 REMOTE/WIRELESS SENSORS

The remote/wireless sensing system is composed of a passive SAW microsensor connected to a small antenna. This is used in conjunction with an interrogation unit (transceiver) that sends and receives the measuring signals. A diagram depicting the principle of operation of this wireless system is shown in Fig. 4.14.

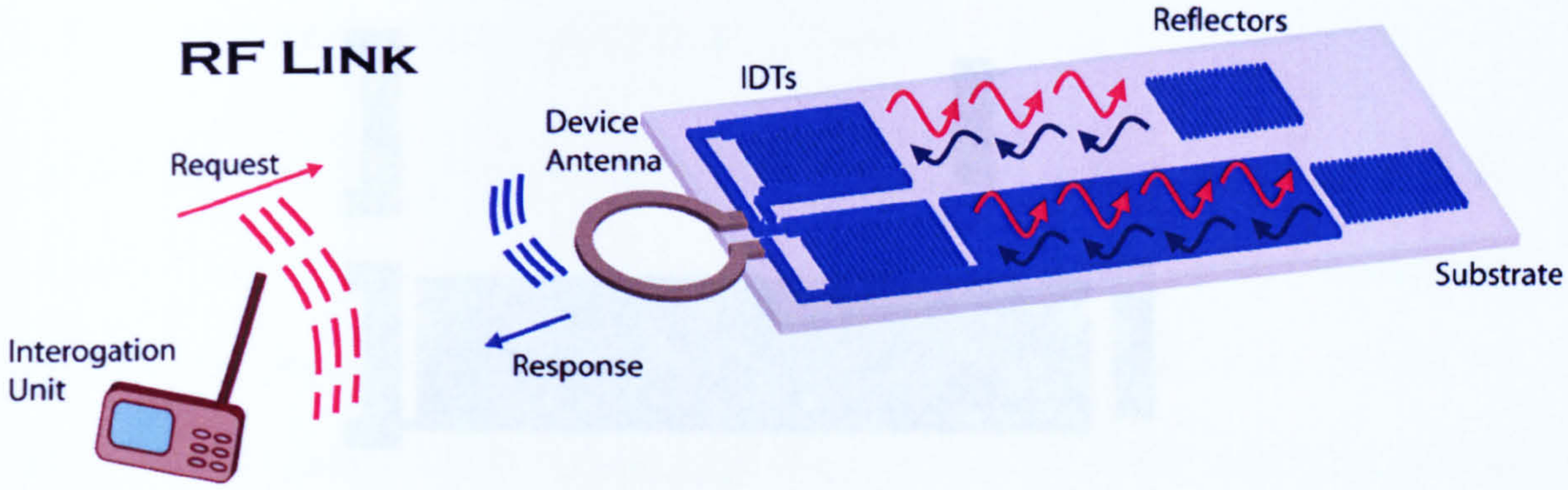

Figure 4.14: Diagram of the wireless sensing system

In this, the electromagnetic waves picked up by the device antenna are applied to the interdigital transducers (IDTs) that convert the electric signals into acoustic waves which in turn propagate along the sensors' surface. Two sets of reflectors are designed to bounce back the acoustic waves and when the waves reach the IDTs again, the converse mechanical to electrical transduction takes place. Then the antenna sends back to the interrogation unit a signal that contains the sensor's response.

4.4.1 **Reflective sensors design**

SAW sensors were also designed for wireless operations. The SAW wave on the free path is quicker than the one on the metallized one, so a time difference between pulses is obtained only due to velocity variations. Bringing the reflector closer to the IDT (essentially shortening the free propagation path) an increased time difference between the reflected pulses on the two delay lines is achieved. In the wireless sensors layout the reflective blocks have 50 fingers each and devices accommodating open circuit reflectors, short circuit reflectors and positive and negative reflectors have been built. A typical wireless sensor layout is shown in Fig. 4.15.

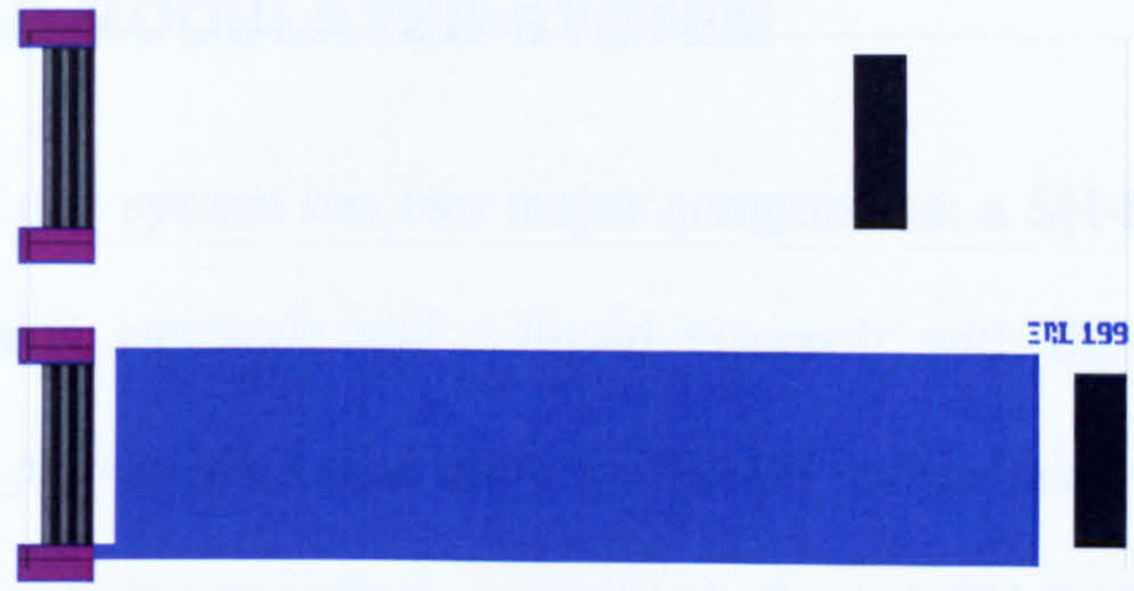

Figure 4.15: Layout of SRL 199 wireless sensor

4.4.2 **Miniature antenna for remote sensors**

Remote interrogation of the SH-SAW sensor could be achieved by the means of a small antenna connected directly to the IDTs. A 24 mm diameter loop antenna has been designed and built for wireless and semi-wireless applications. Figure 4.16 shows the small printed loop antenna that is terminated on a surface mount trimmer that allows fine tuning on the resonating frequency of the SAW sensor. Matching to the input impedance of the sensor can be easily realized by moving the feeding point along the loop. Experimental results obtained with a network analyzer show a return loss figure of 26 dB and a narrow bandwidth of approximately 5 MHz.

a)

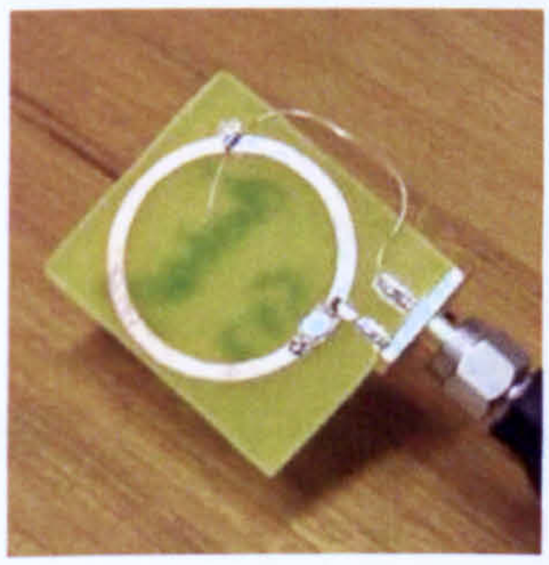

b)

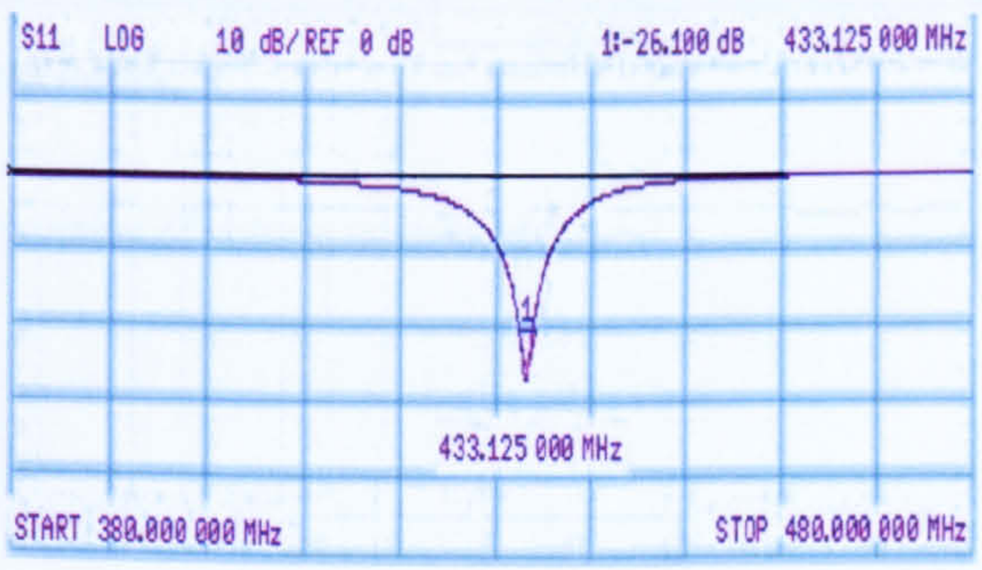

Fig 4.16: Printed small loop antenna (a) and its return loss characteristic (b)

4.5 VOLTAGE MODULATED SYSTEM

The voltage modulated system has two major components: a SH-SAW sensor with an embedded modulating electrode and a liquid reservoir with the counter modulating electrode. The design employs a dual shear horizontal surface acoustic wave (SH-SAW) sensing device comprising a voltage-modulated shorted SH-SAW delay-line device together with a free delay-line, designed for better sensitivity and selectivity.

The principle of operation of this novel system is shown in Figure 4.17. A liquid sample is passed into a micro-reservoir, a DC voltage is applied to the metal electrode thus forcing charged bioparticles to attach themselves to the metallized piezoelectric substrate while the measurement takes place. Bioparticles of different dielectric constant to the liquid are also attracted but with an AC voltage. The voltage level and frequency can be set according to the properties of the bioparticles, e.g. charge/size, dielectric constant. This should result in a significant enhancement of sensor sensitivity.

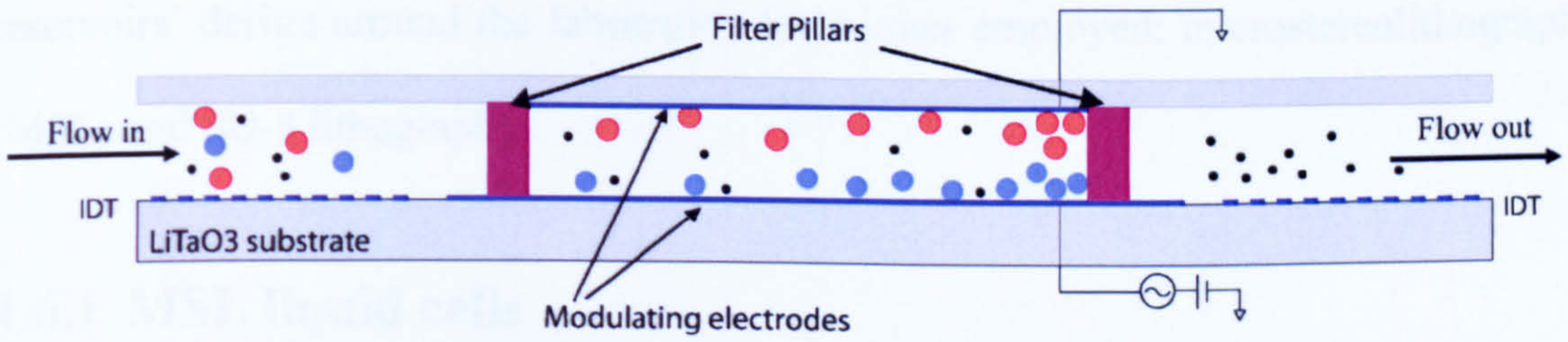

Figure 4.17: Principle of operation of voltage modulated sensor

4.5.1 SH-SAW sensors layout

The voltage modulated SH-SAW sensors are derived from the dual delay line sensors configurations. The metallized delay line is no longer grounded to the input/output IDTs but connected to a DC or AC voltage source. Several layout configurations have been considered and are shown in Figure 4.18 below. Devices SRL 273, SRL 273a and SRL

280 have IDTs with 25 solid finger pairs with a 2.4μm width, while device SRL 273b employs split fingers ITDs where the finger width is 1.2 μm. IDTs aperture is the same for all configurations: 850 μm. Devices SRL 273, 273a and 273b have a completely free delay line, while SRL 280 has a window opening on the free delay line.

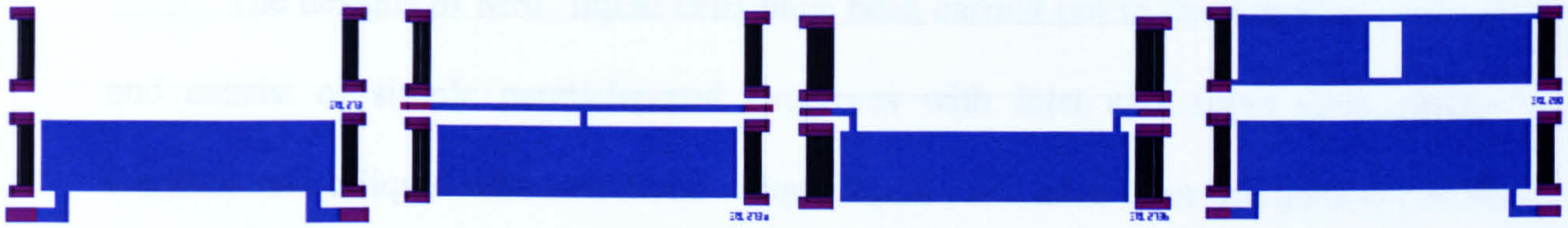

SRL 273 SRL 273a SRL 273b SRL 280

Figure 4.18: Layout of voltage modulated sensors

4.6 LIQUID RESERVOIRS

All sensor configurations need to work in conjunction with a liquid reservoir that will host the samples to be tested. Two micro-fabrication approaches concentrated the reservoirs' design around the fabrication techniques employed: microstereolithography (MSL) and SU-8 lithography.

4.6.1 **MSL liquid cells**

Microstereolithography is a rapid prototyping tool for creating 3 dimensional microstructures from a CAD design employing a photocurable resin. A detailed description of the build process and the system used to manufacture the MSL liquid cells is given in the next chapter. From the design point of view only few system specifications are important, such as the lateral and vertical resolutions, maximum exposure field size and achievable structural height. Two Perfactory MSL machines have been used and depending on the model (Standard or Mini), the lateral resolution

can be either 93 μm or 32 μm while the vertical one is 50 μm or 25 μm. The overall build envelopes of both systems are far from being restrictive for the current application, ranging from 120×96×230 mm^3 (for the Standard model) to 41.98×33.59×230 mm^3 (Mini model).

The designs of MSL liquid cells have been carried out in the AutoCad package and consist of simple parallelepiped structures with inlet and outlet slots, micro-channels and a liquid micro-reservoir. Three liquid cells have been designed for MSL fabrication on Perfactory system: the micro-fluidic cell MSL_1 has a flow through architecture utilisable with various SH-SAW sensors configurations while MSL_2 and MSL_3 were intended for sensors operating in the voltage modulated mode.

SolidView representations of the MSL_1 cell design are given in Figure 4.19 below: Figure 4.19a) gives a wire/faces view of the design that allows visualization of the flow-through structure; a top shade-view of the cell is given in Figure 4.19 b) where the 2.4 mm diameter inlet and outlet slots can be clearly seen; the micro-reservoir that confines the liquid under test to the sensing area of the SH-SAW device can be seen in the bottom view of the cell in Figure 4.19c). Through-holes with 1.6 mm diameter visible in all the shown views are designed to assist attachment of the cell to the sensor's test board.

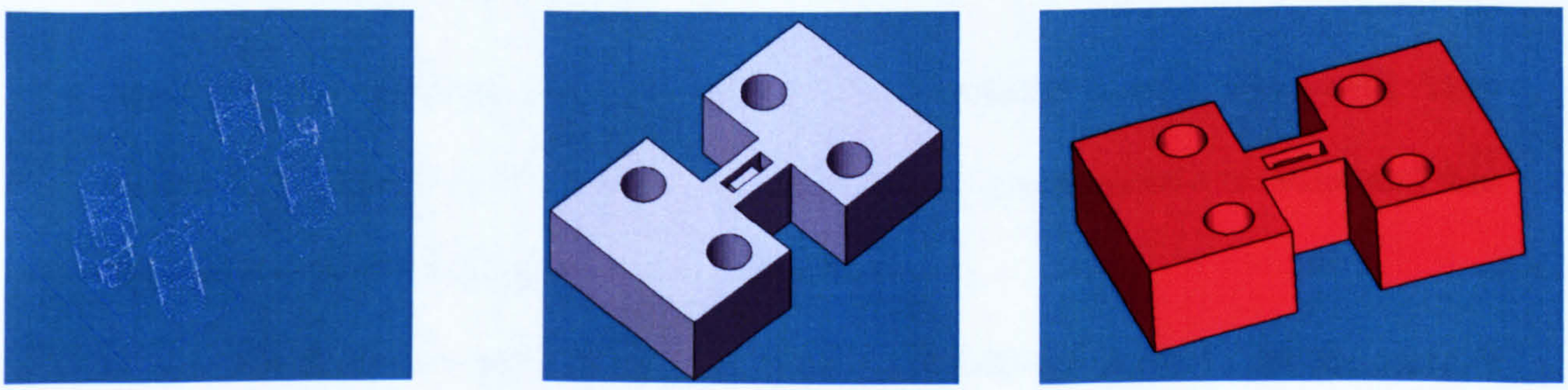

a) Faces view b) Top shaded view c) Bottom shaded view

Figure 4.19: Views of the MSL_1 design

The micro-reservoir is defined by lateral walls with a thickness of 600 μm, has an exposure surface area of 2500 μm × 800 μm and a total capacity of 1 μl. Connection between the reservoir and the inlet/outlet slots is realized by L shape micro-channels that change from 800 μm diameter cylindrical cross-section in the vertical section to square 800 x 800 μm2 cross-section in the horizontal section.

Two variations form this liquid cell were designed for voltage modulated sensor. MSL_2 and MSL_3 are shown in Fig. 4.20 and they allow access to the bottom of the liquid reservoir so that a thin wire can make the electrical connection to the conter-electrode deposited on the bottom of the reservoir

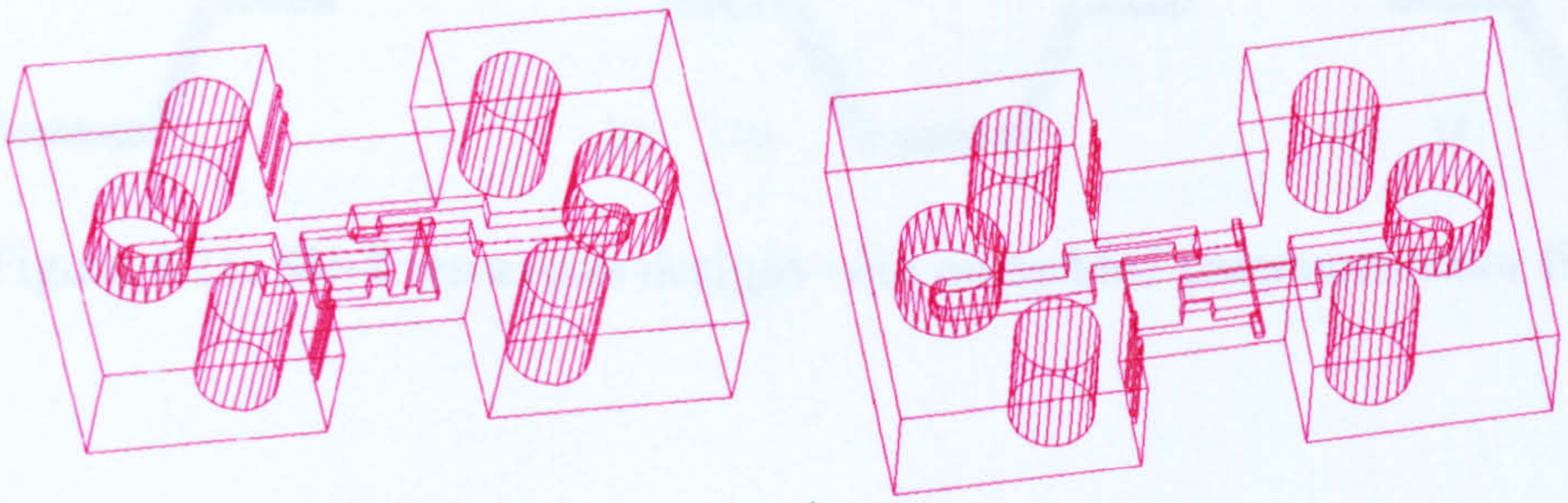

a) MSL_2 b) MSL_3

Figure 4.20: Views of the MSL_2 and MSL_3 designs

4.6.2 **SU-8 reservoirs**

SU-8 reservoirs have also been considered as an alternative to MSL liquid cells. They can be built directly on the sensor's surface or can be structured on a Si wafer and then flipped over the SAW sensors.

The reservoirs are designed such that liquid will not contact with the sensor's IDTs. Several reservoirs shapes were considered (Figure 4.21) and some configurations were containing embedded filters. The preconcentrators filters were implemented with circular, rectangular and trapezoidal pillars positioned in the fluidic path.

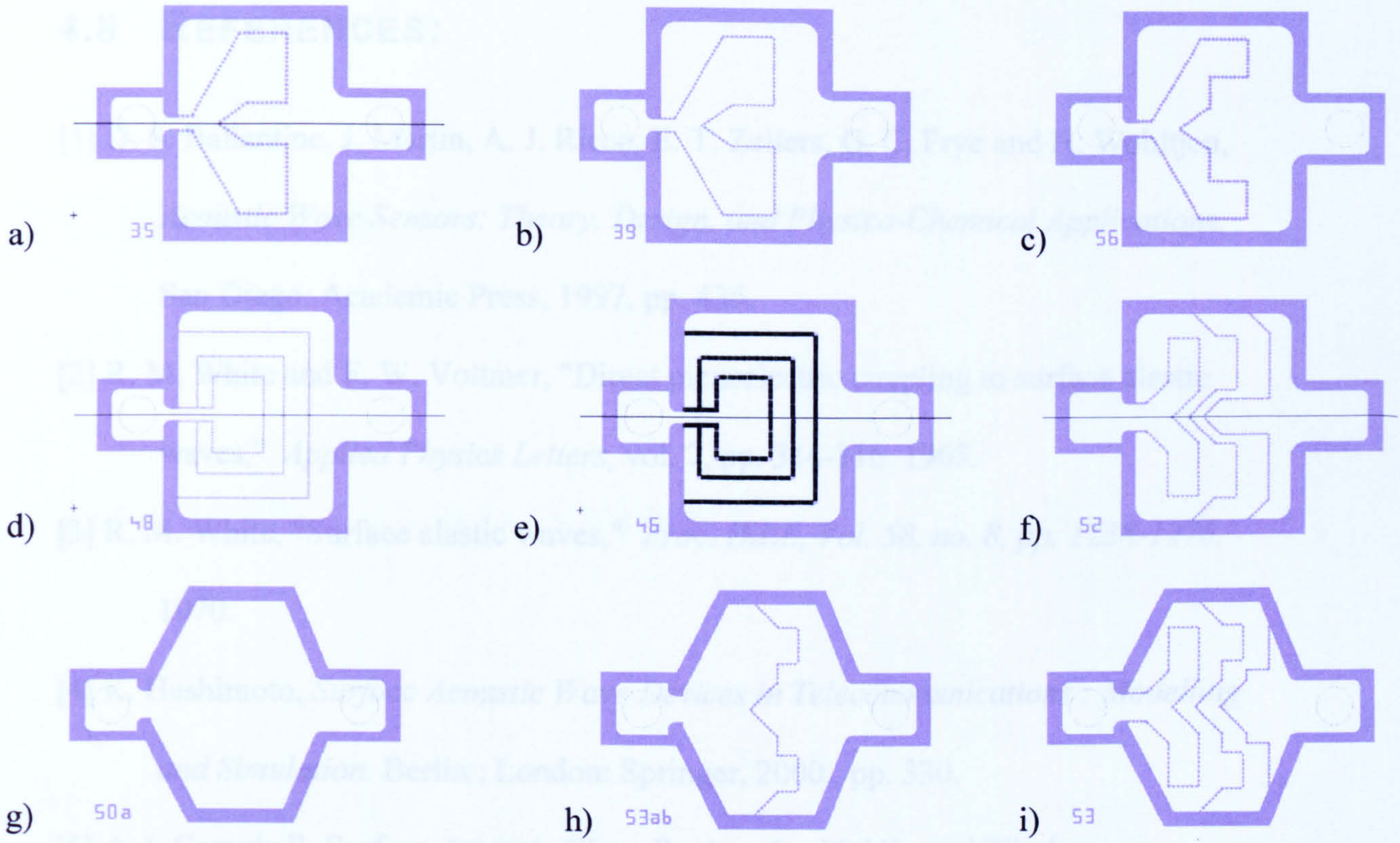

Figure 4.21: SU-8 reservoirs designs with embedded preconcentrator filters

4.7 CONCLUSIONS

The chapter covered the general considerations and rules for SAW devices design and presented some of the configurations chosen for SAW liquid sensors. The sensors were classified into wired configurations, remote/wireless configurations and voltage modulated devices. Designs for MSL liquid reservoirs and SU-8 liquid reservoirs were also briefly covered.

4.8 REFERENCES:

[1] D. S. Ballantine, J. Martin, A. J. Ricco, E. T. Zellers, G. C. Frye and H. Wohltjen, *Acoustic Wave Sensors: Theory, Design, and Physico-Chemical Applications.* San Diego: Academic Press, 1997, pp. 436.

[2] R. M. White and F. W. Voltmer, "Direct piezoelectric coupling to surface elastic waves," *Applied Physics Letters,* vol. 7, pp. 314-316, 1965.

[3] R. M. White, "Surface elastic waves," *Proc. IEEE, Vol. 58, no. 8, pp. 1238-1276,* 1970.

[4] K. Hashimoto, *Surface Acoustic Wave Devices in Telecommunications : Modelling and Simulation.* Berlin ; London: Springer, 2000., pp. 330.

[5] A. I. Campbell, *Surface Acoustic Wave Devices for Mobile and Wireless Communications.* San Diego ; London: Academic Press, 1998., pp. 631.

CHAPTER 5:

DEVICES FABRICATION

5.1 INTRODUCTION

Fabrication at the micron, and more recently nanometre scale is increasingly popular in the sensors field. This chapter presents the microfabrication techniques and equipment employed to implement the devices described in the previous chapter. The sensing system comprises two major components, namely the SH-SAW device and the liquid reservoir; fabrication of each sub-system follows a modular approach.

Standard integrated circuit microfabrication procedures were employed for the creation of the SH-SAW sensors on lithium tantalate wafers. Despite the relative simplicity of the fabrication process, as it involved the patterning of a single metal layer, the overall process requirements were rather stringent. The aim was to define IDT electrodes with 1.2 μm and 2.4 μm width using a contact photolithographic method. The small resolution targeted was rather challenging, reaching the limits of UV contact lithography, and a number of preliminary experiments were necessary to find a

'working solution'. Detailed descriptions of all the steps taken towards the microfabrication of the SH-SAW sensors are presented below.

Liquid reservoirs that sit on top of the SH-SAW devices were defined employing two different technologies. The first one employed a truly 3D rapid prototyping method, called microstereolithography (MSL), to build the liquid reservoirs. Basic MSL principles are reviewed and details on Envisiontec 'Perfactory' system used are presented. A second approach towards the definition of liquid micro-reservoirs used a 2.5D high resolution, high aspect ratio SU-8 photoresist patterning method. SU-8 is extensively used in the MEMS area and for fabrication of microfluidic parts. The fabrication process is based upon a silicon (Si) substrate and is briefly described. A glass to SU-8 reservoir bonding solution, along with its preliminary flow through test, is described at the end of this chapter.

5.2 LITHIUM TANTALATE SENSORS FABRICATION

5.2.1 Substrate properties

SAW liquid sensors have been fabricated on 36° Y-cut X-propagating lithium tantalate wafers purchased from Roditi International [1]. This substrate and particular cut have been chosen due to the SH-SAW/SSBW mode supported, the high surface wave velocity (4160 m/s) and large coupling coefficient (k^2=5.0%). These properties have to be traded off with a group delay time temperature coefficient of 28-32 ppm/°C. The effect of the temperature coefficient can be mitigated by conducting the measurements/experiments in a temperature-controlled environment.

The handling and processing of standard $LiTaO_3$ wafers require a special set of precautions. $LiTaO_3$ is an extremely brittle material; it has a density of 7465 kg/m^3,

which makes the wafers about 3.2 times heavier than an equivalent Si wafers. Lithium tantalate crystal has a strong pyroelectric effect[1]- while this can be a useful material property employed in a numerous applications, for the current fabrication process, the pyroelectric characteristic can be a major impediment. When the wafer is heated, charge accumulates on its surface and sparking can occur between points with different electrical potential, making microfabrication difficult and sometimes even damaging the wafers. To minimize the pyroelectric effect, an ionising gun can be employed when the wafer is exposed to a temperature gradient. If a hotplate is used for the dehydration of the wafers, extra care needs to be taken to prevent particle contamination since, once heated, $LiTaO_3$ essentially becomes a 'dust magnet'. The above measures are required for standard $LiTaO_3$ wafers. Recently, black $LiTaO_3$ wafers with a high ability to neutralise the electrical charges have been introduced and are now commercially available. The new black $LiTaO_3$ wafers make the fabrication process less problematic.

5.2.2 Photomasks

Photomasks are interface microfabrication tools, they are the means by which the design layout is transposed onto the fabricated devices. Lithographic photomasks consist of glass plates with a patterned opaque layer that contains the image to be transferred to the substrate. Masks are fabricated on various types of fused silica using e-beam lithography, a technique that is capable of higher resolution (nanometre level) than UV lithography (micron level). The photomask's most important properties are related to a high degree of optical transparency especially at the UV exposure wavelength, a small thermal expansion coefficient and a flat, highly polished surface [2].

---

[1] Pyroelectricity is the property of certain materials to produce an electric polarization when exposed to a change in temperature.

For the IDTs definition on LT wafers a dark-field chrome photomask with 1 μm CD (critical dimension) was used. Quartz rather than soda-lime was preferred because of its superior temperature stability that is critical when working with very small features (below 5 μm). Quartz also has the advantage of passing a wide range of exposure energies, from approximately 200 nm to more than 550 nm; an equivalent soda-lime mask will not pass energies below a cut-off 380 nm wavelength. In contact lithography there is a proportionality relationship between the achievable minimum feature size and the light wavelength, suggesting that lower exposure wavelengths are desirable for micron and sub-micron resolutions.

5.2.3 LT SAW sensors microfabrication process

The SH-SAW sensors have been fabricated using microfabrication methods similar to the one used in integrated circuits manufacturing. Fabrication at the micro scale requires special environments, where air is filtered of particle contamination, and temperature, humidity, vibrations and electrical disturbances are kept under rigorous control. Such an environment is called a clean room and it has its own set of strict rules and conduit code.

A technical visit at Georgia Institute of Technology, Atlanta, USA facilitated access to the class 10-100 clean room available on site. Preliminary training was required to acquire an understanding of the basic microfabrication processes and to obtain access to the necessary fabrication equipments. The ultimate aim was to fabricate SH-SAW devices with 2.4 μm and 1.2 μm interdigital electrodes via contact optical lithography. After considering and attempting several fabrication approaches, the LT (lithium tantalate) devices were processed using a dry etch technique. A schematic diagram of the process flow is given in Table 5.1 below. Each step is accompanied by

succinct recipe indications and detailed fabrications steps are described in the following paragraphs.

Table 5.1: Microfabrication flow process for LT wafers

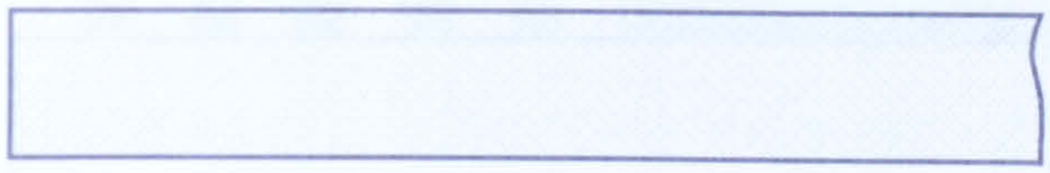	1. Wafer cleaning
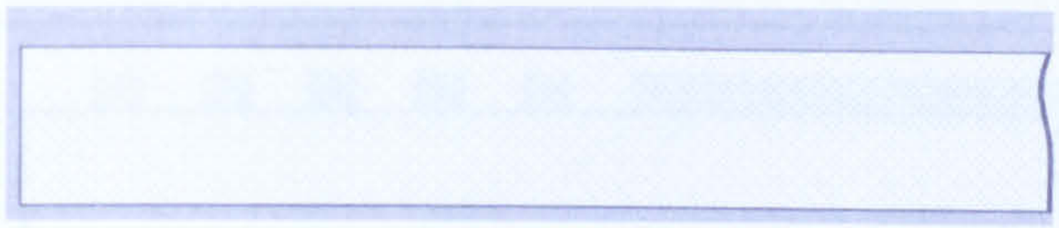	2. Sputter Al: - front side:140 nm - backside of the wafer: 20nm
	3. Spin-coat negative photoresist NR7-1000 (Futurrex)
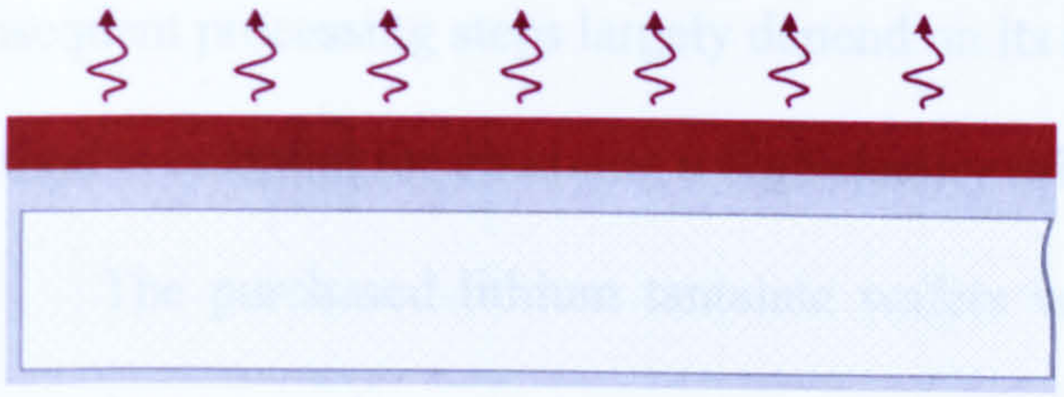	4. 150°C Hot plate backing for 3 min
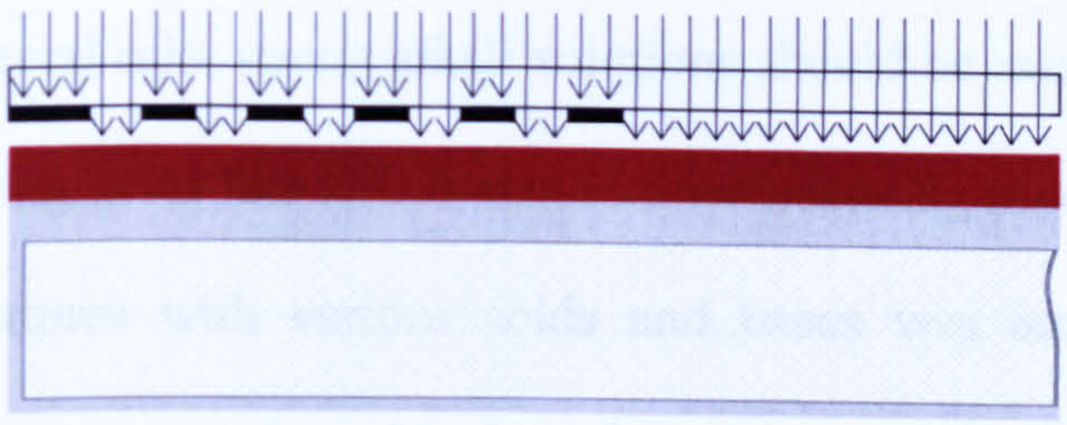	5. Hard contact MA6 exposure - dose: 127 mJ/cm^2
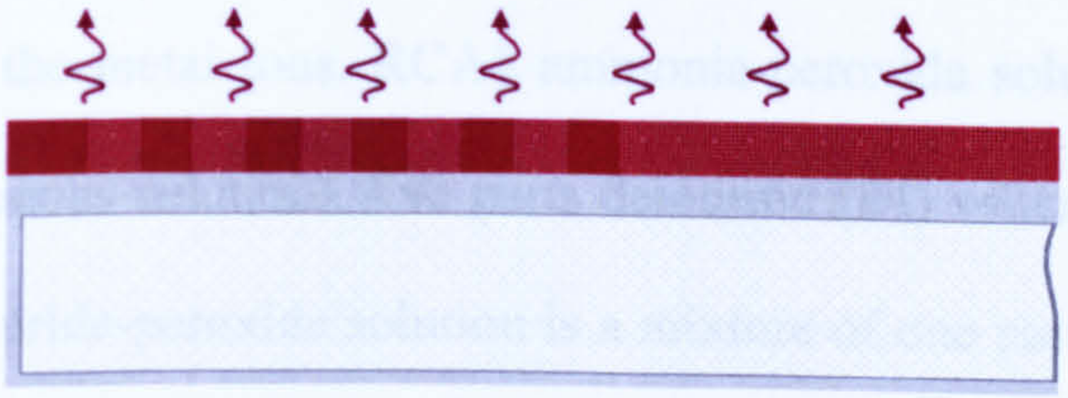	6. Post-exposure baking hot plate – 4 min
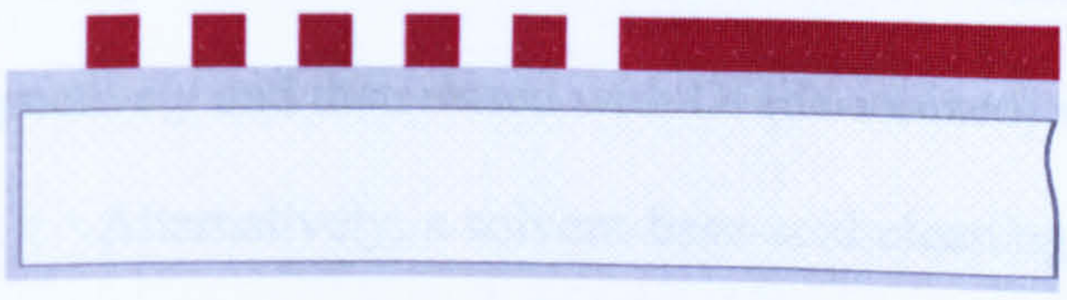	7. Developing in RD6 for 8-9 s

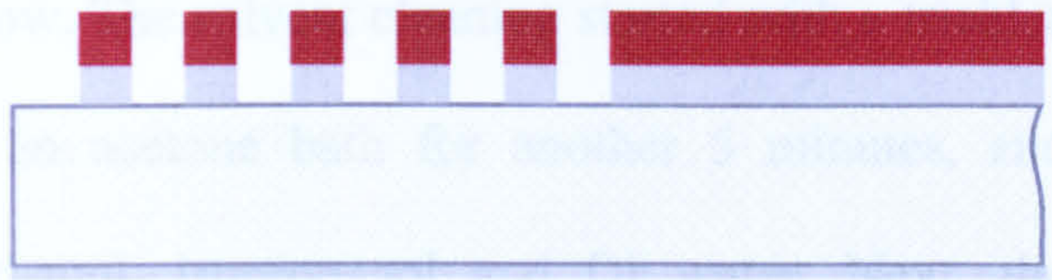	8. Al RIE – 2 min
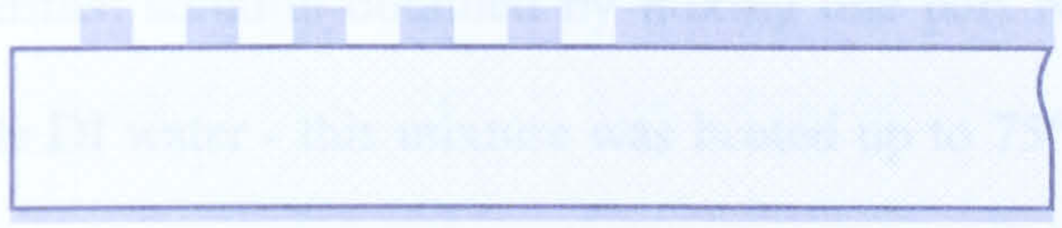	9. Photoresist stripping in RR4
	10. Removal of the back metallisation

5.2.3.1 Wafer cleaning

Wafer cleaning is the first step in microfabrication and has a high importance as the subsequent processing steps largely depend on its success. In particular, a good cleaning method is essential for obtaining a high-quality lithographic pattern.

The purchased lithium tantalate wafers were not pre-factory cleaned and thus appropriate procedures had to be employed to remove possible contaminants. As a general rule, strong alkali solutions should be avoided otherwise LT is compatible with strong acids like HF. A standard wet cleaning procedure based on hydrogen peroxide in mixtures with various acids and bases was attempted: an initial RCA1 clean that removes organic residuals and particles was followed by a RCA2 clean for the removal of the metal ions. RCA1 ammonia-peroxide solution consists of one part NH_3 (25% aqueous solution), five parts deionised (DI) water and one part H_2O_2; RCA2 hydrogen chloride-peroxide solution is a mixture of one part HCl, six parts DI water and one part H_2O_2 [3]. Wafers were immersed into the heated to boil solutions for 10 minutes respectively and then rinsed with DI (de-ionized) water.

Alternatively, a solvent-base-acid cleaning sequence was also successfully used. Details of such a sequence employed during the processing of the LT wafers are given

below. The solvent cleaning started with a trichloroethane bath for 5 minutes, followed by an acetone bath for another 5 minutes, and then the wafers were rinsed with methanol, isopropanol and DI water. Next, the wafers were immersed in a RC1 modified solution obtained by mixing one part NH_4OH with four parts H_2O_2 and six parts DI water - this mixture was heated up to 75°C. Wafers were rinsed again with DI water and subsequently exposed to a diluted Piranha solution (two parts $2H_2SO_4$, one part H_2O_2 and two parts DI water) heated at 120°C. A final DI water rinse was applied to the wafers before they were dehydrated for 15-20 minutes on a hotplate (ramping up and down of the temperature is recommended).

5.2.3.2 Metal deposition

Once cleaned, the LT wafers were ready to be patterned with the mask's geometry. In the current fabrication approach based on etching, the next step involved the deposition of a thin metal layer on the surface of the LT wafers. To this aim a CVC Products DC Sputterer equipment was used along with an Al (aluminium) target with 1% Si (silicon). Sputtering is a physical process performed by accelerating positive ions (e.g. argon) through a potential gradient into the surface of a target, placed at a high negative potential (cathode). Through momentum transfer, the target material is sputtered away mainly as neutral atoms, which subsequently deposit on the wafers placed on the anode. Sputterer depositions have the advantage of uniform layers, excellent adhesion to substrate and tend to coat all exposed surfaces, offering good step coverage [3].

Thus a 130 nm Al layer was sputtered on the front side of the LT wafers. In an attempt to minimise the strong pyroelectric effect a 20 nm thin metal (Al or Cr) layer was deposited on the backside of the wafers. As the DC Sputter equipment ensures a conformal metal deposition, an electrical 'short-circuit' is essentially realized between

the front and backside of the wafers, thus offering a path for the surface pyroelectric charges to neutralize.

5.2.3.3 Lithography

The patterning of the thin Al layer deposited on the LT wafers was achieved via optical lithography. To this aim a radiation-sensitive organic polymer known as photoresist was spun-cast on the wafers and then exposed to UV radiation. The mask for patterning the IDT structures was dark field, and so, a negative tone photoresist had to be employed for a subsequent etching process. NR7-1000P photoresist from Futurrex NR7 series was used as it allows for a uniform, striation free coating and a good selectivity in the RIE process. It also has a superior resolution capability, to less then 0.5 μm that covered the requirements for the current fabrication process. Wafers were mounted and centred on a vacuum chuck in a CEE®100CB spin coater and a static dispense method was used to deposit a few ml of NR7-1000P photoresist near the centre of the substrate. To distribute the photoresist evenly across the surface of the LT substrate, the spin coater was programmed to perform a two steps spin: in the first stage the wafer was rotated with a velocity of 1000 rpm at a 3500 rpm/s acceleration for 5 seconds; the second phase was programmed at 4000 rpm velocity with a 500 rpm/s ramp and lasted 40 seconds. The spin speed and time are the parameters that define the final photoresist thickness. It is recommended that the photoresist layer thickness should be less than the critical dimension [4] – the minimum feature size on the mask was 1.2 μm, thus a thickness of around 850-900 nm was targeted. Acceleration to the final spin speed also has an important role in the coated film properties, particularly in obtaining a good uniformity across the whole wafer.

Following the photoresist spin-casting step the coated wafers are placed on a hotplate and (soft) baked at 150°C for 3 minutes or, alternatively, they can be heated in an oven at 95°C for 35 minutes. During the pre-baking step, most of the solvent remaining in the photoresist layer is dried off. The heating treatment helps eliminate the built-in stress of the coated layer, improve photoresist adhesion to the substrate and establish its exposure characteristics, mainly the dissolution rate in the developer [2, 3].

The soft-baked NR7-1000P coated wafers were then loaded on a lithographic exposure system. A Karl Suss contact printer mask aligner model MA-6 was used for transferring the pattern onto the photoresist. The IDT mask was placed in a frame and then superimposed on a coated wafer chrome side down. As this is the first processing layer, the mask needs no alignment with previous features. However, lithium tantalate is an anisotropic crystal and is important to ensure that the IDTs are strictly perpendicular to the propagation direction of the SAW. To this aim wafer flat windows/marks were defined on the mask. Vernier screws were used to move the wafer relative to the mask so that the last was correctly positioned in respect to the wafer flat, i.e. IDT electrodes parallel to the wafer flat. Once the position adjustments had been done, the mask and the wafer were clamped together and pressed against each other. The mask aligner has several contact modes of exposure. The most intimate contact between the mask and the wafer, and consequently, the best printing resolution is obtained when low pressures of 0.3 down to 0.05 atm (respectively 30400 down to 5066 Pa) are created at the mask-wafer interface via a vacuum system. This hard contact mode of exposure was used to supply a 405 nm wavelength illumination with a dose of 127 mJ/cm^2. The interaction of the negative-tone photoresist with the UV radiation results in a photochemical reaction that strengthens the polymer by random cross-linkage of main chains or pendant side chains, rendering it less soluble in the exposed areas [3].

Contact lithography is widely accepted as a low cost high resolution solution and is a common practice in research and development and MEMS areas. However the use of the contact lithography tool implies a serial exposure - only one wafer being processed at a time – that has an obvious impact on the throughput. Other major disadvantages of the hard contact lithography are the possible contaminations and defects generation during each use, which after several exposure cycles could render the mask unusable for reliable small features applications. Due to these drawbacks, in large scale microcircuit fabrication, contact lithography is substituted by proximity or projection printing that cause far less or practically no defects.

After exposure, NR7-1000P requires a post exposure treatment to complete the reactions initiated during the exposure stage. Wafers were consequently baked on a hotplate at 100°C for 4 minutes.

A wet development process followed in the Futurrex resist developer RD6. Wafers were immersed and slightly agitated in water based RD6 for 8 to 9 seconds. Selective and quicker dissolving of the unexposed areas generated a relief image on the wafer that serves as a mask for the next step. A visual inspection under the microscope was then performed to confirm the successful pattern transfer before wafers were prepared for etching.

5.2.3.4 Reactive ion etching

Once a satisfactory lithographic pattern was obtained in the photoresist layer, wafers were ready for the next processing step. The lateral dimensions of the IDT fingers on the wafers require a highly accurate, directional etch process with good selectivity. Removal of the un-masked Al was achieved via a dry etching technique, more specifically reactive ion etching (RIE). Due to its anisotropy, RIE fulfils the etch

requirements for small features and has also the advantage of being a method with good reproducibility and less chemical waste than wet etching.

Reactive ion etching is based on a chemical-physical process in which a chemical etching reaction is preferentially enhanced in a direction perpendicular to the wafer surface by the physical mechanism of ion bombardment. As ions are not the primary etching species, reactive ion etching (RIE) is somehow a misnomer of the process, a more appropriate name being 'ion-assisted etching' [2].

Chlorine-based plasmas are commonly used to etch Al – chlorinated precursors such as Cl_2, BCl_3, CCl_4 have high vapour pressure and generate volatile chloride that, despite their toxic and corrosive nature are easier to deal with than other etch products like bromides or iodides [2].

A glow discharge is used to generate chemically reactive species in the gas phase: highly energetic plasma electrons impact on the gas molecules dissociating them into radicals[2], atoms, positive ions and electrons. Diffusion and ion bombardment take the reactive species (Cl, Cl_2) to the wafer surface where are adsorbed and react with the material to be etched. The reaction products ($AlCl_3$) desorbs from the wafer, diffuse into the gas phase and are removed by the vacuum pumping system out of the reaction chamber [3, 4].

A parallel-plate Plasma Therm RIE system operating at 13.56 MHz was used to etch away the unwanted aluminium [5]. Wafers were placed on the bottom plate of the reaction chamber that acts simultaneously as the RF-powered electrode (cathode) of the system. The upper neutral electrode was attached to the chamber wall to enlarge its effective area and consequently increase the potential difference from the plasma to the powered electrode. The self-bias accelerates the positive ions towards the wafer,

---

[2] Radicals are more abundant in a glow discharge than ions as they are usually generated at lower threshold energies.

increasing the energy of the ion bombardment and ensuring a high directionality of the etching process.

A mixture of gases was introduced into the reaction chamber via the top showerhead. The exact composition and flow rate of the used gases is given below, where the volumetric flow rate for each gas is given in standard cubic centimeters per minute (sccm): boron trichloride BCl_3 40 sccm, chlorine Cl_2 10 sccm, chloroform $CHCl_3$ 3 sccm. The process pressure was set to 30 mTorr and RF power to 125 W. A 2 minutes etch time resulted in removal of the unwanted Al from the wafer. A picture of the LT patterned wafer after the RIE process is given in Figure 5.1.

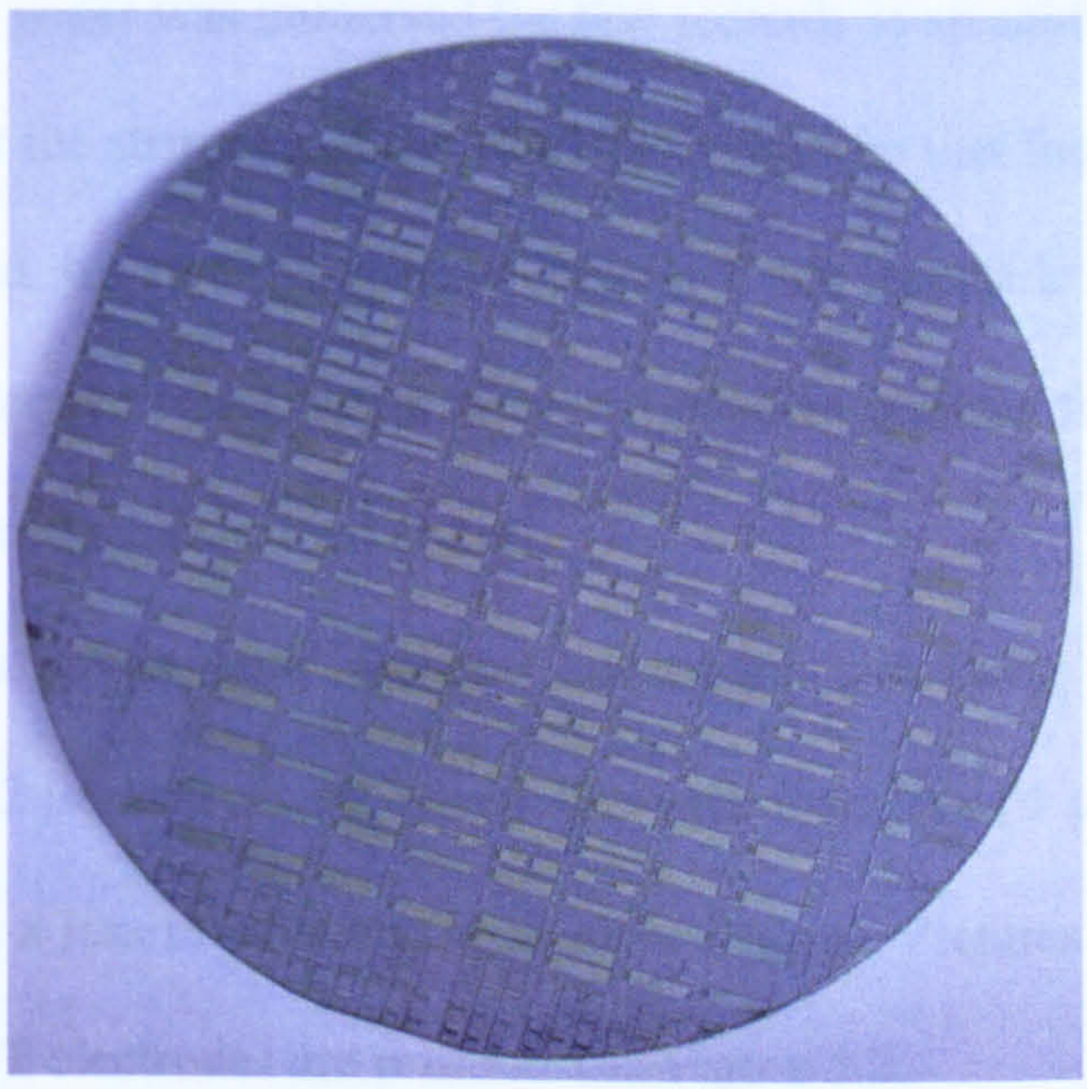

Figure 5.1: Patterned LT wafer

5.2.3.5 Resist removal

The NR7-1000P photoresist was stripped off in a Futurrex resist remover RR4. The solution was heated at 130°C and the wafers were immersed for 10 to 30 min. The photoresist used as a mask material in a reactive ion etching process can be hard to remove and sometimes ultrasonic agitation is needed in addition to the chemical stripping. A low power ultrasonic bath (T8T Otto model 300) heated at the equipment's

maximum temperature (80°C) was used for 5 minutes. Ultrasonic power had to be used with precaution because it can damage the fine IDT pattern - especially in places where the metal adhesion to the wafer is not perfect.

5.2.3.6 Backside metal removal

The backside metal layer being very thin (20nm) could be easily removed by mechanical abrasion with a fine sand paper. Alternatively, a short chemical etching could be used to remove the backside metallization. In this case, a photoresist (Shipley 1818) layer was spun on the top surface of the wafer to protect fully the desired Al pattern and then the wafer was immersed for few seconds in an acid etchant. This step is best performed prior the stripping of the NR-1000P resist so that the fine IDT electrodes are double-protected by two photoresist layers. Once backside metal etching was completed, the protective resist layers were removed in acetone followed by the NR-1000P stripping procedure described above.

The process given here ensured successful patterning of the IDTs with electrodes width of 2 μm and above. Electrodes with features of 1 μm and 1.2 μm were also obtained but in a less reliable and repeatable manner. Pictures with zoomed views on the fabricated IDT electrodes are presented in Figure 5.2.

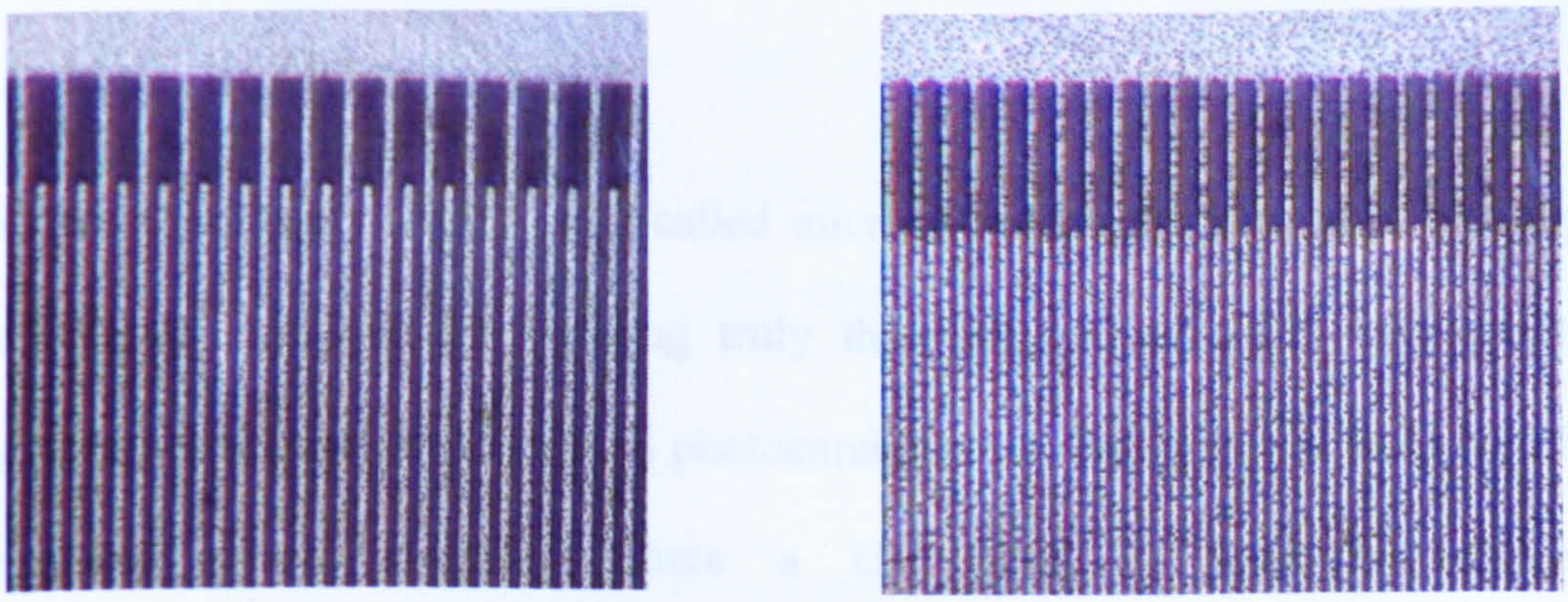

a) IDT fingers with 2.4 μm width b) IDT fingers with 1.2 μm width

Figure 5.2: Zoomed view of IDT electrodes

The distribution of successful devices over the wafer surface revealed the non-uniform tendencies of the process. The Plasma Therm RIE system had several technical problems at the time of the fabrication and was identified as the principal culprit for the non-uniformity of the process and the faced reproducibility issues. Despite the various technological limitations it has to be emphasised that 1 μm features are at the borderline of the theoretical resolution for contact lithography and reliable fabrication of devices with such critical dimensions can be achieved via more expensive lithographic technologies such as Electron-Beam Lithography, Ion-Beam Lithography or X-Ray Lithography.

5.3 LIQUID RESERVOIRS

During testing, the SH-SAW sensors were exposed to various liquid samples. The samples were loaded into liquid micro-reservoirs mounted on top of the SH-SAW device that effectively guide the liquid sample and restrict its spatial distribution to the desired area of the sensor. Two fabrication approaches were considered for the liquid reservoirs - one is employing microstereolithography (MSL) whereas the other one is based on high aspect ratio SU-8 lithography; both techniques are described below.

5.3.1 MSL liquid reservoirs

Microstereolithography (MSL), also called microphotoforming, is a rapid prototyping manufacturing technique for building truly three-dimensional (3D) microstructures using photopolymerisation of a liquid photocurable resin. The principle is derived from conventional stereolithography where a UV beam is used to initiate a (photo)polymerization process linking small molecules (monomers) into chain-like structures to form large molecules (polymers) and ultimately to solidify the exposed

parts of the resin [6]. In contrast with traditional subtractive micromachining methods, MSL objects are formed in an additive manner by superimposing a number of consecutively exposed resin layers.

The MSL process is capable of generating physical objects directly from computer-aided design (CAD) files in several steps. The starting point is the 3-D digital definition of the desired object in a design package, and then the model is sliced into a series of closely spaced horizontal planes that represent the two-dimensional (2-D) cross sections of the 3-D object. All the 2-D slice-models, each with a slightly different z coordinate value, are converted into corresponding digital sequences that are merged together to create a numerical build file. The build file is loaded into the MSL machine and used to control the UV/light exposure on each layer, as well the vertical-axis movement. This is repeated until the whole object is written in the photocurable resin in a layer-by-layer manner [6].

Two major exposure methods are used with MSL systems and are based either on the scanning (vector-by-vector) technique or on the projection (integral) technique. In scanning MSL machines a focused UV laser beam is scanned over the surface of each layer, curing being done spot-by-spot / line-by-line on the 2-D plane. In the projection method, all the points are cured simultaneously by just one exposure through a mask which can be a real photographic mask or a dynamically generated one. With the integral approach the fabrication speed and throughput are increased, but there are more limitations in terms of resolution and build envelope when compared to the scanning counterpart method.

5.3.1.1 'Perfactory' System Description

"Perfactory" equipment from Envisiontec was the rapid prototyping tool used to fabricate the MSL liquid cells (reservoirs) for SAW devices. A user-friendly cost

effective desktop system, ''Perfactory'' employs a light source, more specifically a high-pressure mercury vapour lamp to solidify the photocurable resin. Based on a voxel (volumetric pixel) mask projection technique, the machine builds in a layer-by-layer fashion where all the spots in a layer are cured with a single flash/shot, which make the build speed independent of the model's lateral dimensions. 'Perfactory' can build in layers just 25 μm thick and unlike other classical MSL systems, it builds 'upside down' - the object is leaving the resin tray as it is built as opposed to being submerged into it.

The system's key components are the control unit, the video projector, the photopolymerisation basement and the build platform. A picture of the actual system and a diagram showing the main components are given in Figure 5.3.

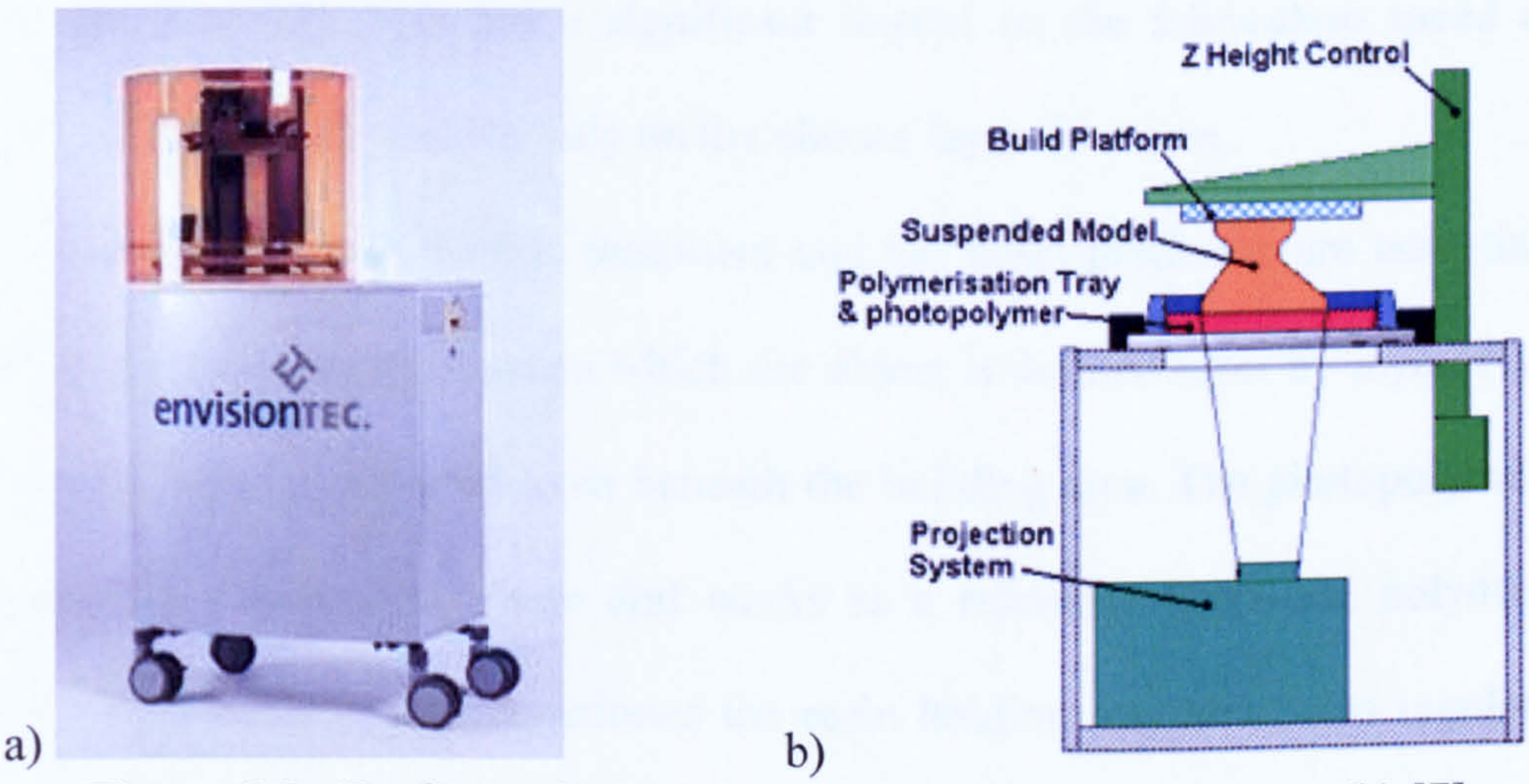

a) b)

Figure 5.3: 'Perfactory' system (a) and its schematic diagram (b) [7]

The system's control unit has an integrated PC with an embedded operating system that allows the machine to work independently and be operated through a simple control panel on the top of the unit. An Ethernet/LAN interface permits 'Perfactory' to be connected to a user PC or integrated into a network. A user PC with 'Perfactory' driver software is used to upload the job file and monitor the build evolution [7].

The video projector employs Digital Light Processing (DLP), an image projection technology implemented with a Digital Micromirror Device (DMD). Originally developed in 1987 at Texas Instruments (by Dr. Larry Hornbeck), DMD is an

extremely precise light switch consisting of a matrix of thousands up to millions of hinge-mounted mirrors laid out on an optical semiconductor chip. Each of the microscopically small mirrors is individually addressable and can tilt to according to an input signal [8, 9]. Every micro-mirror has a corresponding pixel in the projected image and the total number of mirrors defines the image resolution. The 'Perfactory' projector employs a DMD with more than a million digital mirrors (1280×1024 pixels) that tilt towards the light source to reflect and project the light where the resin needs to be cured (ON state) and tilt away to block the light where the resin has to remain uncured (OFF state). In this way the machine effectively generates an ON/OFF bitmap mask for each layer and when the light flashes the whole of the build area is exposed simultaneously, in one operation [7]. This has a significant impact on the fabrication speed and the vertical build rate is dependent only on the chosen layer thickness.

The photopolymerisation basement and the build platforms are essentially two pieces of ground glass in between which the object is defined layer by layer. As shown in Figure 3, light is projected from beneath the building area. The photopolymerisation basement has a transparent base and works as a reference layer and polymerisation surface. The basement also constitutes the resin holding tray and helps regulating the layer thickness. The build platform is fixed to Z-Height Control and is moved vertically by a precision linear drive. At the beginning of a build process the basement and platform come close together. By squeezing the excess resin, the intended layer thickness is trapped between the two glass plates. Light flashes and cures the first layer which bonds to both top and bottom plates. Using a sophisticated tilting mechanism the basement is peeled away from the cured layer which remains attached on the top to the build platform. The Z-Height Control raises the platform with a layer thickness allowing resin replacement in between the plates. A new layer is cured onto the bottom of the

previous one and the process is repeated layer by layer until the object is built [7, 10]. This technique eliminates the need for resin levelling or planarisation which is a critical issue for other types of MSL systems.

Standard and Mini (Multi Lens) Envisiontec 'Perfactory' systems available at University of Warwick were both used to build liquid reservoirs. The two variants are based on the same technology described above, but each provide different capabilities in terms of build envelope and projected pixel resolution. With the best achievable XY resolution of 93 um and a vertical one of 50 um layer thickness the Standard version has a build envelope of 120×96×230 mm^3. The Mini version can build models with layer thickness as thin as 25 μm and achieve a 32 μm XY pixel resolution when an 85 mm focusing lens is employed; the build envelope is restricted to 41.98×33.59×230 mm^3. The above parameters were exact at the time the liquid cells were fabricated, more recent Envisiontec specifications show slight improvements of these data [11].

5.3.1.2 Build Process

Liquid reservoir models were designed in AutoCad 2002 package. The parts were then exported as .stl files (format required by stereolithography applications) and visualised in SolidView. The 3-D objects were subsequently loaded into MAGICS software, a package provided by Envisiontec to prepare model for the 'Perfactory' system. MAGICS checks the .stl data for any triangulation errors and repairs them, allows positioning and orientation of the model, and if required, it generates support structures to assist during the build process.

The pre-processed .stl models and their corresponding support files were then transferred to 'Perfactory' RP Software Suite. Here the user defined the build parameters, choosing the type of RP machine, the size of the building area and the resin to be used. The models and their supports were placed on the build platform and

multiple copies were generated if several parts were required per build. The objects were subsequently sliced depending on the defined layer thickness – parts were built with 25 μm, 50 μm and 100 μm layer thickness. Each data slice was prepared and converted into a bitmap format necessary for the mask projection via DLP-Technology. 'Perfactory' RP merged all the data into a build job that was loaded directly on 'Perfactory' machine. The job preparation was an important stage in the reservoir's MSL fabrication as it defined the build parameters and ultimately the object characteristics. Figure 5.4 presents a generic sequence of steps involved in the MSL definition process, starting with the CAD design up to the final physical model.

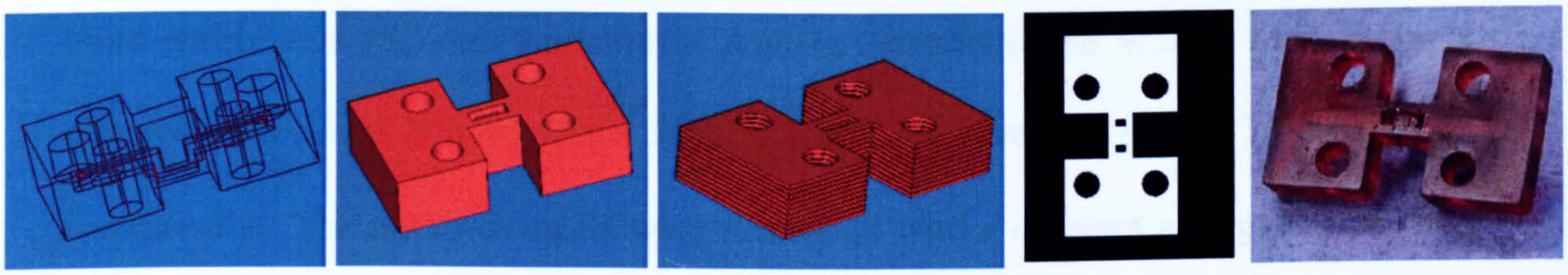

a) AutoCAD model b) STL model c) Sliced model d) Mask projection e) Physical model

Figure 5.4: Flow process in MSL fabrication

In the above flow process visual sequence, two post-fabrication steps were not represented: object cleaning and final curing. Upon completion of the MSL build process the liquid reservoirs remained suspended on the machine's build platform. Once removed from the platform they might still have a film of uncured liquid resin around them or resin trapped into the micro-channels. A cleaning procedure was achieved by immersion in isopropanol alcohol (IP). Cleaning of small features was be enhanced by ultrasonic agitation - parts were placed for 5 minutes into an ultrasonic bath (T8T Otto 300 Model). When all the uncured resin was removed, parts were dried with filtered air and exposed for 10 minutes to UV light in a Primotec Metalight QX1 system for final curing.

A variety of light sensitive photopolymers are available for this system and materials include methacrylates, expoxides and nanoparticle filled materials and compounds [11]. For the liquid reservoirs 'Perfactory' R5/R11 resins were used due to their chemical resistance and good mechanical properties.

Several miniature MSL (microstereolithography) liquid cells have been designed and fabricated using the Envisiontec 'Perfactory' rapid prototyping system. Figure 5.5 a) gives a photograph of MSL_1 cell showing a detailed view of the liquid microreservoir. The micro-reservoir has an opening of 800 μm and a height of 500 μm. The flow channels have 800×800 μm^2 square cross-section, while the cell's overall build envelope is 15.5mm×9mm×4mm. Among the cells in the MSL_2 series, sample pictures of top and bottom views MSL_2.1 cell are given in Figure 5.5 b) and c), respectively. The micro-channels were fabricated with a constant a height of 500 μm and a varying width from 800 μm down to 400 μm (in the reservoir section). As described in the design chapter, characteristic to the MSL_2 series is the fact that the liquid flow is no longer longitudinal through the reservoir, as in MSL_1, but transversal to the microreservoir, with the channel openings positioned sidewise. In MSL_2.1, inlet and outlet channel openings on the top of the reservoir have rectangular cross-sections of 300 μm × 400 μm. The reservoir allows a wider spreading of the liquid across the sensor's surface (2 mm), but in a thinner film, since the reservoir height in this configuration is 300 μm. The overall MSL_2 cells dimensions are 15.5mm×9mm×3mm.

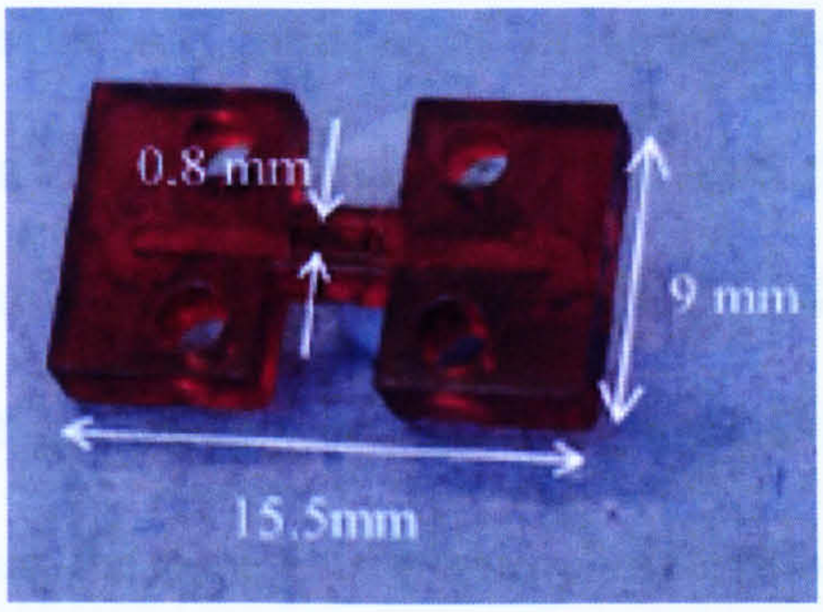

a) MSL_1 cell bottom view on the microreservoir

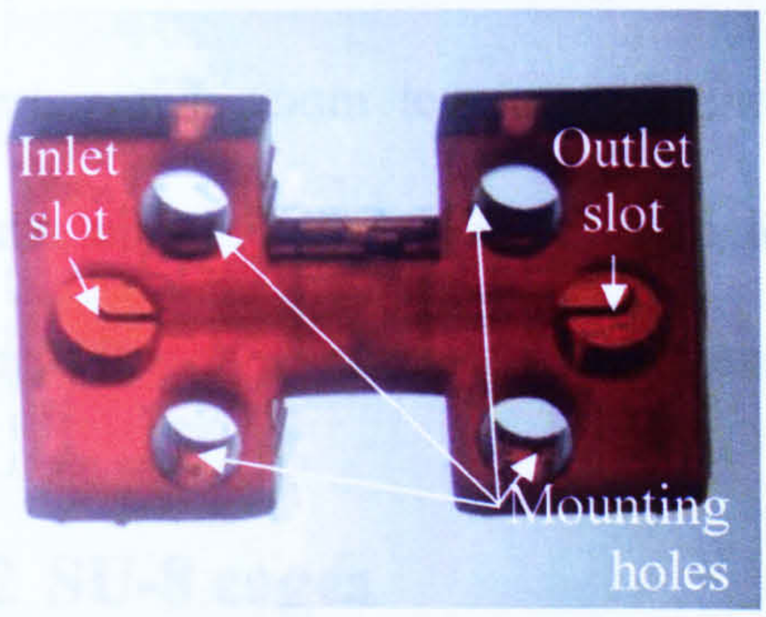

b) Top view of the MSL_2.1 cell with inlet and outlet slots

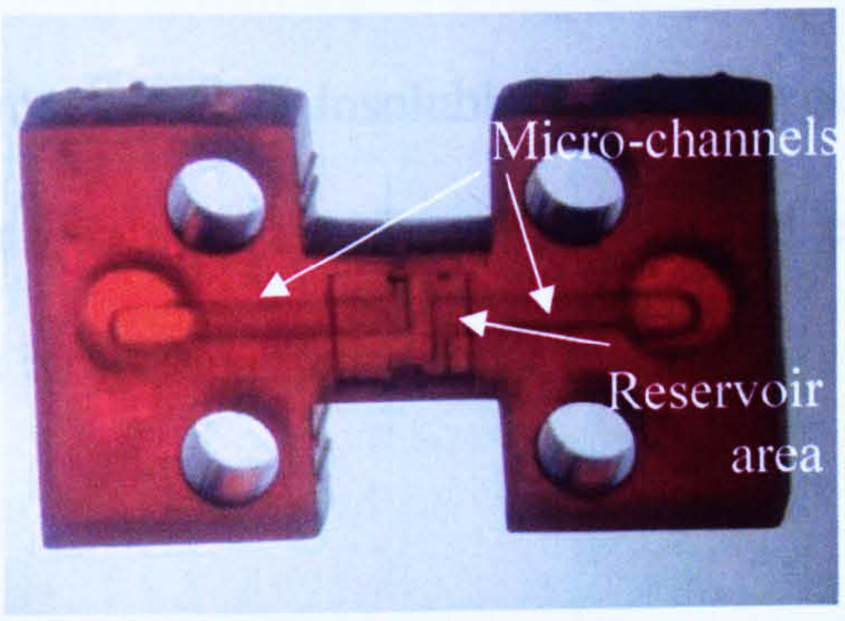

c) Detail of MSL_2.1 cell micro-reservoir (bottom view)

Figure 5.5: Pictures of the fabricated MSL liquid cells

Test trials were conducted to check the influence of part orientation during the build process on the object surface characteristics. Cells were fabricated with reservoir's surface parallel (horizontal) and perpendicular (vertical) arrangements to the build platform. Side positioning on the build platform increases the build throughput at the expense of build time (time, however, is not critical for relatively small parts as in our application), but also has an impact on the surface quality. Due to the slight misalignment between each layer during the fabrication process, surface roughness increases when the surface of interest is perpendicular to the build platform [12]. The reservoir's surface quality was further compromised when builds were run with 100 μm layer thickness on a Standard 'Perfactory' system, and differences in surface quality became visibly evident. Poor surface flatness can lead to liquid leakage when cells are mounted on top of the SAW sensors and high flow rates applied. The best, leakage free

results were obtained for cells built on the Mini 'Perfactory' system, with the reservoir's surface parallel to the fabrication plane and with 25 μm layer thickness.

Following the final curing step involved in the MSL post-process, the liquid cells were coated with 2 μm of parylene C, using a PDS 2010 Labcoater from the Speciality Coating Systems. Parylene C is a hydrophobic, bio-compatible dimer that can be vaporised in vacuum and deposited in pinhole free conformal coatings. Parylene™ is inert, resists room temperature chemical attack and is insoluble in most organic solvents up to 150°C [13]. The coated layer improves the flow in the liquid cell, enhances its chemical resistance and ensures its bio-compatibility.

5.3.2 SU-8 cages

Small samples of the liquid under test can also be accommodated by SU-8 reservoirs. Several configurations were designed and fabricated on silicon wafers employing SU-8 2050, a permanent epoxy resist from MicroChem. SU-8 is an acid-catalyzed negative photoresist with low cost, high resolution, excellent sensitivity, low optical absorption and good thermal and chemical stability. Due to its high aspect ratio capability, SU-8 is frequently used in MEMS applications. Aspect ratios up to 25 were demonstrated for contact lithography [3], though direct write nano lithographic tools proved much higher aspect ratio capabilities: microstructures with aspect ratios of 50 were build using X-rays systems [14], and high aspect ratios up to 160, (with details down to 30 nm width), were written with a focused MeV proton beam tool [15].

SU-8 liquid reservoirs were again fabricated at Georgia Institute of Technology, Atlanta, USA using a conventional contact photolithography method. Reservoirs delimit the liquid sample spreading via wall structures 200-300 μm wide and 75 μm tall. Some of the reservoirs contain embedded microfilters for trapping microparticles or micro-

size cells on the active area of the SAW sensors. When the liquid sample is flowed through the SU-8 reservoir the filter would act as a particle pre-concentrator and thus enhancing the effect of the particles on the SH-SAW sensor. Reversing the liquid flow direction the filters are cleaned and the trapped particles eliminated. Pre-concentrator filters have been implemented using pillar structures with rectangular, circular and trapezoidal shapes. Various filter arrangements have 4 to 12 μm gaps between typically 30 - 50 μm ferret pillars.

The SU-8 2050 patterning process is schematically synthesised in Table 5.2. The reservoir configurations described in the previous design chapter have been grouped together on a photomask that was used for fabrication experiments. Microfabrication of the SU-8 reservoirs started with a similar cleaning procedure described above for the LT wafers. Si wafers were next dehydrated for 30 minutes in an oven at 140°C. A single spin-coat was applied to the wafers to form SU-8 layers of 75 to 100 μm thick. The final layer thickness is dependent on the spin parameters, mainly the speed. SU-8 is highly viscous and prone to air bubble formation if dispensed using a pipette. To avoid this, a few ml of SU-8 were poured on the centre of the wafers directly from the photoresist bottle. To achieve a 75 μm coating thickness, the spread cycle was set to last 10 seconds during which wafers were ramped to 500 rpm at 100 rpm/s acceleration. The spin cycle was performed at 2000 rpm for 30 seconds with acceleration of 300 rpm/s.

Table 5.2: SU-8 single spin-coat process

[redacted]	1. Clean Si wafer
[redacted]	2. SU-8 spin coat

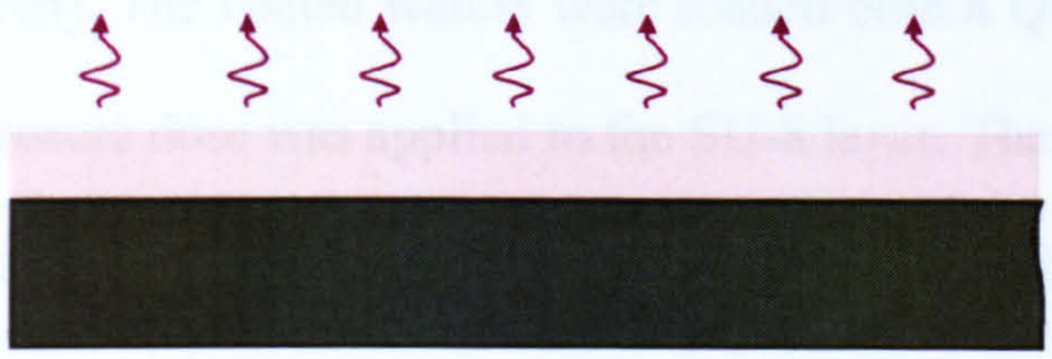

3. Soft bake

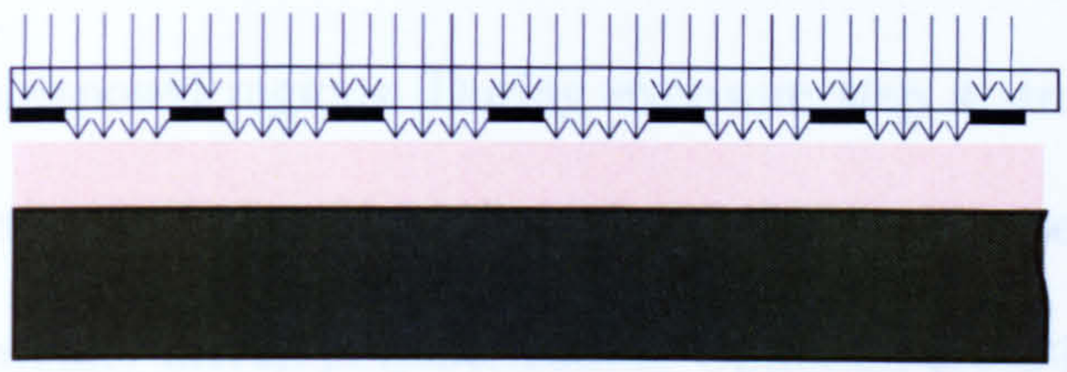

4. Exposure

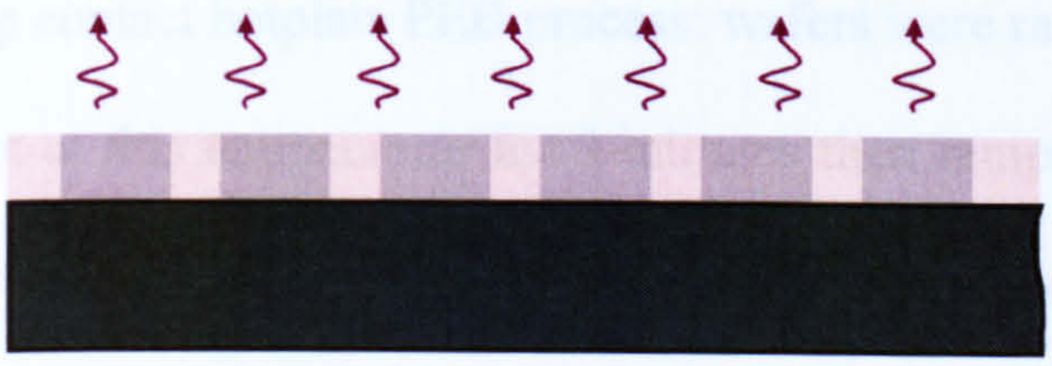

5. PEB

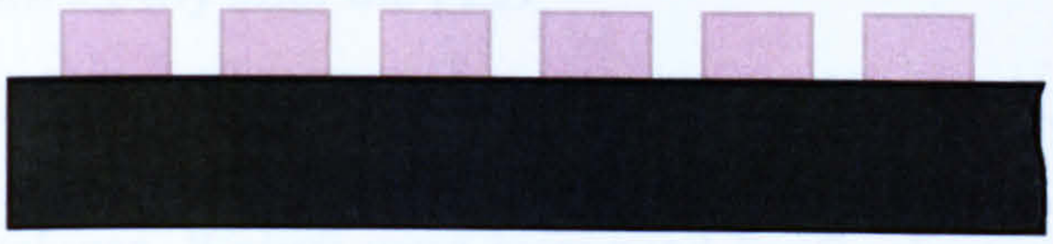

6. Develop, IP rinse and dry

After the resist was applied to the substrate, it was soft-baked to evaporate the solvent and densify the film. The wafers were placed on a levelled hotplate at 65°C and pre-baked for a minimum of 10 minutes, then the temperature was ramped to 95°C and wafers further kept at this temperature for 20 more minutes. The hotplate was turned off and the wafers allowed to cool down slowly to room temperature. Good results were obtained when wafers were left overnight on a levelled flat surface for further planarization.

Exposure of SU-8 layers is commonly achieved with standard contact lithography with near UV (350-400 nm) radiation, although electron and x-ray tools may also be used. I-line exposure tools are recommended as the photoresist is most sensitive at 365 nm (at this wavelength the total absorption of light occurs at a depth of

2 mm). The coated wafers were loaded onto a Quintel mask aligner and a 295 mJ/cm^2 exposure dose was applied to the SU-8 layer. The i-line intensity measured with a probe was 10.2 mW/cm^2 and the exposure time was set to 29 seconds.

Next, a post exposure bake (PEB) must be performed to selectively cross-link the exposed regions. During exposure step a strong acid is generated in the exposed portions of the film; throughout the post exposure bake phase, the acid initiates thermally driven polymerization. Optimum cross-linking density was obtained in a two step contact hotplate PEB process: wafers were ramped from room temperature to 65°C, kept at this temperature for 3 minutes then ramped again up to 95°C where they were kept for a further 7 minutes. A latent image of the pattern becomes visible in the SU-8 coating. To minimize film stress and avoid resist cracking, wafers were left to cool down slowly after the PEB.

Development of the non-exposed regions was carried out in MicroChem's SU-8 developer. Wafers were immersed for 7 minutes in a developer bath that was strongly agitated to facilitate the removal of unwanted resist between the filter pillars. Ultrasonic agitation can also be used to enhance the chemical reaction of the developer, but power needs to be carefully adjusted in order not to damage or even dislocate the filter pillars. A final 10 seconds wash in fresh developer solution was performed before wafers were rinsed with isopropyl alcohol (IPA) for another 10 seconds and dried with nitrogen jet. At this point a further hard bake is optional as the remaining structures on the wafers are suitable for the envisaged application.

The described fabrication procedure resulted in successful patterning of the reservoirs and embedded filters. The 4 μm gap filters were partially successful on some wafers, while 8, 10 and 12 μm filters were reliably obtained. Structures having feature aspect ratio between 1.5 and 2.5 and gap aspect ratio varying from 6 (for 12 μm gaps)

up to 19 (for 4 μm gaps) were achieved on the same wafer. Despite the fact that aspect ratios of 20 to 25 are regularly produced [3,16], they seem to be size dependent, and very small feature sizes are usually avoided. The fabrication procedure described above can be improved and process parameters fine-tuned to improve its resolution, however, it seems that high aspect ratios with features smaller than 3 μm remain difficult to achieve with contact lithography.

A photograph with detailed dimensions of one micro-reservoir configuration with trapezoidal shape pillars and 8 μm filter gaps is shown in Figure 5.6.

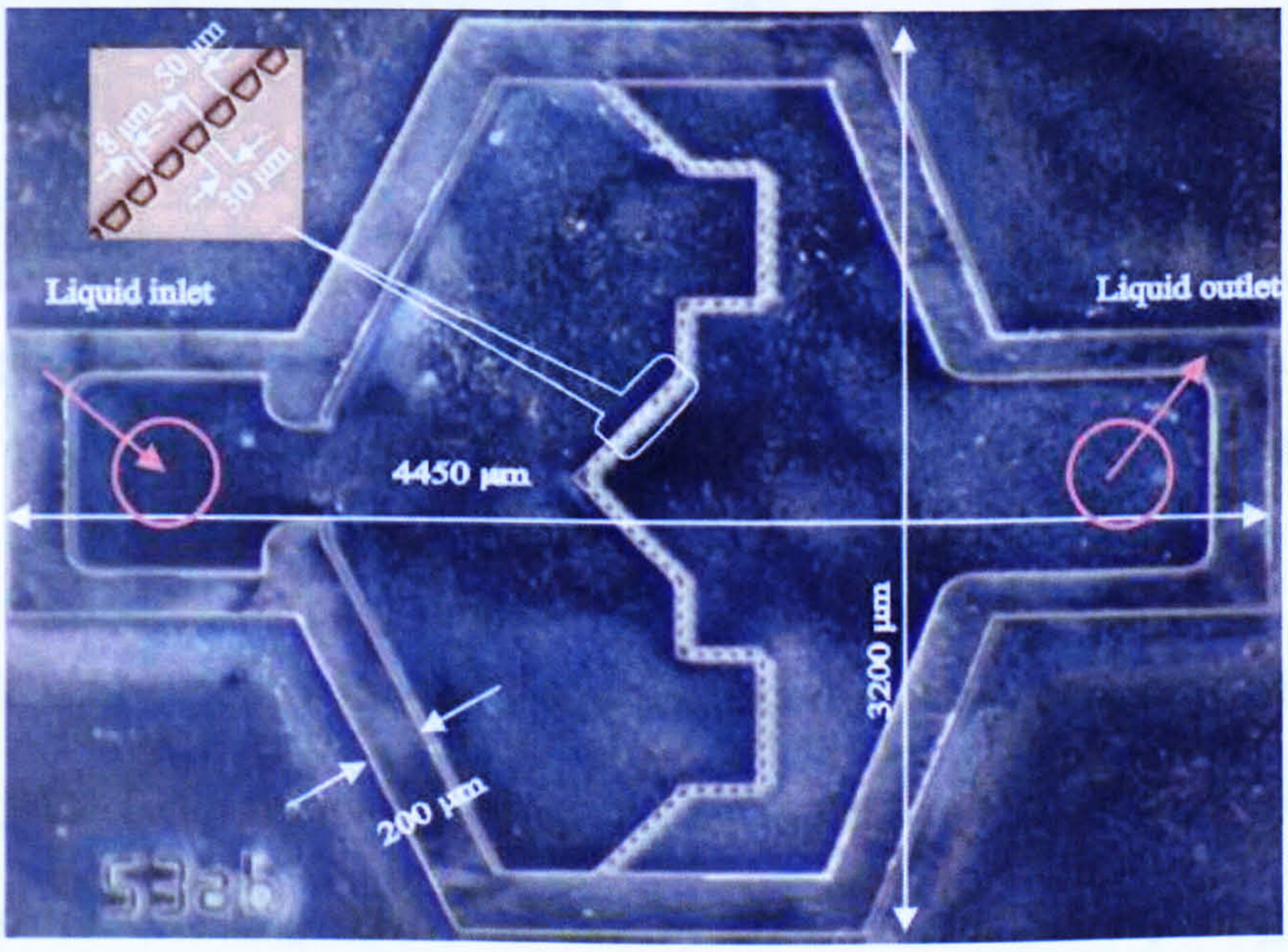

Figure 5.6: Photograph of SU-8 liquid reservoir R53ab with 8 μm trapezoidal filter

Figure 5.7 shows two more reservoir configurations with zoomed views on the patterned pillars.

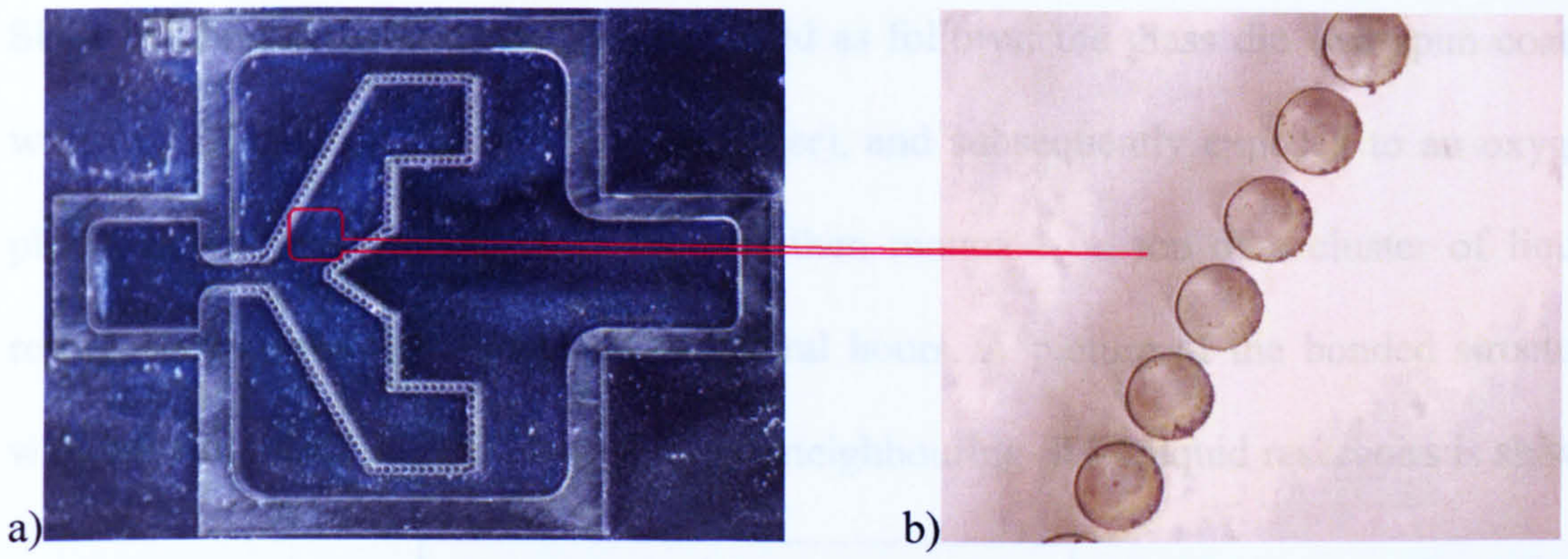

Figure 5.7: Fabricated SU-8 reservoirs: R62 configuration (a) with zoomed view on 12 μm gap round pillar filter (b); R23 multi-stage filter configuration (c) with details on 12 μm, 8μm and 4μm gaps successive filters

Following the fabrication, SU-8 reservoirs were also coated with a thin layer (1 μm) of Parylene C, for the same reasons and using the same procedure as for the MSL liquid cells. This coating method offers an efficient tool for adjusting the filters dimensional resolution. Thus the lithographic requirements can be relaxed and gap size controlled by the deposition thickness: an 8 μm filter can be converted into a 4 μm particle filer by post-definition deposition of 2 μm of Parylene C, etc.

Two 0.5 mm inlet and outlet holes can be drilled in the Si substrate and the reservoir can then be flipped over and placed on top of the sensor. While sealing the Si reservoirs directly on the LT SAW sensors presents several practical difficulties, a preliminary test of the reservoirs was done using a glass slide. Holes with 500 μm diameters were drilled in the glass cover using diamond coated drill bits. A PDMS to

SU-8 bonding procedure was experimented as follows: the glass die was spun coated with PDMS mixture (10:1 base to hardener), and subsequently exposed to an oxygen plasma for activation; the glass die was then mounted on top of a cluster of liquid reservoirs and pressed against it for several hours. A picture of the bonded structure with inlet and outlet tubes attached to two neighbouring SU-8 liquid reservoirs is shown

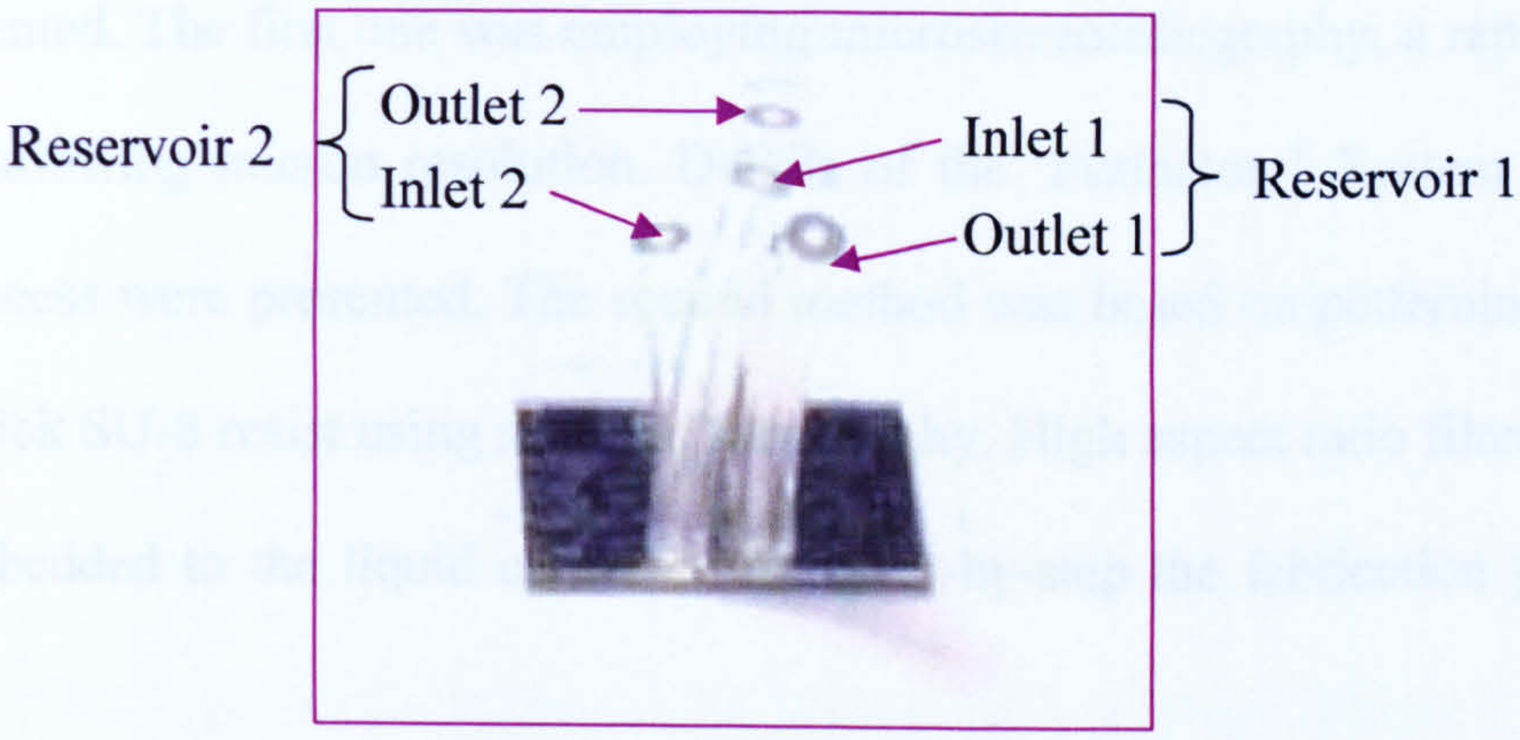

Figure 5.8: Cluster of SU-8 liquid reservoirs bonded onto a glass cover

in Figure 5.8. Water has been injected via the inlet tube into the bonded reservoirs and collected at the output tube. The flow through test was successful with no leakage observed.

5.4 CONCLUSIONS:

This chapter presented the fabrication process of the liquid sensing system. The system implementation followed a modular approach and this chapter offered microfabrication details for both subsystems, namely the LT sensors and the liquid reservoirs.

Standard lithium tantalate crystals have properties that require a special set of precautions when handling and processing the wafers. The SH-SAW sensors patterns were defined using contact lithography and a reactive ion etching method. Electrodes with 1.2 μm and 2.4 μm width were obtained using this method and detailed step-by-

step fabrication procedures and the recipes used are described. Due to technical problems of the dry etching system used, the sensors having 1.2 μm features were not uniformly patterned but the sensors with electrodes of 2 μm and above had a repeatable and larger successful yield.

For the liquid reservoirs, two fabrication methods were considered and experimented. The first one was employing microstereolithography, a rapid prototyping method allowing micron resolution. Details of the 'Perfactory' System and the MSL build process were presented. The second method was based on patterning liquid cages onto a thick SU-8 resist using standard lithography. High aspect ratio filtering structures were embedded to the liquid cages and the step-by-step the fabrication procedure was detailed.

The two fabricated subsystems were mounted together and exposed to various liquid samples. The experimental results are presented in the following chapters.

5.5 REFERENCES:

[1] Roditi International. (2007), "Roditi international - photonic materials" http://www.roditi.com.

[2] S. A. Campbell, *The Science and Engineering of Microelectronic Fabrication.* 2nd ed. New York; Oxford: Oxford University Press, 2001, pp. 603.

[3] M. J. Madou, *Fundamentals of Microfabrication: The Science of Miniaturization.* 2nd ed. Boca Raton; London: CRC Press, 2002, pp. 723.

[4] J. W. Gardner et al., *Microsensors, MEMS, and Smart Devices.* Chichester; New York: J. Wiley and Sons Ltd, 2001, pp. 503.

[5] Georgia Tech, Microelectronics Research Centre. (2005), "Plasma-therm RIE", http://grover.mirc.gatech.edu/equipment/textInstructions.php?id=40.

[6] V. K. Varadan, *Microstereolithography and Other Fabrication Techniques for 3D MEMS.* New York; Chichester: Wiley, 2001, pp. 274.

[7] CRDM Ltd. (2007), "Envisiontec 'Perfactory' mini (multi lens) system - How it works", http://www.crdm.co.uk/technical_micro_modelling.htm.

[8] Texas Instruments. (2007), "What is DLP® technology?", http://focus.ti.com/dlpdmd/docs/resourcedetail.tsp?familyId=767&genContentId=3438&contentType=13.

[9] Texas Instruments. (2007), "How DLP® technology works.", http://www.dlp.com/tech/what.aspx?revkey=0&sid=0&gd=edfa7aed-2e8a-4024-b536-2185c0689158&ct=6331317410343171 18&frm=/tech/default& lnkid=11.

[10] Envisiontec GmbH. (2007). "Micro Modelling, Envisiontec 'Perfactory' System", http://www.envisiontec.de.

[11] Envisiontec GmbH. (2007). "'Perfactory' - technical data." http://www.envisiontec.de/22htecha.htm.

[12] S. Tan, "Smart chemical sensing microsystem: towards a nose-on-a-chip", Ph.D. Thesis, University of Warwick, Coventry, UK, 2005.

[13] Specialty Coating Systems. (2007), "Parylene knowledge-specifications and proprieties" http://www.scscoatings.com/parylene knowledge/specifications.aspx.

[14] C. G. Khan Malek, "SU8 resist for low-cost X-ray patterning of high-resolution, high-aspect-ratio MEMS" *Microelectronics Journal,* vol. 33, pp. 101-105, 2002.

[15] J. A. Van Kan, A. A. Bettiol, K. Ansari, E. J. Teo, T. C. Sum and F. Watt, "Proton beam writing: A progress review", *International Journal of Nanotechnology,* vol. 1, pp. 464-479, 2004.

[16] N. Maluf, *An Introduction to Microelectromechanical Systems Engineering.* Boston; London: Artech House, 2000, pp. 265.

CHAPTER 6:

DEVICE CHARACTERISATION AND EXPERIMENTAL RESULTS

6.1 INTRODUCTION

Once the lithium tantalate wafers were fabricated and diced, the individual SH-SAW sensors were mounted onto customised PCBs. The IDTs' pads were ultrasonically wire-bonded to corresponding pads on the PCBs that were interfaced with the testing equipment via SMA-type connectors.

A preliminary electrical characterization was performed on selected sensor devices. The IDTs performance was evaluated in terms of the complex reflection coefficient, and departures from the characteristic impedance are visualised using a Smith Chart. Several delay-line devices were chosen to study the effect the propagation path has on the insertion loss of the device. Same length free and metallised delay lines were initially characterized, then compared to delay-lines presenting variations to the length and surface boundary conditions of the propagation path.

This chapter briefly reviews the surface acoustic wave sensor set-up and measurement instrumentation, with the use of a network analyser and vector voltmeter for liquid testing. The chapter also presents a wireless SH-SAW measurement set-up and describes its operating principle.

MSL liquid cells were attached to the selected SH-SAW sensors and liquid measurements were performed. Liquid samples were exposed to several sensor configurations and results are presented. Initial experiments were conducted on wired sensors: the dual delay line SRL 280a and the dual resonator SRL 284. Tests were then performed on semi-wireless set-up where the SRL 208a sensor was powered remotely via an antenna attached to the input IDTs. Preliminary experiments were also performed on the voltage modulated sensors (SRL 273) and a mechanism able to explain the results is presented. Graphical representations of the results are included for each sensor category.

6.2 ELECTRICAL CHARACTERIZATION OF DEVICES

High frequency devices are usually characterized with a network analyser; an instrument used to analyse the proprieties of the electrical networks in terms of reflection and transmission signals. A vector network analyzer may also be called a gain-phase meter or automatic network analyser and their operating frequencies typically range from 9 kHz to 110 GHz [1].

A vector network analyser is a two- or four- channel microwave receiver designed to process the magnitude and phase of the transmitted and reflected waves from the electrical network. An embedded RF source is swept over a specified frequency range and a four-port reflectometer samples the incident, reflected and transmitted RF waves. An internal switch allows the network to be driven from either

port 1 or port 2. The signal processing is performed by a powerful internal computer that computes and displays magnitude and phase of the scattering parameters or quantities that can be derived from them (such as return loss, impedance, and group delay). To improve the measurement accuracy, the network analyser uses error correcting software. Errors caused by directional coupler mismatch, imperfect directivity, loss and variations in the frequency response of the analyser are accounted by using a twelve-term error model and performing a calibration procedure prior the measurement [2].

The scattering or S-parameters measured by the network analyser are properties used to describe the electrical behaviour of devices when undergoing various steady state stimuli by small signals. While other parameters used in electrical engineering (Y-, H- or Z-parameters) are practical for characterizing low frequency devices, at high frequencies it is very hard to measure the total voltage and current at the device ports. That is why scattering or S-parameters were developed. Also, unlike other parameters, S-parameters do not require the connection of undesirable loads to the device under test (DUT). S-parameters can be related to familiar measurements such as gain, loss, reflection coefficient or voltage standing wave ratio (VSWR) and are defined in terms of voltage traveling waves, which are relatively easy to measure. The measured S-parameters of multiple devices can be cascaded to predict the overall system performance. In addition, if desired, the H, Y, or Z-parameters can be easily derived from S-parameters. The S-parameters are an essential tool for RF design and represent the shared language between simulation and measurement [3].

A two-port device has four S-parameters (Figure 6.1a). The numbering convention for S-parameters is that the first number following the "S" is the port where the signal emerges, and the second number is the port where the signal is applied. So,

S21 is a measure of the signal coming out port 2 relative to the RF stimulus entering port 1. When the numbers are the same (e.g., S11), it indicates a reflection measurement, as the input and output ports are the same. Details for computing and measuring the S-parameters are given in Figure 6.1b. In this representation the incident terms (a1, a2) and output terms (b1, b2) represent voltage traveling waves [3].

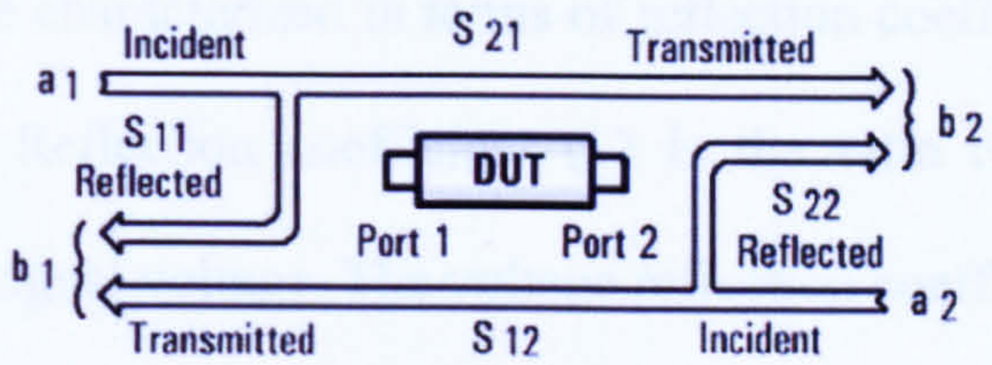

$$b_1 = S_{11} a_1 + S_{12} a_2$$

$$b_2 = S_{21} a_1 + S_{22} a_2$$

a)

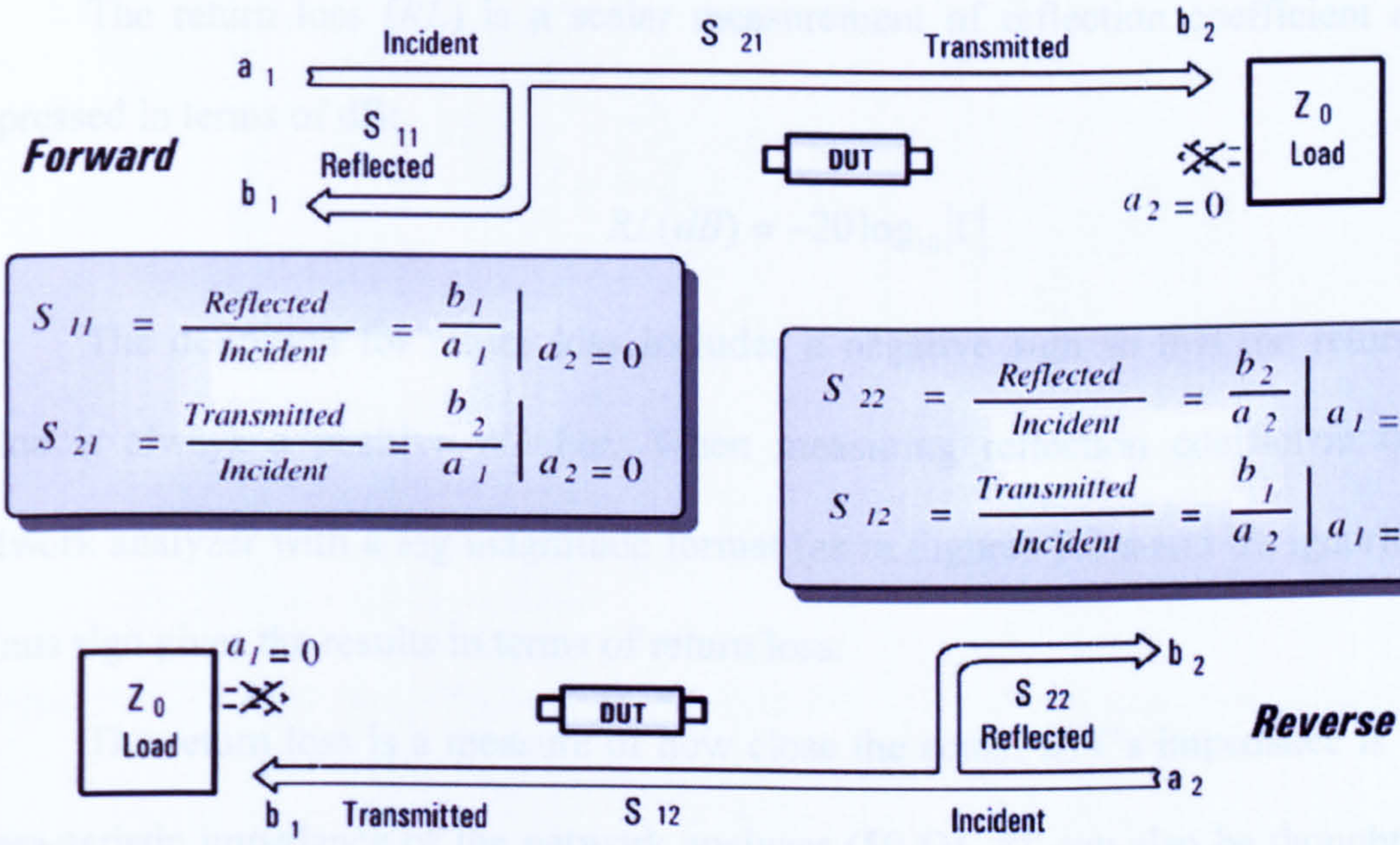

b)

Figure 6.1: Diagrams depicting S-parameters measurements: signal flow of a two-pot device (a) and detailed procedures for computing the S-parameters (b) [3]

With amplitude and phase information of the incident, reflected and transmitted waves, the network analysed can quantify the reflection and transmission characteristics of the device under test (DUT). The SAW sensors were characterized with an Agilent

two port network analyser (model 8753ES). The IDT's reflection coefficients and delay line's transmission coefficients were used to compare the different sensor configurations.

6.2.1 IDTs characterization

The sensors' IDTs were characterized in terms of reflection coefficients measured from the network analyzer. Reflection coefficient (Γ) is the ratio of the reflected signal voltage to the incident signal voltage. The voltage reflection coefficients at the input and output IDTs are equivalent to S11 and S22 parameters, respectively, and are complex quantities that can be represented on polar diagrams or Smith charts.

The return loss (RL) is a scalar measurement of reflection coefficient and is expressed in terms of dB:

$$RL(dB) = -20\log_{10}|\Gamma|$$

The definition for return loss includes a negative sign so that the return loss value is always a positive number. When measuring reflection coefficient on the network analyzer with a log magnitude format (as in Figures 6.2 a and b), ignoring the minus sign gives the results in terms of return loss.

The return loss is a measure of how close the actual IDT's impedance is to the characteristic impedance of the network analyzer (50 Ω). RL can also be thought of as the number of dB that the reflected signal is below the incident signal. While the magnitude of the reflection coefficient can vary between 0 (perfect match) and 1 (open or short circuit conditions), the return loss varies between infinity for a Z_0=50 Ω impedance and 0 dB for an open or short circuit.

All the SAW sensors chosen for electrical characterization and comparison had the same IDT design, consisting of 25 solid electrode finger pairs. Examples of good

IDT reflection coefficients plotted in log magnitude and Smith chart format are given in Figure 6.2.

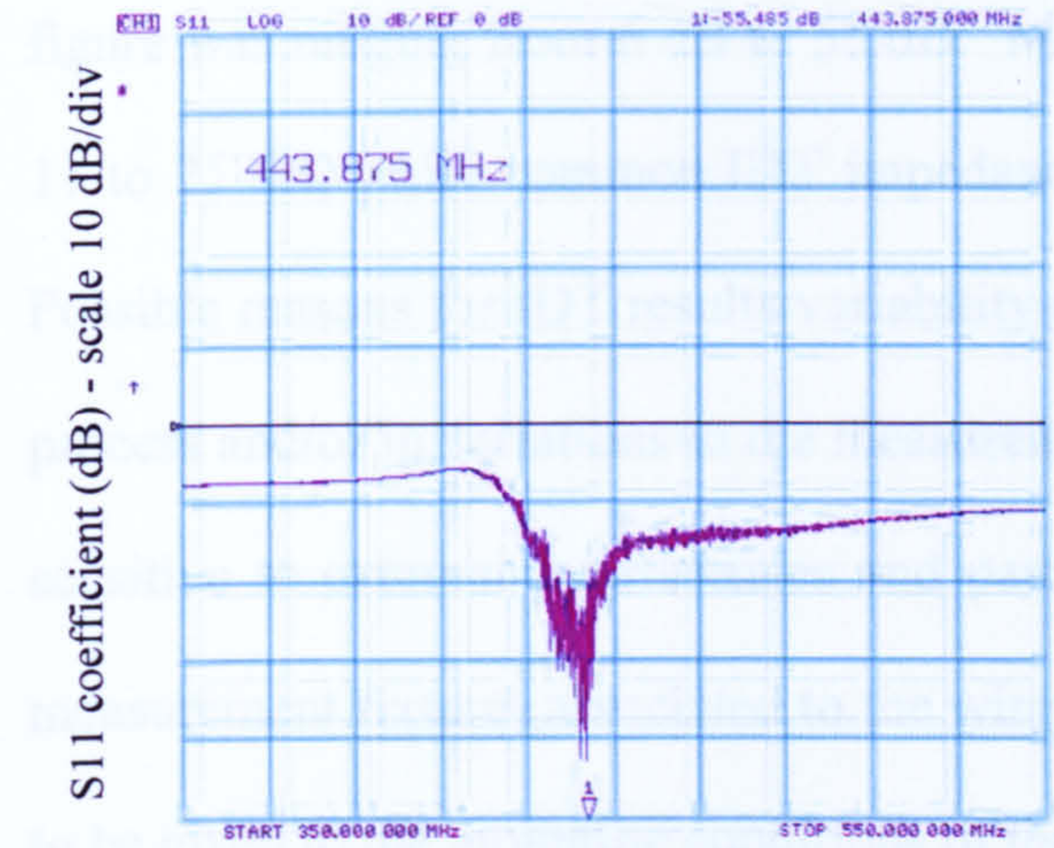

a)

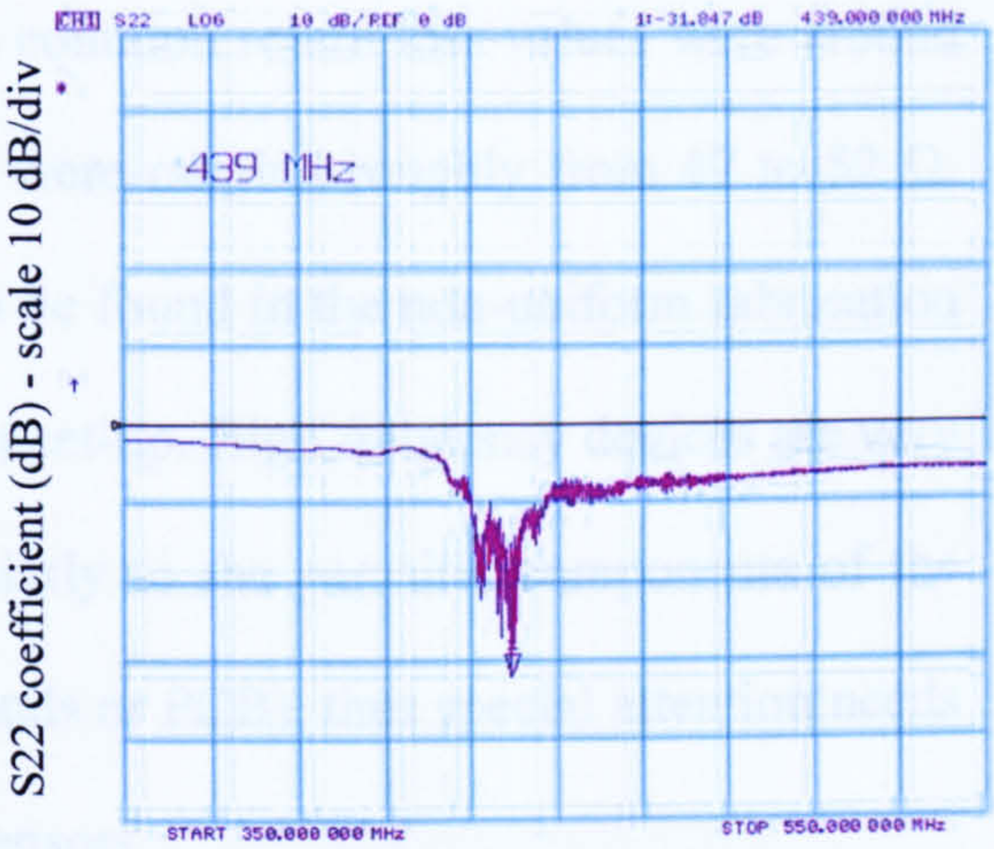

b)

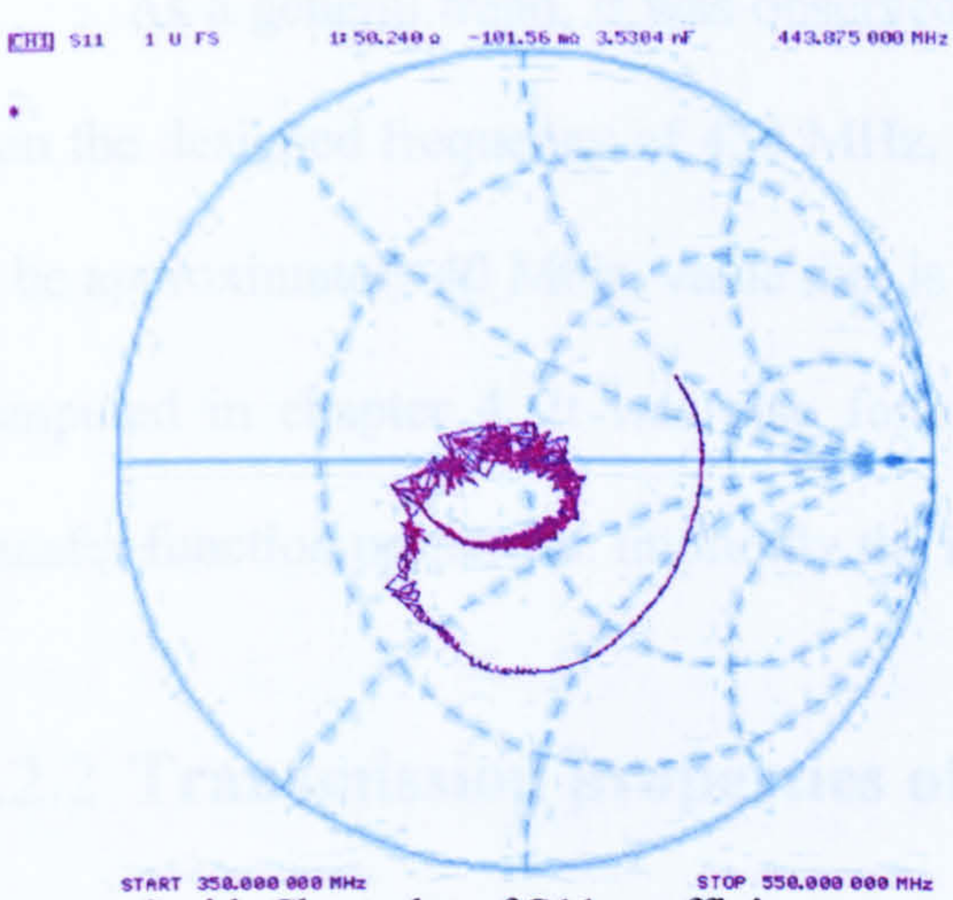

Smith Chart plot of S11 coefficient

c)

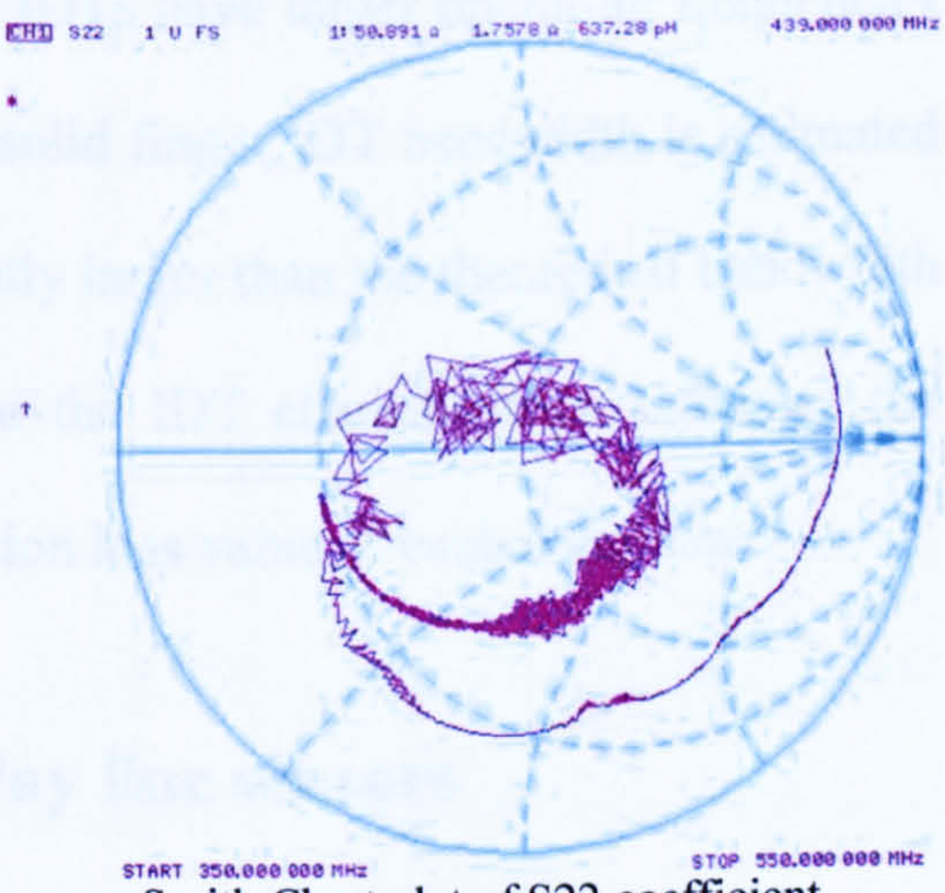

Smith Chart plot of S22 coefficient

d)

Figure 6.2: S11 parameter for the free delay line input IDT (a, c) and S22 parameter for the metallised delay line output IDT (b, d) of a SRL 280a sensor

Both S11 and S22 parameters of the input and output IDTs of SRL 280a show good return loss figure of 45 dB and 31.8 dB respectively (Figures 6.2 a and b). The Smith chart plots of these reflection coefficients show close match to the 50 Ω characteristic impedance: the input IDT has a 50.24 Ω impedance while the output IDT has a 50.89 Ω impedance, both having only very small reactive parts. These values suggest that no impedance matching circuitry is needed for the designed IDTs.

However, from the number of IDTs measured, it was found that the S11 and S22 parameters had a large IDT to IDT and device to device variability - the return loss figure was ranging from 6 dB to 55 dB. Most common return loss values were around 11 to 25 dB, while common IDT impedances were ranging roughly from 47 to 52 Ω. Possible reasons for IDT results variability can be found in the non-uniform fabrication process and/or in variations in the measurement set-up. High frequency devices are very sensitive to external interferences and particularly to the parasitic components of the measurement fixture (associated to the wire bonds or PCB), thus special attention needs to be given to the mounting conditions of the sensors.

As a general trend, it was observed that IDTs have larger operating frequencies than the designed frequency of 433 MHz. The solid finger IDT bandwidth is estimated to be approximately 40 MHz, value that is slightly larger than the theoretical bandwidth computed in chapter 4. It was also found that the IDT characteristics influence the transfer function properties, implicitly the insertion loss value of each delay line.

6.2.2 Transmission properties of delay line sensors

Transmission coefficient (T) is defined as the transmitted voltage (V_{trans}) divided by the incident voltage (V_{inc}). When $|V_{trans}| > |V_{inc}|$, the device is said to have gain and when $|V_{trans}| < |V_{inc}|$, the device under test exhibits attenuation or insertion loss, as is the case with the SH-SAW sensors.

The insertion loss is a scalar measure of the transmission coefficient and, when is expressed in dB a negative sign is added in the definition so that the loss value is expressed as a positive number:

$$IL(dB) = -20\log_{10}|T|$$

The phase portion of the transmission coefficient is called insertion phase. Both insertion loss and insertion phase values can be read directly from the network analyzer as S21/S12 parameters in log magnitude and phase format, respectively.

Among the numerous sensor configurations, several delay-line devices were chosen for electrical characterization. They were subsequently compared in terms of their insertion loss figures. Figure 6.3 shows pictures of the fabricated sensors selected for characterization along with their corresponding SRL codes. The selection included a SRL 207a sensor that had one metallised delay line and a totally free delay line. This device was compared to SRL 280a that had the same overall dimensions but presented a small opening in the path of the free delay line. Sensor SRL 208a had a totally free delay line 1 mm shorter than the free delay line of SRL 207a. SRL 208aa was then chosen due to its grating structure on the propagation path. Its free delay line was of the same length to that of the SRL 208a sensor, allowing thus for a direct evaluation of the effect of the grating on the SAW propagation. The metallised delay line was identical for all the four devices described so far. Finally, the SRL 208b sensor was chosen because it had an even shorter (3 mm) free delay line and 4 mm long metallised delay line.

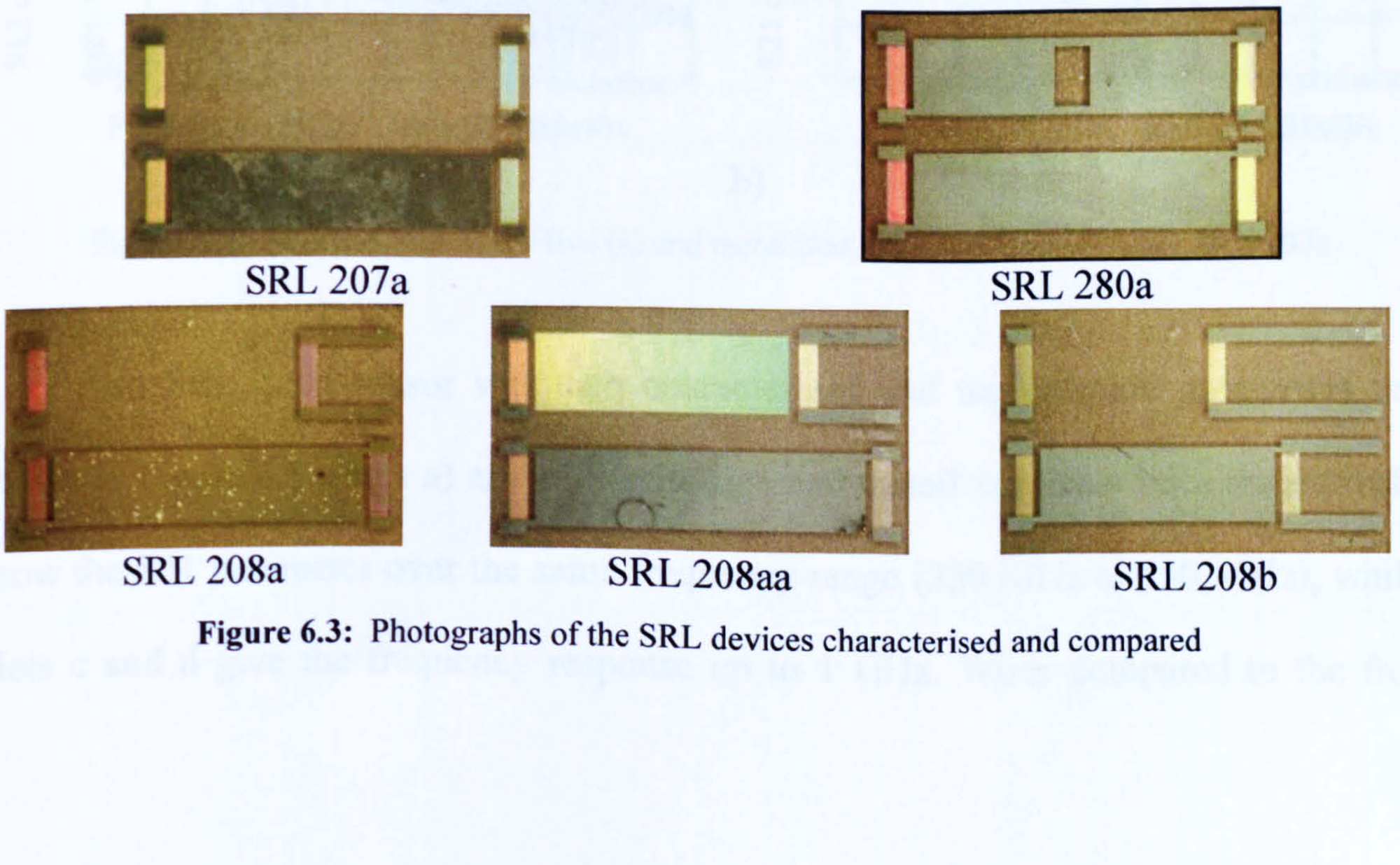

Figure 6.3: Photographs of the SRL devices characterised and compared

The first device to be characterized was SRL 207a and the transmission coefficients for free and metallised delay lines are shown in Figure 6.4. S21-parameters are measured over a 200 MHz bandwidth, where frequency is swept from 350 MHz to 550 MHz. The free delay line has a minimum insertion loss of 18.52 dB at 434 MHz. The transmission coefficient of the metallised delay line shows the effect of the metal layer on the propagation path: the acoustic waves are trapped to the surface and the delay line presents a lower insertion loss compared to the free line. For this device, a 11.89 dB insertion loss was observed at 451.5 MHz. The surface skimming bulk wave (SSBW) mode seems to be dominant on the free surface of the $LiTaO_3$ substrate. It has a higher attenuation but also a good out of band rejection. Metallisation of the propagation path increases the localization of the wave near the surface changing it to a SH-type leaky SAW [4] as observed in Figure 6.4b.

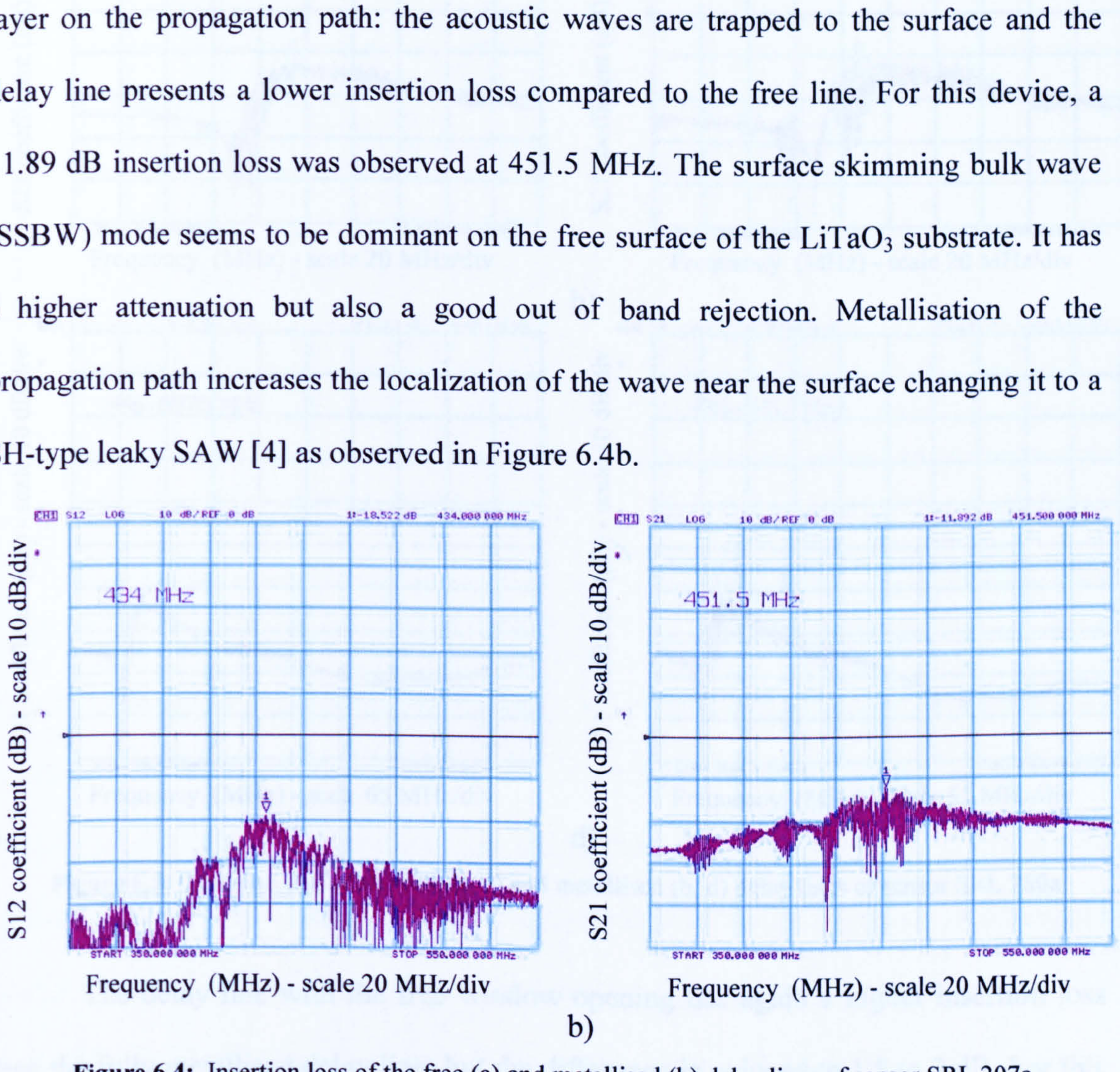

Figure 6.4: Insertion loss of the free (a) and metallised (b) delay lines of sensor SRL 207a

An SRL 280a sensor was then characterized and transmission parameters are shown in Figure 6.5. Plots a) and b) for the free and metallised delay lines respectively show the S21 parameter over the same frequency range (350 MHz to 550 MHz), while plots c and d give the frequency response up to 1 GHz. When compared to the free

delay line of RSL 207a, the S21 plots in Figure 6.5 shows that the delay line bandwidth is significantly increased when totally or partially metallising the surface.

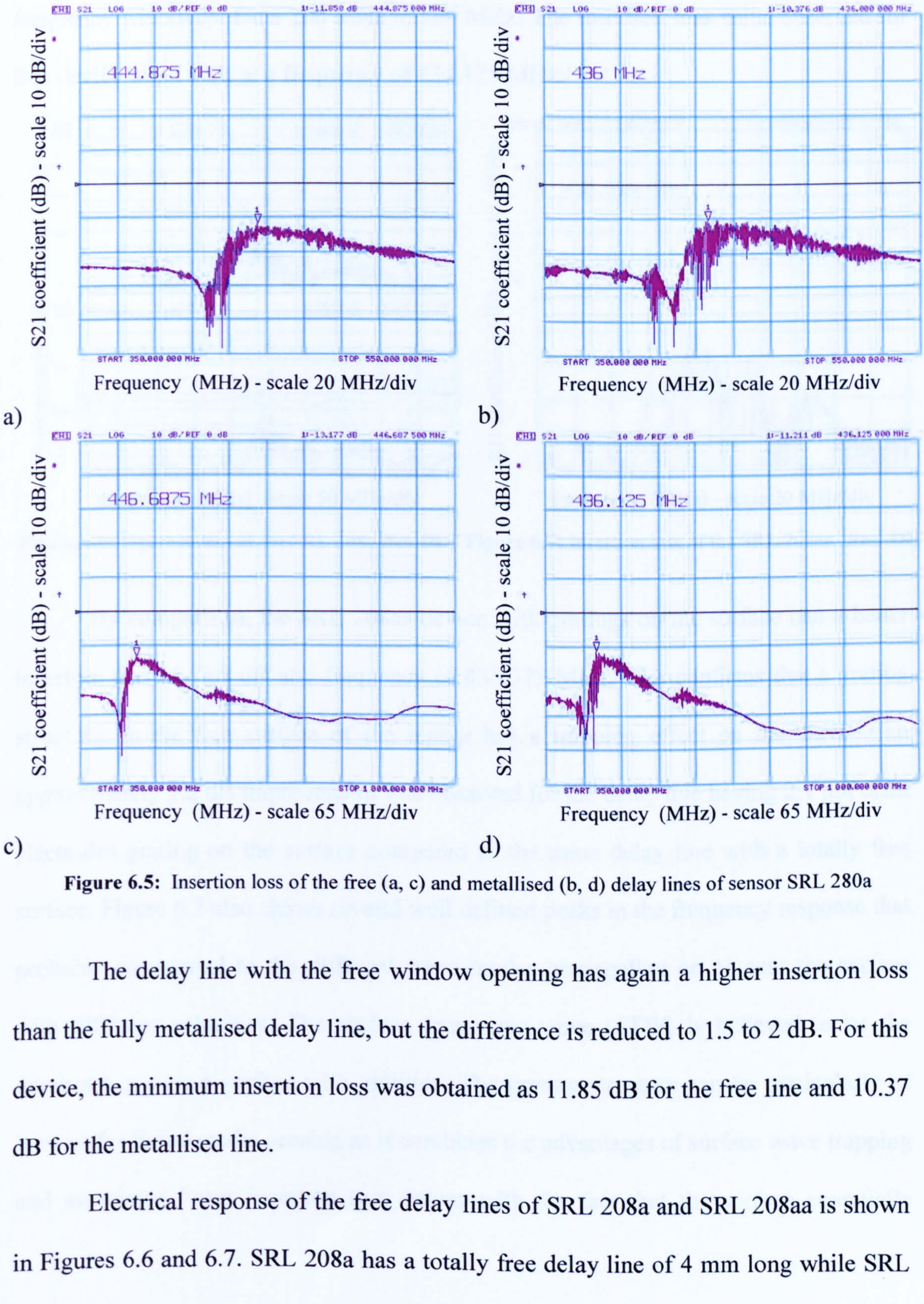

Figure 6.5: Insertion loss of the free (a, c) and metallised (b, d) delay lines of sensor SRL 280a

The delay line with the free window opening has again a higher insertion loss than the fully metallised delay line, but the difference is reduced to 1.5 to 2 dB. For this device, the minimum insertion loss was obtained as 11.85 dB for the free line and 10.37 dB for the metallised line.

Electrical response of the free delay lines of SRL 208a and SRL 208aa is shown in Figures 6.6 and 6.7. SRL 208a has a totally free delay line of 4 mm long while SRL

208aa has a grating structure (with electrodes 2.1 μm wide) on its 4 mm long free line. Figure 6.6 shows all the four S-parameters in a dual multichannel display format, where frequency was swept from 200 MHz to 700 MHz. The insertion loss value observed for this device was 16 dB at a frequency of 434.125 MHz.

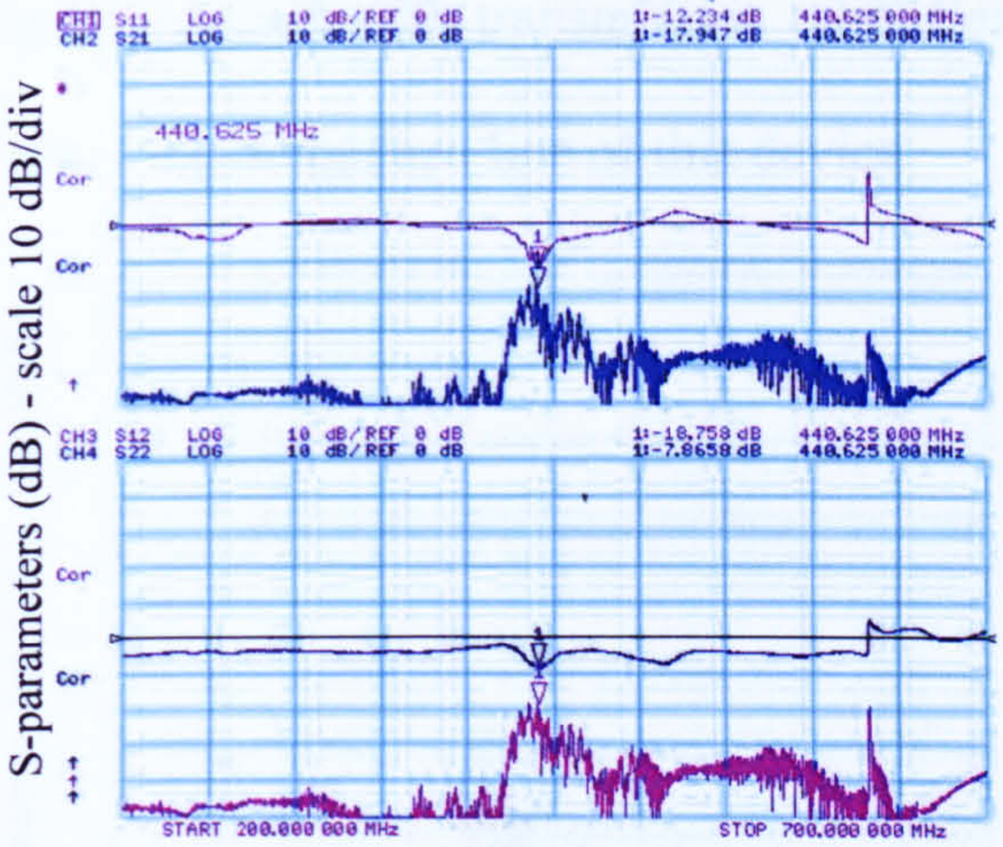

Figure 6.6: S-parameters of the SRL 208a free DL

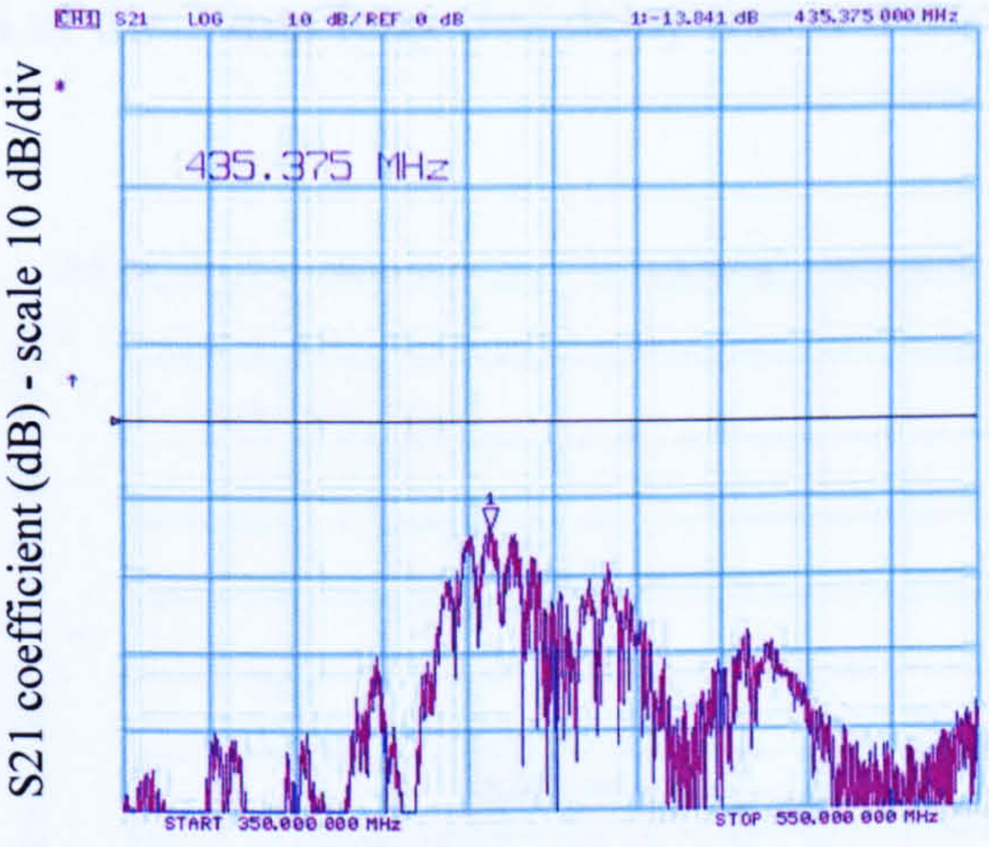

Figure 6.7: Insertion loss of the SRL 208aa 'free' DL

By comparison, the SRL 208aa device with gratings on the surface had a better insertion loss of 13.8 dB at a frequency of 435.375 MHz. This confirms that a grating structure on the free surface of the sensor has a trapping effect on the wave – an approximately 2.2 dB improvement was observed for the delay line having 2.1 μm open electrodes grating on the surface compared to the same delay line with a totally free surface. Figure 6.7 also shows several well defined peaks in the frequency response that probably correspond to the different wave modes propagating on or near the surface with different velocities. The surface transverse wave (STW) is believed to be the dominant one on a surface with gratings. The grating structure can be particularly of interest for liquid media sensing as it combines the advantages of surface wave trapping and associated lower insertion loss values with the fact that the surface essentially

remains electrically free and the wave electrical field can still extend into the liquid allowing for acousto-electrical interactions.

A final comparison was made using the SRL 208b sensor configuration. This device has both free and metallised delay lines 1 mm shorter than the ones in SRL 208a. Figure 6.8 shows the transmission coefficients of the 3 mm long free delay line and the 4 mm long metallised line of this device.

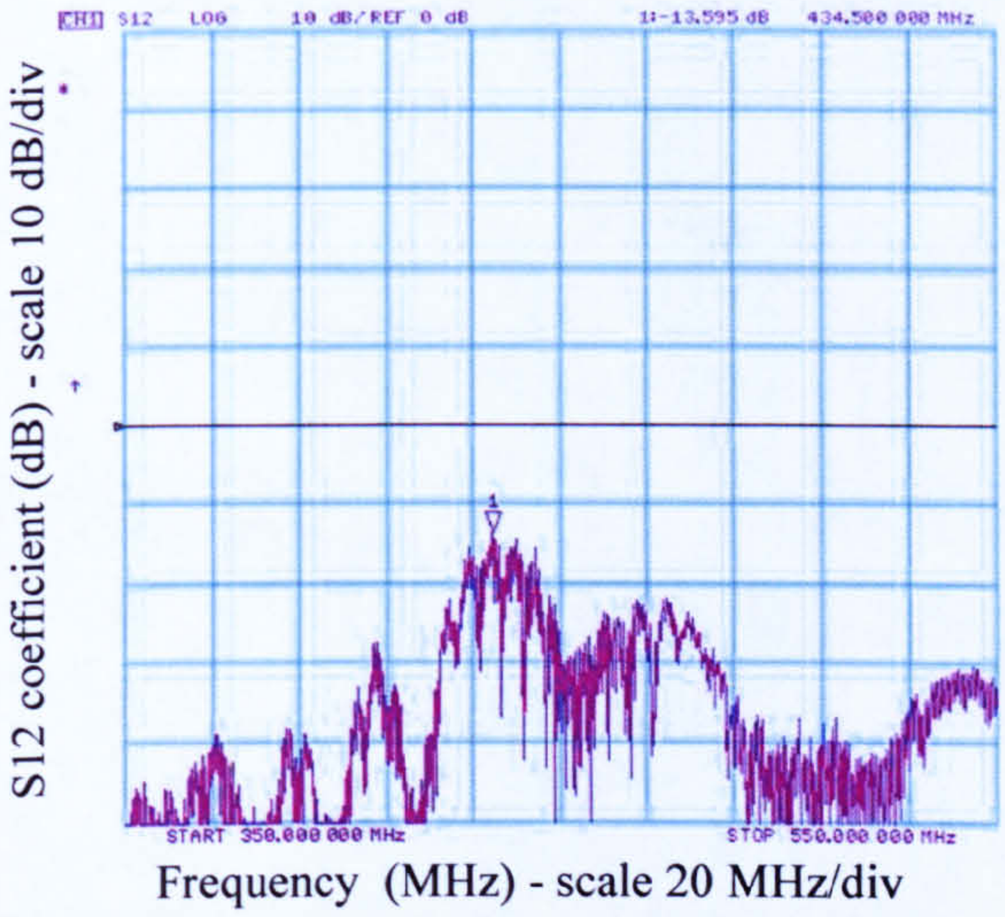

Figure 6.8: Insertion loss of the free (a) and metallised (b) delay lines of the SRL 208b sensor

The free delay line of SRL 208b shows an insertion loss of 13.59 dB at a frequency of 434.5 MHz. The metallised delay line had an insertion loss of 11.55 dB at a frequency of 439.375 MHz. A better transmission figure would have been expected for this delay line, but it was observed that its output IDT had a return loss value of only 6.5, thus influencing the overall delay line performance. Otherwise, the shape of the frequency response was similar to the ones for SRL 207a and SRL 280a.

A comparison between the free delay lines with different lengths allows an estimation of the attenuation per unit length. The results from SRL 207a, SRL 208a and SRL 208b are summarised in Table 6.1. Shortening the propagation path with 1 mm resulted in approximately 2.5 dB improvements in the insertion loss figure. This

corresponds to an attenuation constant of approximately 0.024dB per wavelength. This is an important result as it can be used for further optimization of the $LiTaO_3$ sensors.

Table 6.1: Free delay line insertion loss comparison

Free delay line length	5 mm	4mm	3mm
Insertion loss	18.52 dB	16 dB	13.59 dB

The metallised delay line insertion loss measurements showed fairly consistent results in terms of the frequency response. Some device to device variability has been observed (IL values varied between 10.37 and 11.89 dB) but it can be seen as a reflection of the imperfect variable conditions at the IDT blocks.

6.3 SAW SENSORS MEASUREMENT TECHNIQUES

6.3.1 Oscillator set-up

SAW sensors are most commonly used in oscillator configurations where the sensor serves as the feedback element that controls the oscillation frequency. Figure 6.9 shows a typical SAW sensor oscillator circuit, where an RF amplifier connects the two IDTs on the piezoelectric substrate so that oscillations result due to the feedback of the SAW propagating from one IDT to the other. For stable oscillation the phase shift of the loop must equal $2\pi n$, where n is an integer. The oscillation frequency varies with SAW velocity and distance between the IDTs [5].

Measuring the oscillator frequency accurately, small changes in the properties to be measured can be detected. Frequency provides the simplest and most cost-effective solution for processing the SAW sensor's response, but it lacks the capability to provide information regarding the signal amplitude. Furthermore, for operation in liquid media with heavy loading conditions, oscillations may cease and automatic gain control

techniques must be implemented, thus adding to the complexity of the measurement system.

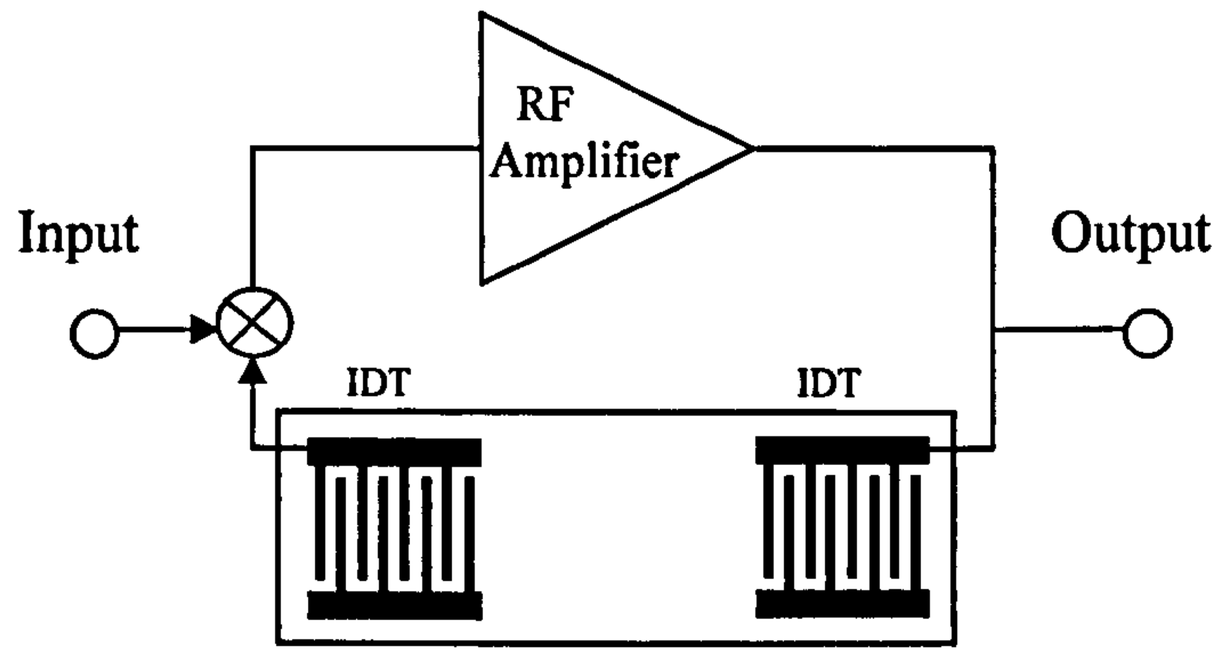

Figure 6.9: Diagram of a SAW device oscillator circuit

6.3.2 Vector voltmeter measurement system

The vector voltmeter is an instrument that can measure RF amplitude (voltage) and relative phase angle between two signals. One signal serves as the reference for the measurement of the other. The common outputs of the vector voltmeter are the phase difference as well as the ratio, difference or individual values of the amplitudes of the two signals.

For measurements on the SH-SAW sensors, a HP 8508A vector voltmeter was used in conjunction with a HP 8648C signal generator. Two measurement configurations were used. In the so called Input/Output configuration a 'T' connector was used to supply the generator signal to both input IDT and the reference port of the vector voltmeter; the other port was connected to the output IDT of the sensor, thus measuring directly the wave attenuation and phase for each delay line. The second configuration was a differential one, and was used for the SRL 208a dual delay line

sensors: the output signal from one delay line was taken as reference for the signal on the other delay line.

6.3.3 Network analyser as measuring system

The network analyser was used both for electrical characterization of the sensors and also for measurements in liquid media. The complex transmission coefficient was providing the wave amplitude (in terms insertion loss) and phase information needed for the liquid classification and identification. The network analyser is a very expensive non-portable piece of equipment that is impractical and too cumbersome for general-purpose measurements. However, it is a valuable investigation tool in exploratory research, delivering very detailed information on a number of important parameters.

6.3.4 Wireless set-up

SAW devices also have the capability to operate remotely in a wireless set-up. A wireless sensing system is composed of a passive SAW device connected to a small antenna and an interrogation unit (transceiver) that sends and receives measuring signals. A diagram depicting the principle of operation of this wireless system is shown in Figure 6.10. In this, the electromagnetic waves picked up by the device antenna are applied to the IDTs that convert the electric signals into acoustic waves which in turn propagate along the sensors' surface. Two sets of reflectors are designed to bounce back the acoustic waves and when the waves reach the IDTs again, the converse mechanical to electrical transduction takes place. Then the antenna sends back to the interrogation unit a signal that contains the sensor's response.

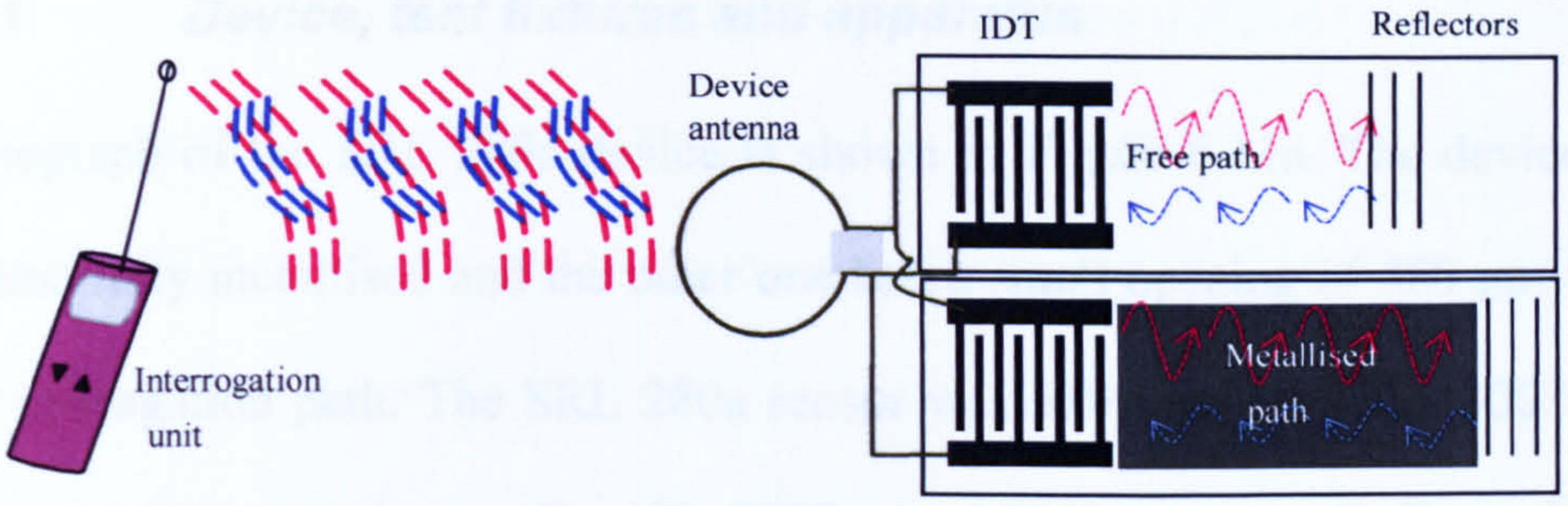

Figure 6.10: Block diagram of the wireless SAW system

The sensing principle employed is the same as for the wired configurations and is based on the interaction between the liquid and the shear horizontal polarized wave mode. The liquid under test perturbs the acoustic waves and hence changes the wave attenuation and phase velocity, which results in a time delay of the signals.

6.4 EXPERIMENTAL RESULTS

A set of experiments were conducted on selected devices. Chosen configurations included SRL 280a, SRL 285, SRL 208a and SRL 273. The first three configurations were exposed to synthetic basic taste solutions. Liquid solutions containing dispersed micro-particles were used for testing the voltage-modulated SRL 273 sensor. Experimental set-up is described for each sensor and samples of obtained test results are presented below.

6.4.1 **Dual delay line sensor SRL 280a**

Low frequency (60 MHz) dual delay line SH-SAW sensors were previously successfully employed to identify liquid solutions in the Sensor Research Laboratory (SRL), University of Warwick [6-8]. The SRL 280a devices are the high frequency correspondents of those low frequency devices, having the similar layout configuration. These sensors were among the first ones to be tested with liquid samples.

6.4.1.1 Device, test fixtures and apparatus

A photograph of the SRL 280a device is shown in Figure 6.11a. The device had one delay line fully metallised and the other one had a small opening of 480 μm × 800 μm on the propagation path. The SRL 280a sensor was 5100 μm long and 3000 μm wide and was accommodated on a die with 5500 μm × 3500 μm overall dimensions. After fabrication the sensors were mounted and ultrasonically wire bonded onto custom PCB boards with SMA connectors as interface with the measuring equipment. A miniature MSL (micro-stereolithography) liquid cell (designed and fabricated using the Envisiontec Prefatory rapid prototyping system) was then attached to the sensor surface. The liquid cell had its 800 μm wide flow channel sitting transversally on top of both delay lines, covering the opening in the free delay line (top in Figure 6.11a). A picture showing attachment of the liquid cell onto the dual delay line senor is shown in the Fig. 6.11b. Inlet and outlet tubes were attached to the liquid cell so that the test samples could be supplied to the sensing area of the device.

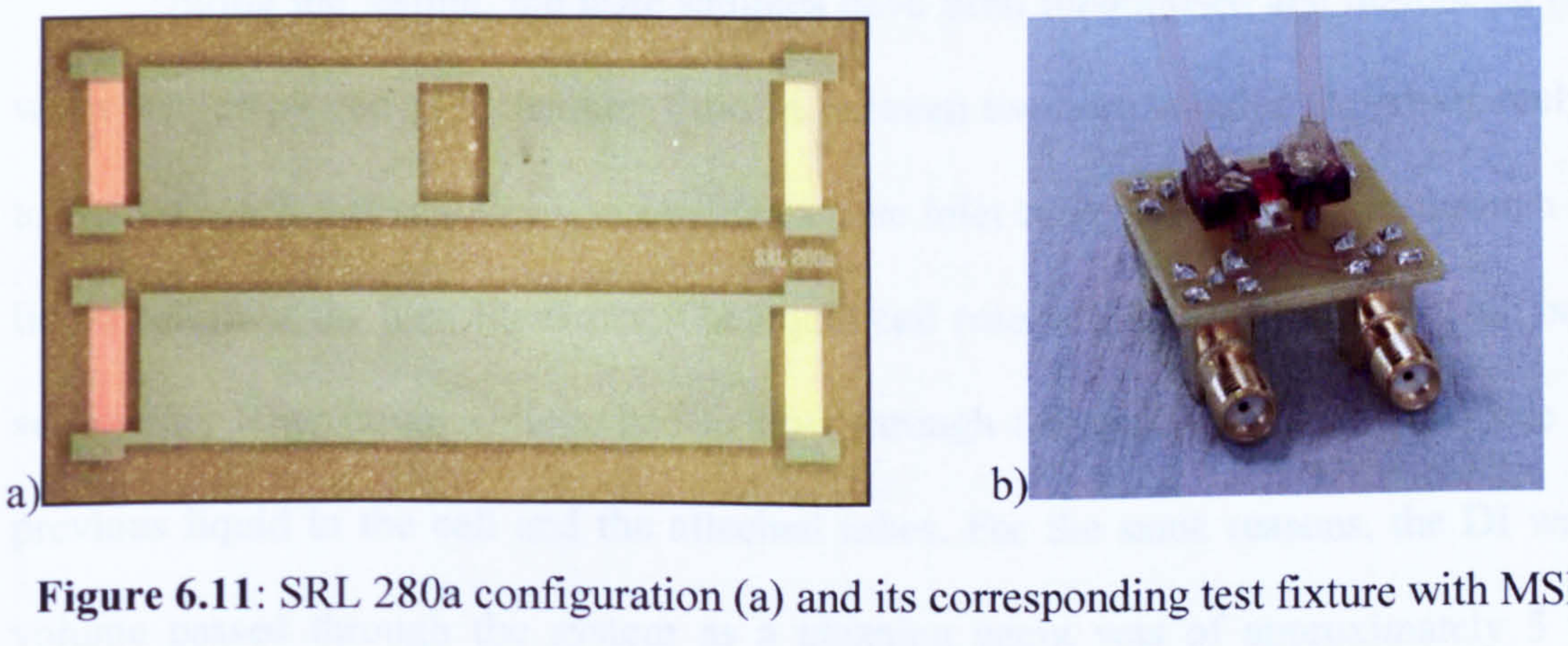

Figure 6.11: SRL 280a configuration (a) and its corresponding test fixture with MSL liquid cell (orange part) on top (b)

During the liquid samples measurements, a signal generator - vector voltmeter set-up was used. A HP 8648C signal generator was used to excite the SH-SAW wave and a HP 8508A vector voltmeter was employed to record the attenuation and phase parameters of both delay lines. For the particular SRL 280a device considered for liquid

measurements, the frequency response of both delay lines indicated minimum insertion loss for frequencies between 449 to 468 MHz. A common operating frequency was chosen for both delay lines - the signal generator was set to 460.84 MHz as this was the trade-off frequency for which both delay lines had reasonable insertion loss values (with the liquid cell mounted on top, the device had approximately 12.7 dB and 15.6 dB IL values).

6.4.1.2 Tests and results

Aqueous solutions representing different tastes were prepared as liquid test samples. Four samples representing the basic tastes of saltiness, sweetness, sourness, and bitterness have been chosen for the tests on the SRL 280a delay line configuration. Saline, sucrose and acetic acid solutions were prepared with concentrations of 0.1 mol while the quinine sulfate solution had a 0.0012 mol concentration. Quinine sulfate has a very low solubility in water that dictated the lower concentration of this sample.

During the testing, the taste samples have been randomised and de-ionised (DI) water was employed as a cleaning fluid in between two test samples. Approximately 2 to 3 ml of each test samples was injected in the inlet tube and were flown through the liquid cell prior the measurements. The liquid cell reservoir had a volume of 1 µl, but a sufficiently large liquid volume had to flow through the system to totally displace the previous liquid in the cell and the attached tubes. For the same reasons, the DI water volume passed through the system as a cleaning agent was of approximately 5 ml. Amplitude and phase measurements where then taken when the test liquid sample was stationary on the sensor surface.

A Dri-Bloc™ (DB-2D) heater accommodated the test fixture during the measurements so that tests were performed at (35±0.1)°C temperature controlled

environment. The DI water and liquid taste samples were also kept in a similar block heater at the same temperature before being supplied to the sensor.

Amplitude and phase information have been recorded for each delay line and their relative difference was computed and scattered plotted in Figure 6.12.

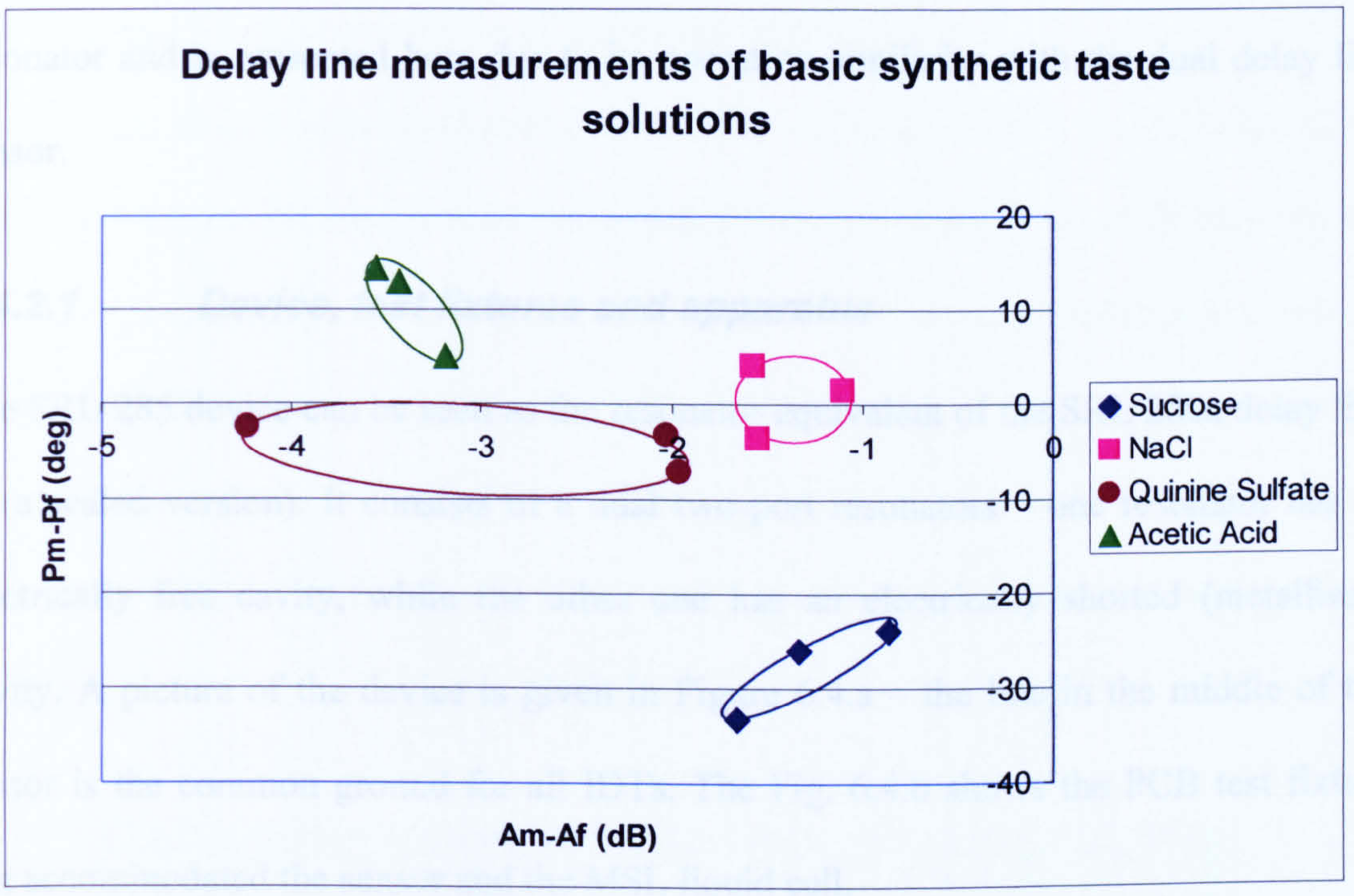

Figure 6.12: SRL 280a delay line measurements of four basic taste solutions

By plotting the data in differential amplitude and phase coordinates, Figure 6.12 gives a measure of the acousto-electric effect each sample had on the SH-SAW sensor, showing that liquid classification can be achieved based on this principle. Quinine sulfate had more variability in amplitude then the rest of the basic taste samples but that is attributed to the significantly lower concentration of the sample (0.0012 mol). The liquid samples with 0.1 mol concentration clustered better and wide apart from each other. Overall, a 100% discrimination has been achieved for all solutions, suggesting that pattern recognition methods can be used to classify and identify samples measured with the delay line SH-SAW sensor.

6.4.2 **Dual resonator sensor SRL 285**

In addition to delay line sensors, taste tests have also been performed on two resonator configurations: devices SRL 283 and SRL 285. Chapter 7 is dedicated entirely to the SRL 283 two-port resonator and discusses its results. Sensor SRL 285 is a dual two-port resonator and is presented here due to its operation similarity with the dual delay line sensor.

6.4.2.1 Device, test fixtures and apparatus

The SRL 285 device can be seen as the resonator equivalent of the SRL 280a delay line (in a scaled version). It consists of a dual two-port resonators – one resonator has an electrically free cavity, while the other one has an electrically shorted (metallised) cavity. A picture of the device is given in Figure 6.4.a – the line in the middle of the sensor is the common ground for all IDTs. The Fig. 6.4.b shows the PCB test fixture that accommodated the sensor and the MSL liquid cell.

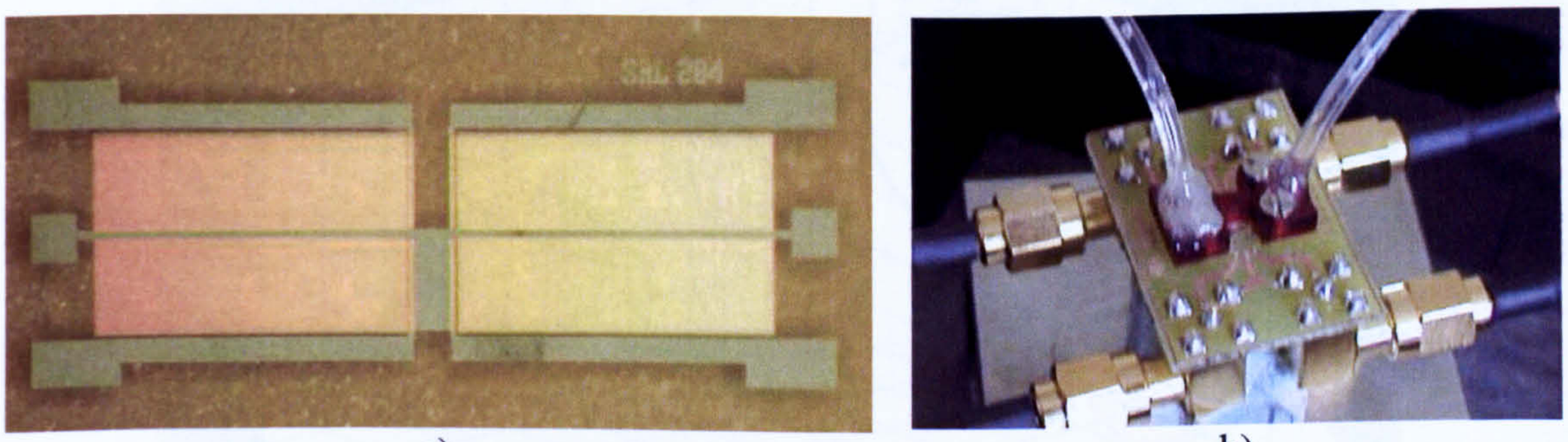

a) b)

Figure 6.13: Dual two port resonator (a) and its test fixture with MSL liquid cell (b)

The device had a minimum insertion loss at a frequency of 860 MHz and this frequency was chosen for liquid sample measurements. Amplitude and phase data were recorded from the vector voltmeter for each of the resonator cavities (free and metallised).

6.4.2.2 Tests and results

The two port resonator was also exposed to basic taste solutions. Test samples consisted again of 0.1 mol sucrose, NaCl and acetic acid solutions . The bitterness taste sample was this time implemented with quinine hydrochloride which had higher water solubility and allowed preparation of a solution with 0.01 mol.

Experiments were conducted in a similar way and set-up to the delay line tests. Samples were randomised and DI water was flowed as cleaning agent in between test samples. Measurements were also taken for DI water and included in the plotted results. Amplitude and phase data from the two resonator cavities were analysed using a principal components analysis (PCA) technique. The PCA plot is given in Figure 6.14 and results show a satisfactory discrimination between the four tastant samples and the DI water.

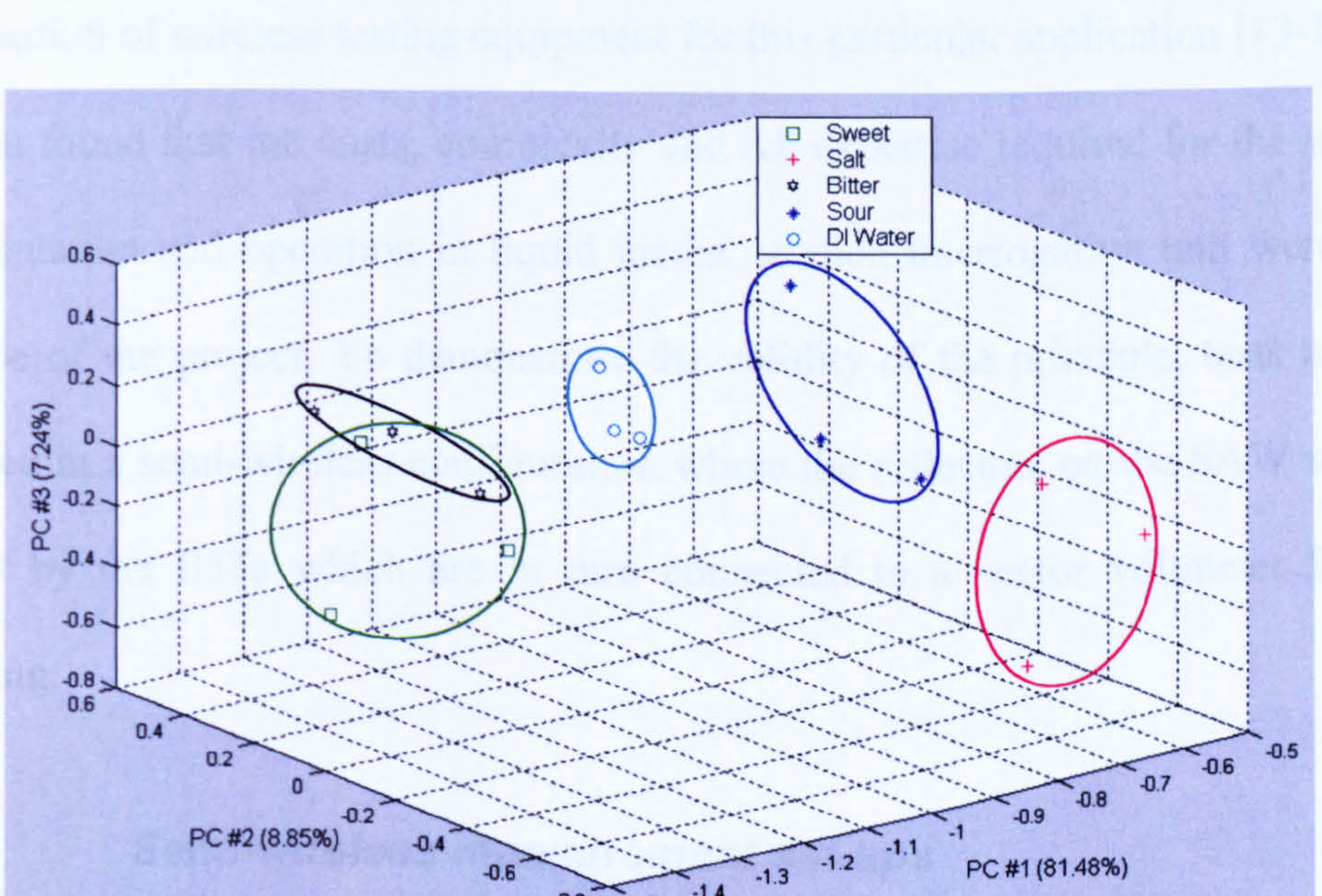

Figure 6.14: PCA plot of the basic taste solutions measure with SRL 285

The SRL 285 resonator results re-confirms the SH-SAW devices ability to work as simple electronic tongue sensors. So far devices have been tested in 'wired' set-ups.

The next sub-section details the SH-SAW operation in a semi-wireless measuring set-up.

6.4.3 Semi-wireless sensor

SAW sensors have proved their potential to work as passive components in several wireless applications [9-11]. Similarly, the SH-SAW liquid sensors also present capabilities for wireless sensing [5, 12]. However, despite the simplicity of the operation principle described in section 6.3.4, the implementation of a fully wireless system for liquid analysis is far from being a straight-forward task. Wireless operation in liquid media requires high-frequency ultra high speed equipment with high resolution and large data processing capability. Commercial transceivers do not offer the full specifications required for a SH-SAW liquid sensor. Attempts have been made towards customisation of wireless testing equipment for this particular application [13-15], but it was soon found that the costs, complexity and RF expertise required for the successful implementation and operation in liquid media of such interrogation unit were beyond the scope of the project. To demonstrate the validity of the principle, tests have been conducted in a semi-wireless configuration where the reflectors on the SAW sensor are replaced by the IDTs which are in turn connected to a vector voltmeter for signal processing.

6.4.3.1 Semi-wireless measurement set-ups

The device employed for semi-wireless tests was the SRL 208a. This sensor configuration was designed with the free delay line 1 mm shorter than the metallised one. SRL 208a had the same layout configuration as the wireless sensors SRL 199, SRL 200 and SRL 201 except that the reflectors are substituted with output IDTs. The 1 mm

shorter delay line of the wireless sensors ensured separation in time between the two reflected wave signals.

The SRL 208a was wire-bonded onto a small custom PCB connected via pins to a mother-board measurement fixture with SMA connectors (Figure 6.15). A picture of the fabricated sensor mounted on the measurement fixture and having a small loop antenna attached to its input IDTs is shown in Figure 6.15 The set-up made use of a T connector and three inter-series adaptors (SMA to BNC). The attenuation introduced by the adaptors serialization is expected to be low as they were all matched to the 50 Ω characteristic impedance.

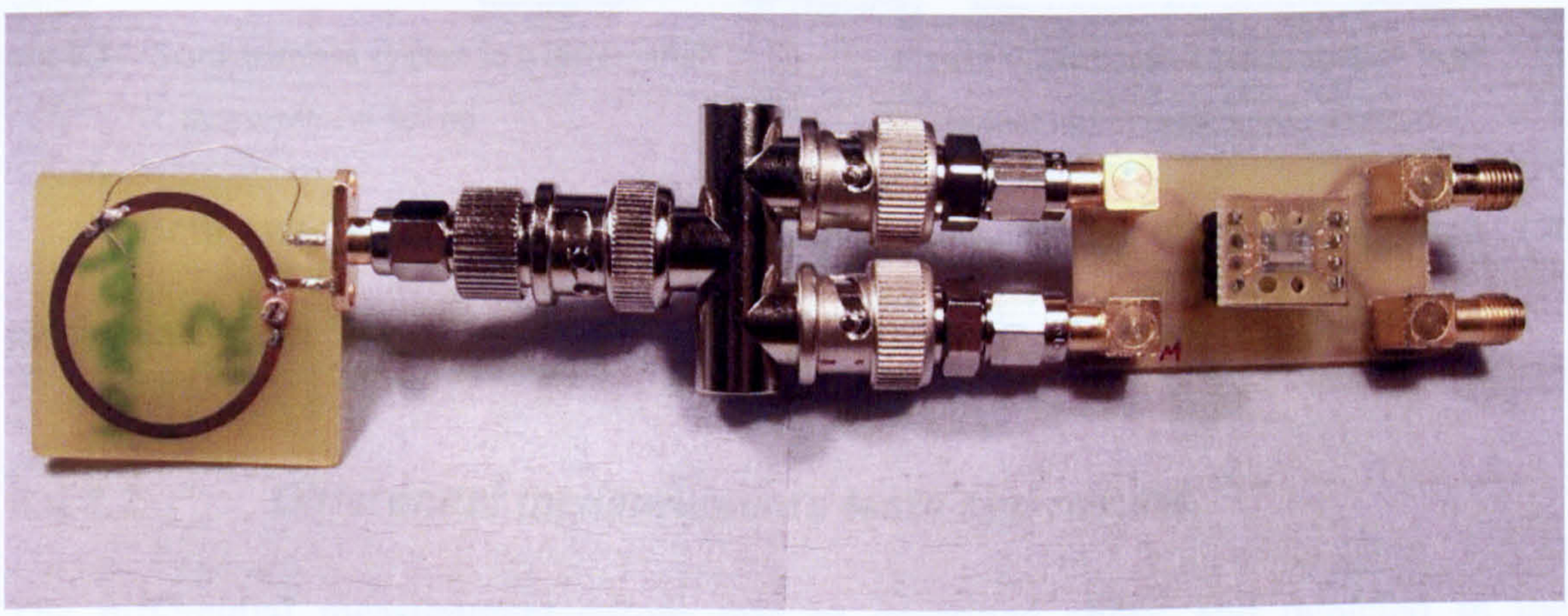

Figure 6.15: Loop antenna and test fixture for semi-wireless set-up

For the semi-wireless tests, two measurement set-ups were used, a differential one and an Input/Output one. For both of them an RF continuous wave signal was connected to a transmitting antenna: the sensor input IDTs were connected to a receiving antenna and the sensor output ITDs to a vector voltmeter. If both vector voltmeter cables are connected to the sensor's output ITDs, a differential measuring configuration is realized (Figure 6.16) - the signal from one delay line is taken as the reference for the other delay line and the vector voltmeter displays directly the amplitude and phase difference between the two delay lines. An alternative way of

collecting data related to the liquid-SAW interactions is via absolute measurements on each delay line. In this Input/Output configuration (Figure 6.17) the reference cable is connected to the receiving antenna and input IDTs, and the other cable is connected successively to the output IDT of each delay line. In this configuration attenuation and phase of each delay line are measured relatively to the device input signal supplied from the antenna.

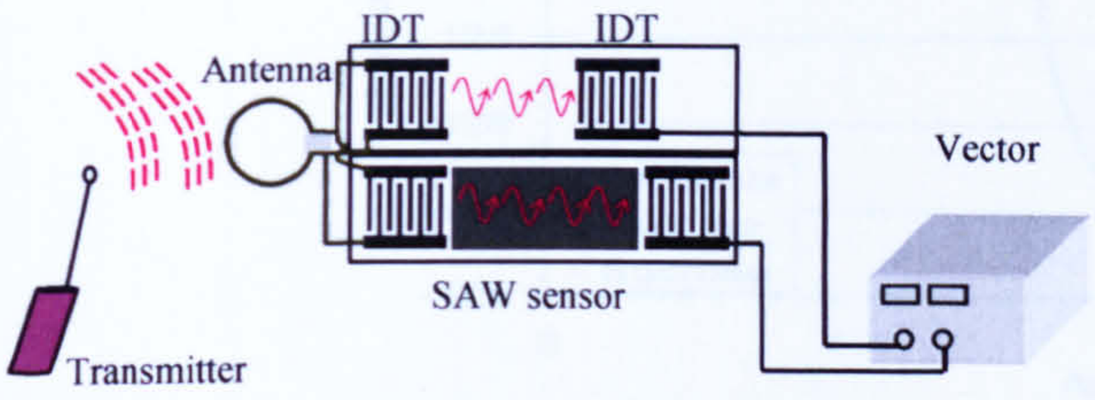

Figure 6.16: Semi-wireless system in a differential measurement set-up

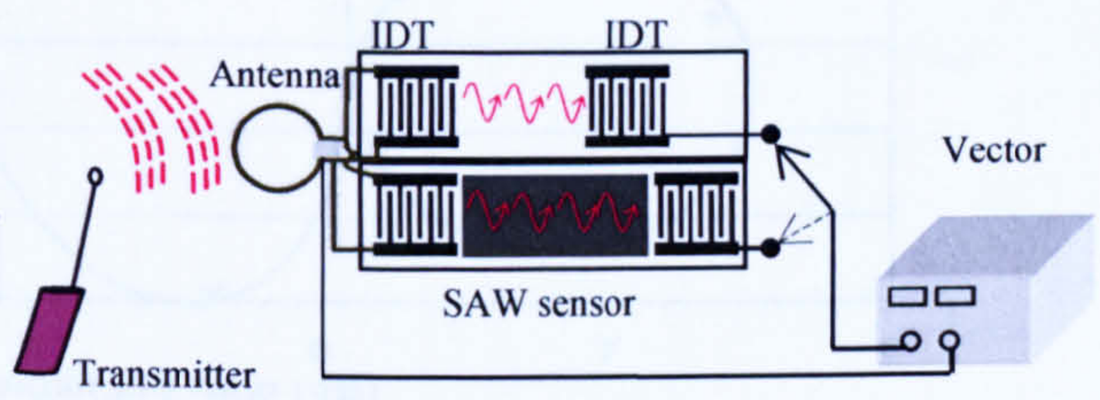

Figure 6.17: Semi-wireless system in an Input/Output measurement set-up

Both set-up differential and Input/Output configurations were used for measurements on SRL 208a sensor and sample results are presented in each case.

6.4.3.2 Differential measurements tests and results

The differential measurement set-up was as described above and depicted in the schematic diagram in Figure 6.12. A 433.9 MHz signal with a 5 V amplitude was supplied to the transmitting antenna. The receiving antenna was positioned 1 m away and its output signal had peak-to-peak amplitude of 1.45 V. A liquid cell was mounted on top of the SRL 208a sensor and preliminary liquid tests were performed. The sensing mechanism is based on differential amplitude and phase measurements taken between the two delay lines. The liquid information is then extracted from the relative magnitude and phase data.

Preliminary tests with sucrose 0.1 mol solution, quinine 0.0012 mol solution and de-ionized water were carried out in this configuration. Figure 6.18 plots the differential amplitude and phase data recorded from the vector voltmeter.

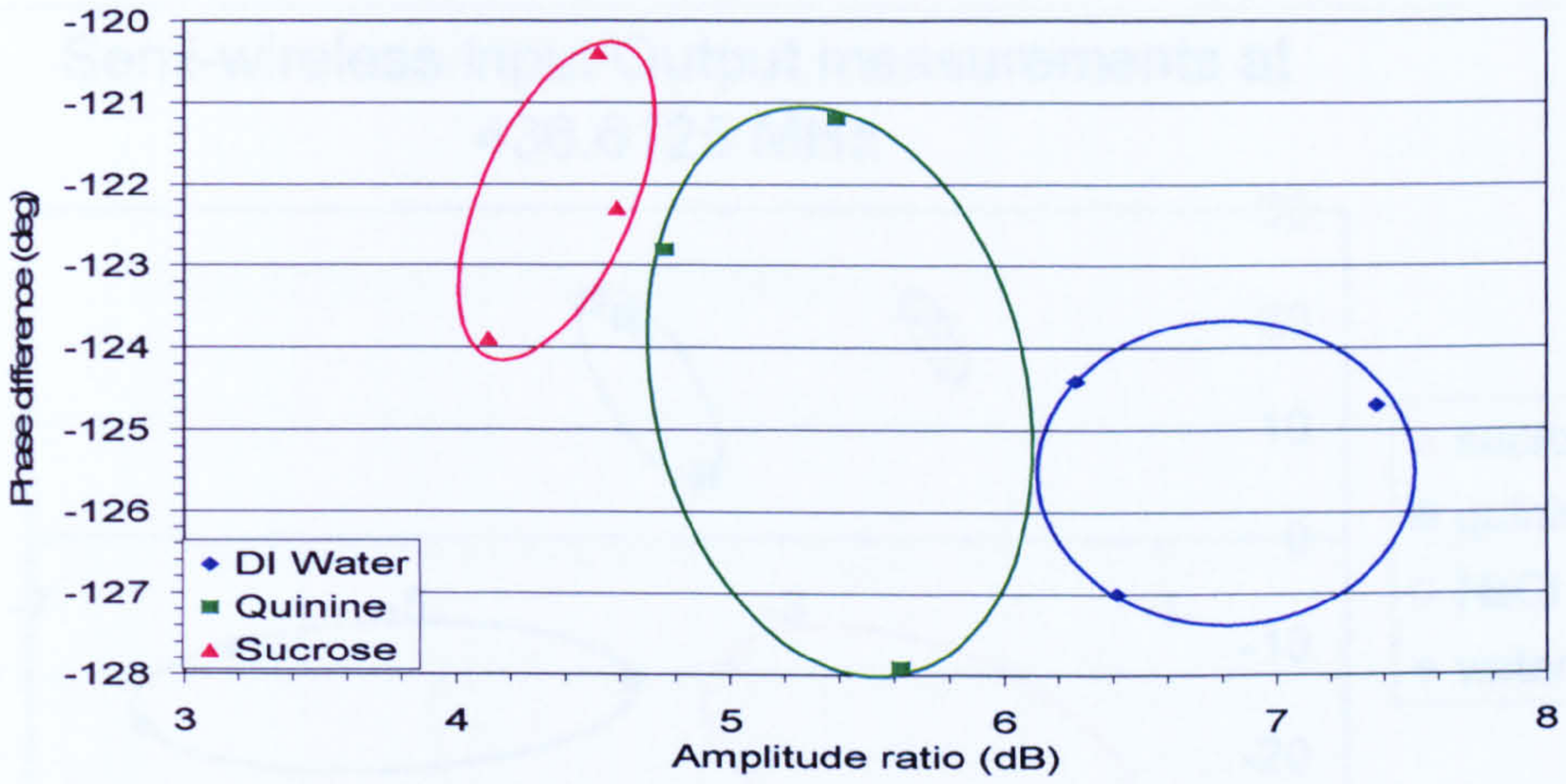

Figure 6.18: Semi-wireless data plot for water, quinine and sucrose solutions

The plotted data are a direct measure of the acousto-electric properties of the tested samples. The results show satisfactory linear discrimination between the two tastes (sweet and bitter) solutions and the DI water included in tests as a reference sample. Further experiments were made by taking Input/Output amplitude and phase measurements for each delay line.

6.4.3.3 Input/Output measurements tests and results

Figure 6.17 depicts the connecting diagram of this set-up: the reference port of the vector voltmeter was attached to the receiving antenna also connected to the sensor's input IDTs; the measuring port was connected in turn to the output IDT of each delay line. A 436.6125 MHz frequency corresponding to the minimum IL on the free delay line was chosen for operation of this semi-wireless set-up.

Three basic taste samples representing the sweetness, bitterness and saltines taste sensations were considered this time for experimentation. They were implemented

with sucrose, quinine sulphate and sodium chloride, and had respective concentrations of 0.1 mol, 0.012 mol and 0.1 mol. Taste samples were supplied to the sensor in a random sequence and DI water was included as a fourth test sample.

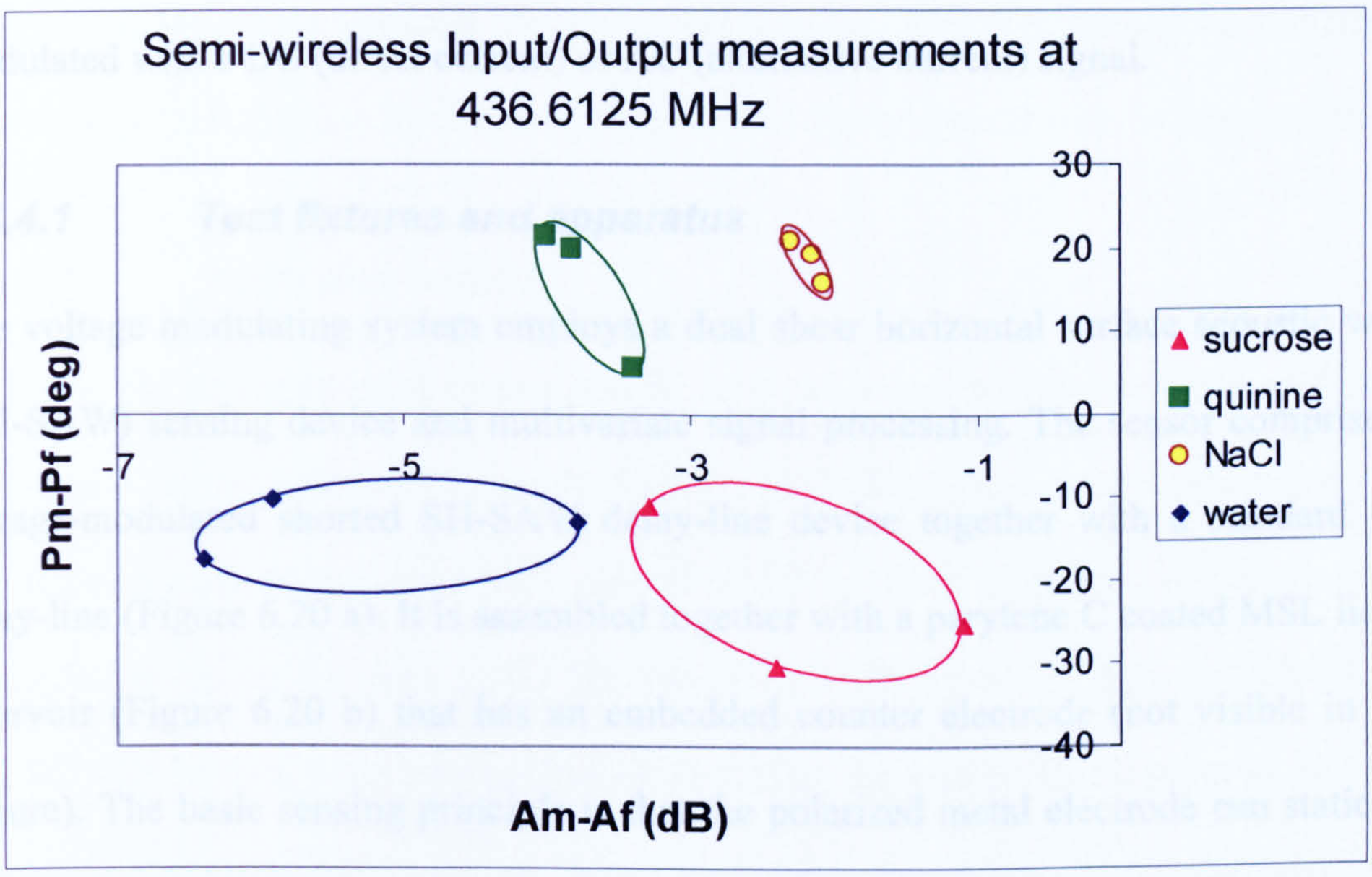

Figure 6.19: Semi-wireless data plot at 436.6125 MHz (Input/Output measurements)

Figure 6.19 gives a graphical representation of the obtained results in differential amplitude and phase coordinates. A good discrimination between the tested samples is observed and a better cluster separation is achieved for this semi-wireless operation mode.

Despite the fairly large variability in the measured data, the semi-wireless results prove that liquid identification can be achieved by remote excitation of the SH-SAW sensors. For operation in a truly wireless set-up, the sensors need to be more stable, less lossy and require a fine tuning of the operation frequency.

6.4.4 **Voltage modulated sensors**

Another class of SH-SAW devices designed and considered for experimentation was the voltage modulated one. It employs a novel operation principle where one delay line is modulated with a DC (direct current) or AC (alternative current) signal.

6.4.4.1 Test fixtures and apparatus

The voltage modulating system employs a dual shear horizontal surface acoustic wave (SH-SAW) sensing device and multivariate signal processing. The sensor comprises a voltage-modulated shorted SH-SAW delay-line device together with a standard free delay-line (Figure 6.20 a). It is assembled together with a parylene C coated MSL liquid reservoir (Figure 6.20 b) that has an embedded counter electrode (not visible in this picture). The basic sensing principle is that the polarized metal electrode can statically or electrokinetically attract bioparticles in the liquid, which perturb the acoustic waves, thus changing their phase velocity and attenuation.

A custom designed PCB has been used to mount the SH-SAW sensor and a micro-stereolithography (MSL) liquid cell has been attached onto it. The bottom of the liquid cell reservoir has been sputtered with gold and used as the top counter electrode.

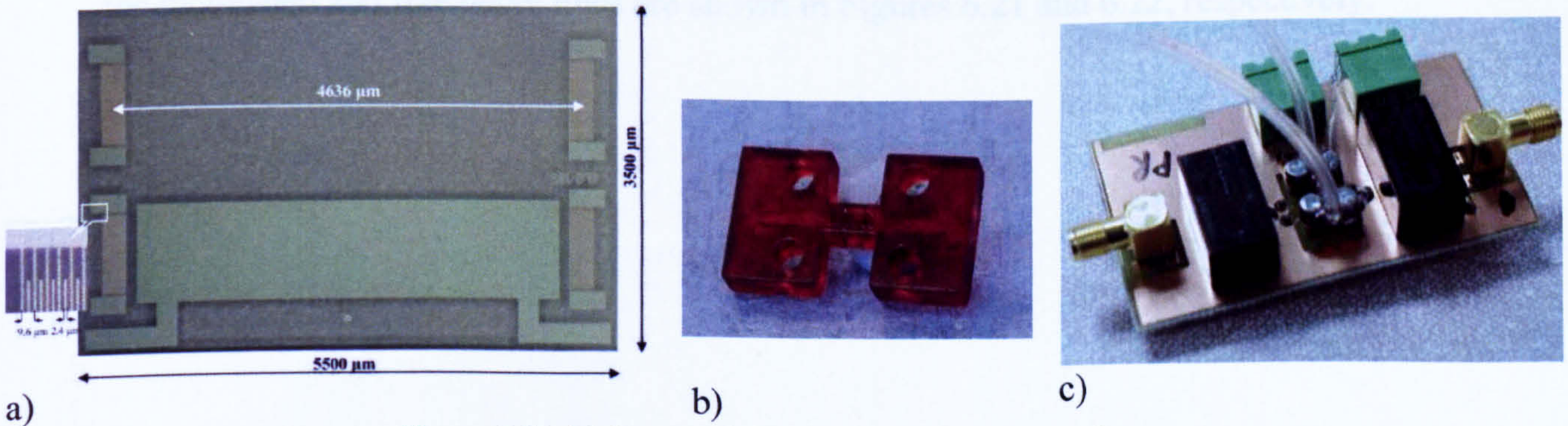

a) b) c)

Figure 6.20: Voltage modulated components and test fixture

Measurements have been performed using a network analyser (Agilent 8753ES) and amplitude and phase information has been recorded for both the free and the voltage

modulated delay line. The switching between the two delay lines was realized by two high frequency relays (Omron G5Y-1) that have been integrated onto the custom PCB. A set-up of the testing board with the SMA connectors, the relays and the MSL cell mounted on top of the sensor is shown in Figure 6.20c. Two 9 V batteries connected in a switching configuration have been used to modulate the sensor with both polarities.

6.4.4.2 Tests and results

To prove the principle of operation, initial tests were carried out with suspensions of sub-micron carbon black (CB) pearls (Cabot, BP 2000) in water and isopropanol (IP). The initial measurements have been carried out at the fixed frequency of the minimum insertion loss in air for each delay line (453.075 MHz for the voltage-modulated one and 445.725 MHz for the free one). Before testing the carbon black samples, the first measurements were performed on pure isopropanol and water, and these have been taken as a reference. The modulating sequence used was (0 V, +9 V, 0 V, –9 V, 0 V) and data have been recorded for each of this voltages. Following this step, samples with the carbon black added to water and IP solutions were applied to the sensor and data recorded. The influence of the DC voltage on both the attenuation and phase values of the modulated and free delay lines are shown in Figures 6.21 and 6.22, respectively.

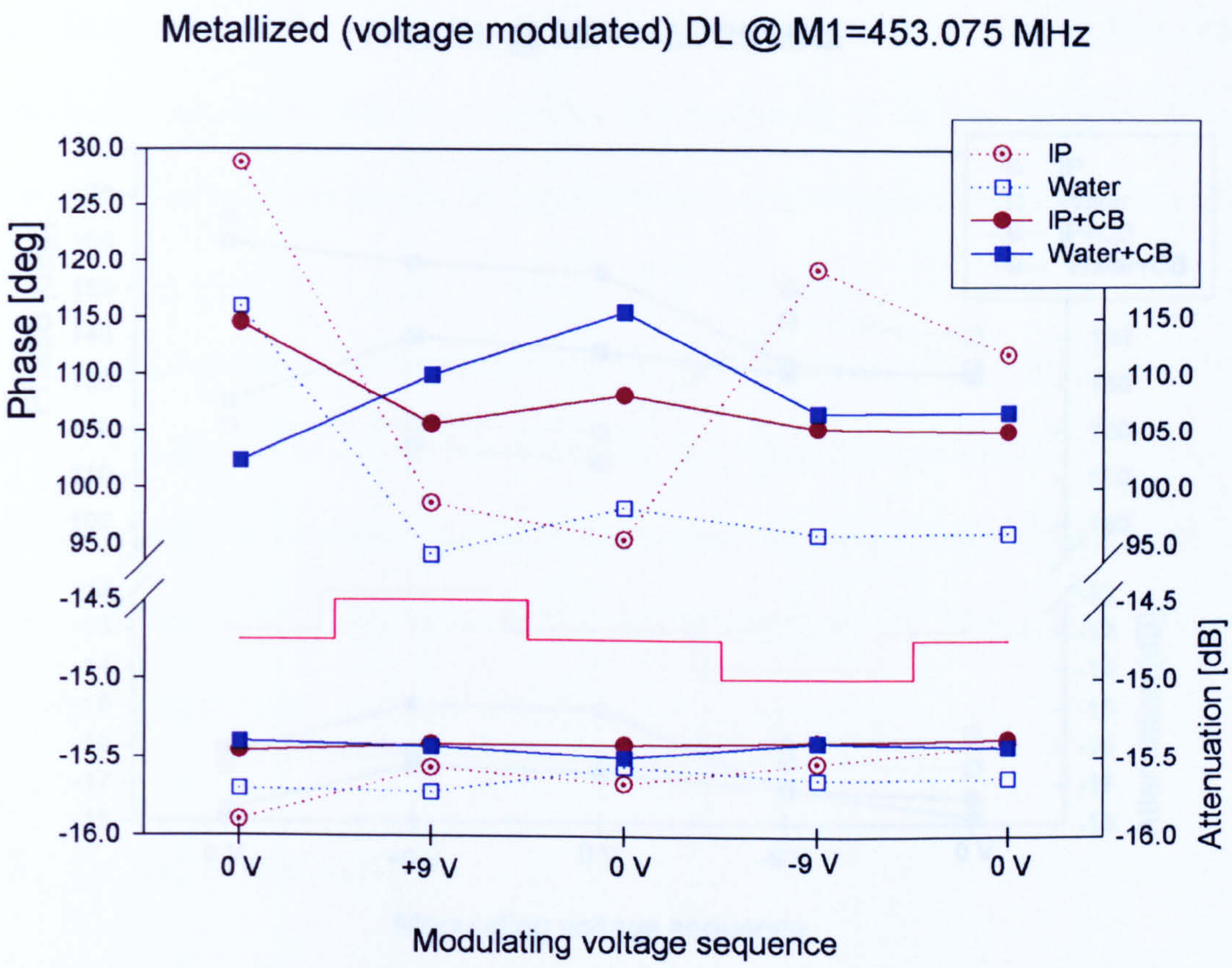

Figure 6.21: Amplitude and phase variations observed on the voltage modulated delay line

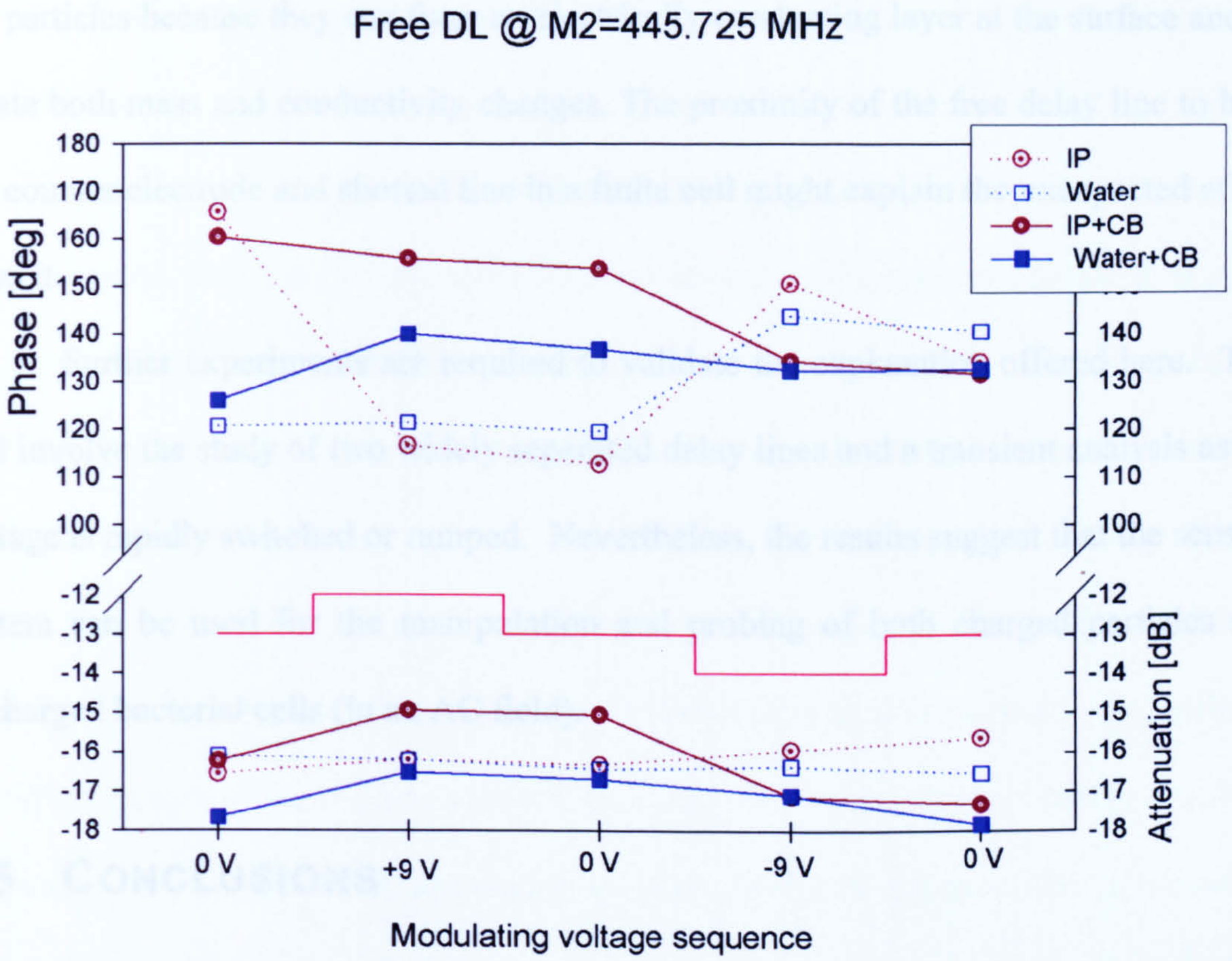

Figure 6.22: Amplitude and phase variations observed on the free delay line

Clearly, an effect has been observed for both the shorted and the free delay line. The following mechanism may explain the results: when a positive DC voltage is applied, the carbon nanospheres are themselves negatively charged and so are attracted to the metallised delay line and away from the neighbouring free line. When the DC voltage is set to zero, the negatively charged particles continue to gravitationally attach themselves to the surface of both delay lines.

Setting the voltage to –9 V, the positive counter electrode attracts some particles away from the free and metallised delay lines, but because of the very weak field in the area of the free delay line, the effect of the gravitational attachment of the particles on the surface is much stronger. On top of this cycle is a slight linear drift down in the signal as particles tend to settle out of the suspension. This settling effect is more apparent in water compared with isopropanol. The free delay line is more sensitive to

the particles because they can form an electrically conducting layer at the surface and so create both mass and conductivity changes. The proximity of the free delay line to both the counter electrode and shorted line in a finite cell might explain the unexpected effect upon it.

Further experiments are required to validate the explanation offered here. This will involve the study of two widely separated delay lines and a transient analysis as the voltage is rapidly switched or ramped. Nevertheless, the results suggest that the sensing system can be used for the manipulation and probing of both charged particles and uncharged bacterial cells (in an AC field).

6.5 CONCLUSIONS

The designed and fabricated SH-SAW sensors were electrically characterized (in air) using a network analyser equipment. While device to device variability has been observed, the reflection coefficients of input and output IDTs of sensors showed large return loss values (up to 45 to 55 dB) and near perfect matching to the 50 Ω characteristic impedance.

Selected sensors were assessed in terms of their transmission coefficients. The metallised delay lines were found to have the smallest insertion loss (10.37 dB). The free delay lines were generally found (as expected) to be more lossy - the 5 mm long free delay line had an 18.5 dB insertion loss. Attenuation on the free propagation path can be minimised by reducing the IDT to IDT distance. By measuring free delay lines with 5, 4 and 3 mm lengths, the sensors attenuation constant was estimated to 0.024 dB per wavelength. An alternative method to reduce the wave propagation attenuation on free surfaces makes use of open electrode gratings. The wave becomes a shear

horizontal surface transversal wave (STW) and has potential for liquid media applications.

The chapter also presented the liquid tests and experiments performed on SH-SAW sensors. Dual delay line and resonator sensor configurations operating at high-frequencies between 433 MHz and 860 MHz were employed. According to the envisaged applications, sensors can be classified as so called 'taste' sensors and voltage modulated sensors.

The SRL 280a, SRL285, SRL208a SH-SAW sensors have been tested with various liquid solutions. All devices were able to discriminate between the synthetic liquid samples without the need of any selective or bio-chemical membrane, in both wired and semi-wireless measurement set ups. The sensing principle is based on physical interaction mechanisms rather than chemical ones and thus taste classification per se can not be achieved with this method; however sample classification based on the unique combination of the physical parameters of each liquid sample is possible and was proved experimentally. The sensitivity of these devices has to be further investigated but these results are encouraging and potential applications are envisaged for the rapid, low-cost and possibly wireless, screening of liquid samples in the food and beverage industries or environmental monitoring.

A voltage modulated sensor system has also been described and preliminary results are presented. The proposed system has the possibility of working as an analytical microsystem for the screening of biological materials. The system comprises a dual delay line SAW device in which the metallised surface is voltage modulated in order to trap charged particles within a non-conducting liquid. The basic sensing principle is that the polarized metal electrode attracts statically or electrokinetically the bioparticles in the liquid, which perturb the acoustic waves, thus changing their phase

velocity and attenuation. In theory the voltage/frequency can be set according to the properties of the particles, e.g. charge/size, dielectric constant. Ideally, the SAW sensors have no bio-chemical layers (as was the case of the preliminary experiments) although a functionalized biocoating may be added for more specific protein-based biological applications. Preliminary tests have been carried out that showed a significant voltage effect on carbon nanoparticles. Further investigations need to be done on bio-samples but the preliminary results obtained for carbon black particles suggest that the voltage modulated microsystem has the potential to offer low-cost solution to the identification of certain bacterial cells.

Further tests and experiments were performed on a single two-port resonator sensor and results and data analysis are presented in the next chapter.

6.6 References

[1] Agilent Technologies, "Network Analysers", 2008.

http://www.home.agilent.com/agilent/product.jspx?cc=US&lc=eng&nid=-536902444.0

[2] D.M. Pozar, *Microwave Engineering*. New York: John Wiley & Sons. 1998, pp.716.

[3] Agilent Technologies, Inc., Application Note 5965-7917E, 2004.

[4] K. Hashimoto, *Surface Acoustic Wave Devices in Telecommunications : Modelling and Simulation.* Berlin; London: Springer, 2000., pp. 330.

[5] V. K. Varadan and J. W. Gardner, "Smart tongue and nose," in Proceedings of Smart Structures and Materials - Smart Electronics and MEMS, pp. 67-76, 1999.

[6] M. Cole, G. Sehra, J. W. Gardner and V. K. Varadan, "Development of smart tongue devices for measurement of liquid properties," *IEEE Sensors J.*, vol. 4, pp. 543-550, 2004.

[7] G. Sehra, M. Cole and J. W. Gardner, "Miniature taste sensing system based on dual SH-SAW sensor device: An electronic tongue," *Sens Actuators, B Chem,* vol. 103, pp. 233-239, 2004.

[8] G. Sehra, *Surface acoustic wave based flavour sensor system*, University of Warwick, PhD Thesis, 2004.

[9] A. Pohl, "A low-cost high-definition wireless sensor system utilizing intersymbol interference," *IEEE Trans. Ultrason., Ferroelect., Freq. Contr.,* 2006.

[10] L. Reindl, G. Scholl, T. Ostertag, A. Pohl and R. Weigel, "Wireless remote identification and sensing with SAW devices," *Proc. IEEE Int. Workshop on Commercial Radio Sensor and Communication Techniques,* pp. 83-96, 1998.

[11] V. K. Varadan, P. T. Teo, K. A. Jose and V. V. Varadan, "Design and development of a smart wireless system for passive temperature sensors," *Smart Mater Struct,* vol. 9, pp. 379-388, 2000.

[12] F. Martin, M. I. Newton, G. McHale, K. A. Melzak and E. Gizeli, "Pulse mode shear horizontal-surface acoustic wave (SH-SAW) system for liquid based sensing applications," *Biosens. Bioelectron.,* vol. 19, pp. 627-632, 2004.

[13] M. Hunt, *Wireless interrogation of passive surface acoustic wave sensors,* University of Warwick, PhD Thesis, 2005.

[14] I. I. Leonte, M. Hunt, G. Sehra, M. Cole and J. W. Gardner, "SAW Bioliquids Sensor with RF Interrogation", *IEEE High Frequency Postgraduate Student Colloquium*, pp. 47-52, 2004.

[15] I. I. Leonte, M. Hunt, G. Sehra, M. Cole and J. W. Gardner, H. S. Noh and P. J. Hesketh, "Towards a wireless microsystem for liquid analysis", *Proceedings of the 3rd IEEE International Conference on Sensors,* pp. 919-922, 2004.

CHAPTER 7:

RESONATOR E-TONGUE SENSOR

7.1 INTRODUCTION

Whilst the previous chapter presented the results that were obtained on dual sensor configurations (mainly delay-line based), this chapter focuses on a single cavity resonator sensor. The device used was SRL 283 and its layout consisted of a two port resonator. The sensor was employed for several experiments involving taste solutions (hence the 'e-tongue' attribute used for the resonator) and the results are presented. First, the sensor proved successful in identification of six liquid samples: alongside the four classical tastes considered before, test samples included aqueous solutions simulating the umami and metallic tastes. The sensor was then also able to separate between solutions of the same taste class (e.g. caffeine and quinine hydrochloride of the bitter class) as well as to detect and classify samples with different concentrations. Furthermore, the potential to identify binary mixtures of solutions was tested and confirmed experimentally.

Measurements were carried out at two frequencies, the peak of the frequency response and a constant frequency of 434.6 MHz, corresponding to the peak frequency

measured in air. Results are presented together thus allowing for a direct comparison of the device behaviour between two operational modes.

A multivariate analysis was carried out on the solutions with varying concentrations and linear regressions have been fitted for both the overall data and substance-dependent data-sets. The statistical approach to analyse the sensor responses allowed identification of linear models capable of explaining large percentages of the sensor's data variance. Simple relations between the observations (measurements) and the independent variables were established and their predictive capability was verified.

7.2 THE TWO PORT RESONATOR SENSOR

This chapter concentrates around the experiments and results obtained with a two port resonator sensor, coded SRL 283, a configuration that was successfully used to identify and classify various liquid samples.

From a signal processing perspective the device is a pseudo-resonator as it does not follow the usual pattern of a standard resonator, i.e. a small number of finger pairs per IDT [1]. This device was designed with both ports having identical parameters with the IDTs of the delay line sensors: 25 solid finger pairs of 2.4 μm pitch and a 384 μm acoustic aperture. The IDTs formed a cavity of 192 μm (20 λ) wide; the reflectors on each side of the cavity consist of 400 strips in a positive and negative reflector arrangement with the same 2.4 μm pitch. The resonator fits within a die with overall dimensions 4600 μm × 3000 μm. A picture of the two-port resonator sensor is shown in Figure 7.1.

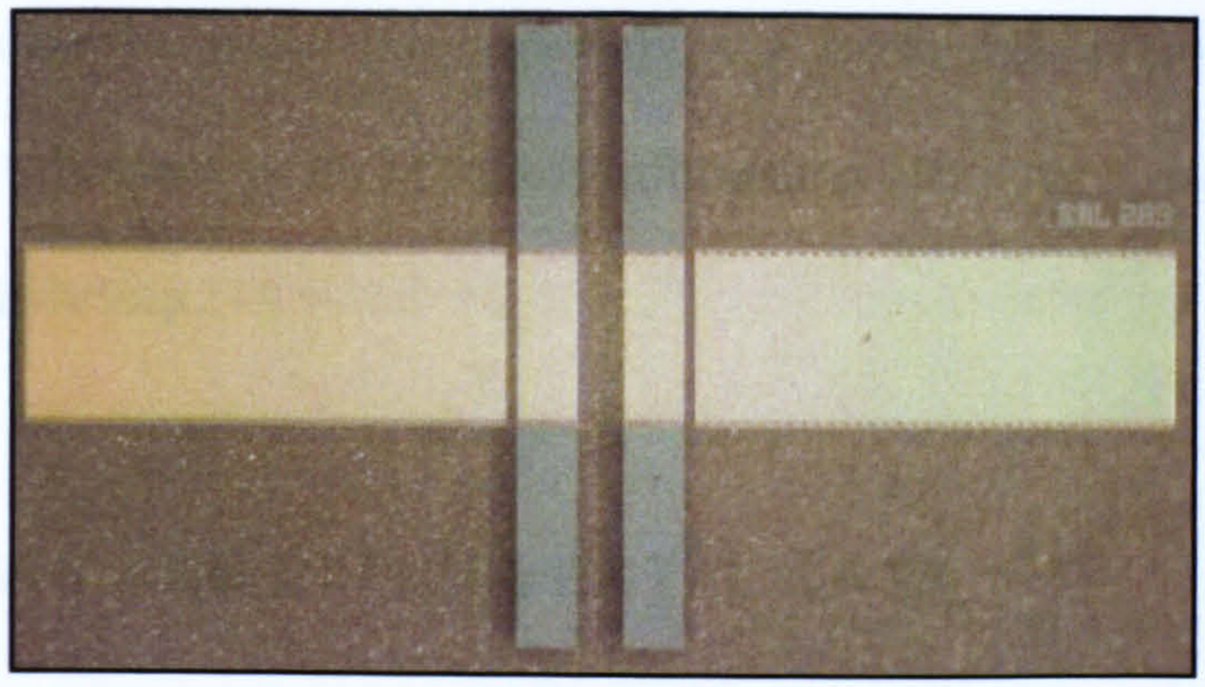

Figure 7.1: SRL 283 – two port resonator sensor

The experimental set-up for the two-port resonator sensor was similar to that used for the dual delay line sensor. A MSL liquid reservoir was placed on top of the sensor and measurements were performed with a network analyser (Agilent 8753ES). Frequency, amplitude and phase information have been recorded for each measurement.

Initial electrical characterisation of the device found a 433.7 MHz operating frequency in air, while a few days later, after a series of experiments, the device had a 434.7 MHz peak frequency. The 1 MHz difference between the two frequencies measured on the same device at two different moments in time could have been caused by the environmental temperature variation (measurements were taken at room temperature), small changes in the actual set-up (possible parasitic components) or even possible device contamination.

During the taste experiments on the SRL 283 resonator sensor, parallel measurements were carried out. The network analyser was set to display two markers: M1 was set to track the peak frequency while M2 measured the sensor's response at constant frequency, the device peak frequency in air. For each sample M1 had associated three measured parameters (frequency, attenuation and phase); marker M2 provided amplitude and phase information at constant frequency (in a similar way to

measurements taken on delay line sensors). In a sense, M1 explores the sensor's resonator effect/behaviour while M2 gives information about the sensor's operation in a delay-line mode/set-up.

7.3 TESTS AND EXPERIMENTAL DATA

The SRL 283 resonator sensor was employed for a variety of investigations on liquid samples implemented with synthetic taste substances. Initial tests were focused on basic taste solutions with a 0.1 molar concentration. Results were encouraging and subsequent experiments were performed on solutions with different molarities. Finally, taste solutions were mixed with each other and the sensor was exposed to the resulting mixtures. Again the resonator sensor was able to separate the binary mixtures. Graphical representations of all the experimental results are given in the following subsections.

7.3.1 Basic tastes solutions

Previous experiments on taste samples presented in Chapter 6 were focused on the four classical basic tastes: sweet, salty, sour and bitter. Scientists have recently accepted the existence of a fifth basic taste called umami and described as savoury (MSG) or meaty. The metallic taste (Cu^{2+}, $FeSO_4$ or blood in the mouth) is considered more of a 'taste sensation' rather than a taste per se and is generally associated with a response from the olfactory receptors. Nevertheless, it is often included in taste investigations on its own or in various combinations. To ensure a more complete analysis of the resonator's sensing capabilities, it was tested with samples representing the six-extended tastes, where umami and the metallic tastes were added to the four classical ones.

All the taste solutions for this first set of experiments were made with concentrations of 0.1 mol. The sweetness solution was prepared dissolving sucrose in DI water, for the saltiness solution sodium chloride was used, bitterness sample was made with quinine hydrochloride and sourness taste solution was obtained from acetic acid. The fifth umami solution has been prepared using monosodium glutamate (MSG) and the solution simulating the metallic taste/sensation has been made with iron sulfate. On a comparative note, quinine hydrochloride has higher water solubility than quinine sulphate used previously in delay-line experiments; the higher water solubility of quinine hydrochloride allowed the preparation of all taste solutions with 0.1 mol concentration.

Each of the liquid sample was exposed 5 times to the resonator sensor in a random sequence. In between two test samples a substantial volume of distilled water was flown through the liquid cell to clean the sensor's surface. The experimental results obtained when the network analyser was set to measure the frequency, amplitude and phase of the sensor's peak response are presented as scattered plots in Figure 7.2.

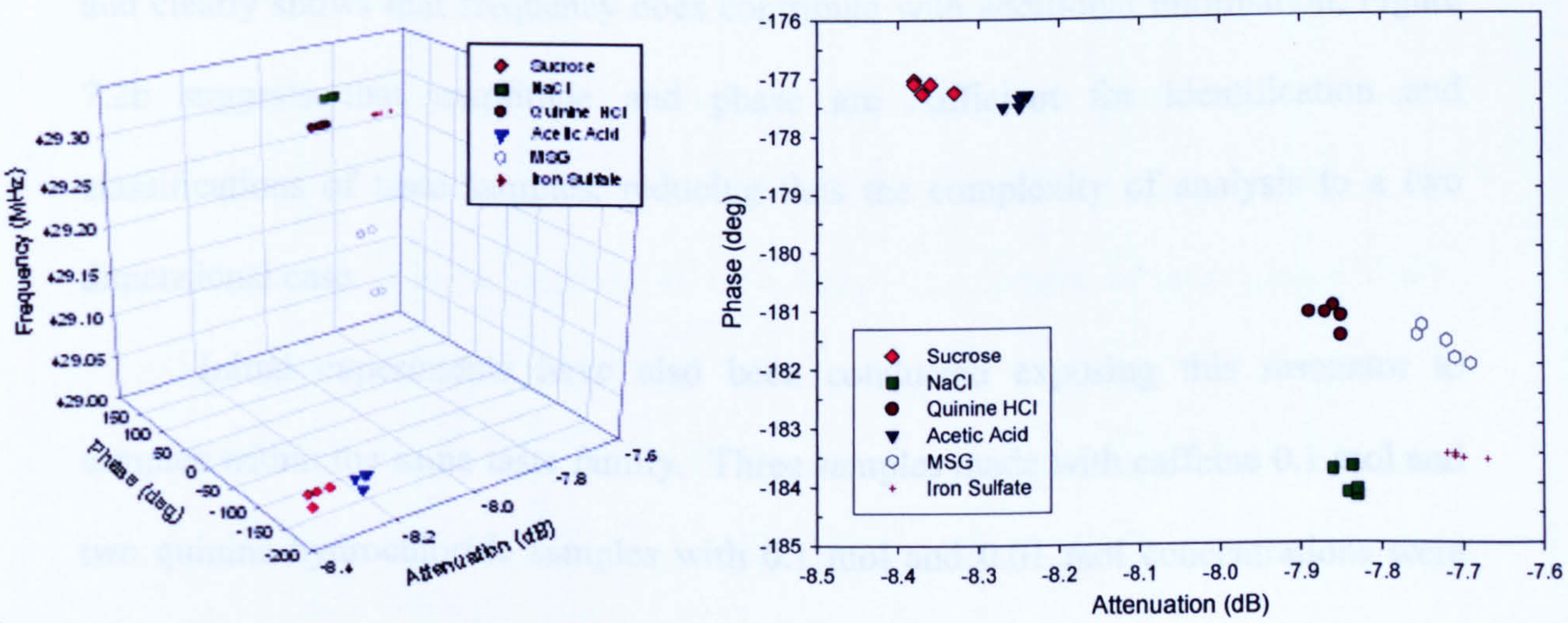

Figure 7.2: Clusters of basic tastes measured at peak frequency: scatter plots in 3D space (a) and 2D projection (b)

A 3D representation of the results in attenuation-phase-frequency space is shown in part a) of Figure 7.2; part b) of the same figure eliminates the third dimension of the data, the frequency component, and essentially projects the results onto a 2D attenuation-phase plane. Both 3D and 2D scatter plots in Figure 7.2 illustrate clustering of the results around locations specific to each substance, and moreover, show a 100% separation between characteristic clusters.

A careful look at the plots reveals that no single measured parameter (amplitude, phase or frequency) is able to provide sufficient sample separation on its own. In other words it can be said that no parameter is bijective in respect to the class of taste samples considered: an attenuation value of -7.85 is typical for both salt and quinine hydrochloride samples, salt and iron sulphate solutions partially overlap in phase, and the 429.25 MHz frequency is characteristic for both quinine hydrochloride and iron sulphate samples. All these examples prove the non-injective nature of the taste sample-measured parameter correspondence and demonstrate the necessity of a multiple parameter space for classification of samples.

On the other hand, while Figures 7.2a gives a complete 'picture' of the results and clearly shows that frequency does contribute with additional information, Figure 7.2b suggests that amplitude and phase are sufficient for identification and classifications of taste samples, reducing thus the complexity of analysis to a two dimensional case.

Initial experiments have also been conducted exposing this resonator to samples within the same taste family. Three samples made with caffeine 0.1 mol and two quinine hydrochloride samples with 0.1 mol and 0.01 mol concentrations were chosen to test the sensor's ability to discriminate between solutions belonging to the

bitter taste. Again Figure 7.3 shows a clear clustering of the bitter samples in both 3D space (a) and 2D plane (b).

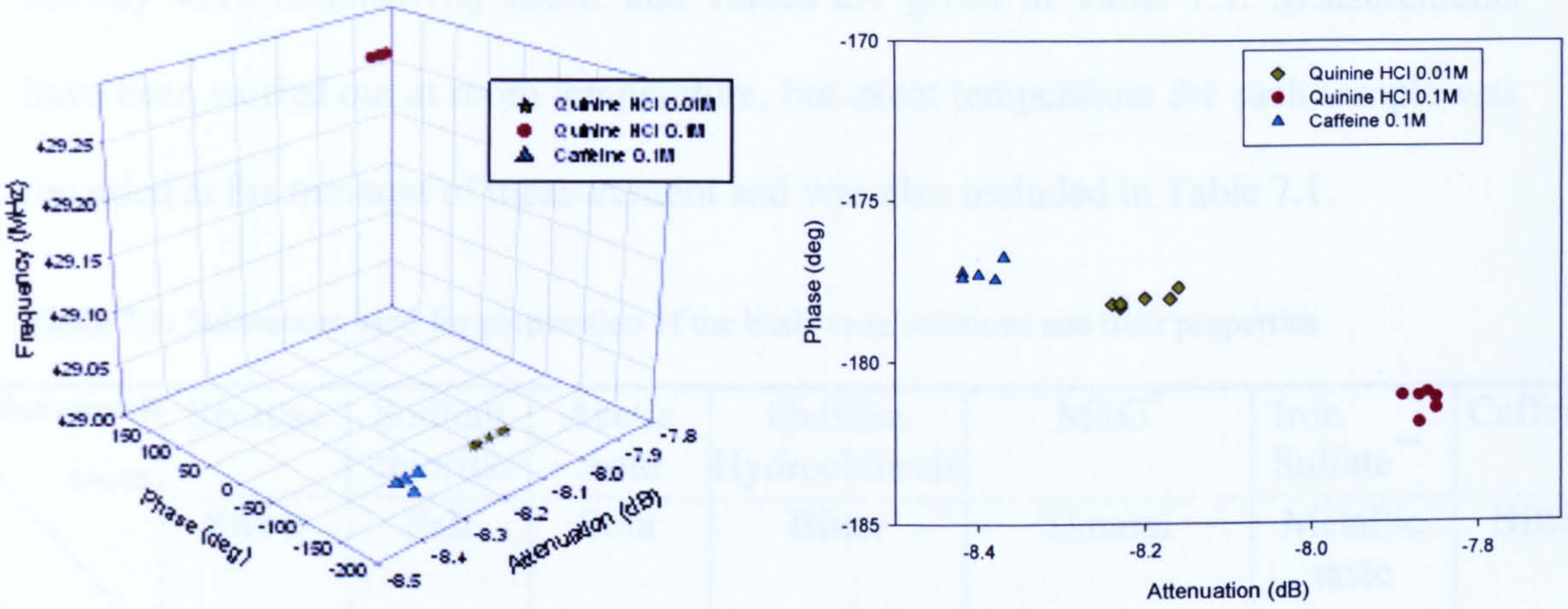

a) b)

Figure 7.3: Bitter solutions measured at peak frequency – in 3D representation (a) and 2D projection (b)

An evaluation of Figure 7.3 a) and b) confirms that a reduction to a 2D coordinate system remains adequate for samples classification. Despite the small number of samples considered, these preliminary results suggest the possibility of discrimination between samples with various concentrations – this inference shall be further demonstrated in subsection 7.3.2.

Comparing taste samples with same concentration (0.1 mol) but implemented with different substances, caffeine and quinine hydrochloride solutions cluster wide apart in opposite corners of the plots. This implies that clustering is achieved according to the physical properties of the sample rather than taste class itself, and thus classification can be achieved as an indirect consequence of measuring different physical properties of the solutions.

Unfortunately, due to the large number of potential parameters that could contribute to the sensor's response, this hypothesis is not easy to be verified exhaustively. Even if a small number of decisive parameters are identified, practical limitations arise due to the lack of specialized equipment to accurately measure the

parameters of interest for every taste sample. The only parameter that was possible to measure for this data-set was conductivity. The taste samples were measured with a Jenway 4310 conductivity meter and values are given in Table 7.1. Measurements have been carried out at room temperature, but exact temperature for each sample was recorded at the moment of measurement and was also included in Table 7.1.

Table 7.1: Substances used for preparation of the basic taste solutions and their properties

Substance & taste / Propr.	Sucrose	Sodium chloride	Acetic Acid	Quinine Hydrochloride	MSG*	Iron Sulfate**	Caffeine
	Sweet	Salt	Sour	Bitter	Umami	Metallic taste	Bitter
Brand	Fisher	BDH	Fisher	Sigma	Fluka	Aldrich	Sigma
Molecular Formula	$C_{12}H_{22}O_{11}$	NaCl	$C_2H_4O_2$	$C_{20}H_{24}N_2O_2 \cdot HCl \cdot 2H_2O$	$NaOOCCH_2CH_2CH(NH_2)COOH \cdot H_2O$	$FeSO_4 \cdot 7H_2O$	$C_8H_{10}N_4O_2$
Molecular Weight [AMU]	342.29	58.43	60.04	396.91	187.14	278.01	194.19
Conductivity of 0.1M solution [μS/cm]	3.11 @23.7°C	$2.62 \cdot 10^3$ @24°C	140.2 @23.7°C	$1.69 \cdot 10^3$ @24.3°C	$1.543 \cdot 10^3$ @24.5°C	$2.52 \cdot 10^3$ @23.8°C	9.08 @24°C

* L-Glutamic acid monosodium salt monohydrate

** Iron(II) sulfate heptahydrate

Conductivity of 0.01 M Quinine Hydrochloride: 234 μs @24.3°C

Studying again Figure 7.2b, it can be seen that in the positive phase range of the plot, samples having the same order of magnitude for the conductivity cluster around the same phase range.

The results included so far focused on measurements taken at the peak frequency of the sensor's response. As mentioned in section 7.2, parallel measurements were carried out: for each test sample there were recorded both the peak values (marker M1) as well as the values characteristic to the constant frequency corresponding to the peak value determined during the initial electrical characterisation in air (marker M2). Thus two data-sets were collected simultaneously: the basic tastes results for peak frequency have already been presented; the

measurements taken at constant frequency are considered next and are represented graphically in Figures 7.4 and 7.5.

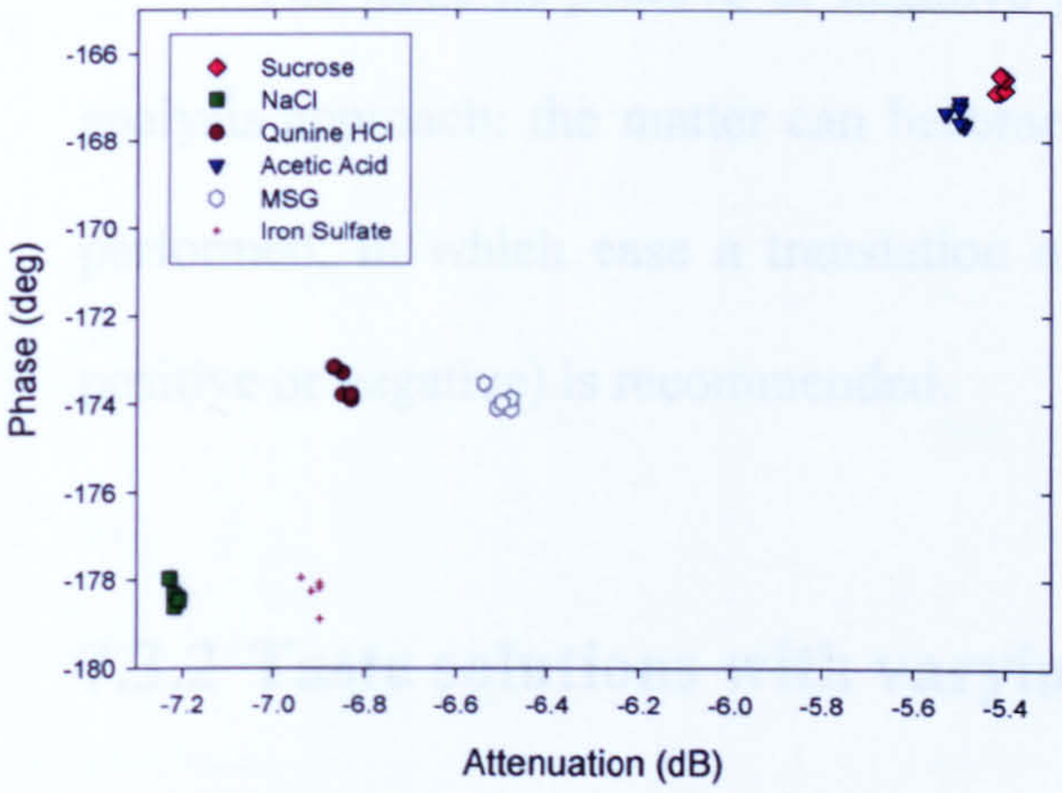

Figure 7.4: Basic tastes clusters measured at constant frequency

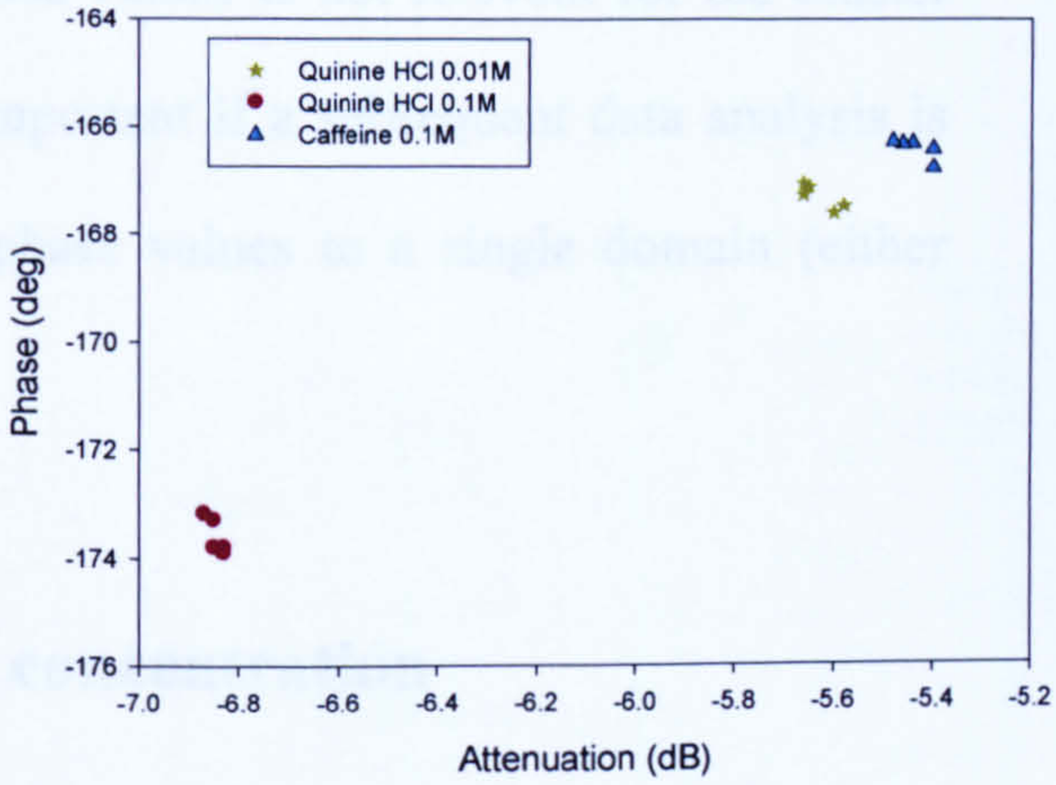

Figure 7.5: Bitter solutions tested at constant frequency

Figure 7.4 gives a 2D scatter plot of the taste samples data measured at constant frequency and Figure 7.5 presents the results of the bitter samples at the constant frequency operation. Both plots display again clear clustering of the samples in the attenuation-phase plane. The actual taste samples were the same ones used for the peak frequency results, as measurements were performed simultaneously for both data-sets. As test conditions were practically identical, all possible external variations similarly affecting both data-sets, a direct comparison can hold between the two data-sets.

The plots in Figure 7.4 seem to suggest that operation at constant frequency mode is more stable phase-wise, as all taste samples exhibit a negative phase.

Phase measured by the network analyzer wraps from -180° to +180° and is related to the time delay introduced by the device according to the equation:

$$phase = -2\pi ft,$$

where f is the source frequency (in MHz) and t is the time delay (in seconds). At constant frequency operation the phase has a linear dependency on the time delay

introduced by each sample. When phase is measured at the peak of the sensor's response, phase incorporates information on both the frequency and the time delay.

The issue of positive or negative phase values is not relevant for the cluster analysis approach; the matter can become important if a subsequent data analysis is performed, in which case a translation of phase values to a single domain (either positive or negative) is recommended.

7.3.2 Taste solutions with varying concentration

Experiments were also performed on selected taste solutions with different weight concentrations. The purpose of this set of tests was to further investigate the sensor's ability to differentiate betweens solutions of the same substance in different concentrations as well as to identify patterns in the sensor response related to substance concentration. Based on the information provided by samples with varying concentrations, the ultimate aim is to relate the sensor's output to the physical characteristics of each sample, but this matter will be covered in more details in section 7.4.

Only three classes of taste samples were tested – this limitation was due to the difficulty in finding the necessary physical data for all of the six basic tastes considered before. Information on sucrose (S), sodium chloride (NaCl) and acetic acid (AA) solutions and their physical properties was found tabulated in respect to anhydrous solute weight per cent concentration. Four weight concentrations were chosen for experimentation on each substance: 0.5%, 1%, 3% and 5%.

Parallel measurements were again taken for the two markers set to track the peak of the frequency response (M1) and constant frequency (M2). The obtained results are graphically presented in Figures 7.6 – 7.11. Separation between samples

with different concentrations has been observed for all solutions in both operation modes.

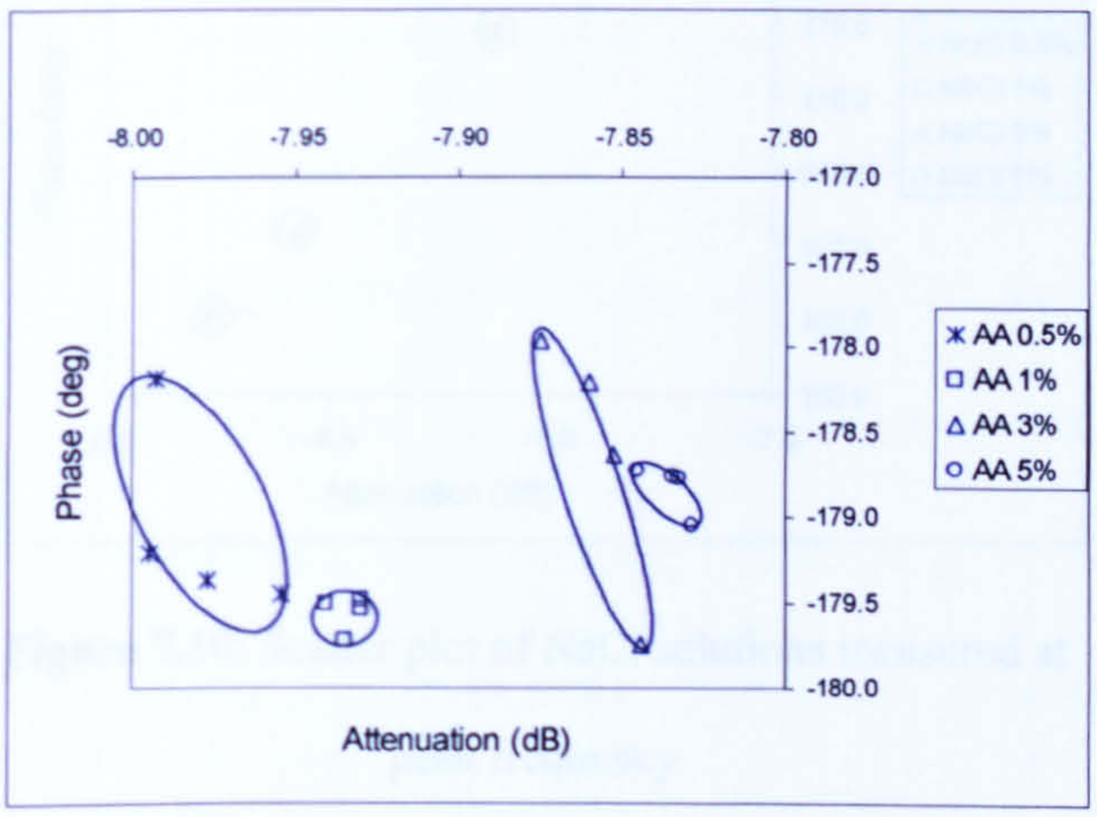

Figure 7.6: Scatter plot of acetic acid solutions measured at peak frequency

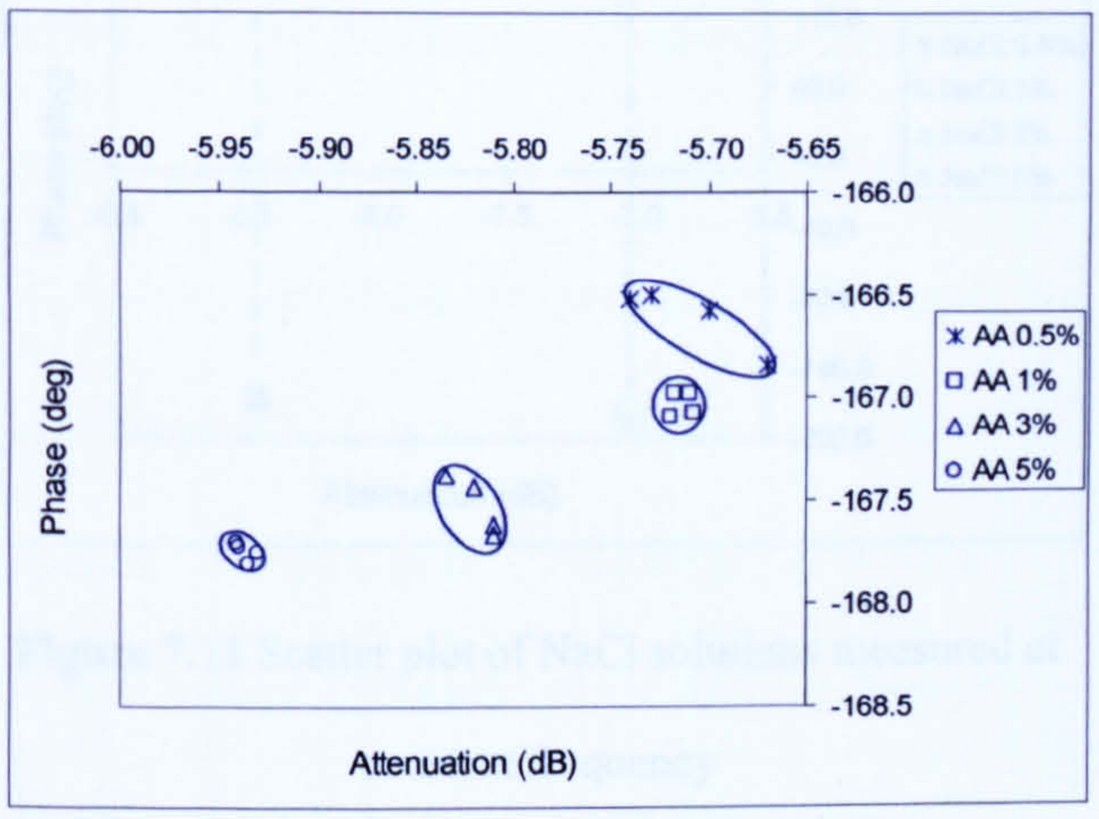

Figure 7.7: Scatter plot of acetic acid solutions measured at constant frequency

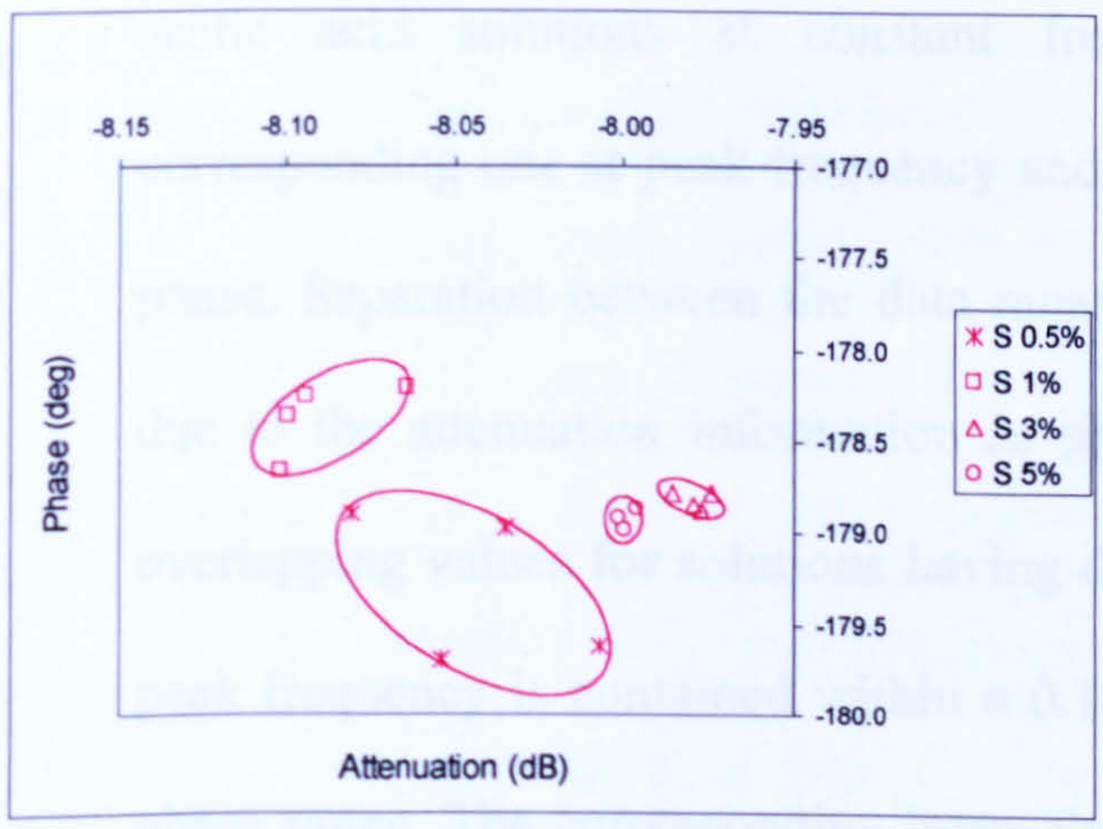

Figure 7.8: Scatter plot of sucrose solutions measured at peak frequency

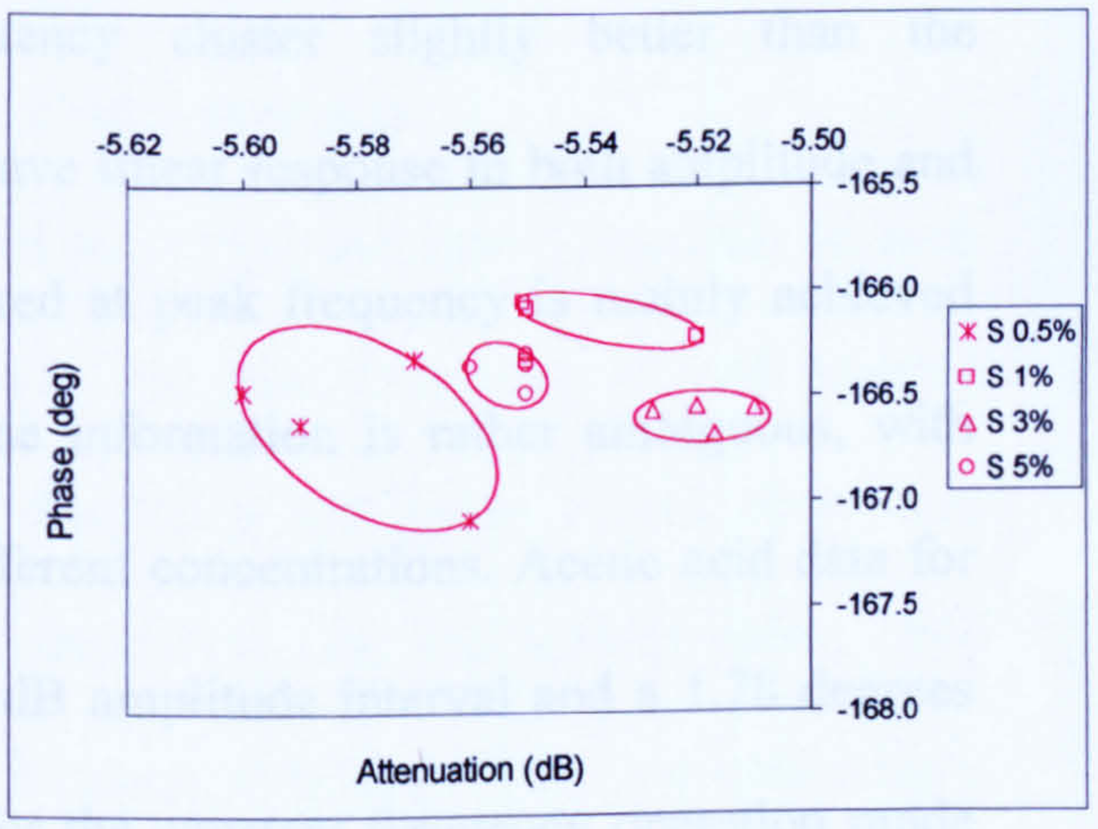

Figure 7.9: Scatter plot of sucrose solutions measured at constant frequency

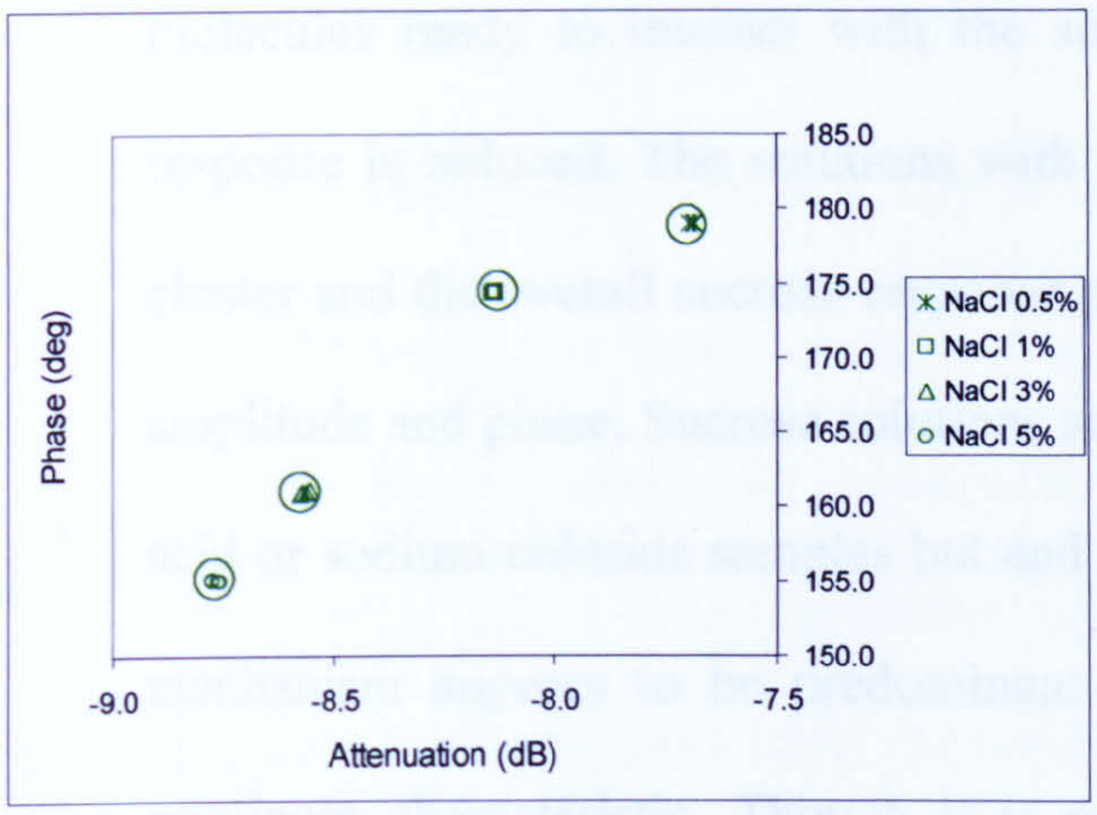

Figure 7.10: Scatter plot of NaCl solutions measured at peak frequency

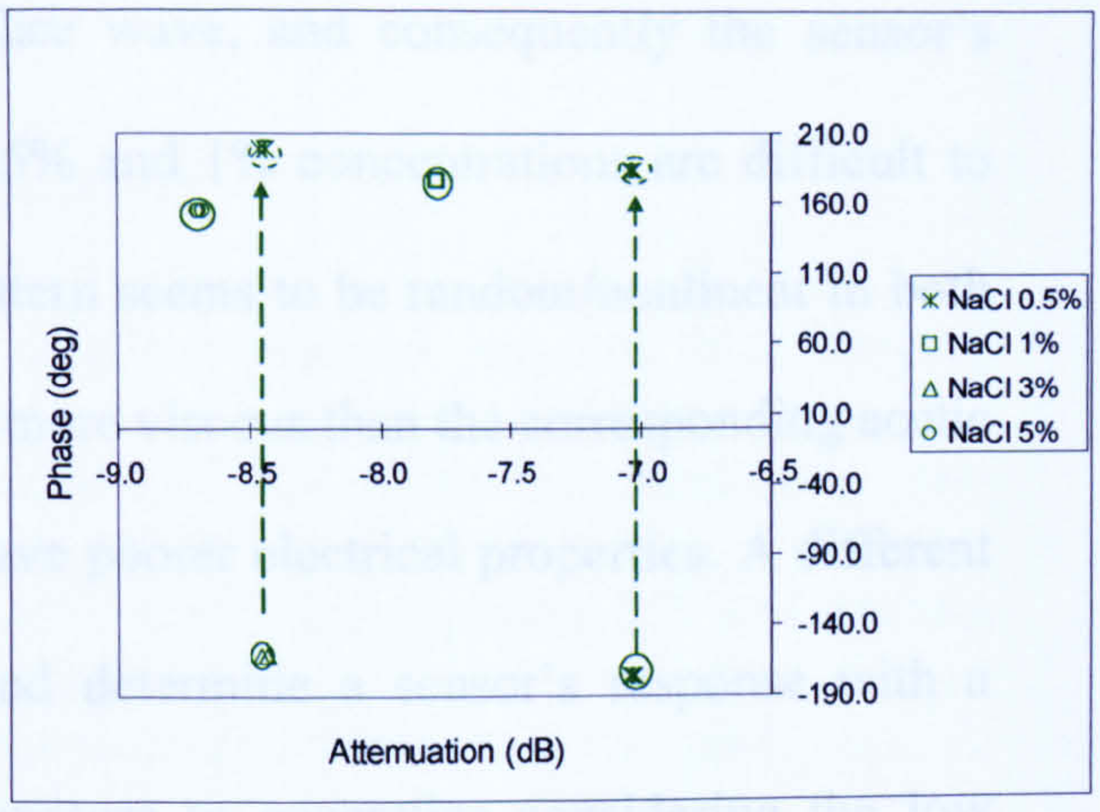

Figure 7.11 Scatter plot of NaCl solutions measured at constant frequency

When comparing Figures 7.6 and 7.7 it can be observed that the results for acetic acid solutions at constant frequency cluster slightly better than the corresponding one at peak frequency and have linear response in both amplitude and phase. Separation between the data measured at peak frequency is mainly achieved due to the attenuation information as phase information is rather ambiguous, with overlapping values for solutions having different concentrations. Acetic acid data for peak frequency is contained within a 0.16 dB amplitude interval and a 1.78 degrees phase range. The corresponding intervals for the constant frequency operation mode are 0.27 dB and 1.31 degrees, respectively. It can be observed that for the same test samples, the sensor's amplitude variation is larger for constant frequency operation while the phase response has a wider spreading for peak frequency measurements.

Sucrose samples have the lowest molar concentration among all considered solutions, up to 6 times smaller than the corresponding acetic acid or sodium chloride samples. This is due to the high molecular weight of sucrose of 342.29 Daltons when compared to the 58.43 Daltons of sodium chloride and 60.04 Daltons of acetic acid (Table 1). Having lower molarities the sucrose solutions have lower number of

molecules ready to interact with the surface wave, and consequently the sensor's response is reduced. The solutions with 0.5% and 1% concentrations are difficult to cluster and the overall sucrose response pattern seems to be random/nonlinear in both amplitude and phase. Sucrose solutions are more viscous than the corresponding acetic acid or sodium chloride samples but and have poorer electrical properties. A different mechanism appears to be predominant and determine a sensor's response with a nonlinear characteristic. Though it is premature to generalise considering the low molar concentrations of sucrose solutions, the sensor behaves as if it has lower sensitivity to non-conductive samples. Amplitude and phase variations are contained within 0.127 dB and 1.49 deg for the peak frequency, respectively 0.09 dB and 1.03 degrees for the constant frequency data. High resolution equipment is required to discriminate between the considered sucrose solution samples.

Sodium chloride solutions show clear clustering and linear responses in both amplitude and phase. Measurements taken at the peak frequency all had positive phases, while data measured at constant frequency had phase values alternating between negative and positive domain depending on the concentration. For consistency with the phase data of the peak frequency, the negative phase values have been translated with 360° to the positive domain. The sensor response shows a strong sensitivity for ionic solutions: amplitude and phase ranges covered by NaCl solutions are 1.09 dB and 24.07 degrees for peak frequency and 1.67 dB and 44.96 degrees for constant frequency.

7.3.3 **Binary mixtures of taste solutions**

In addition to the tests on basic taste solutions and on samples with varying concentration, experiments were also performed on solutions combining two fundamental tastes. Equal quantities of acetic acid (AA), sucrose (S) and sodium chloride (NaCl) solutions with the same concentration were mixed to each other to obtain three binary mixtures: AA+S, AA+NaCl and NaCl+S. Two weight concentrations of 1% and 5% were considered for each basic taste solution and the correspondent binary mixtures were annotated according to the weight percent of the constituent solutions.

The mixture samples were supplied to the resonator sensor and response data were again recorded for both peak and constant frequencies. There was an omission in the records for the 1% acetic acid-sucrose mixture at constant frequency, thus the sample does not appear on subsequent plots. Attenuation-phase scatter plots of the obtained data are given in Figures 7.12 and 7.13.

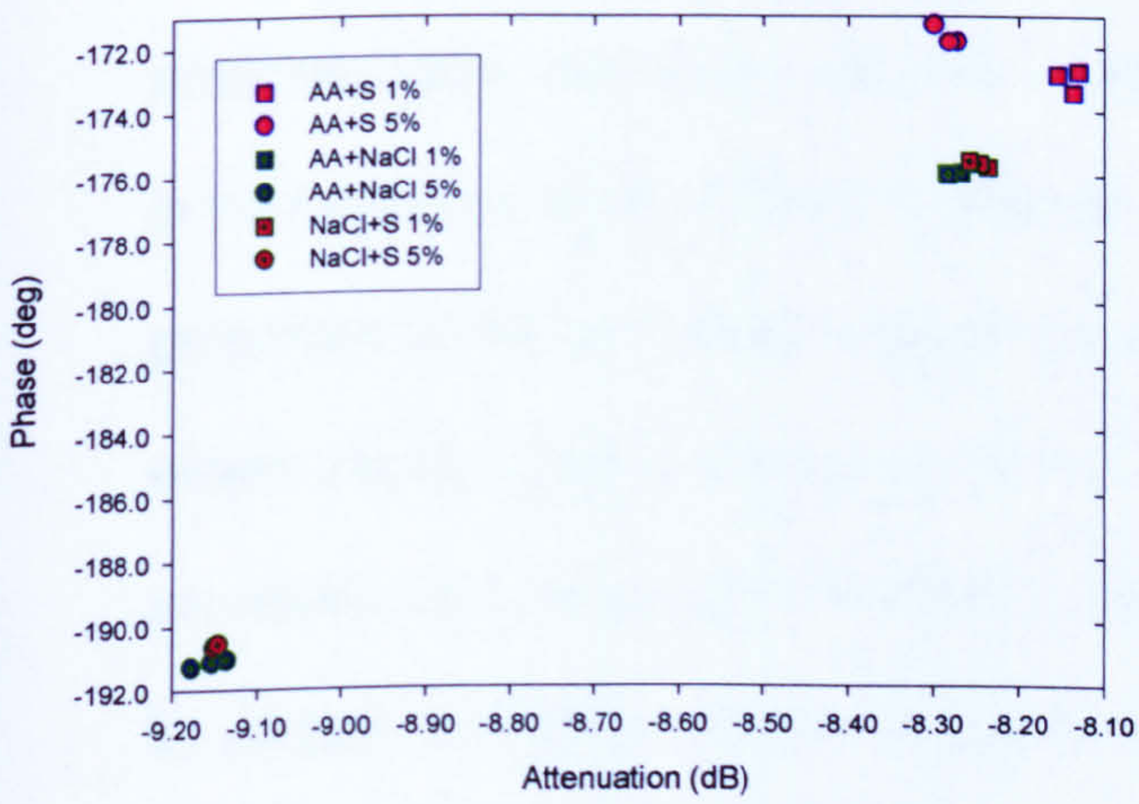

Figure 7.12: Binary mixtures of solutions – measurements at peak frequency

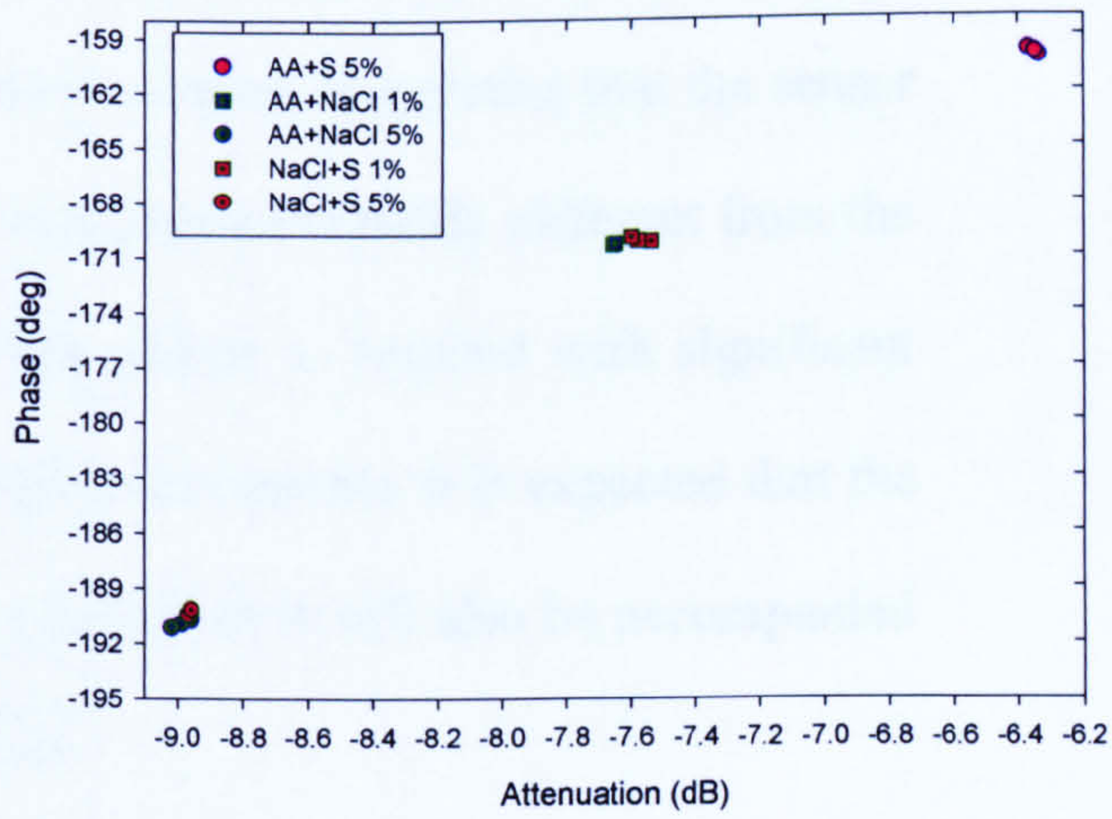

Figure 7.13: Binary mixtures of solutions – measurements at constant frequency

Binary mixtures samples cluster well in the attenuation-phase plane and a distinctive separation between the clusters was observed for measurements at both frequencies. The relative location of the mixtures seems to be determined by the new properties of the solution derived from the binary combination. Sodium chloride tends to dominate the properties of its mixtures, as seen by the relative close proximity of its clusters. While still individually separable, the AA+NaCl 1% and NaCl+S 1% clusters are significantly closer to each other than to any other data cluster; similarly AA+NaCl 5% and NaCl+S 5% have neighbouring locations in the positive range of the plot.

In the absence of information related to the physical properties of the binary mixtures solutions, the results are assessed relatively to the data of the initial constituent samples. To this aim the binary mixtures results were plotted again together/in reference with the acetic acid, sucrose and sodium chloride solutions with 1% and 5% concentrations. Graphical representations of data for peak and constant frequencies are given in Figures 7.14 and 7.15.

The mixtures and initial solutions combined plots show that the binary mixtures cluster well apart from their constituent samples, suggesting that the sensor is very sensitive to the mixture's properties which are sufficiently different from the properties of the individual components for the sensor to respond with significant output changes. Due to the nature of the constituent solutions, it is expected that the parameter with the largest variation is conductivity, but it will also be accompanied by changes in density, viscosity and permittivity.

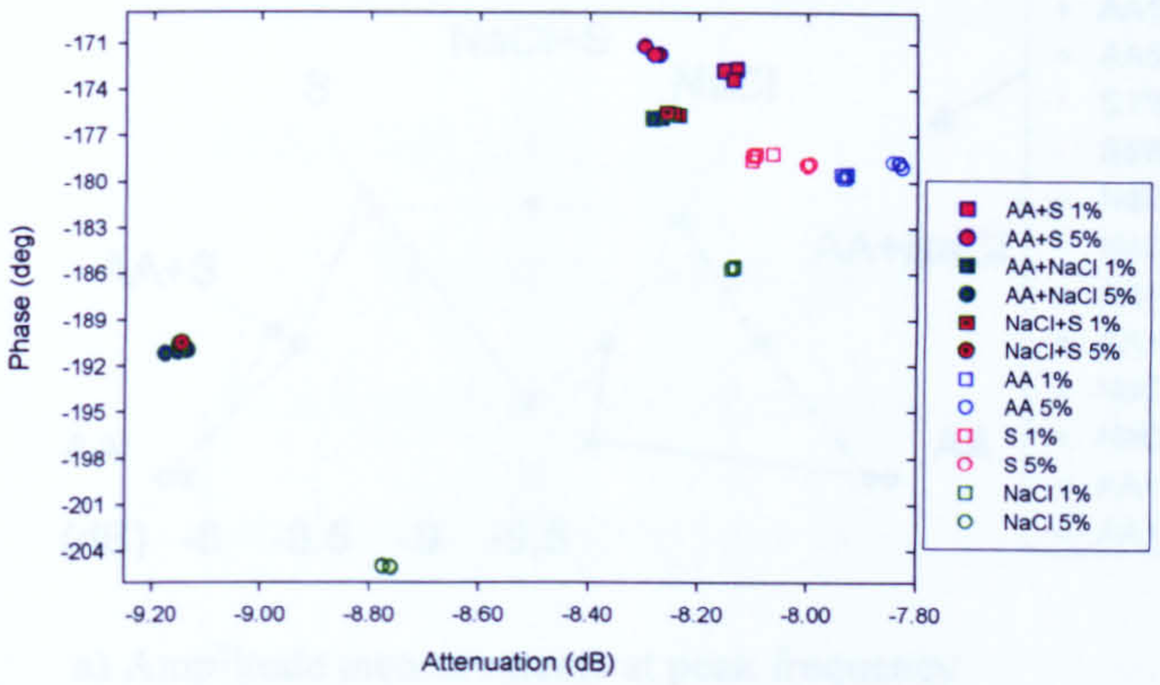

Figure 7.14: Solutions and binary mixtures – measurements at peak frequency

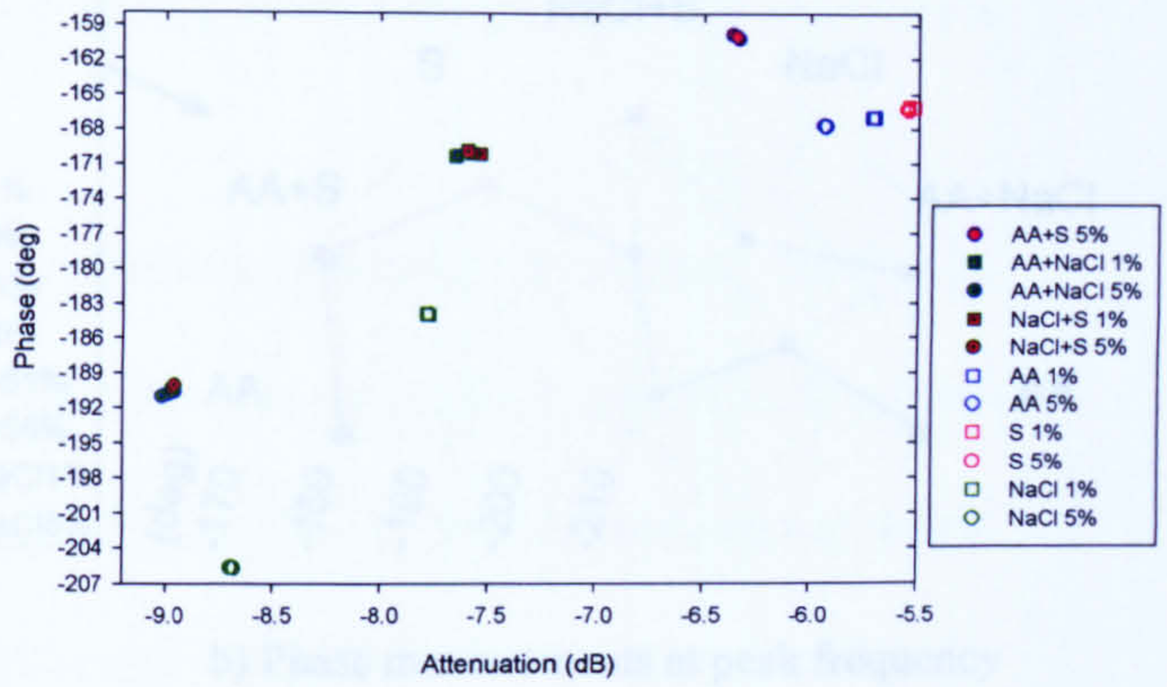

Figure 7.15: Solutions and binary mixtures – measurements at constant frequency (mixture AA+S 1% missing)

For a better assessment of the mixtures relative to mixed samples, data were also organised and displayed in 'radar' plot format (Figure 7.16). This representation has the advantage of allowing mixture data to be intercalated to the initial solutions data so that the variations of mixture's amplitude and phase can now be observed relatively to the neighbouring constituent information. To minimize the spreading of phase data, all positive phase values were translated with 360° to the negative phase domain (phase can thus take values from -360° to 0°).

Figure 7.16 shows plots of amplitude and phase data for both peak (a and b) and constant frequencies (c and d). The 1% weight concentration is considered to be of 'low' concentration while the 5% one to be of 'high' concentration. The sensor appears to have different response patterns for the two concentrations, but at a closer examination will reveal common evolution trends.

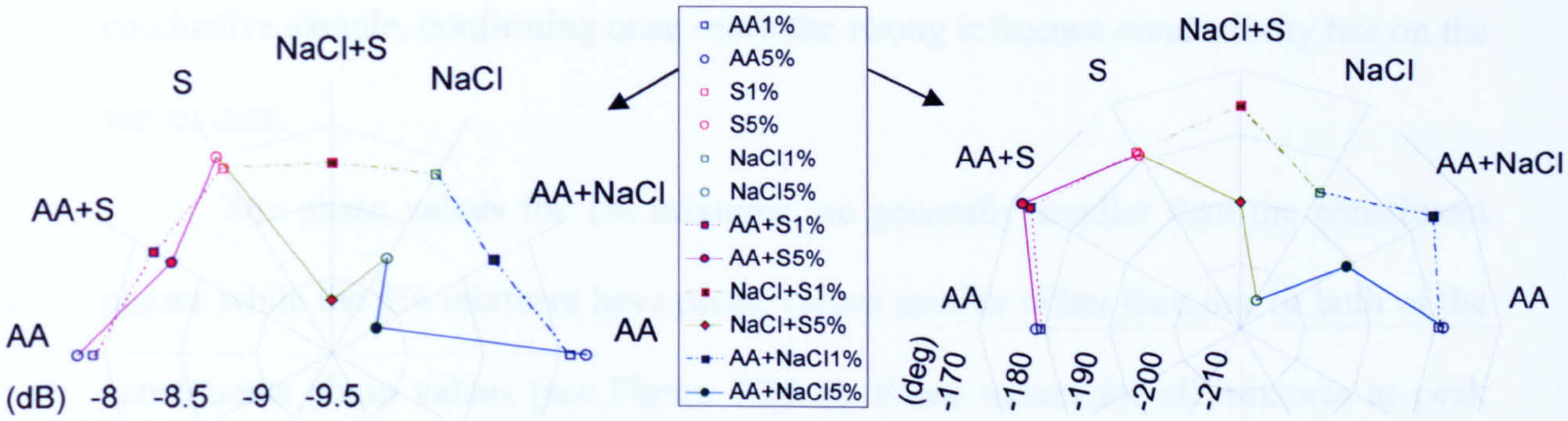

a) Amplitude measurements at peak frequency

b) Phase measurements at peak frequency

c) Amplitude measurements at constant frequency

d) Phase measurements at constant frequency

Figure 7.16: Amplitude and phase radar plots of binary mixtures in reference with constituent solutions

For the peak frequency data, the binary mixtures samples have attenuations larger than the attenuations of the samples they derived from. This is an interesting fact, but is in good agreement with the acetic acid and sucrose amplitude tendency to increase with decreasing sample concentration (see Figure 7.17a). However, the larger attenuations are mainly attributed to the new physical properties of the mixtures that determine a notably different sensor's response. The attenuation values can be approximated by weighted sums of constituent solutions attenuations. Weights of 0.2353 and 0.7849 can be used to estimate the attenuations for 1% mixtures while 0.1116 and 0.9431 weights can be employed for the 5% mixtures. The weighted sum evaluation is based on ordering the constituent solutions according to the sample conductivity and attributing the first weight to the solution with lower conductivity (i.e. S and AA). For both concentrations, larger weights are given to the more

conductive sample, confirming once more the strong influence conductivity has on the sensor data.

The phase values for 1% mixtures are generally smaller than the constituent phases while the 5% mixtures have phase values smaller either than one or both of the constituents phase values (see Figure 7.16 b). Phase values for all mixtures at peak frequency can also be accurately expressed as a weighted sum of the constituent phases with weight parameters of 0.2263 and 0.7327. The component with higher conductivity has again the higher weight in the sum and the larger influence in the estimation of the sensor's response.

Data collected at constant frequency present similarities with both amplitude and phase data at peak frequency. The mixtures amplitude for the lower 1% concentration can be expressed as a weighted average of the amplitudes of constituents. The amplitude evolution pattern for the higher concentrations samples is matching the corresponding pattern from the peak frequency, and can be expressed with the weights of 0.1343 and 0.9441. These weights are close to the ones for the peak frequency estimations, confirming the similar amplitude evolutions observed for the higher concentrations at the two frequencies. Constant frequency phase patterns present similar tendencies with the ones for peak frequency (the one for higher concentrations seem to be visually identical) and they can be expressed as weighted sums with 0.1107 and 0.8334 coefficients.

More light will be thrown on the mixtures data if the exact physical properties are known for each binary solution. It is believed that the sensor's response to the mixtures is determined by unique combinations of their characteristic properties, among which conductivity, density and viscosity appear to have significant influences.

7.4 MULTIVARIATE ANALYSIS OF LIQUID SOLUTIONS

liquid solutions were mainly discussed in terms of the sensor's response and its ability to identify and discriminate between different test samples. This section attempts to determine whether a link exists between the sensor's response and a chosen set of physical properties of the solutions and to investigate the nature of such relationship. To this aim the results presented in section 7.3.2 are further analysed.

Acetic acid, sucrose and sodium chloride data are plotted against the weight per cent concentration of each solution: Figure 7.17 presents amplitude (a, c) and phase (b, d) changes for both operation frequencies (peak and constant frequency). A preliminary analysis of the amplitude and phase variations with concentration reveals tendencies of quasi-linear dependencies. Simple regression lines have been added to the measured data to illustrate amplitude and phase evolution with increasing solute concentrations.

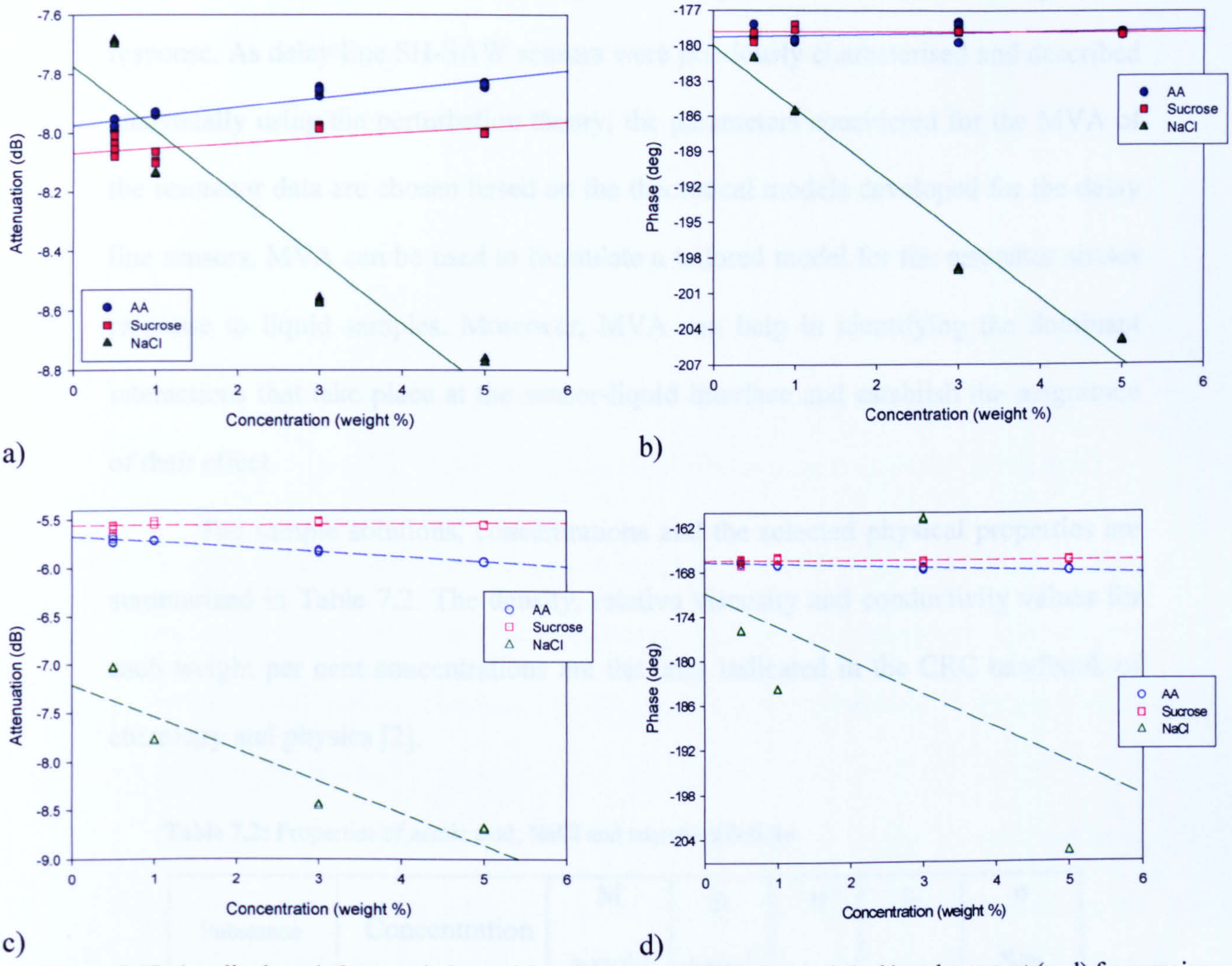

Figure 7.17: Amplitude and phase variations with weight concentration for peak (a, b) and constant (c, d) frequencies

The solute weight percent of a taste solution is reflected in the physico-chemical properties of that solution. The resonator sensor, as all of the SH-SAW sensors considered in this project, relies on a purely physical detection mechanism, described in details in Chapter 3. Thus, from the wide range of biological, physical and chemical properties of solutions, the analysis is focused only on certain physical proprieties of the solutions, in particular the ones defined by mechanical and electrical parameters.

Several reasons justified the MVA (multivariate analysis) approach of the resonator data: The resonator sensor has a configuration that has not been studied

before, and to the author's knowledge, no analytical model exists to explain its response. As delay line SH-SAW sensors were previously characterised and described analytically using the perturbation theory, the parameters considered for the MVA of the resonator data are chosen based on the theoretical models developed for the delay line sensors. MVA can be used to formulate a tailored model for the resonator sensor response to liquid samples. Moreover, MVA can help in identifying the dominant interactions that take place at the sensor-liquid interface and establish the magnitude of their effect.

The sample solutions, concentrations and the selected physical properties are summarized in Table 7.2. The density, relative viscosity and conductivity values for each weight per cent concentrations are the ones indicated in the CRC handbook of chemistry and physics [2].

Table 7.2: Properties of acetic acid, NaCl and sucrose solutions

Substance	Concentration	M g-mol/l	ρ kg/m^3	η	ε_r	σ S/m
Acetic Acid	A% by wt.: **0.5**	0.083	998.9	1.010	80.04	0.03
	A% by wt.: **1**	0.166	999.6	1.020	79.67	0.06
	A% by wt.: **3**	0.501	1002.5	1.061	78.23	0.1
	A% by wt.: **5**	0.837	1005.2	1.103	76.78	0.12
Sodium Chloride	A% by wt.: **0.5**	0.086	1001.8	1.009	79.21	0.82
	A% by wt.: **1**	0.172	1005.3	1.018	77.90	1.6
	A% by wt.: **3**	0.523	1019.6	1.050	72.78	4.4
	A% by wt.: **5**	0.885	1034.0	1.083	68.19	7.01
Sucrose	A% by wt.: **0.5**	0.015	1000.2	1.013	80.28	-(0.000439)
	A% by wt.: **1**	0.029	1002.1	1.026	80.17	-(0.000236)
	A% by wt.: **3**	0.089	1009.9	1.082	79.71	-(0.000148)
	A% by wt.: **5**	0.149	1017.8	1.144	79.25	-(0.000115)

The symbols used in Table 7.2 have the following meaning:

A% = anhydrous solute weight per cent, g solute/100 solution.

M = molar concentration, g-mol/l.

ρ = relative density at 20°C, kg/l.

η = relative viscosity, ratio of the absolute viscosity of a solution at 20°C to the absolute viscosity of water at 20°C.

ε_r = dielectric permittivity

σ = specific electric conductance (volume conductivity) at 20°C (S/m)

The static permittivity values are based on various sources [3-5]; where data characteristic to a specific concentration were not found in literature, interpolation procedures were used for obtaining the necessary values and details of the procedures are given in Appendix B.

The sucrose conductivity values given in brackets in Table 7.2 were the ones measured with the Jenway 4310 conductivity meter. The conductivity decreases with increasing sucrose percent. In the low sucrose concentration limit, this variation that can be explained by the presence of dissolved oxygen in the distilled water used to prepare the test samples (distilled water had higher conductivity values than the sucrose samples, which suggests that sucrose was annihilating the radicals responsible for the water conductivity).

The purpose of this section is to investigate whether the amplitude and phase data from the sensor can be related to selected physical parameters of samples (density, viscosity, conductivity and permittivity). Generically the dependences can be formulated as

$$A, \Phi = f(\rho, \eta, \sigma, \varepsilon)$$

where amplitude A and phase Φ are functions of viscosity, density, conductivity and permittivity of the solutions. The following subsections are checking whether a linear relationship in this multivariable space can approximate the resonator measured data well.

7.4.1 Multiple linear regression – mathematical foundations

Multiple linear regression (MLR) is a mathematical extension of simple linear regression applicable to situations where several independent variables (predictors) are accounting for the variance of a dependent variable. The general formula describing the linear model is

$$y_i = b_0 + b_1 x_1 + b_2 x_2 + \cdots + b_k x_k + e \tag{7.1a}$$

which in abbreviated notation is written as

$$y_i = b_0 + \sum_{j=1}^{k} b_j x_j + e \tag{7.1b}$$

where y_i is the observation variable, also known as response or dependent variable and x_j are the independent variables (also called predictors, regressors or explanatory variables). The b_0 constant is the intercept point and b_j are the regression coefficients (sensitivities) for the corresponding x_j variables; each regression coefficient represents the average amount the dependent increases when the corresponding independent increases one unit and other independents are held constant. The error term or residual is denoted by e.

Regression analysis is using linear algebra to perform the necessary calculations for solving equation (7.1). In matrix form the model can be formulated as

$$\mathbf{y} = \mathbf{XB} + \boldsymbol{\varepsilon} \tag{7.2}$$

where:

y is a n-by-1 vector of observations (input data),

X is a n-by-k matrix of regressors (input data),

B is a k-by-1 vector of coefficients (estimated data),

ε is a n-by-1 vector of random disturbances (estimated data).

Among the different criteria that can be used to best-fit a data-set, the least square criterion is one of the most powerful ones. The least square solution to (7.2) is a vector b which estimates the unknown vector of coefficients, B:

$$\mathbf{b} = \hat{\mathbf{B}} = (\mathbf{X}^T\mathbf{X})^{-1}\mathbf{X}^T\mathbf{y} \tag{7.3}$$

The least squares solution is computed by minimizing the sum of squares of the distances (deviations) from each observation point to the best-fit plane, $\hat{\mathbf{y}} = \mathbf{Xb}$.

The model residuals are defined as the differences between the observed and predicted values:

$$\mathbf{r} = \mathbf{y} - \hat{\mathbf{y}} \tag{7.4}$$

Residuals are useful for detecting failures in the model assumptions, since they correspond to the errors ε in the model equation (7.2). By assumption, these errors have independent normal distributions with mean 0 and constant variance [6]. The smaller the variability of the residuals around the regression line relative to the overall variability, the better a model is.

To assess the goodness of fit, multiple linear regression uses the R^2 coefficient of multiple determination. Also known as the multiple correlation or Multiple-R coefficient, R^2 gives the correlation between the observed values and the values predicted by the regression model. The R^2 multiple coefficient represents the percent of the variance in the observed value explained jointly by the independent variables. It

can also be interpreted as the proportionate reduction in error in estimating the dependent when knowing the independents [7]. R^2 is computed as

$$R^2 = 1 - \frac{ESS}{TSS} \tag{7.5}$$

where *ESS* is the error sum of squares and *TSS* is the total sum of squares. Mathematically, the *ESS* and *TSS* terms are expressed as

$$ESS = \sum (y_i - \hat{y}_i)^2 = \mathbf{y}^T\mathbf{y} - \mathbf{b}^T\mathbf{X}^T\mathbf{y} \tag{7.6}$$

and

$$TSS = \sum (y_i - \bar{y})^2 = \mathbf{y}^T\mathbf{y} - \frac{1}{n}(\mathbf{y}^T\mathbf{u}\mathbf{u}^T\mathbf{y}) \tag{7.7}$$

where **u** is an *n* by 1 unit vector (each element is 1).

The F statistic, also used as F ratio, is used to test the significance of R^2 and implicitly, the significance of the regression model as a whole. It provides information whether the regression model has improved the accuracy of predictions to a statistically significant level. F is a function of R^2, the number of independents (*k*) and the number of cases (*n*) and is computed with k and (*n*-*k*-1) degrees of freedom:

$$F = \frac{R^2 / k}{(1 - R^2)/(n - k - 1)} \tag{7.8}$$

If prob(F) < 0.05 then the model is considered statistical significant at the 95% level and the null hypothesis of no linear relationship of the dependent to the independents (all regression coefficients are zero) can be rejected.

Multiple linear regression analysis relies on several underlying assumptions such as [7-9]:

- linearity of the relationship between the dependent and independent variables; the linear model in (7.1) is assumed to be the correct one, properly specified, with all relevant variables are included in the model;

- reliability of data - the predictor variables values are fixed (none or the x_i is a random variable) and are assumed to be error-free;
- errors are independent and normally distributed with mean 0 and constant variance (homoscedasticity);
- the response variables are independent and are normally distributed with the same variance as the errors.

Regression analysis was performed in MatLab 7.4.0 using the 'regress' function in the Statistics Toolbox. The function returns the least square fit of y, the vector of observations (dependent variables) on the regressors matrix **X** by solving the linear model (7.2). The function can also output the 95% confidence intervals for the regression coefficients, and a statistics vector (stats). The elements of the vector stats are the regression R^2 statistic, the F statistic (for the hypothesis test that all the regression coefficients are zero), the p-value associated with this F statistic, and an estimate of the error variance.

The primary scope of the present regression analysis is the prediction of a model capable to explain the resonator data. Regression analysis can also be used to explore the relationships between independent and dependent variables.

The research hypothesis can be stated as: the sensor's amplitude and phase response are affected by the physical properties of the liquid samples, particularly by the mechanical characteristics determined by density and viscosity and the electrical ones represented by conductivity and permittivity.

Multiple linear analyses was performed on the whole data-set (generalized model) as well as on each substance data individually (substance-dependent models). Sections 7.4.2 and 7.4.3 are presenting the results of the multivariate analysis.

7.4.2 Generalized model

The generalized model attempts to express the resonator results as a linear function of the mechanical and electrical properties of the tested samples. The data-set used for analysis was obtained by cumulating all measurements for acetic acid, sucrose and sodium chloride (with all available weight concentrations of 0.5% 1%, 3% and 5% included), hence the generic name of the model.

For the purpose of regression data with positive phase values (NaCl data) were translated with 360° to the negative phase domain. This transformation allowed phase values down to -205 degrees (for NaCl samples) and achieved a narrowing of the phase interval and implicitly a smaller error variance of the regression model. Regression analysis performed with un-processed phase data resulted in very large error variances rendering the model unusable.

The following notation is used for the rest of the chapter: A_M1 and P_M1 are used to denote amplitude and phase data measured at peak frequency that corresponds to marker M1 and A_M2, P_M2 represent amplitude and phase responses observed at constant frequency and given by marker M2. Before performing the regression analysis, amplitude and phase data were assessed using the normal density plots. Figure 7.18 shows that all measured data are normally or quasi-normally distributed, phase data for constant frequency P_M2 are slightly negatively skewed.

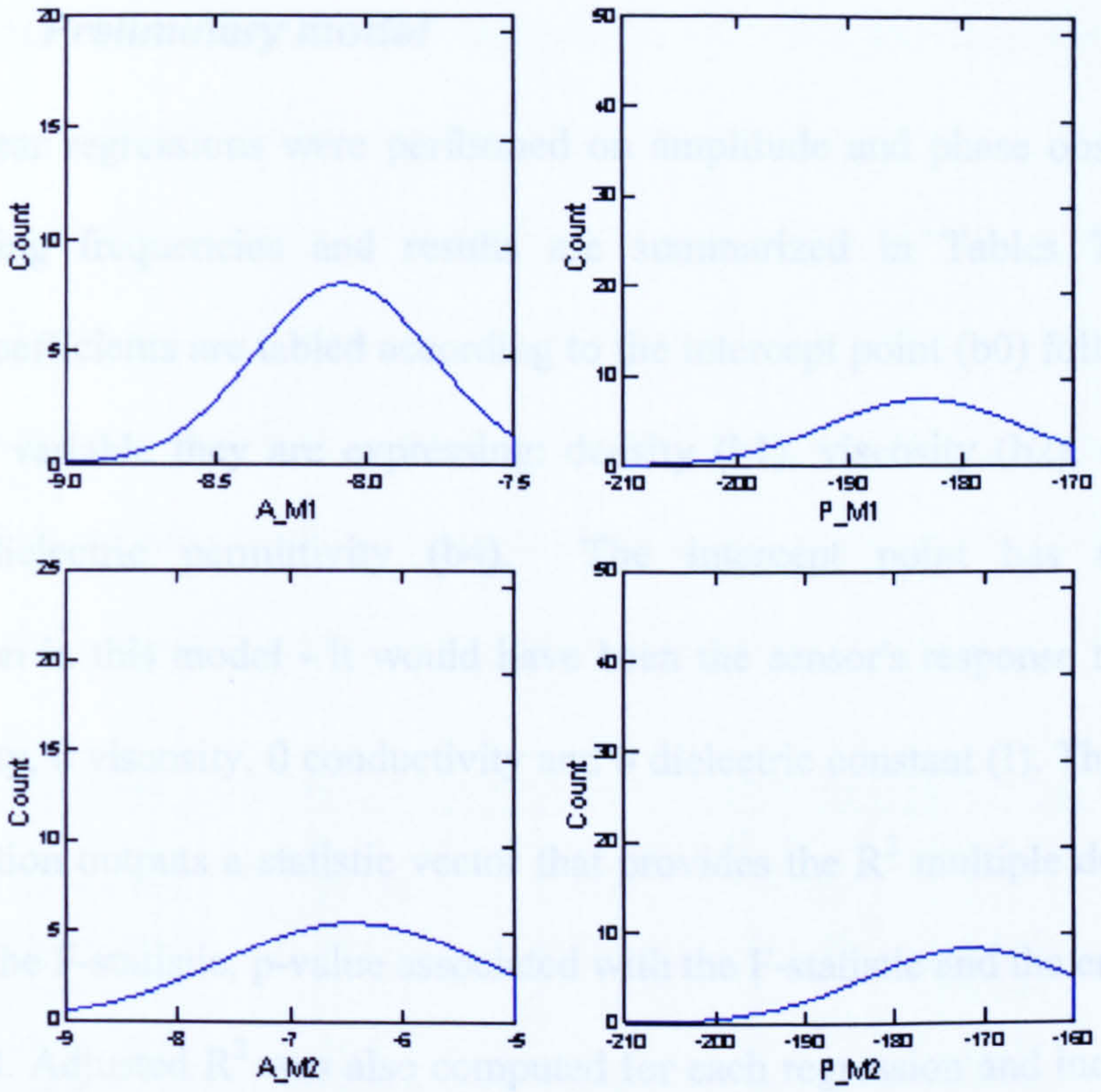

Figure 7.18: Normal density plots of A_M1, P_M1, A_M2 and P_M2 data

The parameters describing the mechanical and electrical behaviour of tested solutions considered for the regression models are listed in Table 7.2. A preliminary regression analysis is considered with the four tabled parameters as predictors: density, relative viscosity, conductivity and permittivity.

Plots of the dependent variables vs. each independent variable are included in Appendix B. These plots are not conclusive regarding the linearity nature of the dependent-independent relationship as the other independents in the model do not remain constant while varying the independent being assessed. As the rest of the parameters change along with the independent under consideration it is not possible to separate graphically the effect of a single independent from the cumulated overall response.

7.4.2.1 Preliminary model

Multiple linear regressions were performed on amplitude and phase observations at both operating frequencies and results are summarized in Tables 7.3-7.5. The regression coefficients are tabled according to the intercept point (b0) followed by the independent variable they are expressing: density (b1), viscosity (b2), conductivity (b3) and dielectric permittivity (b4). The intercept point has no physical representation in this model - it would have been the sensor's response to a medium with 0 density, 0 viscosity, 0 conductivity and 0 dielectric constant (!). The MATLAB regress function outputs a statistic vector that provides the R^2 multiple determination coefficient, the F-statistic, p-value associated with the F-statistic and the error variance of the model. Adjusted R^2 was also computed for each regression and included in the statistics output. Table 7.3 summarizes the computed b-regression coefficients and the associated statistic for each dependent variable considered.

Table 7.3: Summary of MLR analysis of the preliminary model (ρ, η, σ, ε_r as predictors)

	REGRESSION COEFFICIENTS					STATISTICS				
	b0	b1*ρ	b2*η	b3* σ	b4*ε_r	R^2	Adj R^2	F-test	p	error variance
A_M1	58.388	-0.099	15.319	0.593	0.224	0.8697	0.8575	71.755	0	0.012
P_M1	-392.469	0.378	-61.941	-7.350	-1.275	0.9856	0.9843	738.102	0	1.180
A_M2	-462.429	0.744	-117.713	-6.497	-2.099	0.9868	0.9856	806.517	0	0.019
P_M2	-789.835	1.075	-173.674	-13.151	-3.443	0.5029	0.4566	10.875	3.5E-06	75.443

The obtained R^2 regression coefficients are generally good: 85% of the variance in A_M1 and 98% of the variance in P_M1 and A_M2 is explained collectively by the four independent variables. The R^2 coefficient for phase at constant frequency (P_M2) is an exception to the general goodness-of-fit trend: R^2 for P_M2 has a value of 0.50 and an adjusted value of 0.45, indicating that only 50% of the phase variability is explained by the model. The error variance is large for both P_M1

dependent and particularly for P_M2 dependent, for which the error variance has an alerting value of 75.44. F-tests and the associated p-values suggest that the chosen independent variables (ρ, η, σ, ε_r) are able to predict all dependent variables (A_M1, P_M1, A_M2 and P_M2). Despite the validation of the regression models, the error variances on phase dependents remain too large for an accurate fitting of estimated data. More information on the models is obtained by studying the 95% confidence intervals for the regression coefficients, given in Table 7.4.

Table 7.4: Confidence interval limits for regression coefficients in preliminary model

		b0	b1*ρ	b2* η	b3*σ	b4*ε_r
A_M1	Lower Limit	24.095	-0.156	6.053	0.137	0.060
	Upper Limit	92.680	-0.044	24.585	1.049	0.388
P_M1	Lower Limit	-726.507	-0.167	-152.198	-11.791	-2.872
	Upper Limit	-58.430	0.924	28.315	-2.909	0.320
A_M2	Lower Limit	-505.672	0.673	-129.398	-7.072	-2.307
	Upper Limit	-419.186	0.815	-106.029	-5.923	-1.893
P_M2	Lower Limit	-3460.450	-3.287	-895.269	-48.657	-16.205
	Upper Limit	1880.776	5.436	547.921	22.354	9.318

The confidence intervals for a regression coefficient are computed from the estimate bj using the standard deviations and the appropriate critical value t^* from the $t(n\text{-}p\text{-}1)$ distribution [10]. The 95% confidence interval is the plus/minus range around the observed sample regression coefficient within which we can be 95% confident that the real regression coefficient for the population lies. If the confidence interval of an estimated regression coefficient includes 0, there is no significant linear relationship between the dependent and the predictor associated with that coefficient [7]. MatLab can output the lower and upper limits for the confidence intervals of each predictor. These are organized in Table 7.4 according to the dependent of each regression. The confidence intervals for density, viscosity and permittivity in the P_M1 regression contain 0, leaving conductivity the only predictor in the model to explain the 98% of the variance in P_M1 data (as indicated by R^2). In the case of the multiple linear

regression on phase data at constant frequency, P_M2, the confidence intervals for **all** regression coefficients, including the intercept b0, contain 0 in their interval. The confidence intervals are also related to the p-values of each coefficient (given in P_M2 MLR in Appendix B). All the p-values associated to the P_M2 regression coefficients are all larger than 0.05 indicating that none of the coefficients in this model is statistically significant and the P_M2 model needs to be re-specified.

An analysis of the model residuals indicates the presence of outliers for three of the dependents. A_M1 analysis is affected by the samples of NaCl 0.5%, while for P_M1 and P_M2 analysis NaCl 3% phase values are considered as outliers. The residuals case ordered plots for each analysis are shown in Figure 7.19.

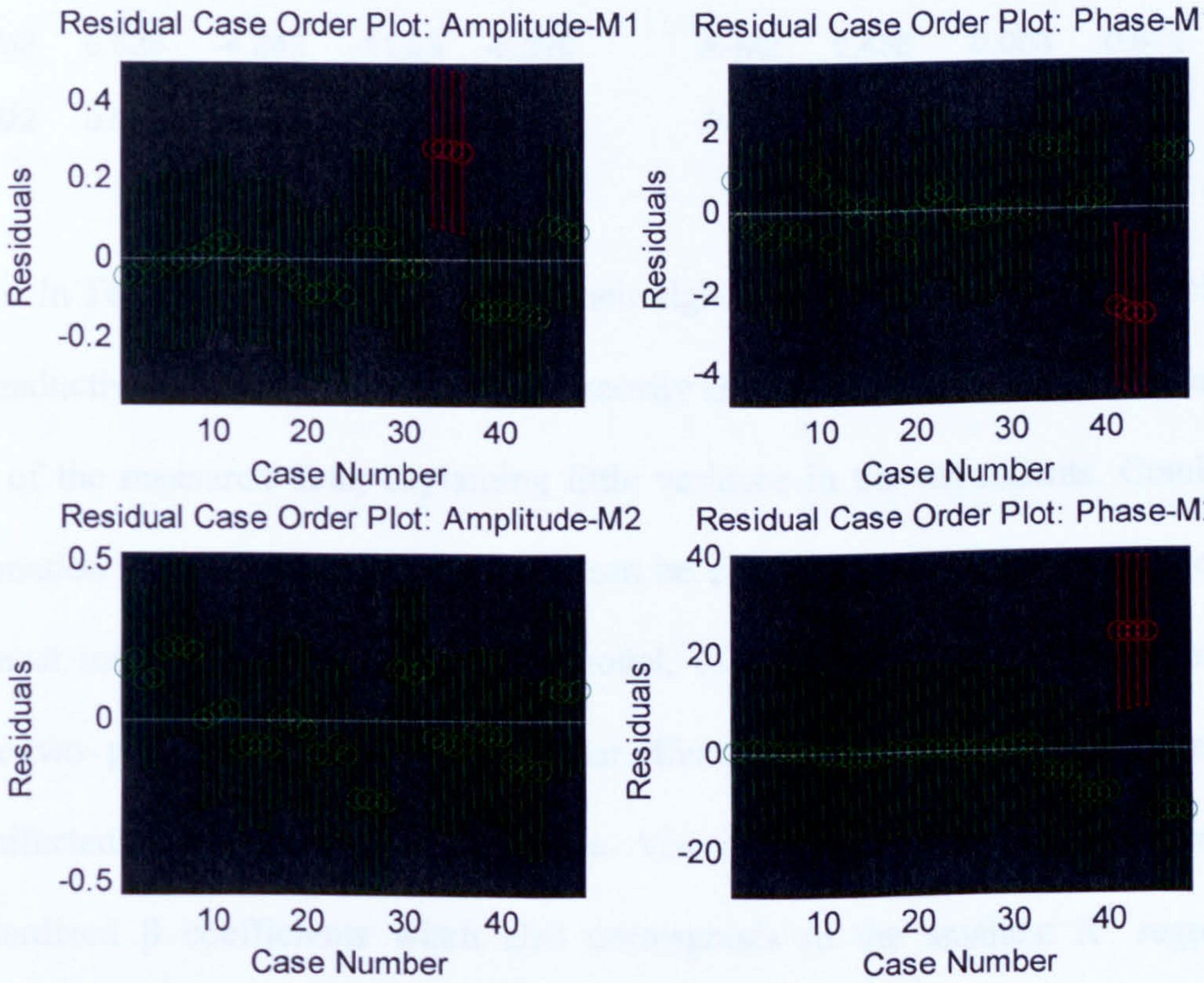

Figure 7.19: Case ordered residual plots for the preliminary model

The standardized regression coefficients for each model were also computed and are included for reference in Table 7.5. The presence of multicollinearity in the independent data makes it difficult to assess the relative importance of each predictor.

This information would have been helpful for the re-definition of the model, when choosing which the predictors to be kept in and which to be eliminated from the model. Table 7.6 provides R^2 coefficients for simple linear regressions performed on dependents vs. each independent at a time. While the relative importance of the predictors in a model can change when introducing a new predictor, the R^2 simple regression coefficients (square root of Pearson correlation coefficients) will remain the same, characterising the dependent-independent individual relationships.

Table 7.5: Standardized regression coefficients - preliminary model

	$\beta1*\rho$	$\beta2*\eta$	$\beta3*\sigma$	$\beta4*\varepsilon_r$
A-M1	-3.475	2.191	4.350	2.679
P-M1	0.449	-0.301	-1.835	-0.519
A-M2	6.528	-4.242	-11.99	-6.326
P-M2	0.938	-0.623	-2.416	-1.032

Table 7.6: R^2 coefficients for simple linear regressions on each independent

	ρ	η	σ	ε_r
A-M1	0.664	0.019	0.810	0.708
P-M1	0.692	0.010	0.984	0.896
A-M2	0.436	0.003	0.819	0.702
P-M2	0.338	0.002	0.498	0.445

In Table 7.6 all dependents have their highest percentage of variance explained by conductivity; at the other extreme, viscosity is the less correlated parameter with each of the measured data, explaining little variance in the dependents. Combining information in both tables 7.5 and 7.6 it can be estimated that conductivity is one of the most influential parameters in the model, followed by density and permittivity (these two parameters seem to have similar effects and their relative importance may be affected by multicollinearity). The viscosity parameter has the smallest standardized β coefficients witch also corresponds to the smallest R^2 regression coefficients in Table 7.6, suggesting that viscosity would be the least significant predictor in a multicollinearity free model. Also, among all of the b_j regression coefficients, viscosity has the highest standard error associated with its coefficient (see SigmaStat regression reports in Appendix B). In order to minimize the model error

variance, viscosity can be either eliminated from the predictors or replaced with an interaction factor.

7.4.2.2 *Improved generalized model*

Following the preliminary exploratory model above, an improved regression model was obtained when viscosity was substituted by the square root of the viscosity-density product and a new predictor in the form of conductivity square was introduced to account for non-linear effects in the data. The new model remains linear in its parameters ($\rho, \sqrt{\eta\rho}$, σ, σ^2, ε_r), even if predictors now include quadratic terms. The regression coefficients for the new generalized model are summarized in Table 7.7. Statistics indicators are also included for each dependent.

Table 7.7: Summary of MLR analysis of the improved model ($\rho, \sqrt{\eta\rho}$, σ, σ^2 and ε_r as predictors)

	REGRESSION COEFFICIENTS						STATISTICS				
	b0	b1*ρ	b2* $\sqrt{\eta\rho}$	b3*σ	b4*σ^2	b5*ε_r	R^2	Adj R^2	F-test	p	error variance
A_M1	133.755	-0.262	2.308	1.462	0.025	0.593	0.8996	**0.8877**	75.307	0	0.009
P_M1	790.493	-1.847	16.384	6.078	0.419	4.445	0.9948	**0.9942**	1626.994	0	0.432
A_M2	-365.909	0.686	-6.060	-5.483	0.039	-1.659	0.9935	**0.9928**	1300.074	0	0.009
P_M2	-11448.5	21.935	-195.664	-134.6	-3.749	-55.162	0.8994	**0.8874**	75.132	0	15.625

The statistics values of the new model show the improvements achieved over the preliminary model. R^2 values are larger for all dependents, indicating that a larger percentage of the data variance is explained by the new set of predictors. An important improvement is observed for P_M2 dependent where R^2 increased from 0.5 to approximately 0.9. A comparison of the goodness-of-fit of two models with different number of predictors has to be based on adjusted R^2 values. The improved model presents larger adjusted R^2 values for all of the dependents, indicating that the new

predictors are indeed contributing to the predictive capability of the improved model. The F-statistics and p-values computed for regressions on each dependent are statistically significant, validating the model and allowing rejection of the null hypothesis. Last but not least, the improved model has a lower error variance for each dependent, allowing for more accurate predictions. Notable improvements are observed for phase dependents: the error variance for P_M1 reduced from 1.18 deg to 0.43 deg, while error variance for P_M2 improved form 75.4 deg to 15.6 deg. While these values represent important improvements to the preliminary model, it is feared that the phase error remain still too large for a very accurate and reliable prediction.

Another improvement to the model is reflected in the confidence intervals for the regression coefficients. Table 7.8 gives the lower and upper limit for each of the regression coefficients for A_M1, P_M1, A_M2 and P_M2 dependents. All confidence intervals exclude 0 and all b regression coefficients are statistically significant.

Table 7.8: Confidence interval limits for regression coefficients of the improved model

		b0	b1*ρ	b2*$\sqrt{\eta\rho}$	b3*σ	b4*σ^2	b5*ε_r
A_M1	Lower Limit	81.385	-0.364	1.394	0.825	0.011	0.339
	Upper Limit	186.124	-0.161	3.222	2.099	0.040	0.846
P_M1	Lower Limit	442.794	-2.520	10.316	1.850	0.322	2.760
	Upper Limit	1138.193	-1.174	22.451	10.307	0.517	6.130
A_M2	Lower Limit	-418.479	0.584	-6.977	-6.122	0.025	-1.914
	Upper Limit	-313.339	0.788	-5.143	-4.844	0.054	-1.404
P_M2	Lower Limit	-13538.7	17.889	-232.142	-160.081	-4.336	-65.291
	Upper Limit	-9358.26	25.981	-159.187	-109.241	-3.161	-45.033

Standardized coefficients for the improved model are given in Table 7.9 and the dependent-independent correlation coefficients are summarized in Table 7.10. If

the model would not have been affected by multicollinearity, the standardized coefficients could have been compared to asses the relative predictive power of each independent. For a multicollinearity-free data-set the model would have been dominated by conductivity, density and permittivity (in this order of importance) for A_M1, A_M2 and P_M2, respectively density, permittivity and conductivity for P_M1. The square root of viscosity-density product would seem to have the fourth hierarchic level among all predictors and conductivity squared would have the smallest beta weights for each dependent (see table 7.9). Dependent-independent correlation coefficients in Table 7.10 agree well with the hierarchical importance of predictors established using the standardized coefficients.

Table 7.9: Standardized regression coefficients of the improved model

	$\beta1*\rho$	$\beta2*\sqrt{\eta\rho}$	$\beta3*\sigma$	$\beta4*\sigma^2$	$\beta5*\varepsilon_r$
A-M1	-9.146	5.940	10.715	1.245	7.090
P-M1	-2.190	1.436	1.517	0.687	1.811
A-M2	6.018	-3.929	-10.123	0.482	-4.998
P-M2	19.146	-12.629	-24.746	-4.516	-16.540

Table 7.10: Correlation coefficients between dependents and independents

	ρ	$\sqrt{\eta\rho}$	σ	σ^2	ε_r
A-M1	-0.814	-0.299	-0.900	-0.884	0.841
P-M1	-0.832	-0.271	-0.992	-0.940	0.946
A-M2	-0.660	-0.094	-0.905	-0.782	0.838
P-M2	-0.581	-0.172	-0.705	-0.758	0.667

The improved model presents a high degree of multicollinearity between its independent variables, and consequently, the above assessment based on β-coefficients may not prove to be a reliable one. Conductivity is highly correlated with permittivity (with a -0.961 Pearson correlation coefficient) and density has correlations coefficients of 0.845 and -0.862 with conductivity, respectively permittivity. Thus, the primary cause for multicollinearity lays in the physical nature of the independent data and the underling relations between them. A secondary cause for the model multicollinearity is due to the introduction of the power and cross-

product terms - this 'type of multicollinearity' is intentional and justified by the theoretical model, but collinearity diagnostics reports it as multicollinearity.

Multicollinearity can lead to high standard errors of the regression coefficients (both standardized and un-standardized) and undermines the ability to rank the importance of the predictors. It is important to note that multicollinearity among the independents does not impact the reliability of the forecast, but rather impacts the interpretation of the independents (explanatory variables). If the main purpose of the regression is sheer prediction (versus causal analysis), high multicollinearity neither invalidates the model, nor affects the efficiency of the regression estimates.

The model improvements are also mirrored in the residual analysis. Plots of residuals are given for each of the four dependent variables as case ordered plots (Figure 7.20) and as residuals vs. predicted value plots (Figure 7.21). The data corresponding to NaCl solution with the lowest concentration (0.5%) are still marked as outliers in the amplitude analysis at peak frequency A_M1, but the residual distributions for phase data P_M1 and P_M2 are improved, presenting no outliers for the model.

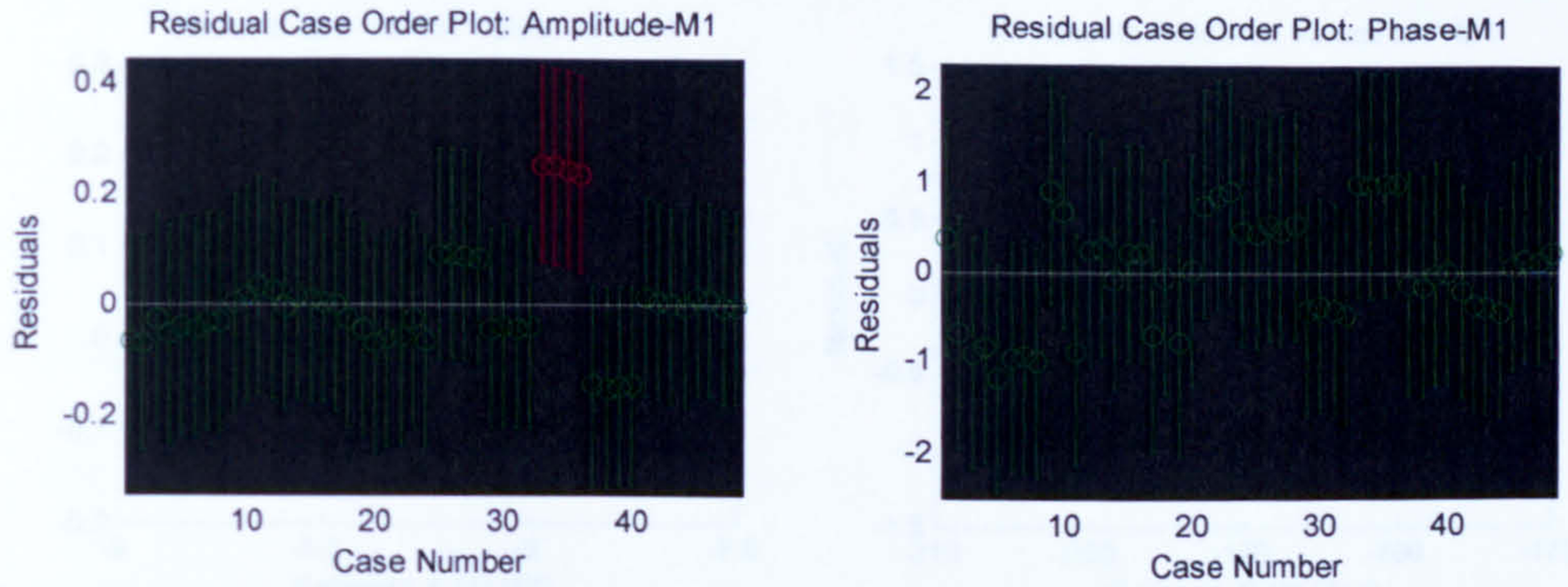

Figure 7.20: Case ordered residual plots for regressions on each dependent in the improved model

Residual vs. predicted value plots (Figure 7.21) are used to check the model assumptions. The symmetrical distribution of residuals around the zero horizontal line confirms the linearity assumption for the model. Violations to the homoscedasticity assumption can also be detected using residual vs. predicted value plots in Figure 7.21. Residuals that are getting larger as a function of the predicted value can be an alerting sign for heteroscedasticity. Such tendencies are observed for A_M1 and P_M2 but appear more clearly for P_M1 data. Indeed, the constant variance test is failed for the P_M1 model. A_M1, A_M2 and P_M2 models all pass the constant variance tests, confirming the homoscedasticity assumption. The constant variance test is part of the SigmaStat reports included in Appendix B.

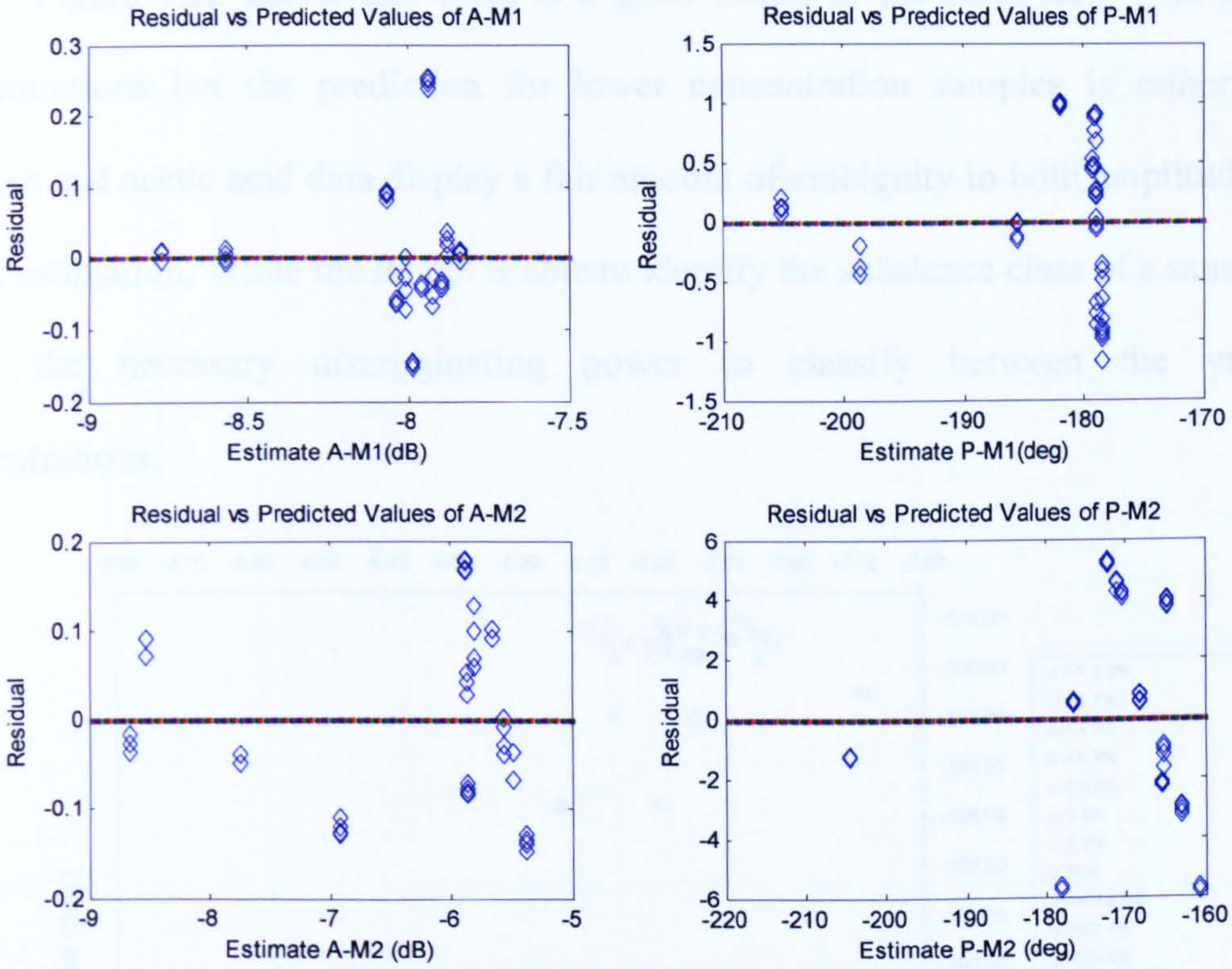

Figure 7.21: Residuals vs. predicted values of each dependent variable

Following the regression analysis, prediction equations can be formulated using the b-regression coefficients for each of the dependents considered. These equations are subsequently used to estimate the sensor's response. Figures 7.22 and 7.23 plot the measured and estimated results for the peak, respectively constant frequency operation modes. In addition to the standard least squares estimate denoted by 'Est', the plots also include the robust fit estimated values (marked as 'Robust Est'). The robust regression is limiting the effects of the outliers by giving them a reduced weight. In MatLab the weighting is done automatically: In the first iteration, the fit is an ordinary least squares fit with each point having the same weight. Then new weights are computed to give lower weight to points that are far from their predicted values, and the fit is repeated using these weights. The process continues until it converges [11]. The robust estimated values are in general close to the least square estimated values, larger differences are obtained for outlier cases.

Figure 7.22 shows that there is a good fitting of the NaCl data with higher concentrations but the prediction for lower concentration samples is rather low. Sucrose and acetic acid data display a fair amount of ambiguity in both amplitude and phase estimation. While the model is able to identify the substance class of a sample, it lacks the necessary discriminating power to classify between the various concentrations.

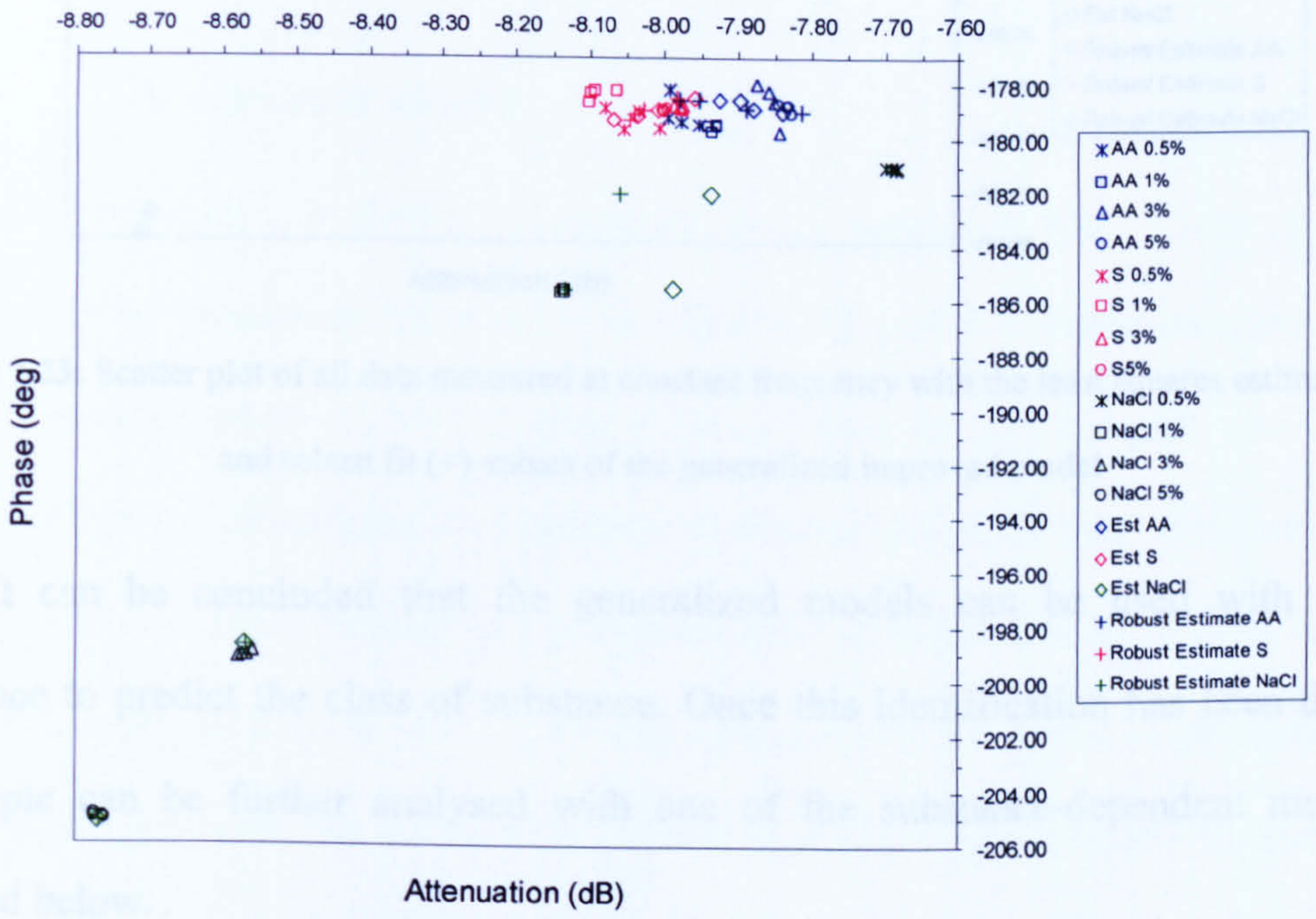

Figure 7.22: Scatter plot of all data measured at peak frequency with the least squares estimated (◊) and robust fit (+) values of the generalized improved model

In the data-estimations plot in Figure 7.23, the effect of the large error variance of the model is clear at first sight. Phase errors can be as large as 6 degrees. Amplitude error is much smaller, helping the discrimination between the three substance classes.

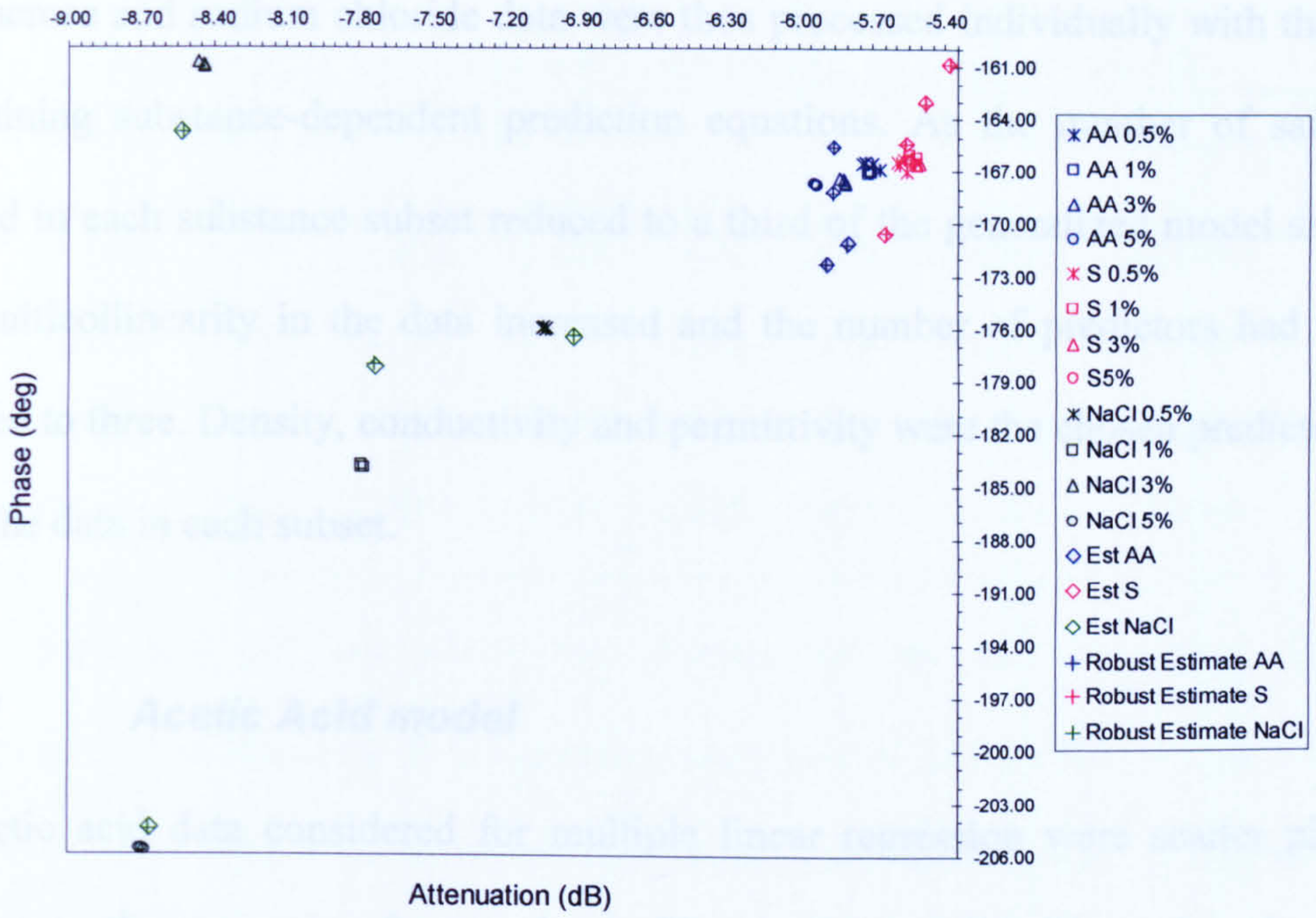

Figure 7.23: Scatter plot of all data measured at constant frequency with the least squares estimated (◊) and robust fit (+) values of the generalized improved model

It can be concluded that the generalized models can be used with high confidence to predict the class of substance. Once this identification has been done, the sample can be further analysed with one of the substance-dependent models discussed below.

7.4.3 Substance-dependent regression models

Despite the good R^2 regression coefficients obtained for the generalized improved model, the error variance remains still too large for a very reliable fitting of data. Introducing more independents in the model (in the form of power or cross-product interaction terms) will further reduce the error but there is the danger of overfitting the data.

The resonator's response was further analysed by evaluating subsets of data in which all samples for the same class of substance were considered at a time. Acetic

acid, sucrose and sodium chloride data were thus processed individually with the aim of obtaining substance-dependent prediction equations. As the number of samples included in each substance subset reduced to a third of the generalized model sample size, multicollinearity in the data increased and the number of predictors had to be restricted to three. Density, conductivity and permittivity were the chosen predictors to model the data in each subset.

7.4.3.1 Acetic Acid model

The acetic acid data considered for multiple linear regression were scatter plotted according to the measuring frequencies in Figures 7.6 and 7.7. Phase data for peak frequency measurements (P_M1) display visible outliers for AA samples with 0.5% and 3% weight concentrations. A regression performed on phase data which include these two visible outliers resulted in a poor coefficient of determination of 0.38, with a corresponding adjusted value of 0.23; the large p-value of 0.11 for the model indicates that the null hypothesis can not be rejected and model is not statistically significant. The two outliers marked in Figure 7.19 were eliminated from the data-set before running the regression analysis. This resulted in a much better, statistically significant model with lower error variance and a larger coefficient of determination of R^2=0.90, with an adjusted value of 0.87. All other dependents have coefficients larger than 0.97 implying that at least 97% of the data variance is explained by density, conductivity and permittivity variables. Regression coefficients and statistics parameters for each dependent are summarized in Table 7.11.

Table 7.11: Summary of MLR analysis for acetic acid data (ρ, σ, ε_r as predictors)

	REGRESSION COEFFICIENTS				STATISTICS				
	b0	b1*ρ	b2* σ	b3*ε_r	R^2	Adj R^2	F-test	p	error variance
A_M1	-97.224	0.077	1.353	0.144	0.970	0.961	108.290	6.35E-08	0.0001
P_M1	-10638.1	9.091	-7.144	17.212	0.903	0.874	31.102	2.21E-05	0.0356
A_M2	122.299	-0.118	1.604	-0.119	0.989	0.985	300.652	4.27E-10	0.0001
P_M2	-907.042	0.650	-17.658	1.141	0.978	0.971	150.174	1.29E-08	0.0064

F-tests and p-values allow the rejection of the null hypothesis for all dependents. The residuals of each regression were plotted against the predicted values in Figure 7.24. Residuals are randomly distributed along the zero-line, confirming the linearity assumption.

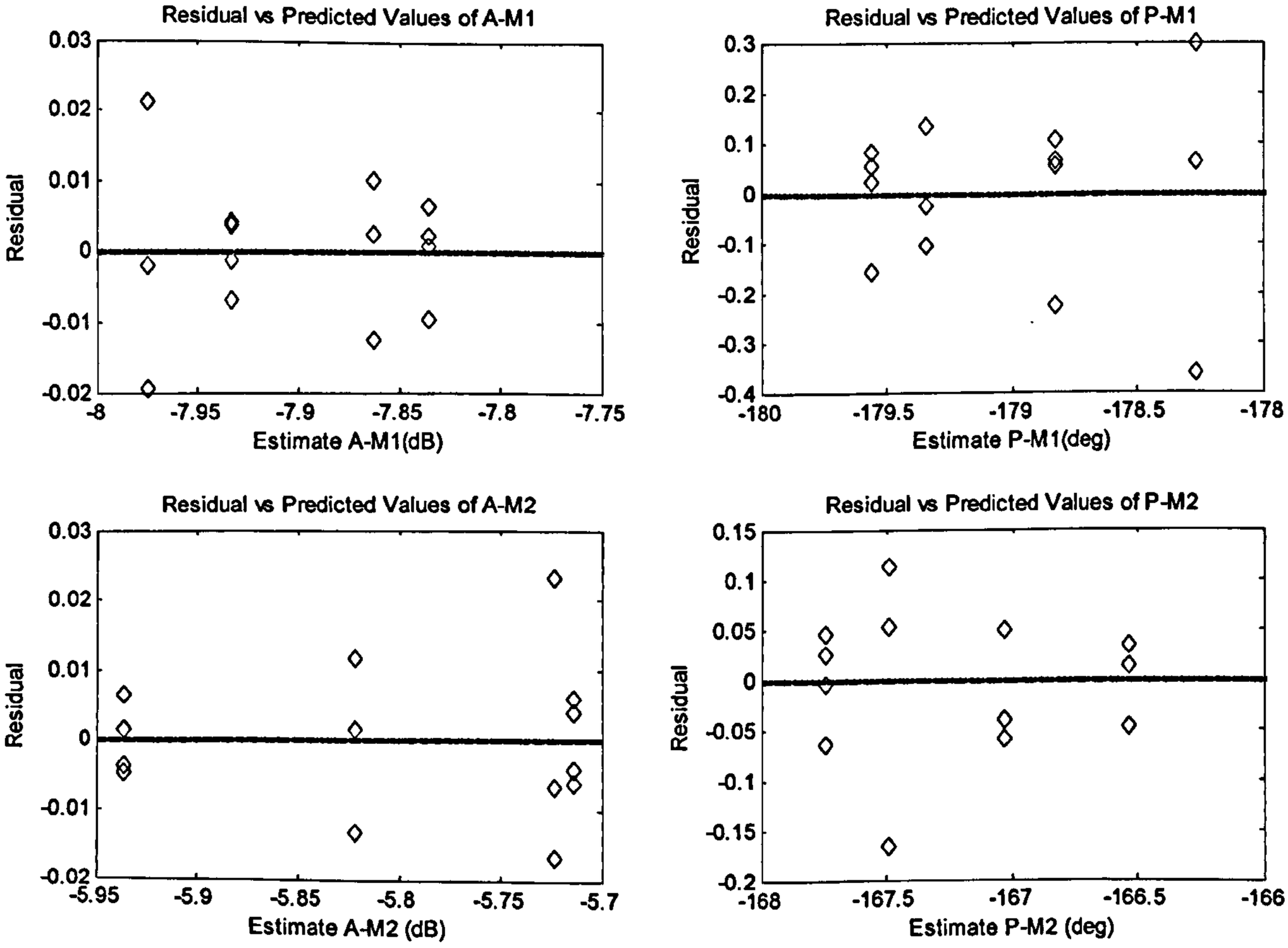

Figure 7.24: Residuals vs. predicted values plots for acetic acid solutions

The regression coefficients in Table 7.11 were used to calculate the estimated sensor's response for the given predictors. Modelled (estimated) data are scattered plotted in respect to the measured data in Figures 7.25 and 7.26. As seen from the plots, the predicted values fit well within the measured clusters, a fact that confirms the predictive power of the regression models for acetic acid data.

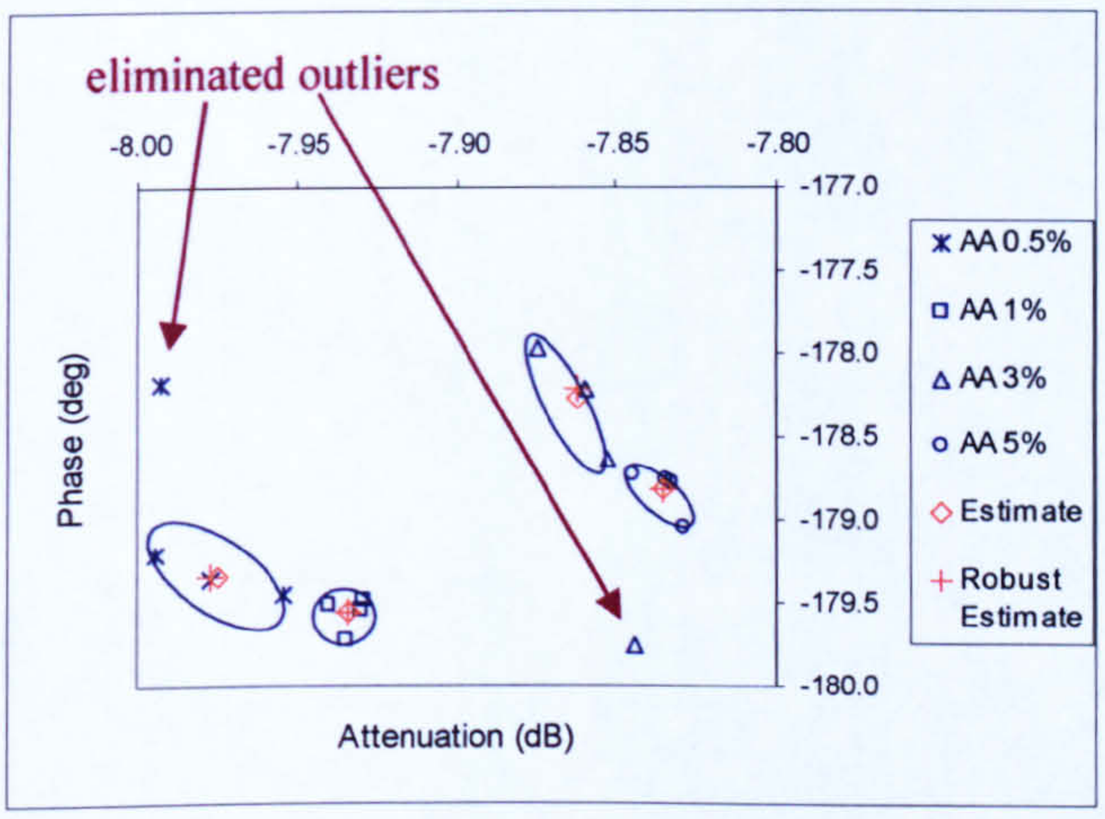

Figure 7.25: Acetic acid solutions measured at peak frequency with predicted values

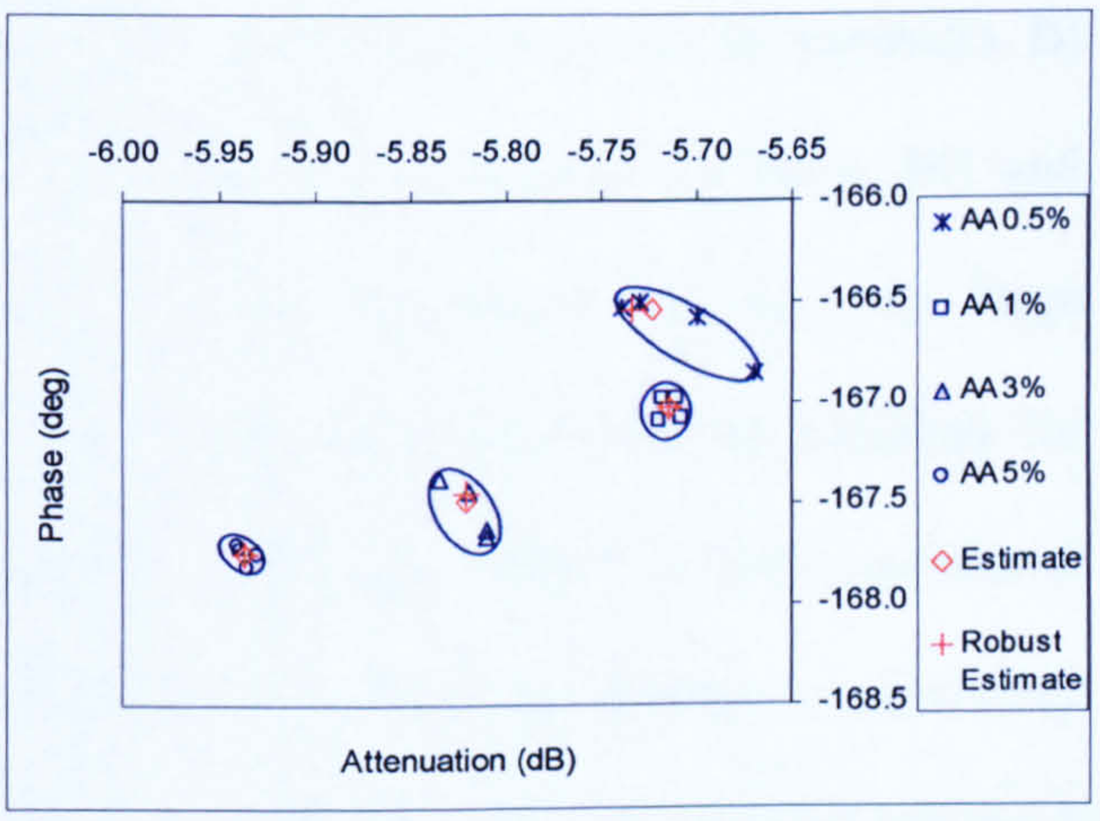

Figure 7.26: Acetic acid solutions measured at constant frequency with predicted values

7.4.3.2 Sucrose model

A similar analysis was performed for sucrose data collected at M1 and M2 markers and the regression results are presented in Table 7.12.

Table 7.12: Summary of MLR analysis for sucrose data (ρ, σ, ε_r as predictors)

	REGRESSION COEFFICIENTS				STATISTICS				
	b0	b1*ρ	b2* σ	b3*ε_r	R^2	Adj R^2	F-test	p	error variance
A_M1	-3210.1	1.354	-2522.09	23.016	0.882	0.853	30.041	0	0.0003
P_M1	13672.73	-5.880	-28875.4	-99.259	0.723	0.653	10.439	0	0.0558
A_M2	-993.05	0.4148	-3764.48	7.132	0.799	0.749	15.978	0	0.0001
P_M2	16732.81	-7.139	3996.764	-121.545	0.569	0.461	5.282	0.01	0.0339

Despite the apparent random nature of sucrose data evolution, the regression models do show some degree of linearity between both amplitude and phase data and the chosen predictors. Higher R^2 coefficients were obtained for amplitude data regressions (A_M1 and A_M2). Conductivity has very large regression coefficients for all regressions - this is probably due to the very small values conductivity takes for sucrose samples. The standardized regression coefficients (included in Appendix B) suggest that the sensor's response is highly dominated by density for the A_M1 and P_M1 and by permittivity for A_M2 and P_M2. However, due to very large multicollinearity in the independent data it is practically impossible to establish the relative effect of each predictor. All regression models in Table 7.12 have significant F-tests and p-values, so all dependents are indeed affected by density, conductivity and permittivity. Residuals for all sucrose models are randomly distributed around 0 (see plots in Figure 7.22) confirming that the linearity assumption is not violated.

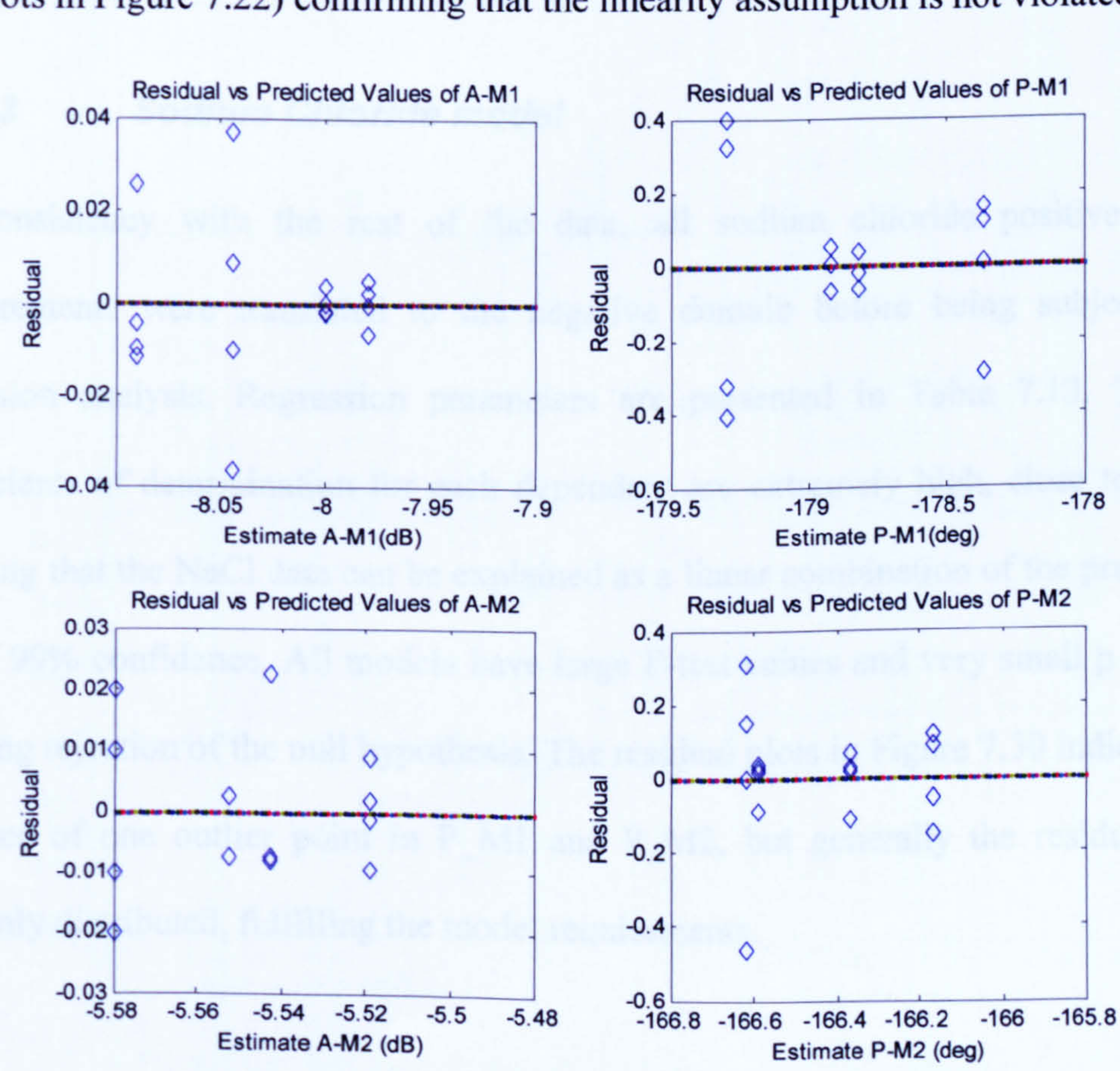

Figure 7.27: Residuals vs. predicted values plots for sucrose solutions

Estimated values were computed using the b- correlation coefficients in Table 7.12 and were plotted in Figures 7.23 and 7.24. Once again, a good correspondence between the model predicted values and the measured values was observed, an it is mainly attributed to the small error variances of the model.

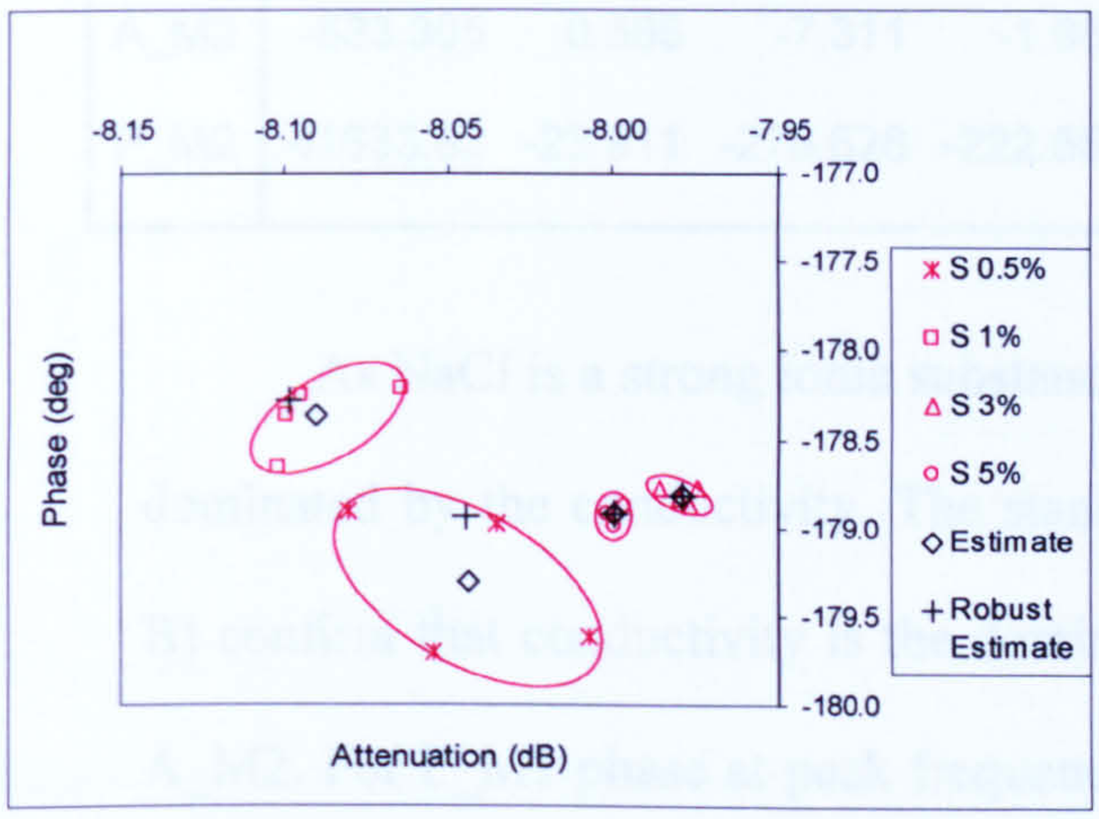

Figure 7.28: Sucrose solutions measured at peak frequency with predicted values

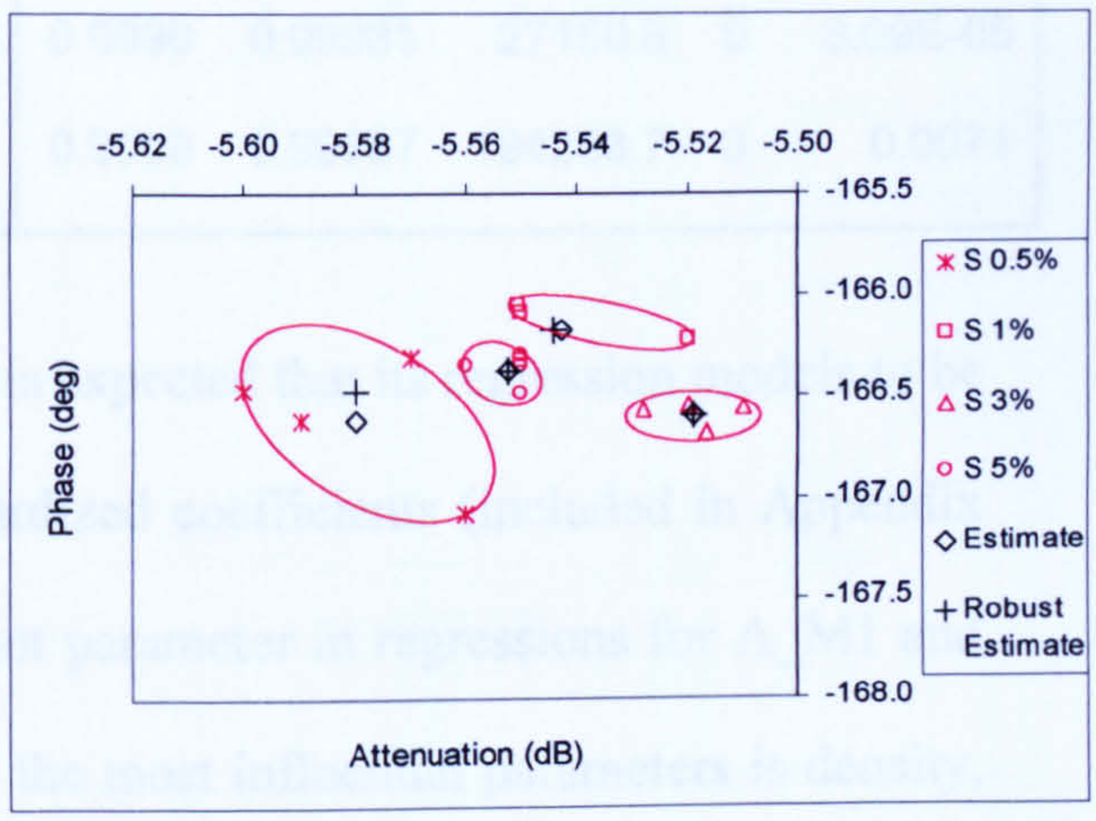

Figure 7.29: Sucrose solutions measured at constant frequency with predicted values

7.4.3.3 Sodium Chloride model

For consistency with the rest of the data, all sodium chloride positive phase measurements were translated to the negative domain before being subjected to regression analysis. Regression parameters are presented in Table 7.13. The R^2 coefficients of determination for each dependent are extremely high, close to unity, implying that the NaCl data can be explained as a linear combination of the predictors with a 99% confidence. All models have large F-test values and very small p values, allowing rejection of the null hypothesis. The residual plots in Figure 7.30 indicate the presence of one outlier point in P_M1 and P_M2, but generally the residuals are randomly distributed, fulfilling the model requirements.

Table 7.13: Summary of MLR analysis for NaCl data (ρ, σ, ε_r as predictors)

	REGRESSION COEFFICIENTS				STATISTICS				
	b0	b1*ρ	b2* σ	b3*ε_r	R^2	Adj R^2	F-test	p	error variance
A_M1	-301.782	0.390	-4.319	-1.186	0.9997	0.99972	17996.15	0	5.1E-05
P_M1	-5339.44	4.313	-7.353	10.649	0.9999	0.99995	100036.8	0	0.0050
A_M2	-533.305	0.685	-7.311	-1.953	0.9998	0.99981	27150.8	0	8.09E-05
P_M2	41633.82	-23.911	-276.626	-222.557	0.9999	0.99997	194283.7	0	0.0071

As NaCl is a strong ionic substance is expected that its regression models to be dominated by the conductivity. The standardized coefficients (included in Appendix B) confirm that conductivity is the dominant parameter in regressions for A_M1 and A_M2. For P_M1 phase at peak frequency the most influential parameters is density, while for phase at constant frequency , the sample's permittivity has the higher effect.

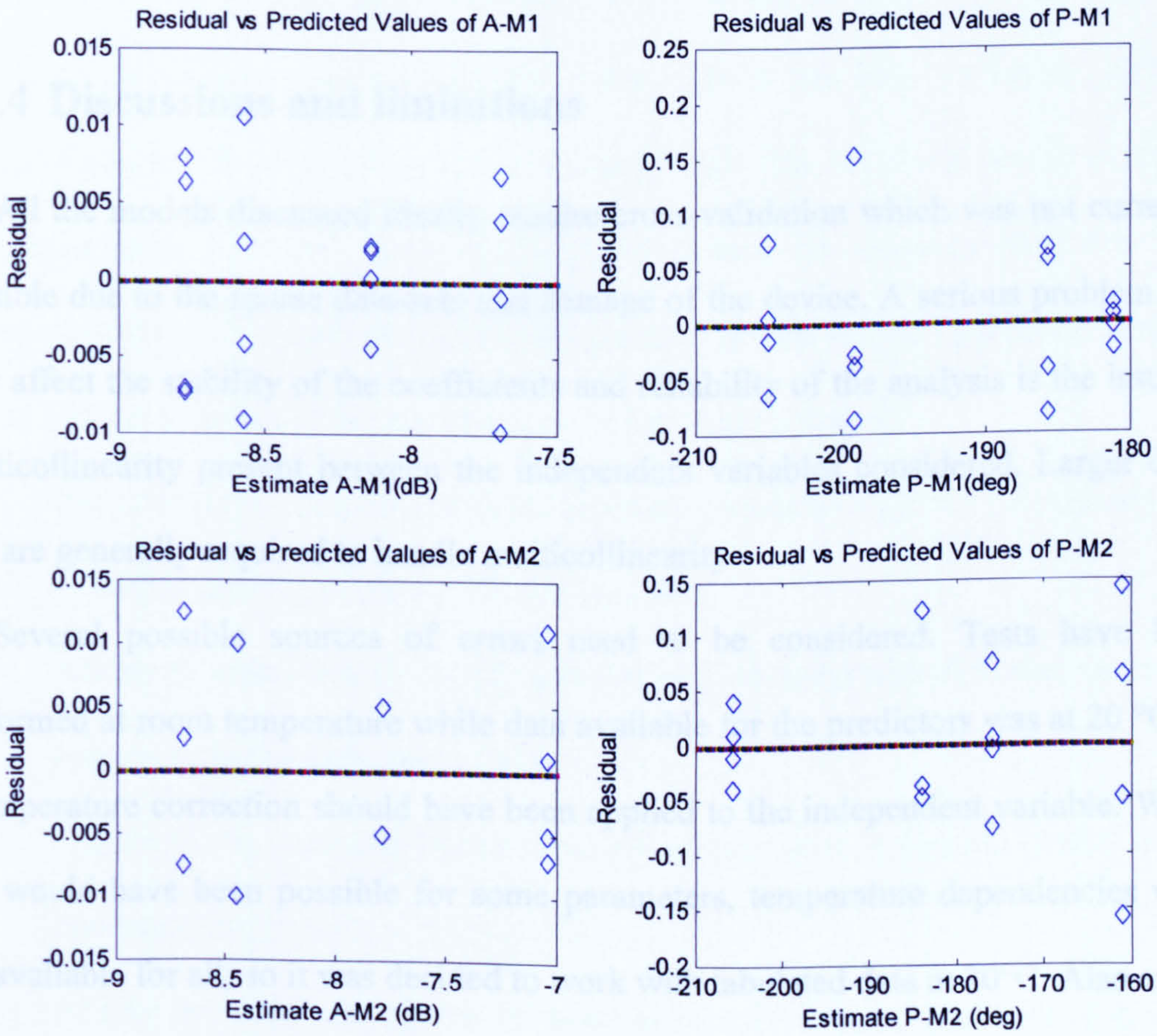

Figure 7.30: Residuals vs. predicted values plots for NaCl solutions

Scatter plots of the estimated data show a precise fitting of the measured data (Figure 7.31 and 7.32), confirming once again the increased predictive power of the substance-dependent models.

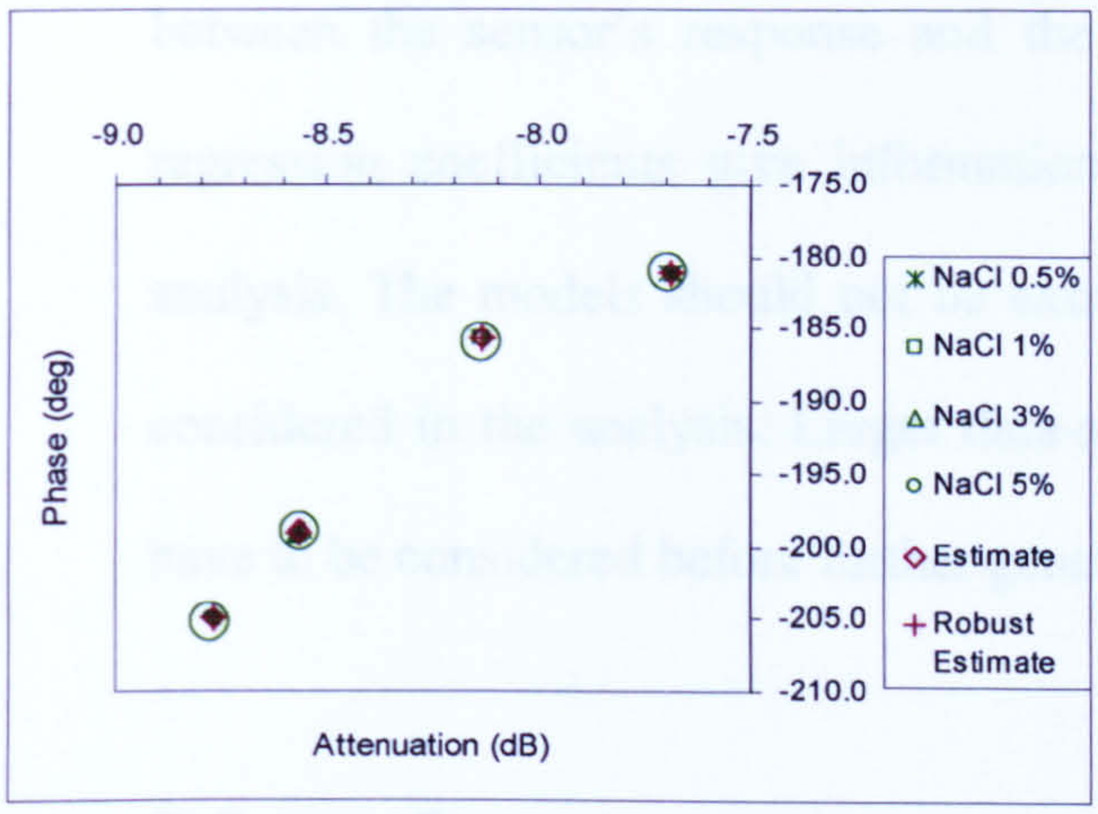

Figure 7.31: NaCl solutions measured at peak frequency with predicted values

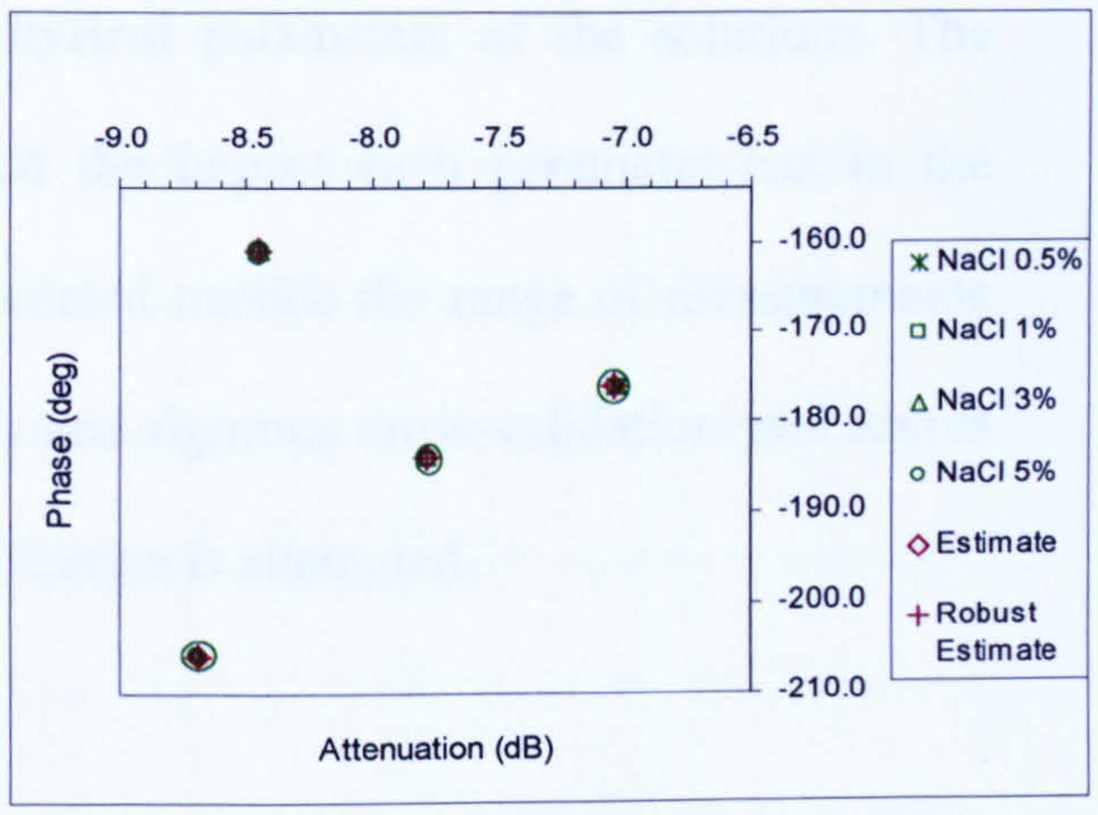

Figure 7.32: NaCl solutions measured at constant frequency with predicted values

7.4.4 Discussions and limitations

All the models discussed ideally require cross-validation which was not currently possible due to the sparse data-sets and damage of the device. A serious problem that may affect the stability of the coefficients and reliability of the analysis is the issue of multicollinearity present between the independent variables considered. Larger data-sets are generally required to handle multicollinearity.

Several possible sources of errors need to be considered. Tests have been performed at room temperature while data available for the predictors was at 20 °C, so a temperature correction should have been applied to the independent variable. While this would have been possible for some parameters, temperature dependencies were not available for all, so it was decided to work with tabulated data at 20°C. Also errors

in measuring the solute weight/volume when preparing the liquid solutions have to be considered as they would also reflect in the values of the predictors.

The analysis performed on the taste data is exploring the possible dependencies between the sensor's response and the physical parameters of the solutions. The regression coefficients give information on the impact each parameter has in the analysis. The models should not be extrapolated outside the range of measurements considered in the analysis. Larger data-sets and rigorous cross-validation procedures have to be considered before further generalization is attempted.

7.5 CONCLUSIONS

The SH-SAW sensor is capable of responding to the physical properties of the liquid solutions. The liquid solutions were chosen as they have been used as standards for taste, and a substantial body of work has been performed on these solutions and is available in the literature. Whilst the SH-SAW sensor is able to discriminate between these solutions, it cannot be assumed that this is a measurement of "taste" per se. The conclusions of this chapter can be summarized as follows in terms of the performance of the sensor system:

- Successful classification of liquid samples associated with different basic tastes – clear clustering of all 0.1 M taste samples;
- Ability to separate and identify samples implemented with different substances belonging to the same taste class;
- Capability to measure liquid samples of the same substance with varying concentrations;
- Ability to detect mixtures of solutions and separate them from original component solutions;

- MVA – confirmed that that resonator's responses are influenced by the physical properties of the tested solutions. Models derived are statistically significant and can used to approximate/explain high percentage of the measured data.
    - o A preliminary generalized model containing the fundamental parameters is able to express a significant percentage of the error variance. The simplest model appears to be noisy and due to large error variance in phase data it lacks the ability to fit the data accurately;
    - o Better prediction for the whole data is obtained using the improved generalized model, which contain interaction and quadratic terms of the fundamental parameters;
    - o Substance-dependent models have a high prediction power; the estimated values are accurately fit to the cluster they belong to.
    - o Ridge regression can be used as a complementary tool to handle the multicollinearity present in the independent variables and to reliably establish the relative predictive importance of the independent variables.

7.6 REFERENCES:

[1] D.S. Ballantine, R. M. White, S. J. Martin, A.J. Ricco, E.T. Zellers. G. C. Frye, H. Wohltjen, *Acoustic Wave Sensors: theory design and physico-chemical applications*, Accademic Press, 1997.

[2] R.C. Weast (Ed.), *CRC handbook of chemistry and physics: a ready-reference book of chemical and physical data*, Boca Raton, CRC Press, 1998.

[3] J. Hilland, "Simple sensor system for measuring the dielectric properties of saline solutions", Meas. Sci. Technol., 8, pp 901-910, 1997.

[4] J. Timmermans, *The Physico-chemical Constants of Binary Systems in Concentrated Solutions*, volume 4, London, Interscience Publishers, 1960.

[5] C.G. Malmberg and A.A. Maryott, "Dielectric Constants of Aqueous Solutions of Dextrose and Sucrose", Journal of Reasearch of the National Bureau of Standards, vol. 45, No. 4, p. 299, 1950.

[6] MATLAB 7.4.0, Documentation – Mathematical Foundations of Multiple Linear Regression.

[7] G. David Garson, (2008). "Multiple Regression", http://www2.chass.ncsu.edu/garson/PA765/regress.htm.

[8] R.F. Nau, (2008). "Testing the assumption of linear regression: Advanced regression methods, GLM and ANOVA" http://www.duke.edu/~rnau/Decision411CoursePage.htm regression.

[9] Northwestern University, (2008). "Multiple linear regression", http://www.basic.northwestern.edu/statguidefiles/mulreg.html

[10] Yale University, (2008). "Multiple linear regression" http://www.stat.yale.edu/Courses/1997-98/101/linmult.htm.

[11] MATLAB 7.4.0, Documentation - Robust Regression.

CHAPTER 8:

CONCLUSIONS

Acoustic wave sensors are highly versatile devices that are just starting to realize their commercial potential. They can be competitively priced, inherently rugged, very sensitive, and intrinsically reliable, and can be interrogated wirelessly.

The focus of this project was on the development of SH-SAW sensors for liquid media applications. Several sensors configurations were designed and experimented.

SH-SAW sensors were designed and fabricated on lithium tantalate substrates. Standard lithium tantalate crystals have properties that require a special set of precautions when handling and processing the wafers. The SH-SAW sensors patterns were defined using contact lithography and a reactive ion etching method. Electrodes with 1.2 μm and 2.4 μm width were obtained using this method and detailed step-by-step fabrication procedures and used recipes are described. Due to technical problems of the dry etching system used, the sensors having 1.2 μm features were not uniformly patterned but the sensors with electrodes of 2 μm and above had a repeatable and larger successful yield.

For the liquid reservoirs two fabrication methods were considered and experimented. The first one employed microstereolithography, a rapid prototyping method allowing micron resolution. Details of the 'Perfactory' System and the MSL build process were presented. The second method was based on patterning liquid cages onto a thick SU-8 resist using standard lithography. High aspect ratio filtering structures were embedded to the liquid cages and the step-by-step the fabrication procedure was detailed.

The two fabricated subsystems were mounted together and exposed to various liquid samples and the experimental results were presented.

An electrical characterization of the fabricated SH-SAW sensors has been done by using a network analyser equipment. While device to device variability has been observed, the reflection coefficients of input and output IDTs of sensors showed large return loss values (up to 45-55 dB) and near perfect matching to the 50 Ω characteristic impedance.

Selected sensors were assessed in terms of their transmission coefficients. The metallised delay lines were found to have the smallest insertion loss (10.37 dB). The free delay lines were generally found to be more lossy - the 5 mm long free delay line had an 18.5dB insertion loss. Attenuation on the free propagation path can be minimised by reducing the IDT to IDT distance. By measuring free delay lines with 5, 4 and 3 mm lengths, the sensors attenuation constant was estimated to 0.024 dB per wavelength. An alternative method to reduce the wave propagation attenuation on free surfaces makes use of open electrode gratings. The wave becomes a shear horizontal surface transversal wave (STW) and has potential for liquid media applications.

Liquids tests and experiments performed on SH-SAW sensors with a dual delay line and resonator sensor configurations operating at high-frequencies between 433

MHz and 860 MHz. According to the envisaged applications, sensors can be classified as electronic tongue devices with potential usage as 'taste' sensors, or voltage modulated sensors with potential usage in screening of biological samples.

The SRL 280a, SRL 285, SRL208a SH-SAW have been tested with liquid solutions implemented with basic substances. All devices can discriminate well between the synthetic samples without the need of any selective or bio-chemical membrane, in both wired and semi-wireless measurements set ups. The sensing principle is based on physical interaction mechanisms rather than chemical ones; while taste classification per se is not achievable based on purely physical interactions, sample classification is achieved based on the amplitude and phase response of the sensor (which is an indirect measure of the physical parameters of each sample). The sensitivity of these devices has to be further investigated but the results were encouraging and applications are envisaged for the rapid, low-cost and possibly wireless screening of liquid samples in the food and beverage industries or environmental monitoring.

A voltage modulated sensor system has also been described and preliminary results are presented. This system is proposed as an analytical microsystem for the screening of biological materials. The system comprises a dual delay line SAW device in which the metallised surface is voltage modulated in order to trap charged particles within a non-conducting liquid. The basic sensing principle is that the polarized metal electrode attracts statically or electrokinetically bioparticles in the liquid, which perturb the acoustic waves; thus changing their phase velocity and attenuation. In theory the voltage/frequency is set according to the properties of the bioparticles, e.g. charge/size, dielectric constant. Ideally, the SAW sensors have no bio-chemical layers (as was the case of the preliminary experiments) although a functionalized biocoating may be added for more specific protein-based biological applications. Preliminary tests have been

carried out that showed a significant voltage effect on carbon nanoparticles. Further investigations need to be done on biosamples but the preliminary results suggest that the voltage modulated microsystem has the potential to offer a robust, low-cost solution to the identification of certain bacterial cells.

More basic liquid experiments were performed on a single two-port resonator sensor. Successful classification of the liquid samples was achieved for all six basic taste samples tested. The resonator was also able to separate and identify samples of the same taste class – caffeine and two quinine samples were tested and results suggest potential applications in pharmaceutical field. The resonator was then exposed to samples of the same substance with varying concentrations and the sensor proved successful in identifying all of these solutions. Further experiments were conducted on binary mixtures of solutions and the resonator was again able to separate them from original component solutions.

Based on the results for samples with various concentrations, a multivariate data analysis was conducted. It confirmed that that resonator's responses are influenced by the physical properties of the tested solutions and for this sensor configuration the most influential parameters are the sample conductivity, density and permittivity. Multiple linear models were derived that were statistically significant and can explain high percentage of the measured data.

A preliminary generalized model containing the fundamental parameters is able to express a significant percentage of the error variance. The simplest model appears to be noisy and due to large error variance in phase data it lacks the ability to fit the data accurately. Better prediction for the whole data is obtained using the improved generalized model, which contains interaction and quadratic terms of the fundamental

parameters. Substance-dependent linear models have also been derived and they had a high prediction power.

It can be concluded that the SH-SAW sensors can be successfully used for liquid analysis. The sensors have no bio-chemical selective layer making them non-specific but create a robust/durable and low-cost system. This sensing system may be applied in the food beverage industry, medical applications; a functionalized coating can be added for more specific biological application.

BIBLIOGRAPHY

Ali, Z. 1999, "Acoustic wave mass sensors", *Journal of Thermal Analysis and Calorimetry,* vol. 55, no. 2, pp. 397-412.

Andrew McGill, R., Chung, R., Chrisey, D.B., Dorsey, P.C., Matthews, P., Piqué, A., Mlsna, T.E. and Stepnowski, J.L. 1998, "Performance optimization of surface acoustic wave chemical sensors", *IEEE Transactions on Ultrasonics, Ferroelectrics, and Frequency Control,* vol. 45, no. 5, pp. 1370-1380.

Arana, N., Puente, D., Ayerdi, I., Castaño, E. and Berganzo, J. 2006, "SU8 protective layers in liquid operating SAWs", *Sensors and Actuators, B: Chemical,* vol. 118, no. 1-2, pp. 374-379.

Auld, B.A. 1990, *Acoustic fields and waves in solids,* 2nd edn, R.E. Krieger, Malabar, Fla.

Ballantine, D.S., Martin, J., Ricco, A.J., Zellers, E.T., Frye, G.C. and Wohltjen, H. c1997., *Acoustic wave sensors: theory, design, and physico-chemical applications,* Academic Press, San Diego.

Baltes, H., GoÌˆpel, W. and Hesse, J. 2001., *Sensors update,* Wiley-VCH, Weinheim ; Chichester.

Bard, A.J. and Faulkner, L.R. 1980., *Electrochemical methods : fundamentals and applications,* Wiley, New York ; Chichester.

Barié, N., Wessa, T., Bruns, M. and Rapp, M. 2004, "Love waves in SiO2 layers on STW-resonators based on LiTaO 3", *Talanta,* vol. 62, no. 1, pp. 71-79.

Baszun, M. and Grzeda, D. 2003, "Applications of shear horizontal surface acoustic waves to thin film evaluation", *Journal of Materials Processing Technology,* vol. 133, no. 1-2, pp. 34-38.

Bender, F., Cernosek, R.W. and Josse, F. 2000, "Love-wave biosensors using cross-linked polymer waveguides on LiTaO3 substrates", *Electronics Letters,* vol. 36, no. 19, pp. 1672-1673.

Bender, F., Dahint, R., Josse, F., Ricco, A.J. and Martin, S.J. 1999, "Characteristics of acoustic plate modes on rotated Y-cuts of quartz utilized for biosensing applications", *Analytical Chemistry,* vol. 71, no. 22, pp. 5064-5068.

Benes, E., Groschl, M., Seifert, F. and Pohl, A. 1997, "Comparison between BAW and SAW sensor principles", *Proceedings of the 1997 IEEE International Frequency Control Symposium*, ed. Anon, IEEE, Piscataway, NJ, United States, pp. 5.

Berkenpas, E., Bitla, S., Millard, P. and Da Cunha, M.P. 2004, "Pure shear horizontal SAW biosensor on langasite", *IEEE Transactions on Ultrasonics, Ferroelectrics, and Frequency Control,* vol. 51, no. 11, pp. 1404-1411.

Berkenpas, E., Millard, P. and Pereira da Cunha, M. 2006, "Detection of Escherichia coli O157:H7 with langasite pure shear horizontal surface acoustic wave sensors", *Biosensors and Bioelectronics,* vol. 21, no. 12, pp. 2255-2262.

Borngräber, R., Hartmann, J., Lucklum, R., Rösler, S. and Hauptmann, P. 2000, "Detection of ionic compounds in water with a new poly-carbon acid coated quartz crystal resonator", *Sensors and Actuators, B: Chemical,* vol. 65, no. 1, pp. 273-276.

Branch, D.W. and Brozik, S.M. 2004, "Low-level detection of a Bacillus anthracis simulant using Love-wave biosensors on 36°YX LiTaO3", *Biosensors and Bioelectronics,* vol. 19, no. 8, pp. 849-859.

Caliendo, C., Verona, E. and Anisimkin, V.I. 1997, "Surface acoustic wave humidity sensors: A comparison between different types of sensitive membrane", *Smart Materials and Structures,* vol. 6, no. 6, pp. 707-715.

Campbell, A.I. 1998., *Surface acoustic wave devices for mobile and wireless communications,* Academic Press, San Diego ; London.

Campbell, C.K. 1989, "Applications of surface acoustic and shallow bulk acoustic wave devices", *Proceedings of the IEEE,* vol. 77, no. 10, pp. 1453-1484.

Campitelli, A.P., Wlodarski, W. and Hoummady, M. 1998, "Identification of natural spring water using shear horizontal SAW based sensors", *Sensors and Actuators, B: Chemical,* vol. B49, no. 3, pp. 195-201.

Casalnuovo, S., Cernosek, R., Josse, F., Ricco, A. and Zhou, R. 1999 Jul 20, "SH-SAW Sensor Platform for Chemical Detection in Aqueous Solutions", *196th Meeting of the Electrochemical Society, Chemical Sensors IV Symposium.*

Čavić, B.A., Hayward, G.L. and Thompson, M. 1999, "Acoustic waves and the study of biochemical macromolecules and cells at the sensor-liquid interface", *Analyst,* vol. 124, no. 10, pp. 1405-1420.

Cavic, B.A. and Thompson, M. 2002, "Interfacial nucleic acid chemistry studied by acoustic shear wave propagation", *Analytica Chimica Acta,* vol. 469, no. 1, pp. 101-113.

Cheeke, J.D.N. and Wang, Z. 1999, "Acoustic wave gas sensors", *Sensors and Actuators, B: Chemical,* vol. 59, no. 2, pp. 146-153.

Chono, K., Shimizu, N., Matsui, Y., Kondoh, J. and Shiokawa, S. 2004, "Development of novel atomization system based on SAW streaming", *Japanese Journal of Applied Physics, Part 1: Regular Papers and Short Notes and Review Papers,* vol. 43, no. 5, pp. 2987-2991.

Cicala, G., Bruno, P., Dragone, A., Losacco, A.M., Sadun, C. and Generosi, A. 2005, "PECVD a-C:H films for STW resonant devices", *Thin Solid Films,* vol. 482, no. 1-2, pp. 264-269.

Cole, M., Gardner, J.W., Leonte, I.I., Sehra, G., Noh, H.S. and Hesketh, P.J. 2005, "Voltage modulated SAW microtrap system: Smart assaying of biomaterials", *Fourth IEEE Conference on Sensors 2005*, pp. 1300.

Cole, M., Sehra, G., Gardner, J.W. and Varadan, V.K. 2004, "Development of smart tongue devices for measurement of liquid properties", *IEEE Sensors Journal,* vol. 4, no. 5, pp. 543-550.

Cole, M., Sehra, G.S., Gardner, J.W. and Varadan, V.K. 2002, "Fabrication and Testing of Smart Tongue Devices for Liquid Sensing", *First IEEE International Conference on Sensors - IEEE Sensors 2002*, pp. 237.

Collings, A.F. and Caruso, F. 1997, "Biosensors: recent advances", *Reports on Progress in Physics,* vol. 60, no. 11, pp. 1397-1445.

Deisingh, A.K., Stone, D.C. and Thompson, M. 2004, "Applications of electronic noses and tongues in food analysis", *International Journal of Food Science and Technology,* vol. 39, no. 6, pp. 587-604.

Drafts, B. 2001, "Acoustic wave technology sensors", *IEEE Transactions on Microwave Theory and Techniques,* vol. 49, no. 4 II, pp. 795-802.

Drobe, H., Leidl, A., Rost, M. and Ruge, I. 1993, "Acoustic sensors based on surface-localized HPSWs for measurements in liquids", *Sensors and Actuators, A: Physical,* vol. 37-38, no. 2, pp. 141-148.

Ezaki, S. and Iiyama, S. 2001, "Detection of interactions between lipid/polymer membranes and taste substances by quartz resonator", *Sensors and Materials,* vol. 13, no. 2, pp. 119-127.

Fox, C.G. and Alder, J.F. 1989, "Surface acoustic wave sensors for atmospheric gas monitoring : A review", *The Analyst,* vol. 114, pp. 997-1004.

Freudenberg, J., Von Schickfus, M. and Hunklinger, S. 2001, "A SAW immunosensor for operation in liquid using a SiO2 protective layer", *Sensors and Actuators, B: Chemical,* vol. 76, no. 1-3, pp. 147-151.

Gardner, J.W., Cole, M., Dowson, C.G., Newton, P. and Sehra, G. 2005, "Smart acoustic sensor for the detection of bacteria in milk", *3rd IASTED International Conference on Medical Engineering 2005*, ed. Hamza M.H., pp. 539-542.

Gardner, J.W., Varadan, V.K. and Awadelkarim, O.O. 2001., *Microsensors, MEMS and smart devices : technology, applications and devices,* John Wiley and Sons, Chichester.

Gizeli, E. 1997, "Design considerations for the acoustic waveguide biosensor", *Smart Materials and Structures,* vol. 6, no. 6, pp. 700-706.

Gizeli, E., Goddard, N.J., Lowe, C.R. and Stevenson, A.C. 1992, "A Love plate biosensor utilising a polymer layer", *Sens. Actuators B,* vol 6, pp 131-137.

Gizeli, E., Liley, M., Lowe, C.R. and Vogel, H. 1997, "Antibody Binding to a Functionalized Supported Lipid Layer: A Direct Acoustic Immunosensor", *Analytical Chemistry,* vol. 69, no. 23, pp. 4808-4813.

Gizeli, E. and Lowe, C.R. 1996, "Immunosensors", *Current Opinion in Biotechnology,* vol. 7, no. 1, pp. 66-71.

Gizeli, E., Lowe, C.R., Liley, M. and Vogel, H. 1996, "Detection of supported lipid layers with the acoustic Love waveguide device: Application to biosensors", *Sensors and Actuators, B: Chemical,* vol. 34, no. 1-3, pp. 295-300.

Gizeli, E., Stevenson, A.C., Goddard, N.J. and Lowe, C.R. 1993, "Acoustic Love plate sensors: comparison with other acoustic devices utilizing surface SH waves", *Sensors and Actuators, B: Chemical,* vol. B14, no. 1 -3 pt 2, pp. 638-639.

Gronewold, T.M.A. 2007, "Surface acoustic wave sensors in the bioanalytical field: Recent trends and challenges", *Analytica Chimica Acta,* vol. 603, no. 2, pp. 119-128.

Gulyaev, Y.V. 1998, "Review of shear surface acoustic waves in solids", *IEEE Transactions on Ultrasonics, Ferroelectrics, and Frequency Control,* vol. 45, no. 4, pp. 935-938.

Harding, G.L. 2001, "Mass sensitivity of Love-mode acoustic sensors incorporating silicon dioxide and silicon-oxy-fluoride guiding layers", *Sensors and Actuators, A: Physical,* vol. 88, no. 1, pp. 20-28.

Harding, G.L. and Du, J. 1997, "Design and properties of quartz-based Love wave acoustic sensors incorporating silicon dioxide and PMMA guiding layers", *Smart Materials and Structures,* vol. 6, no. 6, pp. 716-720.

Hashimoto, K. 2000., *Surface acoustic wave devices in telecommunications : modelling and simulation,* Springer, Berlin ; London.

Herrmann, F., Hahn, D. and Büttgenbach, S. 1999, "Separate determination of liquid density and viscosity with sagittally corrugated Love-mode sensors", *Sensors and Actuators, A: Physical,* vol. 78, no. 2, pp. 99-107.

Herrmann, F., Weihnacht, M. and Büttgenbach, S. 2001, "Properties of sensors based on shear-horizontal surface acoustic waves in LiTaO3/SiO2 and quartz/SiO2 structures",

IEEE Transactions on Ultrasonics, Ferroelectrics, and Frequency Control, vol. 48, no. 1, pp. 268-273.

Herrmann, F., Weihnacht, M. and Büttgenbach, S. 1999, "Properties of shear-horizontal surface acoustic waves in different layered quartz-SiO2 structures", *Ultrasonics,* vol. 37, no. 5, pp. 335-341.

Hossenlopp, J.M. 2006, "Applications of acoustic wave devices for sensing in liquid environments", *Applied Spectroscopy Reviews,* vol. 41, no. 2, pp. 151-164.

Howe, E. and Harding, G. 2000, "A comparison of protocols for the optimisation of detection of bacteria using a surface acoustic wave (SAW) biosensor", *Biosensors and Bioelectronics,* vol. 15, no. 11-12, pp. 641-649.

Hughes, R.C., Ricco, A.J., Butler, M.A. and Martin, S.J. 1991, "Chemical microsensors", *Science,* vol. 254, no. 5028, pp. 74-80.

Hur, Y., Han, J., Seon, J., Pak, Y.E. and Roh, Y. 2005, "Development of an SH-SAW sensor for the detection of DNA hybridization", *Sensors and Actuators, A: Physical,* vol. 120, no. 2, pp. 462-467.

Iiyama, S., Kuga, H., Ezaki, S., Hayashi, K. and Toko, K. 2003, "Peculiar change in membrane potential of taste sensor caused by umami substances", *Sensors and Actuators, B: Chemical,* vol. 91, no. 1-3, pp. 191-194.

Jakoby, B., Eisenschmid, H. and Herrmann, F. 2002, "The potential of microacoustic SAW-and BAW-based sensors for automotive applications - A review", *IEEE Sensors Journal,* vol. 2, no. 5, pp. 443-451.

Jakoby, B. and Vellekoop, M.J. 1998, "Analysis and optimization of love wave liquid sensors", *IEEE Transactions on Ultrasonics, Ferroelectrics, and Frequency Control,* vol. 45, no. 5, pp. 1293-1302.

Jakoby, B. and Vellekoop, M.J. 1997, "Properties of love waves: Applications in sensors", *Smart Materials and Structures,* vol. 6, no. 6, pp. 668-679.

Jakoby, B. and Vellekoop, M.J. 1998, "Viscosity sensing using a Love-wave device", *Sensors and Actuators, A: Physical,* vol. 68, no. 1 -3 pt 2, pp. 275-281.

James, D., Scott, S.M., Ali, Z. and O'Hare, W.T. 2005, "Chemical sensors for electronic nose systems", *Microchimica Acta,* vol. 149, no. 1-2, pp. 1-17.

Josse, F., Bender, F. and Cernosek, R.W. 2001, "Guided shear horizontal surface acoustic wave sensors for chemical and biochemical detection in liquids", *Analytical Chemistry,* vol. 73, no. 24, pp. 5937-5944.

Khlebarov, Z.P., Stoyanova, A.I. and Topalova, D.I. 1992, "Surface acoustic wave gas sensors", *Sensors and Actuators, B: Chemical,* vol. B8, no. 1, pp. 33-40.

Kikuchi, T. and Moriizumi, T. 1985, "Effects of liquid viscosity on ultrasonic propagation in liquid/solid structure.", *Japanese Journal of Applied Physics, Supplement,* vol. 25 suppl 25-1, pp. 43-45.

Kondoh, J., Hayashi, S. and Shiokawa, S. 2001, "Simultaneous detection of density and viscosity using surface acoustic wave liquid-phase sensors", *Japanese Journal of Applied Physics, Part 1: Regular Papers and Short Notes and Review Papers,* vol. 40, no. 5, pp. 3713-3717.

Kondoh, J., Imayama, T., Matsui, Y. and Shiokawa, S. 1996, "Enzyme biosensor based on surface acoustic wave device", *Electronics and Communications in Japan, Part II: Electronics (English translation of Denshi Tsushin Gakkai Ronbunshi),* vol. 79, no. 7, pp. 69-75.

Kondoh, J., Matsui, Y. and Shiokawa, S. 2003, "Identification of electrolyte solutions using a shear horizontal surface acoustic wave sensor with a liquid-flow system", *Sensors and Actuators, B: Chemical,* vol. 91, no. 1-3, pp. 309-315.

Kondoh, J., Muramatsu, T., Nakanishi, T., Matsui, Y. and Shiokawa, S. 2003, "Development of practical surface acoustic wave liquid sensing system and its application for measurement of Japanese tea", *Sensors and Actuators, B: Chemical,* vol. 92, no. 1-2, pp. 191-198.

Kondoh, J., Muramatsu, T., Nakanishi, T. and Shiokawa, S. 2001, "Development of surface acoustic wave liquid sensing system and application for Japanese tea measurements", *Proceedings of the Annual IEEE International Frequency Control Symposium*, pp. 497-501.

Kondoh, J., Saito, K., Shiokawa, S. and Suzuki, H. 1996, "Simultaneous measurements of liquid properties using multichannel shear horizontal surface acoustic wave microsensor", *Japanese Journal of Applied Physics, Part 1: Regular Papers and Short Notes and Review Papers,* vol. 35, no. 5 B, pp. 3093-3096.

Kondoh, J. and Shiokawa, S. 1998, "Liquid-phase microsensor based on surface acoustic wave devices", *Electronics and Communications in Japan, Part II: Electronics (English translation of Denshi Tsushin Gakkai Ronbunshi),* vol. 81, no. 11, pp. 9-17.

Kondoh, J. and Shiokawa, S. 1993, "SH-SAW taste sensor based acoustoelectric interaction", *Proceedings of the IEEE Ultrasonics Symposium* 1, pp. 421-424.

Kondoh, J. and Shiokawa, S. 1992, "Measurements of conductivity and pH of liquid using surface acoustic wave devices", *Japanese Journal of Applied Physics,* vol. 31, no. SUPPL., pp. 82-84.

Kondoh, J., Shiokawa, S., Rapp, M. and Stier, S. 1998, "Simulation of viscoelastic effects of polymer coatings on surface acoustic wave gas sensor under consideration of film thickness", *Japanese Journal of Applied Physics, Part 1: Regular Papers and Short Notes and Review Papers,* vol. 37, no. 5, pp. 2842-2848.

Kondoh, J., Tabushi, S., Matsui, Y. and Shiokawa, S. 2008, "Development of methanol sensor using a shear horizontal surface acoustic wave device for a direct methanol fuel cell", *Sensors and Actuators, B: Chemical,* vol. 129, no. 2, pp. 575-580.

Kondoh, J., Matsui, Y. and Shiokawa, S. 1993, "New biosensor using shear horizontal surface acoustic wave device", *Japanese Journal of Applied Physics, Part 1: Regular Papers and Short Notes and Review Papers,* vol. 32, no. 5, pp. 2376-2379.

Kondoh, J., Matsui, Y., Shiokawa, S. and Wlodarski, W.B. 1994, "Enzyme-immobilized SH-SAW biosensor", *Sensors and Actuators, B: Chemical,* vol. B20, no. 2-3, pp. 199-203.

Kondoh, J., Saito, K., Shiokawa, S. and Suzuki, H. 1995, "Multichannel shear horizontal surface acoustic wave microsensor for liquid characterization", *Proceedings of the IEEE Ultrasonics Symposium* 1, pp. 445-449.

Kondoh, J. and Shiokawa, S. 1999, "Shear - Horizontal Surface Acoustic Wave Sensors", *Sensors Update,* vol. 6, no. 1, pp. 59-78.

Kondoh, J. and Shiokawa, S. 1995, "Identification of liquid samples using shear-horizontal surface acoustic wave sensors", *Electronics and Communications in Japan, Part II: Electronics (English translation of Denshi Tsushin Gakkai Ronbunshi),* vol. 78, no. 8, pp. 50-59.

Kondoh, J. and Shiokawa, S. 1995, "Liquid identification using SH-SAW sensors", *International Conference on Solid-State Sensors and Actuators, and Eurosensors IX, Proceedings* 2, pp. 716-719.

Kondoh, J. and Shiokawa, S. 1995, "Shear surface acoustic wave liquid sensor based on acoustoelectric interaction", *Electronics and Communications in Japan, Part II: Electronics (English translation of Denshi Tsushin Gakkai Ronbunshi),* vol. 78, no. 1, pp. 101-112.

Kondoh, J. and Shiokawa, S. 1994, "New application of shear horizontal surface acoustic wave sensors to identifying fruit juices", *Japanese Journal of Applied Physics, Part 1: Regular Papers and Short Notes and Review Papers,* vol. 33, no. 5; -, pp. 3095-3099.

Kondoh, J. and Shiokawa, S. 1994, "SH-SAW devices as effective identification system for liquids", *Proceedings of the IEEE Ultrasonics Symposium* 1, pp. 507-512.

Kondoh, J. and Shiokawa, S. 1993, "Liquid sensor based on a shear horizontal SAW device", *Electronics and Communications in Japan, Part II: Electronics (English translation of Denshi Tsushin Gakkai Ronbunshi),* vol. 76, no. 2, pp. 69-82.

Kondoh, J., Shiokawa, S. and Georgiev, Z. 1993, "Shear-horizontal SAW device as a pH monitor", *Sensors and Actuators, B: Chemical,* vol. B13, no. -3, pp. 429-431.

Kondoh, J., Yamazaki, T., Matsui, Y. and Shiokawa, S. 1999, "Identification of ion species in electrolytic solutions using surface acoustic wave liquid flow sensing system based on new pattern recognition method", *Proceedings of the IEEE Ultrasonics Symposium* 1, pp. 471-476.

Kovacs, G. 1994, "Love wave sensor for (bio)chemical sensing in liquids", *Sensors and Actuators, A: Physical,* vol. 43 (1-3), pp. 38-43.

Kovacs, G., Anhorn, M., Engan, H.E., Visintini, G. and Ruppel, C.C.W. 1990, "Improved material constants for LiNbO3 and LiTaO3", *Proceedings of the IEEE Ultrasonics Symposium,* pp. 435-438.

Kovacs, G. and Venema, A. 1992, "Theoretical comparison of sensitivities of acoustic shear wave modes for (bio)chemical sensing in liquids", *Applied Physics Letters,* vol. 61, no. 6, pp. 639-641.

Kwon, Y. and Roh, Y. 2004, "Development of SH-SAW sensors for underwater measurement", *Ultrasonics,* vol. 42, no. 1-9, pp. 409-411.

Lavigne, J.J., Savoy, S., Clevenger, M.B., Ritchie, J.E., McDoniel, B., Yoo S.-, J., Anslyn, E.V., McDevitt, J.T., Shear, J.B. and Neikirk, D. 1998, "Solution-based analysis of multiple analytes by a sensor array: Toward the development of an 'electronic tongue'", *Journal of the American Chemical Society,* vol. 120, no. 25, pp. 6429-6430.

Lee, Y.S., Yoon, D.S. and Kim, T.S. 2005, "Improvement of the mass sensitivity in flexural plate wave biosensor based on PZT thin film", *Integrated Ferroelectrics* 69, pp. 391-400.

Legin, A., Rudnitskaya, A., Vlasov, Y.G., Di Natale, C., Davide, F. and D'Amico, A. 1997, "Tasting of beverages using an electronic tongue", *Sensors and Actuators, B: Chemical,* vol. 44, no. 1-3, pp. 291-296.

Leidl, A., Oberlack, I., Schaber, U., Mader, B. and Drost, S. 1997, "Surface acoustic wave devices and applications in liquid sensing", *Smart Materials and Structures,* vol. 6, no. 6, pp. 680-688.

Leonte, I., Hunt, M., Sehra, G., Cole, M. and Gardner, J.W. 2004, "SAW bioliquids sensor with RF interrogation", *IEEE High Frequency Postgraduate Student Colloquium*, pp. 47-52.

Leonte, I.I., Hunt, M.S., Sehra, G., Cole, M., Gardner, J.W., Noh, H.S. and Hesketh, P.J. 2004, "Towards a wireless microsystem for liquid analysis", *Proceedings of IEEE Sensors* 2, pp. 919-922.

Leonte, I.I., Sehra, G., Cole, M., Hesketh, P. and Gardner, J.W. 2006, "Taste sensors utilizing high-frequency SH-SAW devices", *Sensors and Actuators, B: Chemical,* vol. 118, no. 1-2, pp. 349-355.

Li, Z., Jones, Y., Hossenlopp, J., Cernosek, R. and Josse, F. 2005, "Analysis of liquid-phase chemical detection using guided shear horizontal-surface acoustic wave sensors", *Analytical Chemistry,* vol. 77, no. 14, pp. 4595-4603.

Martin, F., McHale, G. and Newton, M.I. 2004, "Experimental Study of Love Wave Sensor Response by Phase and Group Velocity Measurement", *IEEE Sensors Journal,* vol. 4, no. 2, pp. 216-220.

Martin, F., Newton, M.I., McHale, G., Melzak, K.A. and Gizeli, E. 2004, "Pulse mode shear horizontal-surface acoustic wave (SH-SAW) system for liquid based sensing applications", *Biosensors and Bioelectronics,* vol. 19, no. 6, pp. 627-632.

Martin, S.J. and Ricco, A.J. 1989, "Effective utilization of acoustic wave sensor responses: Simultaneous measurement of velocity and attenuation", *IEEE Ultrasonics Symposium Proceedings* 1, pp. 621-625.

Martin, S.J., Ricco, A.J., Niemczyk, T.M. and Frye, G.C. 1989, "Characterization of SH acoustic plate mode liquid sensors", *Sensors and Actuators,* vol. 20, no. 3, pp. 253-268.

Mauder, A. 1995, "SAW gas sensors: comparison between delay line and two port resonator", *Sensors and Actuators, B: Chemical,* vol. B26, no. 1-3, pp. 187-190.

McMullan, C., Mehta, H., Gizeli, E. and Lowe, C.R. 2000, "Modelling of the mass sensitivity of the Love wave device in the presence of a viscous liquid", *Journal of Physics D: Applied Physics,* vol. 33, no. 23, pp. 3053-3059.

Morgan, D.P. 1973, "Surface acoustic wave devices and applications - Introductory Review.", *Ultrasonics,* vol. 11, no. 3, pp. 121-131.

Morgan, D.P. 1985., *Surface-wave devices for signal processing,* Elsevier, Amsterdam ; New York.

Murochi, N., Sugimoto, M., Matsui, Y. and Kondoh, J. 2007, "Deposition of thin film using a surface acoustic wave device", *Japanese Journal of Applied Physics, Part 1: Regular Papers and Short Notes and Review Papers,* vol. 46, no. 7, pp. 4754-4759.

Myers, R.H. 1990, *Classical and modern regression with applications,* 2nd edn, Duxbury, Boston.

Nakamura, K. and Hanaoka, T. 1993, "Propagation characteristics of surface acoustic waves in ZnO/LiNbO3 structures", *Japanese Journal of Applied Physics, Part 1: Regular Papers and Short Notes and Review Papers,* vol. 32, no. 5 B, pp. 2333-2336.

Newton, M.I., Banerjee, M.K., Starke, T.K.H., Rowan, S.M. and McHale, G. 1999, "Surface acoustic wave-liquid drop interactions", *Sensors and Actuators, A: Physical,* vol. 76, no. 1-3, pp. 89-92.

Niemczyk, T.M., Martin, S.J., Frye, G.C. and Ricco, A.J. 1988, "Acoustoelectric interaction of plate modes with solutions", *Journal of Applied Physics,* vol. 64, no. 10, pp. 5002-5008.

Nomura, T., Saitoh, A. and Horikoshi, Y. 2001, "Measurement of acoustic properties of liquid using liquid flow SH-SAW sensor system", *Sensors and Actuators, B: Chemical,* vol. 76, no. 1-3, pp. 69-73.

Nomura, T., Saitoh, A. and Miyazaki, T. 2003, "Liquid sensor probe using reflecting SH-SAW delay line", *Sensors and Actuators, B: Chemical,* vol. 91, no. 1-3, pp. 298-302.

Nomura, T. and Yasuda, T. 1993, "Surface acoustic wave liquid sensors based on one-port resonator", *Japanese Journal of Applied Physics, Part 1: Regular Papers and Short Notes and Review Papers,* vol. 32, no. 5 B, pp. 2372-2375.

Oliner, A. 1978, *Acoustic Surface Waves,* Springer-Verlag, Berlin.

Pastureaud, T., Solal, M., Biasse, B., Aspar, B., Briot, J.B., Daniau, W., Steichen, W., Lardat, R., Laude, V., Laens, A., Friedt, A., Friedt, J.-. and Ballandras, S. 2007, "High-Frequency Surface Acoustic Waves Excited on Thin-Oriented LiNbO3 Single-Crystal Layers Transferred Onto Silicon",*IEEE Transactions on Ultrasonics, Ferroelectrics, and Frequency Control,* vol. 54 (4), pp. 870-876.

Peach, R. 2001, "On the existence of surface acoustic waves on piezoelectric substrates", *IEEE Transactions on Ultrasonics, Ferroelectrics, and Frequency Control,* vol. 48, no. 5, pp. 1308-1320.

Pearce, T.C., Schiffman, S.S., Nagle, H.T. and Gardner, J.W. 2003., *Handbook of machine olfaction: electronic nose technology,* Wiley-VCH, Weinheim.

Penza, M., Antolini, F. and Antisari Vittori, M. 2004, "Carbon nanotubes as SAW chemical sensors materials", *Sensors and Actuators, B: Chemical,* vol. 100, no. 1-2, pp. 47-59.

Pohl, A. 2006, "A low-cost high-definition wireless sensor system utilizing intersymbol interference", *IEEE Transactions on Ultrasonics, Ferroelectrics, and Frequency Control,* vol. 45, no. 5, pp. 1355-1362.

Pollard, T.B., Kenny, T.D., Vetelino, J.F. and Cunha, M.P.D. 2006, "Pure SH-SAW propagation, transduction and measurements on KNbO3", *IEEE Transactions on Ultrasonics, Ferroelectrics, and Frequency Control,* vol. 53, no. 1, pp. 199-207.

Pozar, D.M. 1998., *Microwave engineering,* 2nd edn, Wiley, New York.

Razan, F., Zimmermann, C., Rebière, D., Déjous, C., Pistré, J., Destarac, M. and Pavageau, B. 2005, "Radio frequency thin film characterization with polymer-coated Love-wave sensor", *Sensors and Actuators, B: Chemical,* vol. 108, no. 1-2, pp. 917-924.

Reindl, L., Scholl, G., Ostertag, T., Pohl, A. and Weigel, R. 1998, "Wireless remote identification and sensing with SAW devices", *Proc. IEEE International Workshop on Commercial Radio Sensor and Communication Techniques* , pp. 83-96.

Ricco, A.J. and Martin, S.J. 1987, "Acoustic wave viscosity sensor", *Applied Physics Letters,* vol. 50, no. 21, pp. 1474-1476.

Ricco, A.J. and Martin, S.J. 1993, "Multiple-frequency SAW devices for chemical sensing and materials characterization", *Sensors and Actuators, B: Chemical,* vol. B10, no. 2, pp. 123-131.

Ricco, A.J. and Martin, S.J. 1991, "Thin metal film characterization and chemical sensors: monitoring electronic conductivity, mass loading and mechanical properties with surface acoustic wave devices", *Thin Solid Films,* vol. 206, no. 1-2, pp. 94-101.

Ricco, A.J., Martin, S.J. and Zipperian, T.E. 1985, "Surface acoustic wave gas sensor based on film conductivity changes.", *Sensors and actuators,* vol. 8, no. 4, pp. 319-333.

Ro, R., Yang, S.-K., Lee, H.-Y. and Shen, C.-Y. 2001, "Effects of conducting liquid loadings on propagation characteristics of surface acoustic waves", *Proceedings of the National Science Council, Republic of China, Part A: Physical Science and Engineering,* vol. 25, no. 2, pp. 131-136.

Ro, R., Chang, S., Hwang, R. and Lee, D.H. 1999, "Identification of ionic solutions using a SAW liquid sensor", *Proceedings of the National Science Council, Republic of China, Part A: Physical Science and Engineering,* vol. 23, no. 6, pp. 810-815.

Ro, R., Chang, S. and Lee, D.H. 1999, "Measurement of SAW liquid sensors", *Proceedings of the National Science Council, Republic of China, Part A: Physical Science and Engineering,* vol. 23, no. 2, pp. 274-280.

Saha, K., Bender, F., Rasmusson, A. and Gizeli, E. 2003, "Probing the viscoelasticity and mass of a surface-bound protein layer with an acoustic waveguide device", *Langmuir,* vol. 19, no. 4, pp. 1304-1311.

Schweyer, M.G., Andle, J.C., McAllister, D.J. and Vetelino, J.F. 1996, "An acoustic plate mode sensor for aqueous mercury", *Sensors and Actuators, B: Chemical,* vol. 35, no. 1-3, pp. 170-175.

Sehra, G., Cole, M. and Gardner, J.W. 2004, "Miniature taste sensing system based on dual SH-SAW sensor device: An electronic tongue", *Sensors and Actuators, B: Chemical,* vol. 103, no. 1-2, pp. 233-239.

Shen, Y.-T., Huang, C.-L., Chen, R. and Wu, L. 2005, "A novel SH-SAW sensor system", *Sensors and Actuators, B: Chemical,* vol. 107, no. 1 Special Issue, pp. 283-290.

Shibata, H., Suzuki, H., Sugimoto, M., Matsui, Y. and Kondoh, J. 2006, "Development of dual-LED fiber optic surface plasmon sensor for liquid refractive index detection", *Progress in Biomedical Optics and Imaging - Proceedings of SPIE* 6377, art. no. 63770G.

Shiokawa, S. and Kondoh, J. 2004, "Surface acoustic wave sensors", *Japanese Journal of Applied Physics, Part 1: Regular Papers and Short Notes and Review Papers,* vol. 43, no. 5 B, pp. 2799-2802.

Shiokawa, S. and Kondoh, J. 1996, "Surface acoustic wave microsensors", *Electronics and Communications in Japan, Part II: Electronics (English translation of Denshi Tsushin Gakkai Ronbunshi),* vol. 79, no. 3, pp. 42-50.

Shiokawa, S. and Kondoh, J. 1999, "Surface acoustic wave sensor for liquid-phase application", *Proceedings of the IEEE Ultrasonics Symposium* 1, pp. 445-452.

Stevenson, A.C., Gizeli, E., Goddard, N.J. and Lowe, C.R. 1993, "Acoustic Love plate sensors: a theoretical model for the optimization of the surface mass sensitivity", *Sensors and Actuators, B: Chemical,* vol. B14, no. 1 -3 pt 2, pp. 635-637.

Strashilov, V.L. and Yantchev, V.M. 2005, "Surface transverse waves: Properties, devices, and analysis", *IEEE Transactions on Ultrasonics, Ferroelectrics, and Frequency Control,* vol. 52, no. 5, pp. 812-821.

Stubbs, D.D., Lee, S. and Hunt, W.D. 2002, "Molecular recognition for electronic noses using surface acoustic wave immunoassay sensors", *IEEE Sensors Journal,* vol. 2, no. 4, pp. 294-300.

Suzuki, A., Kondoh, J., Matsui, Y., Shiokawa, S. and Suzuki, K. 2005, "Development of novel optical waveguide surface plasmon resonance (SPR) sensor with dual light emitting diodes", *Sensors and Actuators, B: Chemical,* vol. 106, no. 1, pp. 383-387.

Suzuki, A., Kondoh, J., Matsui, Y., Shiokawa, S. and Suzuki, K. 2003, "Development of a novel waveguide surface plasmon resonance sensor with dual led", Toronto, Ont., pp. 1092.

Teston, F., Feuillard, G., Tessier, L., Certon, D. and Lethiecq, M. 1996, "Mass sensitivity of acoustic plate mode in liquids", *Proceedings of the IEEE Ultrasonics Symposium,* pp. 327-330.

Toko, K. 1998, "Electronic tongue", *Biosensors and Bioelectronics,* vol. 13, no. 6, pp. 701-709.

Toko, K. 1998, "A taste sensor", *Measurement Science and Technology,* vol. 9, no. 12, pp. 1919-1936.

Toko, K. 2000, *Biomimetic sensor technology,* Cambridge University Press, Cambridge, UK.

Turton, A., Bhattacharyya, D. and Wood, D. 2006, "Liquid density analysis of sucrose and alcoholic beverages using polyimide guided Love-mode acoustic wave sensors", *Measurement Science and Technology,* vol. 17, no. 2, pp. 257-263.

Varadan, V.K., Teo, P.T., Jose, K.A. and Varadan, V.V. 2000, "Design and development of a smart wireless system for passive temperature sensors", *Smart Materials and Structures,* vol. 9, no. 4, pp. 379-388.

Varadan, V.K. and Gardner, J.W. 1999, "Smart tongue and nose", *Proceedings of SPIE - The International Society for Optical Engineering* 3673, pp. 67-76.

Vlasov, Y., Legin, A. and Rudnitskaya, A. 2002, "Electronic tongues and their analytical application", *Analytical and Bioanalytical Chemistry,* vol. 373, no. 3, pp. 136-146.

Wang, Z., Cheeke, J.D.N. and Jen, C.K. 1994, "Sensitivity analysis for Love mode acoustic gravimetric sensors", *Applied Physics Letters,* vol. 64, no. 22, pp. 2940-2942.

Welsch, W., Klein, C., Öksüzoglu, R.M., Von Schickfus, M. and Hunklinger, S. 1997, "Immunosensing with surface acoustic wave sensors", *Sensors and Actuators, A: Physical,* vol. 62, no. 1-3, pp. 562-564.

Wenzel, S.W. and White, R.M. 1989, "Analytic comparison of the sensitivities of bulk-wave, surface-wave, and flexural plate-wave ultrasonic gravimetric sensors", *Applied Physics Letters,* vol. 54, no. 20, pp. 1976-1978.

White, R.M. 1997, "Acoustic interactions from Faraday's crispations to MEMS", *Faraday Discussions,* vol. 107, pp. 1-13.

White, R.M. 1970, "Surface elastic waves", *Proceedings of the IEEE,* vol. 58, no. 8, pp. 1238-1276.

White, R.M. and Voltmer, F.W. 1965, "Direct piezoelectric coupling to surface elastic waves", *Applied Physics Letters,* vol. 7, no. 12, pp. 314-316.

White, R.M. 1998, "Acoustic sensors for physical, chemical and biochemical applications", *Proceedings of the Annual IEEE International Frequency Control Symposium*, pp. 587-594.

Winquist, F., Krantz-Rülcker, C., Wide, P. and Lundström, I. 1998, "Monitoring of freshness of milk by an electronic tongue on the basis of voltammetry", *Measurement Science and Technology,* vol. 9, no. 12, pp. 1937-1946.

Winquist, F., Wide, P. and Lundström, I. 1997, "An electronic tongue based on voltammetry", *Analytica Chimica Acta,* vol. 357, no. 1-2, pp. 21-31.

Yamaguchi, M. 2003, "Early days of SH-type surface acoustic wave research", *Japanese Journal of Applied Physics, Part 1: Regular Papers and Short Notes and Review Papers,* vol. 42, no. 5 B, pp. 2909-2917.

Yamazaki, T., Kondoh, J., Matsui, Y. and Shiokawa, S. 2000, "Estimation of components and concentration in mixture solutions of electrolytes using a liquid flow system with SH-SAW sensor", *Sensors and Actuators, A: Physical,* vol. 83, no. 1, pp. 34-39.

Yamazaki, T., Kondoh, J., Matsui, Y. and Shiokawa, S. 1998, "Estimation of components and concentrations in mixture solutions of electrolytes using a liquid flow system with acoustic wave sensor", *Proceedings of the IEEE Ultrasonics Symposium,* vol. 1, pp. 505-508.

Zhang, C., Caron, J.J. and Vetelino, J.F. 2001, "The Bleustein-Gulyaev wave for liquid sensing applications", *Sensors and Actuators, B: Chemical,* vol. 76, no. 1-3, pp. 64-68.

Appendix A:

SRL SH-SAW sensors configurations

SRL SH-SAW sensors configurations are summarized in the following table:

SRL	Freq [MHz]	Config.	IDT	Reflector	DESCRIPTION	SIZE	LEdit Design
196	433	Wireless	Solid	Open circuit (50 strips)	Dual delay line same length L=465λ	5×2.5 mm	
1960	433	Wireless	Solid	NO Reflectors (experiment the edge reflections)	Dual delay line same length L=445λ=4272μm	5×2.5 mm	
196a	433	Wireless	Solid	Open Circuit Reflectors (150)	Dual delay line same length L=445λ=4272μm	5.3×2.5 mm	
196aa	433	Wireless	Split	150 Open Circuit Reflectors	Dual delay line same length L=445λ=4272μm	5.3×2.5 mm	
197	433	Wireless	Solid	Short circuit	Dual delay line same length	5×2.5 mm	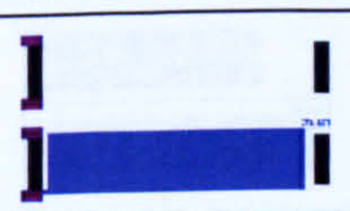
197a	433	Wireless	Solid	150 Short Circuit	Dual delay line same length L=445λ=4272μm	5.3×2.5 mm	
197aa	433	Wireless	Solid	150 Short Circuit	Dual delay line same length L=445λ=4272μm Metalized area starting from last finger	5.3×2.5 mm	
197b	433	Wireless	Solid	Short circuit	Dual delay line same length L=465λ Grating a=2.1μm	5×2.5 mm	
197bb	433	Wireless	Split	Short circuit	Dual delay line same length L=465λ Grating a=2.1μm	5×2.5 mm	
197c	433	Wireless	Solid	SC 4% metalization a=1.9 p=4.8	Dual delay line same length L=465λ	5×2.5 mm	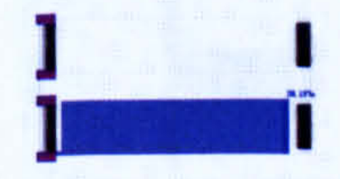
198	433	Wireless	Solid	Positive & negative	Dual delay line same length L=465λ	5×2.5 mm	
198a	433	Wireless	Solid	75 Positive & negative (150 strips)	Dual delay line same length L=445λ	5.3×2.5 mm	
198b	433	Wireless	Solid	75 Positive & negative (150 strips)	Dual delay line same length L=444.75λ ; Metalization to REFLECTOR =1.5λ	5.3×2.5 mm	

SRL	Freq [MHz]	Config.	IDT	Reflector	DESCRIPTION	SIZE	LEdit Design
198c	433	Wireless	Solid	75 Positive & negative (150 strips)	Dual delay line same length L=444.75λ; Opening 1mm closer; Metalization to REFLECTOR =1.5λ	5.3×2.5 mm	
199	433	Wireless	Solid	Open circuit	Dual delay line one shorter L=465.25λ ; l=361.083λ	5×2.5 mm	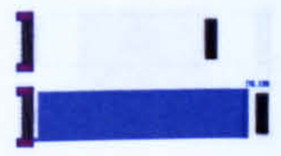
199a	433	Wireless	Solid	Open circuit Metalization 4%	Dual delay line one shorter L=465.25λ ; l=361.083λ	5×2.5 mm	
200	433	Wireless	Solid	Short circuit	Dual delay line one shorter	5×2.5 mm	
200a	433	Wireless	Solid	Short circuit Metalization 4% a=1.9μm	Dual delay line one shorter Grating a=2.1μm	5×2.5 mm	
200aa	433	Wireless	Solid	300 SC per free path 50 SC for the metalized	Dual delay line one shorter	5×2.5 mm	
200b	433	Wireless	Solid	300 SC 4% Metaliz. a=1.9μm	Dual delay line one shorter Grating a=2.1μm	5.3×2.5 mm	
201	433	Wireless	Solid	Positive & negative	Dual delay line one shorter L=464.75 ; l=361.083λ	5×2.5 mm	
201a	433	Wireless	Solid	Positive & negative	Dual delay line one shorter Metalized with opening L=464.75 l=361.083λ	5×2.5 mm	
202	433	Wireless	Solid	Positive & negative	Resonator	10×1.5mm	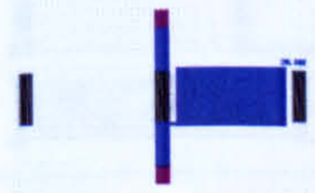
203	433	Wireless	Solid	Positive & negative	Resonator one side shorter	10×1.5mm	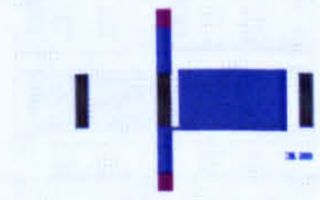
204	433	Wireless	Solid	Open circuit	Dual frequency dual delay line	5×2.5 mm	
205	433	Wireless	Solid	Short circuit	Dual frequency dual delay line	5×2.5 mm	

SRL	Freq [MHz]	Config.	IDT	Reflector	DESCRIPTION	SIZE	LEdit Design
206	433	Wireless	Solid	Positive & negative	Dual frequency dual delay line	5×2.5 mm	
207	433	Wired	Solid		Dual delay line same length Oxide opening	5×2.5 mm	
207a	433	Wired	Solid		Dual delay line same length	5×2.5 mm	
207aa	433	Wired	Solid		Dual delay line same length Top electrode (connected to the IDT)	5×2.5 mm	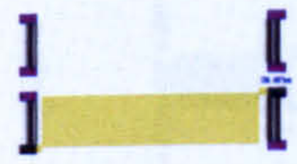
207b	433	Wired	Split 6 finger pairs		Dual delay line same length	5×2.5 mm	
207c	433	Wired	Solid 6 finger pairs		Dual delay line same length	5×2.5 mm	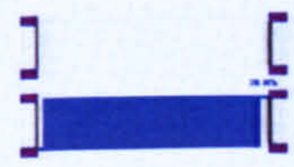
207ac	433	Wired	Solid		Dots array a=1.2μm in the 'free' path 	5×2.5 mm	
207ab	433	Wired	Solid		Dots array a=2.1μm in the 'free' path 	5×2.5 mm	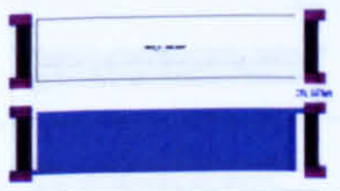
208	433	Wired	Solid		4mm/3mm DDL one shorter Resin 'Absorbers' 	5×2.5 mm	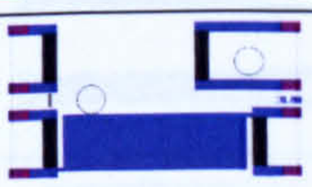
208a	433	Wired	Solid		Dual delay line one shorter	5×2.5 mm	
208b	433	Wired	Solid		4mm Dual delay line one shorter	5x2.5 mm	
208aa	433	Wired	Solid		Dual delay line one shorter Grating a=2.1	5×2.5 mm	
208aaa	433	Wired	Solid		Dual delay line one shorter IDT to IDT Grating a=2.1μm (λ/4 between IDT and the grating)	5×2.5 mm	

SRL	Freq [MHz]	Config.	IDT	Reflector	DESCRIPTION	SIZE	LEdit Design
208c0	433	Wired	UDT Solid	SC Reflectors on the side of the IDTs	4mm/3mm DDL one shorter IDT to reflector distance =λ/4	5×2.5 mm	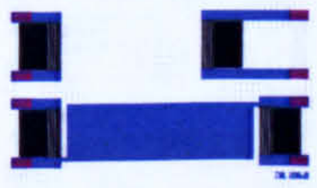
208c1	433	Wired	UDT Solid	SC Reflectors on the side of the IDTs	4mm/3mm DDL one shorter IDT to reflector distance =λ/2 Comparison with 208	5×2.5 mm	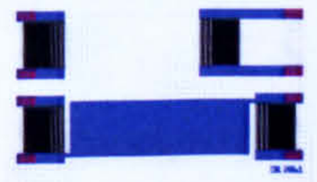
208c2	433	Wired	Input: Split IDT Output: Solid IDT	SC Reflectors on the side of the IDTs	4mm/3mm DDL one shorter IDT to reflector distance =λ/2	5×2.5 mm	
209	433	Wired	Solid		Central input IDT	5×3 mm	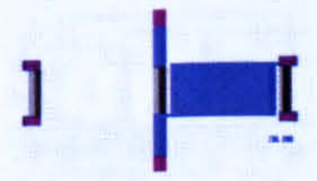
210	433	Wired	Solid		Central input IDT, one path shorter	5×3 mm	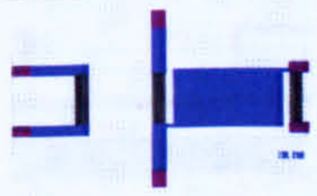
244	433	Wired	Solid		Dual frequency dual delay line, same length	5×2.5 mm	
245a	869	Wired	Solid		Dual delay line same length	5×2.5 mm	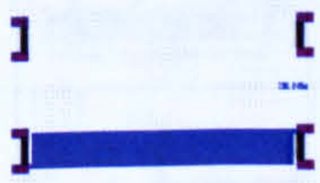
245	869	Wired	Solid		Dual delay line same length Grating a=1 Longer out pads (to fit the folded liquid cage)	6×2.5 mm	
245aa	869	Wired	Solid		Dual delay line same length mirrored config. of 245a (free path - opening in the metal)	6x2.5 mm	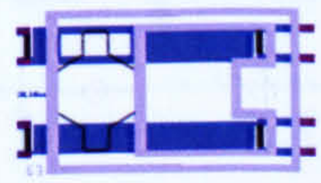
245aaa	869	Wired	Solid		Dual delay line same length 245a – Mirrored – smaller opening and cage	6x2.5 mm	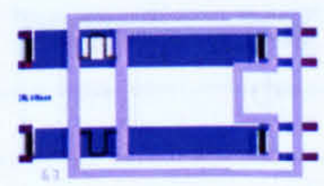
245ab	869	Wired	Solid		Dual delay line same length Small metalization path	6x2.5 mm	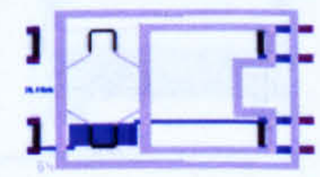
245ac	869	Wired	Solid		Dual delay line same length 3 delay lines – one for temp. reference	5x2.5 mm	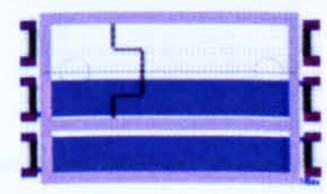

SRL	Freq [MHz]	Config.	IDT	Reflector	DESCRIPTION	SIZE	LEdit Design
245bb	869	Wired	Solid		Dual delay line same length Top electrode	5x2.5 mm	
245c	869	Wired	Solid 6 finger pairs		Dual delay line same length	5×2.5 mm	
245cc	869	Wired	Solid		Dual delay line same length Oxide opening	6x2.5mm	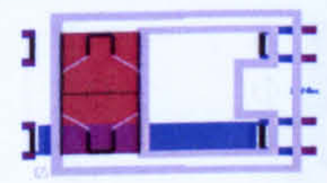
246	869	Wired	Solid		Dual delay line one shorter	6×2.5 mm	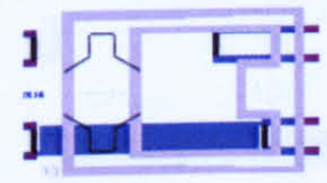
246a	869	Wired	Solid		Dual delay line one shorter 'Grove' in oxide layer	5×2.5 mm	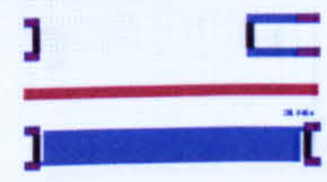
246b	869	Wired	Solid		Dual delay line one shorter grating	6×2.5 mm	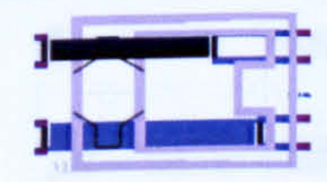
246c	869	Wired	Solid		1mm shorter	5×2.5 mm	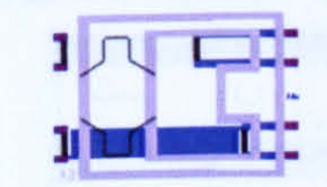
247	869	Wired	Solid		Central input IDT	5×2.6 mm	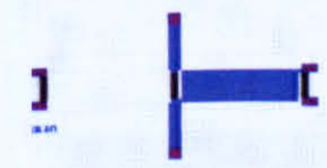
248	869	Wired	Solid		Central input IDT, one path shorter	5×2.6 mm	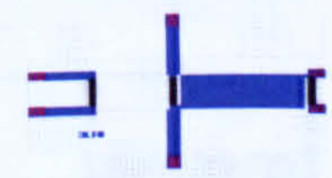
249	869	Wired	Solid		Dual frequency dual delay line	5×2.5 mm	
273	433	Wired	Solid		Dual delay line same length with +/- field	5×3 mm	
273a	433	Wired	Solid		Dual delay line same length with +/- field One line feed	5×2.5 mm	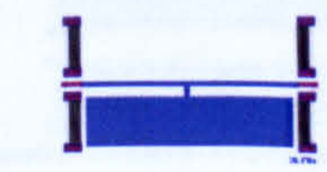

SRL	Freq [MHz]	Config.	IDT	Reflector	DESCRIPTION	SIZE	LEdit Design
273aa	433	Wired	Solid		Dual delay line same length Top floating electrode (with +/- field)	5×2.5 mm	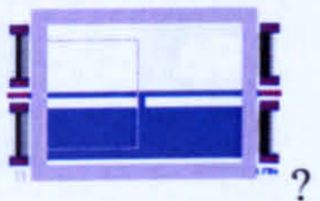 ?
273b	433	Wired	40 Split		Dual delay line same length L=442λ	5×2.5 mm	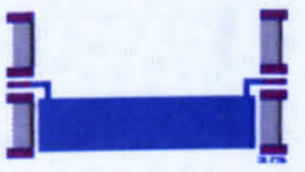
273bb	433	Wired	40 Split		Dual delay line same length Top floating electrode	5×3 mm	
274	869	Wireless	Solid	Open circuit	Dual delay line one shorter	5×2.5 mm	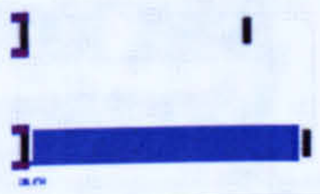
275	869	Wireless	Solid	Short circuit	Dual delay line one shorter	5×2.5 mm	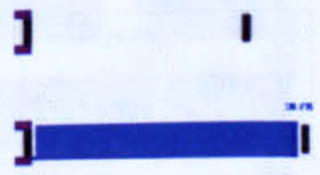
275a	869	Wireless	Solid	500 Short circuit	Dual delay line one shorter	5×2.5 mm	
275b	869	Wireless	Solid	500 Short circuit	Dual delay line one shorter Gratings on the 'free' path	5×2.5 mm	
276	869	Wireless	Solid	Positive & negative	Dual delay line one shorter	5×2.5 mm	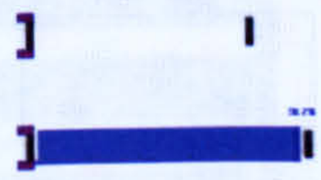
277	433	Wired	Solid		3 delay line same length	5×.4 mm	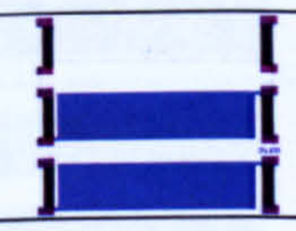
278	433	Wired	25 Split Finger Pairs		Dual delay line same length	5×.2.5 mm	
278a	433	Wired	Split		Grating a=2.1 on the free path	5×2.5 mm	
278b	433	Wired	Solid		Grating a=1	5×.2.5 mm	

SRL	Freq [MHz]	Config.	IDT	Reflector	DESCRIPTION	SIZE	LEdit Design
278c	433	Wired	Split		Dual delay line 4mm UDIDTs (Reflectors on th sides of the IDTs) 208c1 adapted	5×.2.5 mm	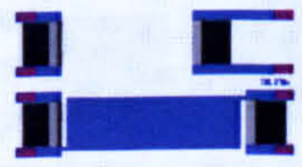
279	433	Wired	Solid		Dual delay line same length Smaller metalized area	5×.2.5 mm	
279a	433	Wired	Solid		Dual delay line same length Oxide opening	5×2.5 mm	
280	433	Wired	Solid	Floating electrode	Dual delay line same length Reverse of 279 (opening area 50λ)	5×3 mm	
280a	433	Wired	Solid		Dual delay line same length Reverse of 279 (smaller opening area)	5×2.5 mm	
280b	433	Wired	Solid	opening area 50λ)	Dual delay line same length Reverse of 279 (smaller opening area) + Opening in oxide	5×2.5 mm	
281	433	Wired			Mixed delay Line 5x1mm	5×3.1 mm	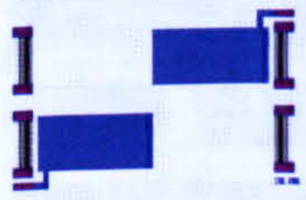
282	433	Wired	Solid	Grating for trapping	Dual delay line same length Open gratings λg=8.4=>a=2.1=>f=495MHz	5×2.5 mm	
282a	433	Wired	Solid	Grating for trapping a=2.1=>f=495 MHz	Dual delay line same length L=450λ=4320um d(IDT to metalized)=λ/4 'looks like metalized all'	5×2.5 mm	
282b	433	Wired	Solid	Grating for trapping a=2.1=>f=495 MHz	Dual delay line same length L=450λ=4320 μm d (IDT to metalized) =5λ=48um	5×2.5 mm	
282c	433	Wired	Solid	Grating for trapping a=2.3=> f=452.17 MHz	Dual delay line same length L=450λ=4320um d (IDT to metalized) =5λ=48um	5×2.5 mm	
Resonators							
283	433	Wired	Solid		Two port resonator 5x1mm	5×3 mm	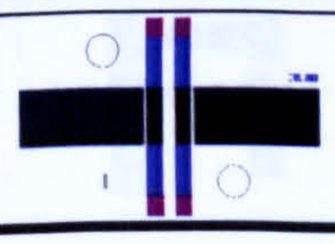

SRL	Freq [MHz]	Config.	IDT	Reflector	DESCRIPTION	SIZE	LEdit Design
284	433	Wired	Solid		Dual resonator 5x1mm Open and metalized cavities	3.7×1.4 mm	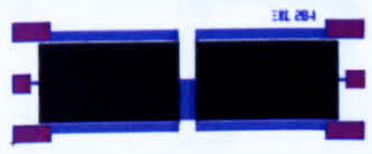
285	433	Wired	Solid	Grating inside the cavity a=2.1	Dual resonator 5x1mm Open (graitings) and metalized cavities	3.7×1.4 mm	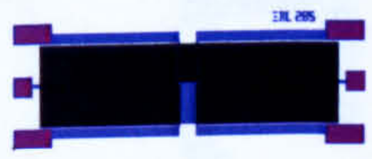
286	433	Wired	Solid	Grating same width as IDT and reflectors	Dual resonator 5x1mm Open and metalized cavities	3.7×1.4 mm	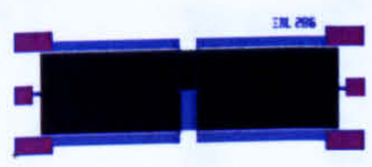
287	869	Wired	Solid	2traping electrodes on the free path	Dual delay line same length	5×3.4 mm	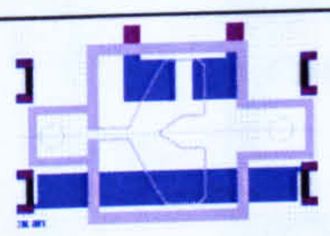
288	433	Wired	FEUDT		Opening area =50λ=480µm	5×2.5 mm	
288a	433	Wired	FEUDT	Metalization from last finger d=7λ/2	Opening area =50λ=480µm	5×2.5 mm	
288b	433	Wired	FEUDT	Modulatig electrodes	Opening area =50λ=480um	5×3 mm	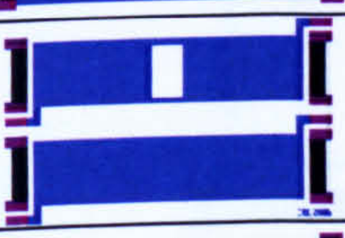
288c	433	Wired	FEUDT	Full free path	Opening area =50λ=480um	5×2.5 mm	
289	λ=12um	Wired	FEUDT 315IDT	Modulatig electrodes	IDT to metal area = λ=12um Opening area =50λ=480um	5×3 mm	
289a	λ=12um	Wired	FEUDT 315IDT	Modulatig electrodes	Free path	5×2.85 mm	
290-298	869	Wired	Solid		IDT to IDT distance L=200λ // +d=λ/8	1.5x1.5 mm	
300-304	869	Wired	Solid UDT	Short Circuit	L=200λ +d=λ/4 Reflectors on the sides of the IDTs	1.5x1.5 mm	

SRL	Freq [MHz]	Config.	IDT	Reflector	DESCRIPTION	SIZE	LEdit Design
305-309	869	Wired	Solid UDT	Open Circuit	L=200λ +d=λ/4 Reflectors on the sides of the IDTs	1.5x1.5 mm	
319-314	869	Wired	Solid UDT	PNR	L=200λ +d=λ/4 Reflectors on the sides of the IDTs	1.5x1.5 mm	
302a	869	Wired	Solid UDT	Short Circuit	No reflector for output IDT	1.5x1.5 mm	
307a	869	Wired	Solid UDT	Open Circuit	No reflector for output IDT	1.5x1.5 mm	
312a	869	Wired	Solid UDT	PNR	No reflector for output IDT	1.5x1.5 mm	
310a	869	Wired	Solid UDT		No OUTPUT reflectors	1.5x1.5 mm	
315-322	869	Wireless	Solid UDT	OC	L=200λ +d=λ/8	1.5x1.5 mm	
315a-322a	869	Wireless		PNR	L=200λ +d=λ/8	1.5x1.5 mm	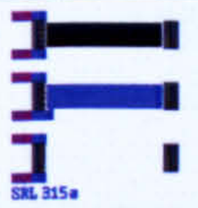
315b-322b	869	Wireless		SC	L=200λ +d=λ/8	1.5x1.5 mm	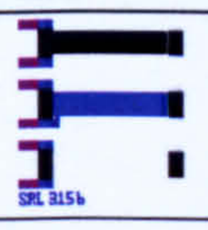
330		Wired	Solid IDT_3 Harm		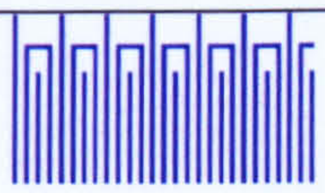 'snake' floating electrode???	5x2.5 mm	
550		Wired	Solid IDT_3 Harm		Input IDT as shown in picture // Output IDT standard solid fingers 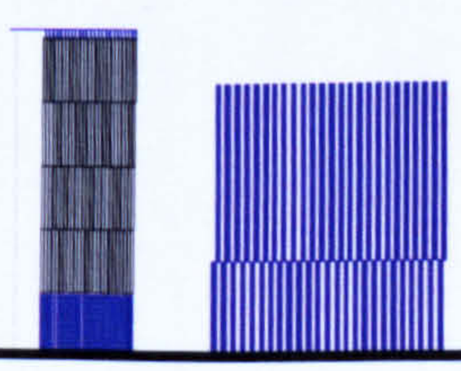	5x2.5 mm	

SRL	Freq [MHz]	Config.	IDT	Reflector	DESCRIPTION	SIZE	LEdit Design
551		Wired	Solid IDT_3 Harm		Both Input and Output IDTs as shown in picture 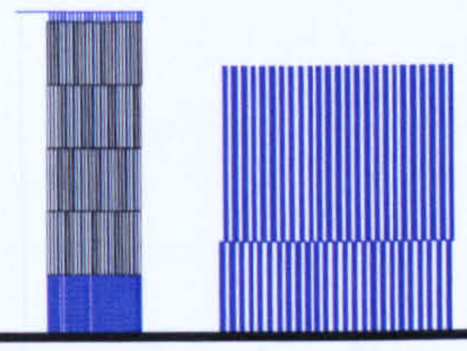	5x2.5 mm	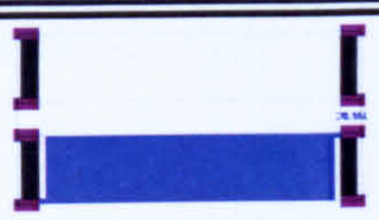

Appendix B:

B1: Dielectric constants of sucrose, acetic acid and sodium chloride solutions

B2: Dependent vs. independent data plots

B3: Generalised Model: SigmaStat Multiple Linear Regressions Reports

B4: Improved Model: SigmaStat Multiple Linear Regressions Reports

B5: Standardized coefficients of substance-dependent models

B1: Dielectric constants of sucrose, acetic acid and sodium chloride solutions

The dielectric constants (static relative permittivity) of the solutions analysed in Chapter 7, have been obtained from experimental data reported in literature as follows:

Sucrose solutions:
Dielectric constant of sucrose solutions at 20°C was found in Timmermans with a reference to an article of Malmberg and Maryott. The equation determined to fit the experimental data with an average deviation of 0.01 and maximum deviation of less than 0.03 was:

$$\varepsilon(\text{sucrose})=\varepsilon_w-0.226\cdot C-[6.75\cdot10^{-4}-1.5\cdot10^{-5}(t-25)]\cdot C^2-[1.09\cdot10^{-5}+4\cdot10^{-8}(t-25)]\cdot C^3$$

where ε_w is the dielectric constant of water at the temperature t, in degrees Celsius, and C is the weight percent of sucrose. This equation has been used to obtain the dielectric constants of sucrose solutions at 20°C for concentrations in the 0.5-5 weight % interval. The obtained values are expected to be accurate to 0.05 percent or better.

Concentration (wt %)	0.5%	1%	3%	5%
Dielectric constant ε	80.286	80.17	79.715	79.249

Acetic Acid solutions
Timmermans gives values for the dielectric constant of several concentrations of acetic acid in water at 15°C. These data are plotted in Figure B1.1 as grey circles along with their linear regression line.

Values for the static permittivity of acetic acid solutions at 20°C could not be found in the reviewed literature. The only available data for this substance were the ones for pure water and pure acetic acid. Pure water has a dielectric constant of 80.4 at 20°C, and 100% pure acetic acid has a dielectric constant of 6.2 at 20°C. A parallel plate capacitor model is used to compute the permittivity values for solutions with intermediate concentrations. This model is verified versus the Timmermans' temperature corrected estimates and good agreement was found for low concentrations (See Figure B1.1).

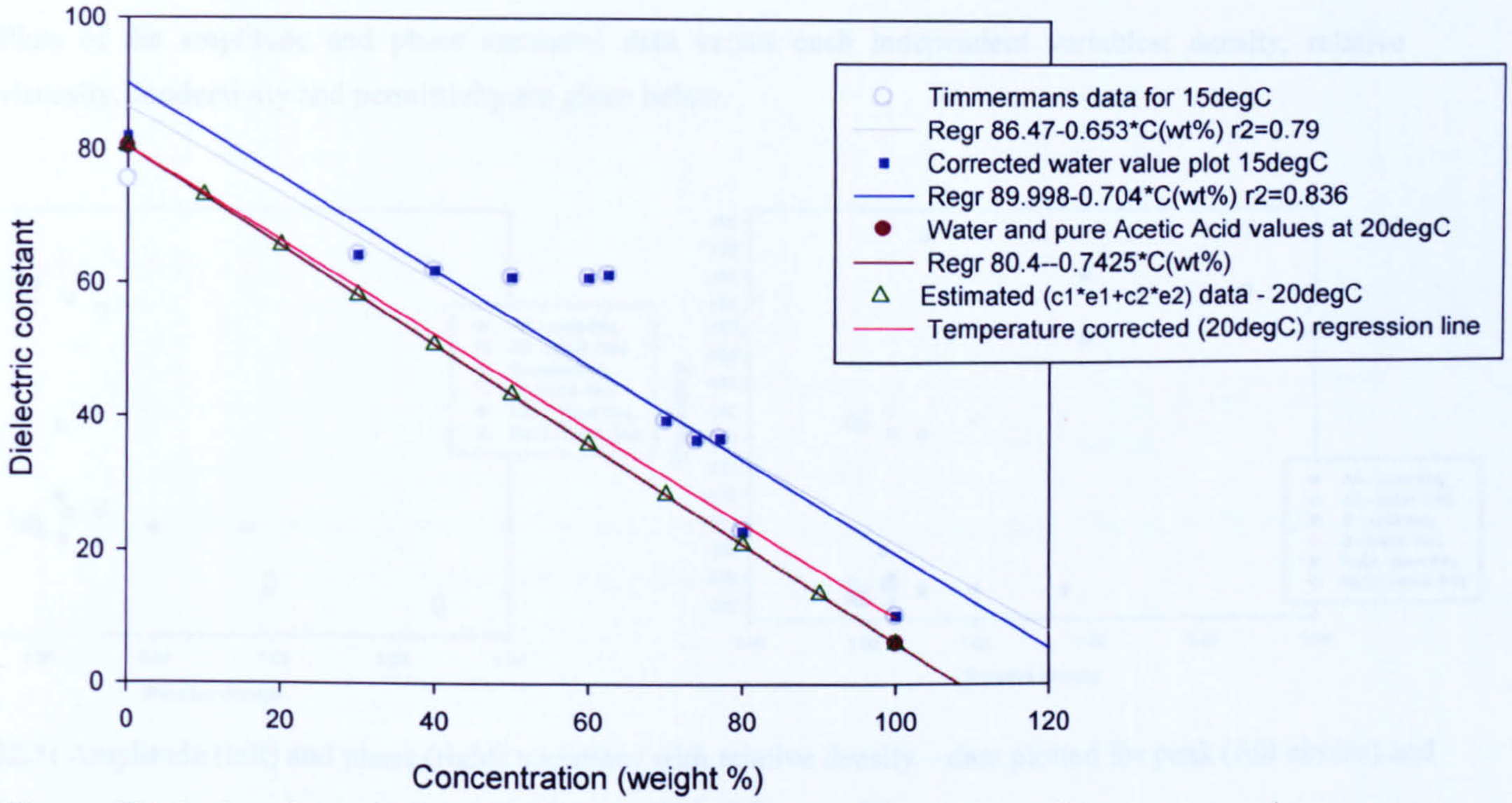

Figure B1.1: Acetic Acid solutions – dielectric constant variation with concentration

Sodium chloride solutions

Permittivity values for sodium chloride solutions were taken form the data reported by Hilland or was estimated using the reported model: ε_S=80.44-2.45C(wt%)

References:

Hilland J., "Simple sensor system for measuring the dielectric properties of saline solutions", Meas. Sci. Technol., 8 (1997), pp 901-910.

Malmberg C.G. and Maryott A.A., "Dielectric Constants of Aqueous Solutions of Dextrose and Sucrose", Journal of Reasearch of the National Bureau of Standards, vol. 45, No. 4, p. 299, (1950).

Timmermans J., *The Physico-chemical Constants of Binary Systems in Concentrated Solutions*, volume 4, London, Interscience Publishers (1960).

B2: Dependent vs. independent data plots

Plots of the amplitude and phase measured data versus each independent variables: density, relative viscosity, conductivity and permittivity are given below.

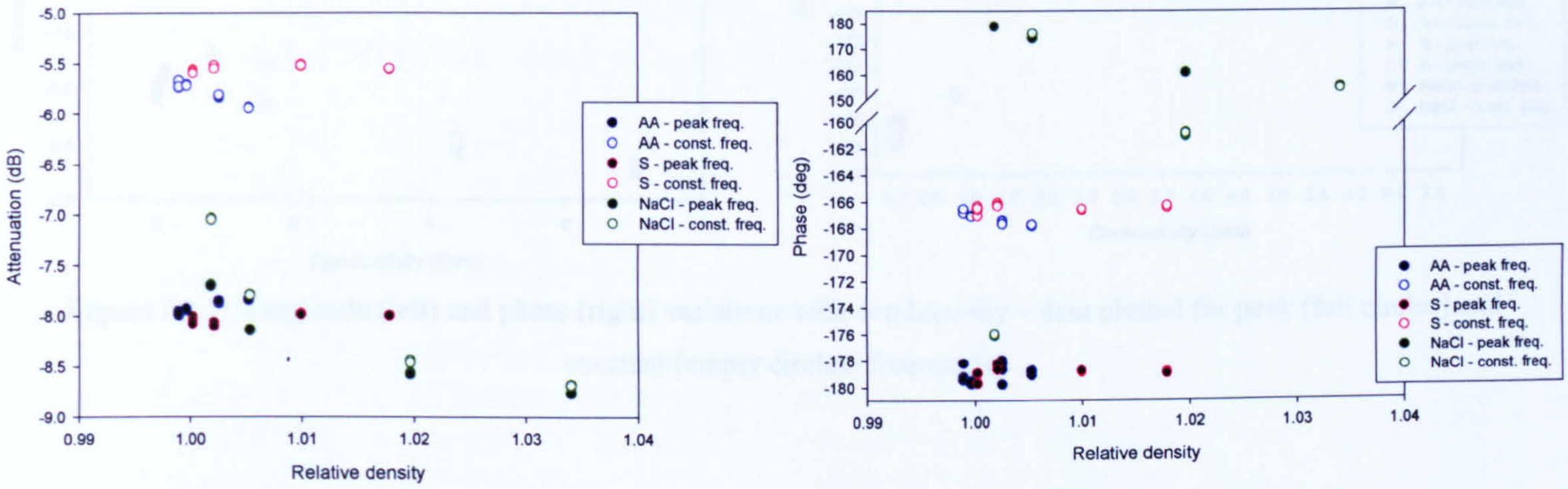

Figure B2.1: Amplitude (left) and phase (right) variations with relative density – data plotted for peak (full circles) and constant (empty circles) frequencies

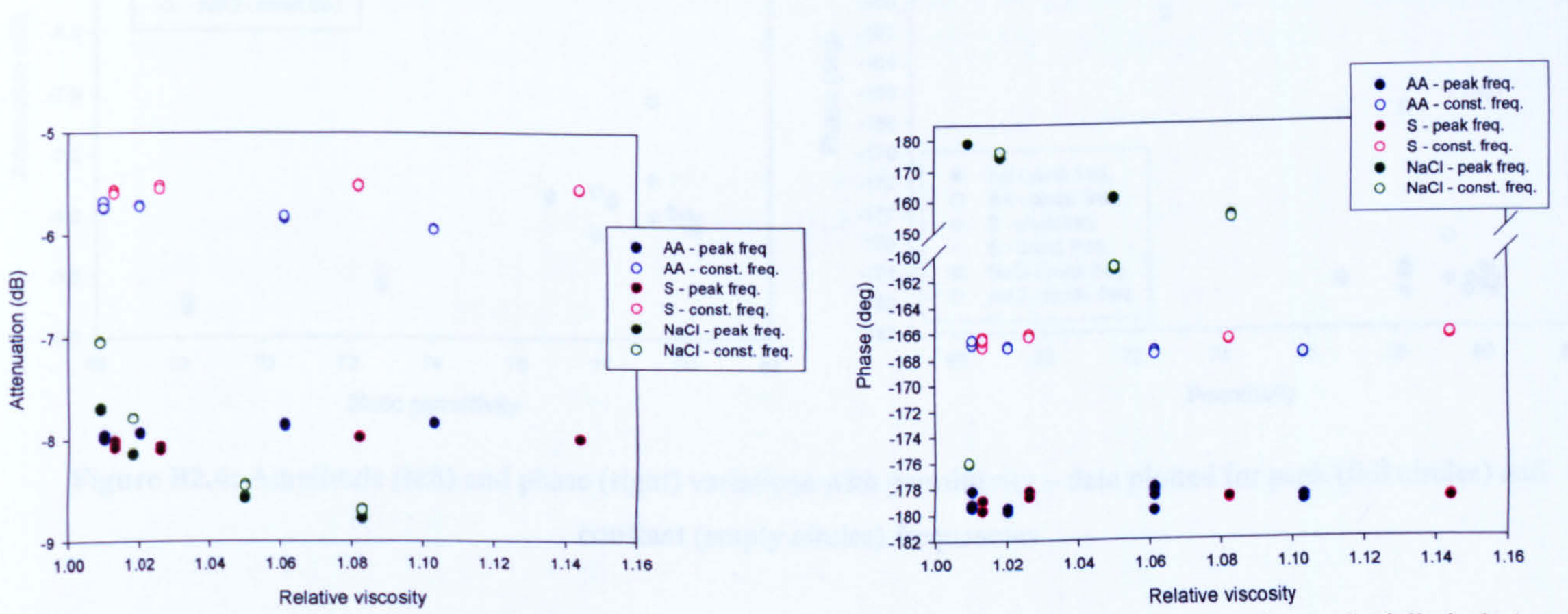

Figure B2.2: Amplitude (left) and phase (right) variations with relative viscosity – data plotted for peak (full circles) and constant (empty circles) frequencies

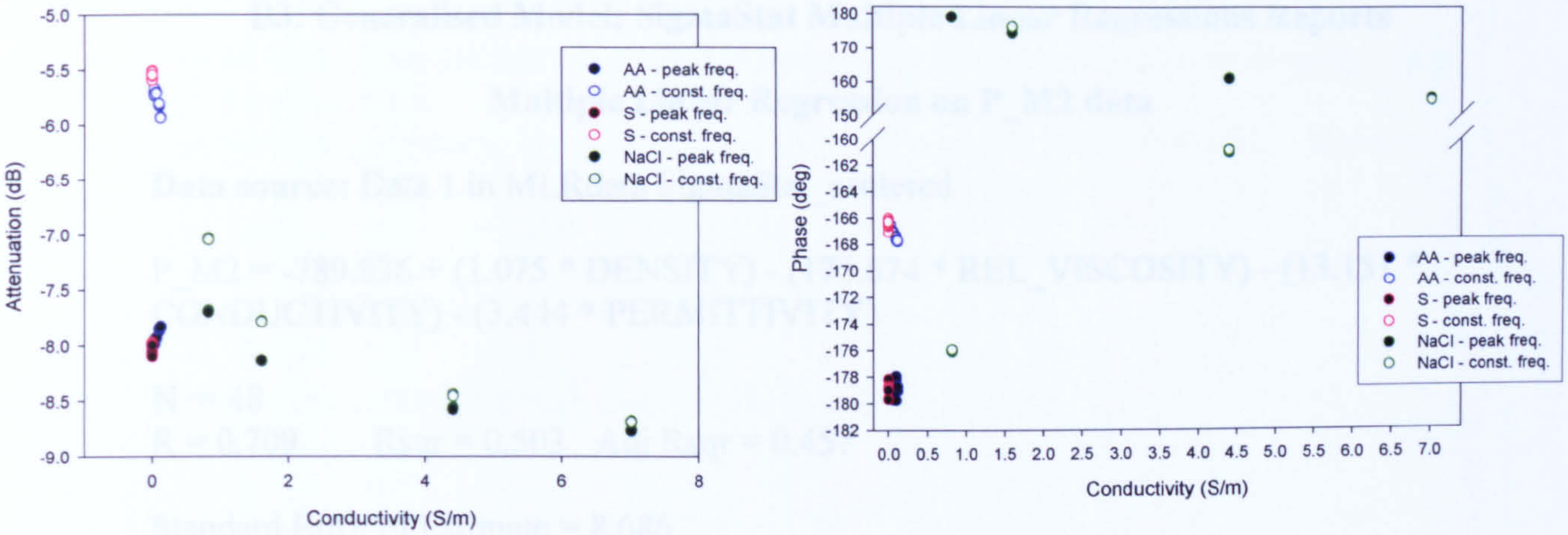

Figure B2.3: Amplitude (left) and phase (right) variations with conductivity – data plotted for peak (full circles) and constant (empty circles) frequencies

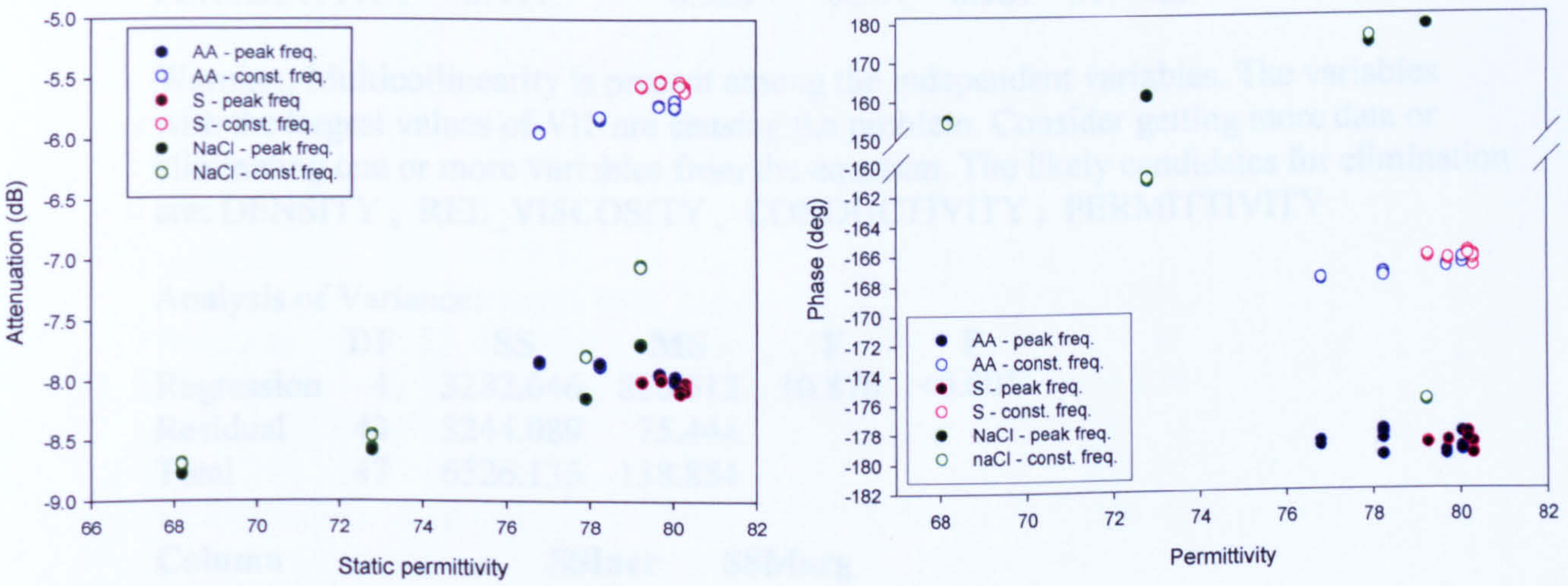

Figure B2.4: Amplitude (left) and phase (right) variations with permittivity – data plotted for peak (full circles) and constant (empty circles) frequencies

B3: Generalised Model: SigmaStat Multiple Linear Regressions Reports

Multiple Linear Regression on P_M2 data

Data source: Data 1 in MLRdata SigmaStat_centered

P_M2 = -789.836 + (1.075 * DENSITY) - (173.674 * REL_VISCOSITY) - (13.151 * CONDUCTIVITY) - (3.444 * PERMITTIVITY)

N = 48
R = 0.709 Rsqr = 0.503 Adj Rsqr = 0.457

Standard Error of Estimate = 8.686

	Coefficient	Std. Error	t	P	VIF
Constant	-789.836	1324.253	-0.596	0.554	
DENSITY	1.075	2.163	0.497	0.622	308.264
REL_VISCOSITY	-173.674	357.811	-0.485	0.630	142.541
CONDUCTIVITY	-13.151	17.606	-0.747	0.459	905.533
PERMITTIVITY	-3.444	6.328	-0.544	0.589	311.462

Warning: Multicollinearity is present among the independent variables. The variables with the largest values of VIF are causing the problem. Consider getting more data or eliminating one or more variables from the equation. The likely candidates for elimination are: DENSITY , REL_VISCOSITY , CONDUCTIVITY , PERMITTIVITY

Analysis of Variance:

	DF	SS	MS	F	P
Regression	4	3282.046	820.512	10.876	<0.001
Residual	43	3244.089	75.444		
Total	47	6526.135	138.854		

Column	SSIncr	SSMarg
DENSITY	2209.722	18.640
REL_VISCOSITY	859.674	17.774
CONDUCTIVITY	190.310	42.096
PERMITTIVITY	22.340	22.340

The dependent variable P_M2 can be predicted from a linear combination of the independent variables:

	P
DENSITY	0.622
REL_VISCOSITY	0.630
CONDUCTIVITY	0.459
PERMITTIVITY	0.589

Not all of the independent variables appear necessary (or the multiple linear model may be underspecified).
The following appear to account for the ability to predict P_M2 (P < 0.05): [None]

Normality Test: Failed (P = <0.001)

Constant Variance Test: Failed (P = <0.001)

Power of performed test with alpha = 0.050: 1.000

Multiple Linear Regression on A_M1 data

Data source: Data 1 in Notebook 1

A_M1 = 58.388 - (0.0999 * DENSITY) + (15.319 * REL_VISCOSITY) + (0.594 * CONDUCTIVITY) + (0.224 * PERMITTIVITY)

N = 48

R = 0.933 Rsqr = 0.870 Adj Rsqr = 0.858

Standard Error of Estimate = 0.112

	Coefficient	Std. Error	t	P	VIF
Constant	58.388	17.004	3.434	0.001	
DENSITY	-0.0999	0.0278	-3.596	<0.001	308.264
REL_VISCOSITY	15.319	4.595	3.334	0.002	142.541
CONDUCTIVITY	0.594	0.226	2.627	0.012	905.533
PERMITTIVITY	0.224	0.0813	2.758	0.009	311.462

Warning: Multicollinearity is present among the independent variables. The variables with the largest values of VIF are causing the problem. Consider getting more data or eliminating one or more variables from the equation. The likely candidates for elimination are: DENSITY , REL_VISCOSITY , CONDUCTIVITY , PERMITTIVITY

Analysis of Variance:

	DF	SS	MS	F	P
Regression	4	3.570	0.893	71.756	<0.001
Residual	43	0.535	0.0124		
Total	47	4.105	0.0873		

Column	SSIncr	SSMarg
DENSITY	2.726	0.161

REL_VISCOSITY	0.741	0.138
CONDUCTIVITY	0.00848	0.0858
PERMITTIVITY	0.0946	0.0946

The dependent variable A_M1 can be predicted from a linear combination of the independent variables:

	P
DENSITY	<0.001
REL_VISCOSITY	0.002
CONDUCTIVITY	0.012
PERMITTIVITY	0.009

All independent variables appear to contribute to predicting A_M1 ($P < 0.05$).

Normality Test: Failed ($P = 0.003$)

Constant Variance Test: Failed ($P = <0.001$)

Power of performed test with alpha = 0.050: 1.000

Multiple Linear Regression on P_M1 data

Data source: Data 1 in Notebook 1

P_M1 = 709.102 - (1.440 * DENSITY) + (228.027 * REL_VISCOSITY) + (4.975 * CONDUCTIVITY) + (3.998 * PERMITTIVITY) + (0.404 * Conduct2)

There are independent variables in the regression model that appear to be highly correlated with other independent variables or have no variability. These variables have been removed from the regression model. The specific variables are:
Removed Rel_Visc*DENSITY because it is collinear.

Removed Permittiv2 because it is collinear.

N = 48

R = 0.997 Rsqr = 0.995 Adj Rsqr = 0.994

Standard Error of Estimate = 0.673

	Coefficient	**Std. Error**	**t**	**P**	**VIF**
Constant	709.102	166.984	4.247	<0.001	
DENSITY	-1.440	0.275	-5.244	<0.001	826.667

REL_VISCOSITY	228.027	44.399	5.136	<0.001	365.241
CONDUCTIVITY	4.975	2.009	2.477	0.017	1961.314
PERMITTIVITY	3.998	0.799	5.004	<0.001	825.964
Conduct2	0.404	0.0483	8.364	<0.001	48.832

Warning: Multicollinearity is present among the independent variables. The variables with the largest values of VIF are causing the problem. Consider getting more data or eliminating one or more variables from the equation. The likely candidates for elimination are: DENSITY , REL_VISCOSITY , CONDUCTIVITY , PERMITTIVITY , Conduct2

Analysis of Variance:

	DF	**SS**	**MS**	**F**	**P**
Regression	5	3516.462	703.292	1551.371	<0.001
Residual	42	19.040	0.453		
Total	47	3535.503	75.223		

Column	**SSIncr**	**SSMarg**
DENSITY	2447.430	12.465
REL_VISCOSITY	824.859	11.958
CONDUCTIVITY	209.395	2.782
PERMITTIVITY	3.066	11.353
Conduct2	31.713	31.713

The dependent variable P_M1 can be predicted from a linear combination of the independent variables:

	P
DENSITY	<0.001
REL_VISCOSITY	<0.001
CONDUCTIVITY	0.017
PERMITTIVITY	<0.001
Conduct2	<0.001

All independent variables appear to contribute to predicting P_M1 ($P < 0.05$).

Normality Test: Passed ($P = 0.619$)

Constant Variance Test: Failed ($P = 0.031$)

Power of performed test with alpha = 0.050: 1.000

B4: Improved Model: SigmaStat Multiple Linear Regressions Reports

Multiple Linear Regression on A_M1

Data source: Data 1 in MLRdata

A_M1 = 133.755 - (0.263 * DENSITY) + (2.308 * SQRT(Visc*Dens)) + (1.462 * CONDUCTIVITY) + (0.0259 * Conduct2) + (0.593 * PERMITTIVITY)

N = 48

R = 0.948 Rsqr = 0.900 Adj Rsqr = 0.888

Standard Error of Estimate = 0.099

	Coefficient	Std. Error	t	P	VIF
Constant	133.755	25.950	5.154	<0.001	
DENSITY	-0.263	0.0502	-5.232	<0.001	1278.973
SQRT(Visc*Dens)	2.308	0.453	5.097	<0.001	568.478
CONDUCTIVITY	1.462	0.316	4.634	<0.001	2237.864
Conduct2	0.0259	0.00730	3.553	<0.001	51.396
PERMITTIVITY	0.593	0.126	4.717	<0.001	945.952

Warning: Multicollinearity is present among the independent variables. The variables with the largest values of VIF are causing the problem. Consider getting more data or eliminating one or more variables from the equation. The likely candidates for elimination are: DENSITY , SQRT(Visc*Dens) , CONDUCTIVITY , Conduct2 , PERMITTIVITY

Analysis of Variance:

	DF	SS	MS	F	P
Regression	5	3.693	0.739	75.307	<0.001
Residual	42	0.412	0.00981		
Total	47	4.105	0.0873		

Column	SSIncr	SSMarg	
DENSITY	2.726	0.269	
SQRT(Visc*Dens)		0.738	0.255
CONDUCTIVITY		0.00953	0.211
Conduct2	0.00138	0.124	
PERMITTIVITY	0.218	0.218	

The dependent variable A_M1 can be predicted from a linear combination of the independent variables:

	P
DENSITY	<0.001
SQRT(Visc*Dens)	<0.001

CONDUCTIVITY<0.001
Conduct2 <0.001
PERMITTIVITY<0.001

All independent variables appear to contribute to predicting A_M1 (P < 0.05).

Normality Test: Failed (P = <0.001)

Constant Variance Test: Passed (P = 0.849)

Power of performed test with alpha = 0.050: 1.000

Multiple Linear Regression on P_M1

Data source: Data 1 in MLRdata

P_M1 = 790.494 - (1.847 * DENSITY) + (16.384 * SQRT(Visc*Dens)) + (6.079 * CONDUCTIVITY) + (0.420 * Conduct2) + (4.446 * PERMITTIVITY)

N = 48

R = 0.997 Rsqr = 0.995 Adj Rsqr = 0.994

Standard Error of Estimate = 0.658

	Coefficient	Std. Error	t	P	VIF
Constant	790.494	172.292	4.588	<0.001	
DENSITY	-1.847	0.334	-5.540	<0.001	1278.973
SQRT(Visc*Dens)	16.384	3.007	5.449	<0.001	568.478
CONDUCTIVITY	6.079	2.095	2.901	0.006	2237.864
Conduct2	0.420	0.0484	8.668	<0.001	51.396
PERMITTIVITY	4.446	0.835	5.325	<0.001	945.952

Warning: Multicollinearity is present among the independent variables. The variables with the largest values of VIF are causing the problem. Consider getting more data or eliminating one or more variables from the equation. The likely candidates for elimination are: DENSITY , SQRT(Visc*Dens) , CONDUCTIVITY , Conduct2 , PERMITTIVITY

Analysis of Variance:

	DF	SS	MS	F	P
Regression	5	3517.343	703.469	1626.994	<0.001

Residual	42	18.160	0.432
Total	47	3535.503	75.223

Column	**SSIncr**	**SSMarg**
DENSITY	2447.430	13.269
SQRT(Visc*Dens)	822.351	12.838
CONDUCTIVITY	211.919	3.639
Conduct2	23.384	32.483
PERMITTIVITY	12.259	12.259

The dependent variable P_M1 can be predicted from a linear combination of the independent variables:

	P
DENSITY	<0.001
SQRT(Visc*Dens)	<0.001
CONDUCTIVITY	0.006
Conduct2	<0.001
PERMITTIVITY	<0.001

All independent variables appear to contribute to predicting P_M1 ($P < 0.05$).

Normality Test: Passed ($P = 0.778$)

Constant Variance Test: Failed ($P = 0.015$)

Power of performed test with alpha = 0.050: 1.000

Multiple Linear Regression on A_M2

Data source: Data 1 in MLRdata

A_M2 = -365.909 + (0.686 * DENSITY) - (6.061 * SQRT(Visc*Dens)) - (5.484 * CONDUCTIVITY) + (0.0399 * Conduct2) - (1.659 * PERMITTIVITY)

N = 48

R = 0.997 Rsqr = 0.994 Adj Rsqr = 0.993

Standard Error of Estimate = 0.099

	Coefficient	**Std. Error**	**t**	**P**	**VIF**
Constant	-365.909	26.049	-14.047	<0.001	

DENSITY	0.686	0.0504	13.612	<0.001	1278.973
SQRT(Visc*Dens)	-6.061	0.455	-13.331	<0.001	568.478
CONDUCTIVITY	-5.484	0.317	-17.310	<0.001	2237.864
Conduct2	0.0399	0.00732	5.449	<0.001	51.396
PERMITTIVITY	-1.659	0.126	-13.147	<0.001	945.952

Warning: Multicollinearity is present among the independent variables. The variables with the largest values of VIF are causing the problem. Consider getting more data or eliminating one or more variables from the equation. The likely candidates for elimination are: DENSITY , SQRT(Visc*Dens) , CONDUCTIVITY , Conduct2 , PERMITTIVITY

Analysis of Variance:

	DF	**SS**	**MS**	**F**	**P**
Regression	5	64.249	12.850	1300.074	<0.001
Residual	42	0.415	0.00988		
Total	47	64.664	1.376		

Column	**SSIncr**	**SSMarg**
DENSITY	28.218	1.831
SQRT(Visc*Dens)	20.207	1.757
CONDUCTIVITY	7.072	2.961
Conduct2	7.044	0.293
PERMITTIVITY	1.708	1.708

The dependent variable A_M2 can be predicted from a linear combination of the independent variables:

	P
DENSITY	<0.001
SQRT(Visc*Dens)	<0.001
CONDUCTIVITY	<0.001
Conduct2	<0.001
PERMITTIVITY	<0.001

All independent variables appear to contribute to predicting A_M2 ($P < 0.05$).

Normality Test: Passed ($P = 0.065$)

Constant Variance Test: Passed ($P = 0.285$)

Power of performed test with alpha = 0.050: 1.000

Multiple Linear Regression on P_M2

Data source: Data 1 in MLRdata

P_M2 = -11448.481 + (21.936 * DENSITY) - (195.665 * SQRT(Visc*Dens)) - (134.661 * CONDUCTIVITY) - (3.749 * Conduct2) - (55.162 * PERMITTIVITY)

N = 48

R = 0.948 Rsqr = 0.899 Adj Rsqr = 0.887

Standard Error of Estimate = 3.953

	Coefficient	Std. Error	t	P	VIF
Constant	-11448.481	1035.745	-11.053	<0.001	
DENSITY	21.936	2.005	10.941	<0.001	1278.973
SQRT(Visc*Dens)	-195.665	18.075	-10.825	<0.001	568.478
CONDUCTIVITY	-134.661	12.596	-10.691	<0.001	2237.864
Conduct2	-3.749	0.291	-12.874	<0.001	51.396
PERMITTIVITY	-55.162	5.019	-10.991	<0.001	945.952

Warning: Multicollinearity is present among the independent variables. The variables with the largest values of VIF are causing the problem. Consider getting more data or eliminating one or more variables from the equation. The likely candidates for elimination are: DENSITY , SQRT(Visc*Dens) , CONDUCTIVITY , Conduct2 , PERMITTIVITY

Analysis of Variance:

	DF	SS	MS	F	P
Regression	5	5869.864	1173.973	75.132	<0.001
Residual	42	656.272	15.626		
Total	47	6526.135	138.854		

Column	SSIncr	SSMarg
DENSITY	2209.722	1870.524
SQRT(Visc*Dens)	859.614	1830.993
CONDUCTIVITY	190.717	1785.905
Conduct2	722.286	2589.754
PERMITTIVITY	1887.524	1887.524

The dependent variable P_M2 can be predicted from a linear combination of the independent variables:

	P
DENSITY	<0.001
SQRT(Visc*Dens)	<0.001
CONDUCTIVITY	<0.001
Conduct2	<0.001

PERMITTIVITY<0.001

All independent variables appear to contribute to predicting P_M2 ($P < 0.05$).

Normality Test: Failed ($P = 0.003$)

Constant Variance Test: Passed ($P = 0.573$)

Power of performed test with alpha = 0.050: 1.000

B5: Standardized coefficients of substance-dependent models

Sucrose Model Standardized Coefficients

	b1*ρ	b3*σ	b4*e
A_M1	207.3344	-0.69863	207.2411
P_M1	-105.414	-0.93639	-104.629
A_M2	117.813	-1.93375	119.0969
P_M2	-204.824	0.207417	-205.032

Acetic Acid Standardized Coefficients

	b1*ρ	b3*σ	b4*e
A_M1	3.566857	0.836703	3.422555
P_M1	45.43358	-0.48074	44.33579
A_M2	-3.22705	0.587676	-1.67646
P_M2	3.634289	-1.32856	3.286333

Sodium Chloride Standardized Coefficients

	b1*ρ	b3*σ	b4*e
A_M1	12.01049	-25.4501	-12.5024
P_M1	5.654309	-1.8486	4.788432
A_M2	13.62292	-27.8529	-13.31
P_M2	-18.8644	-41.8497	-60.2258